UNIVERSITY OF Southampton

University of Southampton Research Repository
ePrints Soton

Copyright © and Moral Rights for this thesis are retained by the author and/or other copyright owners. A copy can be downloaded for personal non-commercial research or study, without prior permission or charge. This thesis cannot be reproduced or quoted extensively from without first obtaining permission in writing from the copyright holder/s. The content must not be changed in any way or sold commercially in any format or medium without the formal permission of the copyright holders.

When referring to this work, full bibliographic details including the author, title, awarding institution and date of the thesis must be given e.g.

AUTHOR (year of submission) "Full thesis title", University of Southampton, name of the University School or Department, PhD Thesis, pagination

http://eprints.soton.ac.uk

UNIVERSITY OF SOUTHAMPTON

Faculty of Engineering, Science & Mathematics

School of Engineering Sciences

Identification of Damage in Composite Materials using Thermoelastic Stress Analysis

by

Trystan Ross Emery

Thesis for the degree of Doctor of Philosophy

May 2007

UNIVERSITY OF SOUTHAMPTON

ABSTRACT

Faculty of Engineering, Science & Mathematics

School of Engineering Sciences

Doctor of Philosophy

Identification of Damage in Composite Materials
using Thermoelastic Stress Analysis

by Trystan Ross Emery

A quantitative damage assessment methodology for composite materials has been achieved using Thermoelastic Stress Analysis (TSA). The TSA technique provides full-field data which is collected in a non-contacting and real time manner. The damage assessment methodology proposed requires a means of calibrating and temperature correcting the thermoelastic signal; these are developed and presented in this thesis.

The thermoelastic theory for calibrating thermoelastic data from orthotropic bodies has traditionally been based on a stress formulation. There are difficulties in calibrating orthotropic materials in this manner and an alternative calibration routine has been devised and validated. The calibration routine provides the thermoelastic theory as a function of strain and permits a simplified calibration route as the laminate strains are the basis and can be measured in a straightforward manner.

During damage propagation in laminated structures the specimen heats. The increase in temperature has a significant effect on the thermoelastic data and necessitates that the thermoelastic data be corrected to remove the effect of temperature from the data. A routine is developed that enables the correction of the thermoelastic data in a point-by-point manner.

By combining the strain calibration and temperature correction procedures a damage assessment methodology has been devised. The application of the methodology is demonstrated on glass / epoxy laminate specimens that are fatigue damaged and the damage state assessed using this method; the extent and type of damage is verified qualitatively using visual inspection methods. The work described is applicable to any orthotropic material. The effect of fatigue damage is assessed by periodically collecting thermoelastic data during the specimen life. This data is analysed using damage metrics based on the calibrated strain obtained from the TSA.

The wider application of the TSA damage assessment methodology is considered by assessing the ability to locate subsurface damage. A complementary IR technique is used in conjunction with TSA known as Pulse Phase Thermography (PPT). Initial studies demonstrate the ability to resolve the spatial extents of subsurface damage. The purpose of this step is to guide TSA to areas of concern that can subsequently be assessed using the damage metrics to characterise the effect of damage on the residual life of the component.

The strain calibration and temperature correction methods that enable TSA to be applied quantitatively to damaged composite materials have not been accomplished prior to this work. They provide novel methods by which TSA data can be assessed, and their application is not restricted to damage studies alone. The ability to temperature correct TSA data has been shown to be of vital importance if thermoelastic data is to be compared in a quantitative fashion. The strain calibration procedure presented will enable thermoelastic studies to be reported quantitatively and expand the application of TSA particularly in validation studies. The damage assessment methodology presented represents a step forward in the application of TSA to the damage assessment of composite materials.

Contents

List of figures

List of tables

DECLARATION OF AUTHORSHIP

I, *Trystan Ross Emery*, declare that the thesis entitled

Identification of Damage in Composite Materials using Thermoelastic Stress Analysis

and the work presented in the thesis are both my own, and have been generated by me as the result of my own original research. I confirm that:

this work was done wholly or mainly while in candidature for a research degree at this University;

where any part of this thesis has previously been submitted for a degree or any other qualification at this University or any other institution, this has been clearly stated;

where I have consulted the published work of others, this is always clearly attributed;

where I have quoted from the work of others, the source is always given. With the exception of such quotations, this thesis is entirely my own work;

I have acknowledged all main sources of help;

where the thesis is based on work done by myself jointly with others, I have made clear exactly what was done by others and what I have contributed myself;

parts of this work have been published (Appendix E)

Signed: ……..

Date:…….

Acknowledgements

I would like to express my gratitude to my supervisor Dr Janice Dulieu-Barton for her reserve of patience, skill and wide ranging guidance over the course of this work. In addition I would also like to thank Dr Paul Cunningham and Dr Simon Quinn for their input.

My gratitude is also due to Brad Boyce of Stress Photonics for providing expertise on the intricacies of the DeltaTherm system. I would also like to acknowledge the Engineering and Physical Science Research Council (EPSRC) for loaning the DeltaTherm system and FLIR infra-red equipment.

Thanks to the technical guys; in particular Erik Roszkowiak and Dave Beckett in the laboratory, Clive Stafford and James Rabbetts for the provision of electronic know-how and equipment, and James Chitty and his team in the workshop.

I am grateful to the TSA users group at the University of Southampton for the incubation of ideas and discussion; in particular thanks to Moss and Jimmy for mutual knowledge transfer regarding the DeltaTherm system.

I would like to thank my office mates and the Fluid Structure Interaction group who over the years have provided an excellent sounding board, knowledge pool and welcomed distraction.

Finally I would like to extend my special gratitude to my parents and family for their ongoing support and thoughtful reassurance. I am also indebted to Jess who has provided loving motivation and bafflement for the work contained within.

To all involved – thanks, Trystan

Notation

Symbol	Meaning	Units
c	Speed of light	ms^{-1}
k	Midplane curvatures	-
n	Temperature correction power index	-
A	Isotropic calibration constant	$MPaU^{-1}$
A^*	Orthotropic calibration constant	$MPaU^{-1}$
A^{**}	Further orthotropic calibration constant	$MPaU^{-1}$
$[A]$	Extensional stiffness matrix	-
B	Stefan Boltzmann constant	$Wm^{-2}K^{-4}$
B^*	Strain calibration constant	$MPaU^{-1}$
B'	Stefan Boltzmann constant for photodetectors	$Wm^{-2}K^{-4}$
$[B]$	Coupling stiffness matrix	-
C_1	First radiation constant	Wm^2
C_2	Second radiation constant	mK
C_ε	Specific heat at constant strain	$Jkg^{-1}K^{-1}$
C_p	Specific heat at constant pressure	$Jkg^{-1}K^{-1}$
$[C]$	Stiffness matrix	-
E	Young's modulus	MPa
G	Shear modulus	MPa
K	Thermoelastic constant	MPa^{-1}
N_b	Photon flux (blackbody)	$phs^{-1}m^{-2}sr^{-1}$
$[N]$	Load	kN
P	Pressure	MPa
Q^*	Heat input	J

Q_{ij}	Reduced stiffness terms	-
R	Temperature correction factor	-
R^*	Detector response factor ($_{SPATE}$ / $_{DT}$)	-
S	Thermoelastic signal	U
S_{m}	Thermoelastic signal modified by temperature	U
S_{c}	Corrected thermoelastic signal	U
S_0	Baseline thermoelastic signal	U
$[S^*]$	Stiffness matrix	-
T	Absolute temperature	K
T_m	Temperature (due to increase)	K
T_o	Baseline temperature	K
$[T]$	Transformation matrix	-
U	Uncalibrated thermoelastic signal	-
V	Volume	M^3
Z	Detector response factor	$phs^{-1}m^{-3}sr^{-1}K^{-1}V^{-1}$
α	Coefficient of linear thermal expansion	K^{-1}
ε	Direct strain	-
γ	Shear strain	-
η	Emissivity	-
λ	Wavelength	m
ρ	Density	kgm^{-3}
σ	Stress	MPa
$(\sigma_x + \sigma_y)$	Sum of principal stresses	MPa
$(\sigma_1 + \sigma_2)$	Sum of direct surface stresses in the principal material directions	MPa
$(\sigma_L + \sigma_T)$	Sum of the principal laminate stresses	MPa
τ	Shear stress	MPa
ν	Poisson's ratio	-
$\Delta( )$	Change in $( )$	-
Φ_b	Spectral radiant power (blackbody)	Wm^{-2}

Abbreviations

Abbreviation	Full version
AE	Acoustic Emission
ASCII	American Standard Code for Information Interchange
ASIP	Aircraft Structural Integrity Program
CCD	Charge Coupled Device
CFRP	Carbon Fibre Reinforced Polymer
CLT	Classical Laminate Theory
CMC	Ceramic Matrix Composite
CMT	Cadmium Mercury Telluride
DIC	Digital Image Correlation
DT1000	DeltaTherm 1000
DT1400	DeltaTherm 1400
EASA	European Aviation Safety Agency
EPSRC	Engineering Physical Sciences Research Council
ESPI	Electronic Speckle Pattern Interferometry
FAA	Federal Aviation Authority
FFT	Fast Fourier Transform
FPA	Focal Plane Array
FRP	Fibre Reinforced Polymer
GFRP	Glass Fibre Reinforced Polymer
InSb	Indium Antimonide
IR	Infra-red
IRT	Infra-red Thermography
MATLAB	Matrix Laboratory (MathWorks Trade name)
MT	Modulated Thermography
NDE	Non Destructive Evaluation
PPT	Pulse Phase Thermography
PT	Pulse Thermography

PTFE	Polytetrafluoroethylene
QWIP	Quantum Well IR Photodetector
SCF	Stress Concentration Factor
SP	Structural Polymer
SPATE	Stress Pattern Analysis by measurement of Thermal Emissions
TSA	Thermoelastic Stress Analysis
UD	Unidirectional
VBM	Vibration Based Methods

To my parents

Chapter 1

Introduction

1.1 Background and motivation

A composite material consists of two or more constituents, whose resultant mechanical performance and properties are designed to be superior to those of the constituent acting independently [1]. Composite materials are defined by their constituents; a typically stiff and strong reinforcement and a more compliant but weaker matrix. The composite materials discussed in this thesis, are classified in this manner as Fibre-Reinforced Polymer (FRP) composites. The ultimate strength and stiffness of a FRP component is a product of the fibre reinforcement, typically a fibre filament. The mechanical strength is therefore directional and can be optimised through the understanding of the fibre-reinforcement mechanical properties with respect to the loading axis. Through such an optimisation composite structures can provide excellent specific strength and stiffness making composite materials an attractive proposition in engineering design.

In general FRP composite materials have found application in structures where high mechanical performance and low weight [1] are of prime importance to the design. The aircraft industry has been at the forefront of exploiting high performance FRPs and it is here where the first documented use for structural composite components occurred. Composite structures were incorporated into commercial transport aircraft as part of the National Aeronautics and Space Administration (NASA) Aircraft Energy Efficiency

Program and entered into flight service during 1972-1986 [2]. The results from the programme indicated an excellent in-service performance during the 15-year evaluation period [3]. Following these initial developments and successes in the aerospace field, composite materials have since been applied in many engineering applications. Examples are illustrated in Figure 1.1: aircraft and aerospace industry [3] (Figure 1.1a), marine industry [4, 5] (Figure 1.1b), automotive industry [6] (Figure 1.1c), energy [7] (Figure 1.1d), and biomedical applications [8] (Figure 1.1e). They have also found application in the lucrative leisure market [9] in applications from luxury yachts to golf clubs.

a) Airbus A380

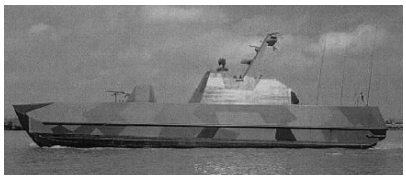

b) Skjold class patrol boat [5]

d) Wind turbine [7]

c) Formula 1 composite chassis [6]

e) Typical prosthetic leg [8]

Figure 1.1. Structures using composite components

The first generation of composite components had remained the preserve of non-critical secondary structures or in applications where longevity was not an issue. However, recently composite structures have been specified where structural integrity is crucial

throughout the component life. For example in 2002 a watershed came, again in the highly competitive aerospace industry, when Airbus Industry developed a new version of the A340 fitted with composite primary structures including the rear pressure bulkhead and keel beam [10] which are in-service. These primary components are safety critical and failure would result in major loss of life. It is therefore essential that designers understand the mechanics of failure in order to produce an optimal design that ensures safe operation whilst reducing weight.

The manner in which composite materials are known to degrade and subsequently fail is highly dependent on material configuration, e.g. stacking sequence, volume fraction and manufacture. A review of observed failure modes for composites is provided in Chapter 2. The reliability criteria for primary structures means that quality, reproducibility and predictability of behaviour over the lifetime of the structure must be guaranteed [1]. These requirements incur financial consequences and the ability to guarantee the quality must be balanced against the benefit of improved efficiency. Economically it is clear that the specification of composite structures cannot be made in isolation on increases in strength and performance alone but the cost of the overall weight reduction and subsequent savings must be offset against the full spectrum of operating expenses. A major operating expense is the cost of routine inspections of the FRP structure and assessing the condition in terms of the required structural performance. The inspection techniques currently available for assessing the condition of FRP structures are reviewed in Chapter 2.

The necessity to guarantee the performance of a composite component coupled with a current lack of understanding of the failure mechanisms (Chapter 2), has led to a damage tolerant approach being adopted by the aircraft industry [11]. The damage tolerant approach results in components that are conservatively designed. Furthermore in operation these components tend to be prematurely replaced [12] resulting in considerable cost to the operator, as at present there is an inability to reliably assess the residual life of the component. It has been reported [13] that the real fatigue life of a composite component can easily exceed the predicted fatigue life by a factor of two. The development of a quantitative damage assessment procedure would allow the current time-based maintenance philosophies to evolve into potentially more cost effective condition-based maintenance philosophies [14].

Taking advantage of the full life performance without compromising safety clearly necessitates an extensive understanding of composite fatigue behaviour and the associated damage mechanisms, neither of which are well understood. The initial

integrity of a manufactured component is controlled by standards such as the Military Aircraft Structural Integrity Program (ASIP), as discussed by Flynn *et al.* [15], that offers some safeguard against errors in the manufacturing process. The standard necessitates rigorous inspectional control. A better understanding of damage evolution from manufacturing defects and their relationship with component failure would, perhaps, allow lower quality, and hence lower cost manufacturing processes. Moreover, with in-service it is not possible to accurately predict the degradation of composite structures for the following reasons that are discussed in more detail in Chapter 2.

Degradation of composite structures is difficult to assess for a number of reasons**:** firstly, it is difficult to predict where damage might initiate, unlike metallic structures that are generally susceptible to fatigue cracking originating from known stress raisers (such as sharp radii), composites are sensitive to damage that can appear anywhere on the structure [16] and crack growth cannot be predicted using traditional techniques, e.g. Paris crack growth law. Furthermore, a multitude of damage mechanisms exist that can act simultaneously and coalesce to cause final failure. Poor through thickness strength of composite laminates cause internal damage that occurs at interfaces and may not be apparent from a surface inspection. The constituent materials of composites are brittle, so failure can occur quickly; therefore there is a small window in which to locate and rectify damage before it becomes critical.

The above discussed factors impede the designers' ability to predict the behaviour of composite materials and have resulted in over-design of components with associated weight and cost penalties. For example, in the marine industry it has been reported [17] that composite boats are 'overlaminated' by at least 10 %. Clearly this is not optimal and partly negates the reason for specifying composite materials.

To mitigate against the unpredictable behaviour of composite materials conservative inspection routines have been employed to monitor critical structures in service. For example the Federal Aviation Authority (FAA) requires composite parts to be designed to survive with 'invisible' damage and be visually inspected every 150 flights which relates to an interval of less than 2000 flight hours. By way of contrast critical metallic components require an inspection every 6000-12000 flight hours. The effect of these requirements is an increased cost to the operator; it has been calculated that 27 % of the aircraft life cycle cost is spent on inspections [18]. The cost of inspection for a commercial airline fleet has been estimated to be 10 billion USD per year [18]; excluding the opportunity cost associated with the time the aircraft is grounded.

It is clear that if the inspection interval could be increased or the integrity of in-service components be reliably assessed then a significant cost saving would be achieved. Without this increase the combination of a lightweight but safe component, achievable with modern composite materials, is expensive and is a limiting factor in the widespread application of composite components in safety critical structures. Therefore any technique that can offer an insight into the failure behaviour of composite materials and inform the inspection process is highly desirable.

Existing Non-Destructive Evaluation (NDE) [19] techniques offer information on the existence of damage and sometimes on its nature. However, they do not provide the stress state at the time of inspection. Therefore, whilst it is possible to inform the user of the probability of damage being present, making a definitive judgement regarding the effect of the damage on the component life is not possible. Referring to the discussion in Chapter 2 Thermoelastic Stress Analysis (TSA) is a full-field technique that has the potential to assess the mechanisms that determine failure in composites. This is possible as the output is based on the stresses on the specimen surface. TSA is an experimental technique that is based on the well documented thermoelastic effect, e.g. [20, 21]. The technique uses a highly sensitive infra-red (IR) detector to measure the small temperature changes (of the order of mK) within the field of view that can in turn be related to the change in the sum of the principal stresses $\Delta(\sigma_x + \sigma_y)$, (see Chapter 3), as follows:

$$\Delta T = \frac{\alpha T}{\rho C_p} \Delta(\sigma_x + \sigma_y) \tag{1.1}$$

where α is the coefficient of linear thermal expansion, T is the absolute temperature, ρ is the density and C_p is the specific heat at constant pressure.

The analogue output from the IR detector is digitally processed into the thermoelastic signal (S) and is related to the change in the sum of the principal stresses using a calibration constant (A) which can be experimentally determined [22], as follows [23]:

$$\Delta(\sigma_x + \sigma_y) = AS \tag{1.2}$$

The technique has not been widely applied to the assessment of composite structures due to the difficulties presented by the material anisotropic behaviour. However, with recent developments in the instrumentation, that has allowed more detailed data to be gathered

in virtually real time, the incentive to apply TSA to damage studies of composite components has been provided. Through calibration of the signal, the output can be related to the stresses in the structure and therefore life assessments are possible. In comparison most NDE techniques, such as ultrasound and radiography, highlight anomalies (damage) in the structure that may only be distinguished against a homogeneous background. These techniques do not provide information on the stress distribution in the structure and cannot directly provide a means of relating the data to the remaining life.

From the above discussion it would seem that TSA provides an ideal means of achieving the quality assurance required to facilitate the widespread use of composite materials. The technique is non-contact, non-destructive, full-field, real time and provides data that can be directly related to the stresses. However, there are some limitations to the application of the technique. The most obvious is that a stress change is required to generate a response. This has limited TSA to the laboratory environment where this change can be applied using a standard test machine. The object of this work is not to identify a means of overcoming this obstacle and develop TSA into a NDE technique, although this would be highly desirable. However, in applying TSA to composite materials there are some more challenging fundamental issues that need to be addressed before effort is targeted making the technique into an NDE tool. The object of this thesis is to tackle these fundamental issues and demonstrate that TSA can be used in quantitative damage studies of composite materials. These challenging issues form the objectives of this work described in this thesis and are presented in Section 1.2.

1.2 Aims, objectives and novelty

The goal of this research is to develop TSA so it can be quantitatively applied to damaging composite structures with a view to making assessments of the effect of damage. To achieve this goal it is necessary to address a number of objectives in order that it is possible to analyse the thermoelastic response from composite components.

Equation (1.2) is applicable for an isotropic homogeneous material. Orthotropic materials have markedly different mechanical properties in the principal material directions and consequently the simple thermoelastic theory devised for an isotropic body is not valid for orthotropic composite materials [24]. The thermoelastic theory has been developed [24] into an equation for an orthotropic homogeneous material as follows:

$$(\alpha_1 \Delta\sigma_1 + \alpha_2 \Delta\sigma_2) = A^* S \tag{1.3}$$

where α_1 and α_2 are the coefficients of linear thermal expansion in the principal material directions, $\mathbf{\Delta}\sigma_1$ and $\mathbf{\Delta}\sigma_2$ are the changes in the direct surface stresses in the principal material directions and A^* is an orthotropic calibration constant.

Equation (1.3) is developed [24] in terms of the principal surface stresses. To calibrate the thermoelastic theory it is therefore necessary to obtain values of the surface stress. In laminated composite materials this can be achieved by applying classical laminate theory (CLT) provided the elastic properties of the lamina, the thickness of the manufactured plies and the loads are known. This can provide a route to calibration [25] based on Equation (1.3) but is laden with possible sources of error due to estimates of material properties etc. A better approach is to formulate Equation (1.3) in terms of strain. This provides a direct approach to calibration, as the strain is constant through the thickness of a laminate and furthermore can be measured using extensometers or strain gauges. Therefore an objective of the work is to develop a strain based calibration approach this is developed in Chapter 4 and the approach is validated. This develops a generic approach for orthotropic materials with a resin-rich surface layer and permits a simplified route to providing quantitative thermoelastic data in orthotropic materials.

Equation (1.1) shows that the thermoelastic response is a function of absolute temperature, T. In Equation (1.2) this has been dealt with by assuming any absolute temperature changes during testing are small and therefore practically constant. The absolute temperature can then be packaged into the calibration constants, A and A^*. This approach is acceptable when there is a negligible change in the surface temperature. However, in damaging composite materials, large absolute temperature changes occur that significantly affect the thermoelastic signal. Therefore the second objective of this work is to develop an understanding of the manner in which the absolute temperature affects the recorded thermoelastic signal; this topic is covered in Chapters 5 and 6. Therefore if the surface temperature is not considered during the analysis the thermoelastic signal will be dependent on both the surface stress state and the surface temperature of the component under investigation [26]. The latter dependent variable has implications not only due to expected variation in the ambient temperature during testing but is further complicated due to viscoelastic heating evident as damage evolves in FRPs. As polymers are generally good insulators the heat local to the damage is not dissipated quickly and 'hot-spots' form on the surface of the material creating a temperature gradient. As TSA can record data in virtually real time the proposed damage assessment is to be demonstrated by comparing data sets as the material is damaging

therefore a temperature correction procedure is required that can be applied in a full-field manner during post processing of the thermoelastic data and thus de-couple the stress change from the absolute temperature change. A technique for achieving this is developed based on the theory presented in Chapter 5 and validated experimentally in Chapter 6.

To enable damage assessment in a quantitative manner using TSA it is important that the strain calibration and temperature correction procedures are incorporated in the analysis of the collected thermoelastic data. Additionally it is important to consider the effect of damage on the testing parameters applied as it is important that the loading regime does not complicate the source of the recorded thermoelastic signal. Therefore a loading approach must be commensurate with the manner in which fatigue damage affects the test settings. A methodology is presented in Chapter 7 that incorporates these aspects into a full-field damage assessment procedure which is applied on glass /epoxy laminates.

In summary the objectives of this work are:

i. thermoelastic strain calibration approach for orthotropic materials
ii. temperature correction procedure
iii. full-field damage assessment methodology

The challenges that have been presented in order that TSA can be applied quantitatively to composite materials (subject to damage) have not been met prior to this work. Whilst studies presented in literature have reported the development of a damage procedure using the thermoelastic signal it is evident that they have not been fully explored nor indeed provided quantitative solutions. Therefore the ability to correct thermoelastic data for temperature variations and strain calibrate this data provides two fundamental stepping-stones in the application of TSA in a robust fashion. The combination of the procedures in the damage procedure presented represents a step forward in the application of TSA to the damage assessment of composite materials.

1.3 Overview of thesis

The research presented in this thesis is broken down into nine chapters:

Chapter 2 provides a review of composite damage and the state-of the-art damage assessment techniques applicable to composite materials. In order that the techniques

may be appraised the progression of damage within a component and how the damage mechanisms affect the residual integrity is classified. The techniques are appraised against the classification defined. The chapter concludes by critically reviewing the techniques and the selection of TSA is discussed.

Chapter 3 details the current status of the theory and application of TSA to orthotropic composite components through the derivation of the thermoelastic theory. The practical application of TSA is considered with respect to the physics of the data collection using IR detectors. The response of IR detectors is shown to be temperature dependent. The traditional method of a stress based calibration is reviewed; the difficulties in applying this method to orthotropic composites are discussed and the benefit of an alternative calibration in terms of strain is presented. The state of the scientific understanding with regard to the use of TSA for damage assessment in composite materials is reviewed and highlights areas in need of revision. The strain calibration, temperature dependence of the thermoelastic signal and lack of a definitive damage assessment are defined as deficiencies in the current methodology and determined as areas of further work to be tackled in the thesis.

The strain based thermoelastic theory is developed in Chapter 4 that provides a generalised routine by which the thermoelastic data can be calibrated. During the process of the calibration development it was found that the thermoelastic response did not to emanate from the orthotropic surface ply but from the isotropic resin-rich surface layer and as such the calibration approach accounts simultaneously for the laminate orthotropic mechanical and the isotropic surface response. Fortuitously the existence of the resin rich layer considerably simplifies the calibration analysis and means that during damage evolution a quantitative measure of the strain distribution can be made.

Chapter 5 theoretically quantifies the effect of surface temperature on the thermoelastic signal. The approach presented revisits the derivation of Planck's law from Chapter 3 but importantly evaluates the response with respect to the operating parameters of the TSA operating system. The foundation for a correction factor method is presented and is based on the theoretical findings presented.

In Chapter 6 the results presented in Chapter 5 are verified against experimental results which are collected using a specially designed rig. Practicalities involved with applying the correction factor to full-field data are considered including the calibration of the thermal data. A temperature correction procedure to manipulate the thermoelastic signal is devised and the methodology is validated through a number of practical case studies

and illustrates that the application decouples the absolute temperature response from the thermoelastic signal.

The strain and temperature procedures are combined in Chapter 7 to form a method of damage assessment. The methodology introduces a revised TSA loading routine that allows for stiffness degradation during damage propagation in composite laminates. TSA data is collected from glass / epoxy laminates during the propagation of fatigue damage and results demonstrate that TSA can provide valuable information into the way the combined damage mechanisms result in final failure of a laminated composite component.

In Chapter 8 the damage assessment procedure is complemented with an IR technique (Pulse Phase Thermography) which is demonstrated to offer the capability to locate subsurface damage within the structure and thus define the area in which TSA should be targeted. A method of propagating delamination damage in fatigue is devised and a modified IR damage assessment approach is applied using the two IR techniques. The work displays the potential of TSA for non-destructive assessment of damage.

Areas of future work and the main conclusions of the work are presented in Chapter 9.

Chapter 2

Composite damage and assessment

2.1 Introduction

Chapter 1 has defined the goal of the work as developing a technique capable of quantitatively analysing the effect of damage on a composite structure. The purpose of this chapter is to provide a review that puts the work described in this thesis into context. The review includes the manner in which damage initiates, techniques that are used to characterise the damage types that occur in composites and the effect of damage on the structural performance. The review shows what is currently achievable in damage assessment of composite structures and reveals the areas that require attention. The chapter concludes by discussing the merits of selecting TSA as a potential approach to enable the assessment capability.

2.2 Damage

The inspection of engineering materials at sufficient resolution will reveal some quantity of defects; the difficulty is to put this into context and decide when a structure will not perform as required due to damage and is faulty. Referencing the definitions established by Worden and Dulieu-Barton [27] the steps leading to a *fault* in a structure are firstly defined as a *defect* which if unchecked leads to *damage*. As discussed defects are inherent in engineering materials and thus statistically all materials will contain some

unknown quantity of defects. Thus it is possible for a structure to operate at its design condition even if the constituent materials contain defects. Progressing from a structure with defects, a structure with damage is deemed to be no longer operating in its ideal condition but can still function satisfactorily. The unchecked evolution of damage in a structure will eventually lead to a fault marked by an unacceptable reduction in quality or performance. The nature of damage evolution can thus be related through a hierarchical relationship: defects leading to damage and damage leading to faults [27]. The effect of a fault will lead to a change in the structural behaviour from that expected at the design stage through the reduction of mechanical properties such as strength and stiffness, consequently limiting the operational suitability and life of a structure. The manner in which a fault limits the suitability will vary dependent on the structure and operating conditions but it is important to be able to avoid the structure operating outside of the ultimate design limits whilst loaded within the expected operating parameters.

It is the purpose of this work to provide a means of identifying the extent of damage in order that further propagation may be averted and a fault, i.e. failure, may be avoided. The detection of damage within a structure should be accomplished with no prior knowledge of how the system will behave when damaged. The ability to localise the damage with a suitable method will provide information about the probable position of the damage. Once it is clarified that damage is present and its position located, further investigation is necessary in order that an estimate of the effect of the damage of the structure may be achieved. In addition to information providing the effect of the damage it is vital to gain an understanding of the damage type to help classify the physics of the damage. For this information to be useful to structural engineers, it is necessary to gauge the residual strength/life and thus decide if the damage is critical. This means a prediction is necessary to estimate the safety of the structure's continued service. An estimation of residual life is only possible with an understanding of the physics of the damage by obtaining data that allows a characterisation based on the stress in the structure.

2.3 Damage in composite materials

The mechanical degradation of metallic materials due to damage in the structure can be assessed by traditional fatigue methodologies [28] and can often be determined by such features as crack growth per cycle. The growth of a fatigue crack can thus be predicted and the time or loading cycles to reach a critical size can be obtained with some certainty allowing residual strength calculations to be made. However, in laminated composite materials the fatigue process is stochastic and involves different non-localised

damage mechanisms acting simultaneously which complicates and to some extent precludes failure modelling [29]. Predominant damage mechanisms include matrix cracking, delamination, fibre-matrix debonding and fibre breakage [1]. Often a number of these damage mechanisms combine before failure. Due to the many damage types and the indiscriminate manner in which damage initiates and propagates in composite materials [11] methodologies to assess fatigue life of composite structures are not robust. Of the degradation models reviewed by Tserpes *et al.* [11] none explicitly take into account the fundamental damage mechanisms or prescribe the dominant mechanisms that are responsible for the reduction of residual strength or how they cause final failure. The inadequacies of the current failure theories is exemplified by the results from long-term test ('Worldwide Failure Exercise') which reported variations in predictions of to 200 – 300 % [1]. In order to allow a better prediction of the extent of degradation or supplement the posed models, the ability to experimentally determine the damage state would provide beneficial information from which a better understanding of the residual life can be evaluated. To apply models with confidence assurance must be provided that ensures the relevant models have appropriate accuracy; i.e. the model of structure must be correct and the model of the *damage* must be correct [30].

To tackle all defects observed in composite structures is a large task and the work in this thesis only concentrates on a select number of damage mechanisms. In order that this may provide a useful addition to the understanding with regard to significant damage types a review of the most prevalent damage mechanisms is required. The behaviour of the dissimilar constituents of composite materials dictate that the damage observed must be split into two mechanisms**:** damage of the ductile matrix and the failure of the brittle fibre reinforcement [31]. Fatigue damage of the matrix is characterised by the initiation and growth of a crack, growth is load dependent and will propagate until the crack strikes an interface. At this time the propagation will be determined by the mechanics and loading; the crack will propagate further either through the fibre breakage (if the stress at the crack tip is great enough) or the fibre/matrix interface may fail if the shear stress is sufficient. At low strains the cracking will be confined to the matrix alone. The interaction of matrix cracking in two ply orientations will often coalesce and lead to delamination on the application of further fatigue loading. The fibre constituents are by comparison brittle and do not display fatigue failure, fibres will fail at the weakest point or at a point of local stress concentration, i.e. a geometric discontinuity or at the tip of a matrix crack. Through the results from the research project 'Monitoring on-line integrated technologies for operational reliability' (MONITOR*)* [32], which performed an end user survey regarding the most common and/or important damage types in aircraft composite structures, the damage mechanism of delamination was considered as

one of the major concerns [13]. Delamination is defined as the separation of two adjacent plies of a laminate. The susceptibility of laminated composite materials to delamination through fatigue (as discussed above) is a major weakness and it has been reported as the most feared failure mode in a structural composite [33] and has been reported as limiting the use of composite materials for primary structures [34]. Poor through thickness performance also leaves composite laminates prone to delamination because of poor laminate design that does not adequately account for loading or in-service impacts. In both cases delamination may be propagated by fatigue loading. If the laminate is not successfully designed with respect to the loading conditions, internal stresses can initiate damage through the initiation of defects in the laminate [35]. Further detrimental fatigue mechanisms can be developed due to the mismatch in material properties at each ply through the laminate thickness. The further development of delamination damage and indeed the complex nature of the cause and effect of damage in composites are covered in depth in Chapters 7 & 8 with particular relevance to the materials used in this work.

Regardless of the manner in which the damage initiates, continued loading of the structure will lead to fatigue damage that degrades the microstructure, nucleating further defects. As damage in FRPs may propagate from the fibre / matrix interface, detection is often hindered because the damage occurs at interlaminar sites beneath the outer surface of the laminate. Damage is therefore not readily detectable by visual inspection that forms the majority of pre-flight checks as designated by authorities such as the FAA. It is essential that any damage assessment provide a full-field capability to monitor a structure rather than isolated point measurements as the stochastic nature of damage in composite materials means that damage can initiate anywhere. The limitations of single point measurements are well documented and it has been shown that strain gauges were inadequate to identify damage-initiation and growth when composite structures failed [36, 37]. The research in this thesis concentrates on damage of the type that is caused in service due to fatigue loading. Some predictions of the possible residual life may be made from *S-N* curves. However, TSA has the benefit of providing a full-field stress-based metric throughout the fatigue life history. This approach has the potential to provide a better residual life predication whilst also providing a means of visualising damage progression.

2.4 Damage assessment

The previous section shows that there is a need to assess the integrity of a composite structure. It is clear that it would be desirable for any approach to provide a means to

evaluate the effect of damage on the surrounding structure. It is also important that the structure is examined without impairing its future usefulness and therefore NDE techniques are of interest. The information that can be ascertained from various NDE techniques varies significantly. The choice of NDE technique is dependent on the material and damage type under inspection and therefore it is appropriate to review the range of techniques available with respect to their applicability to assess damage in composite structures. In order that the various NDE techniques can be assessed against designated criteria a review has been carried out considering the following [27]:

(i) can the technique detect damage?
(ii) can the technique localise the damage?
(iii) can the technique identify the extent of the damage?
(iv) can the technique characterise the type of damage?
(v) can the technique predict the residual life of the structure / component?

In the present work, the target is to identify a procedure that can provide damage assessment so the last three categories are the most important. Additionally to identify the versatility of the approach the following considerations are discussed:

(i) is the technique suitable for on-line and off-line inspections?
(ii) is the technique suitable for assessing surface or internal damage?
(iii) is the technique portable?
(iv) is the technique contact or non-contact?
(v) does the technique provide single point, full-field or the structural global response?

Ultimately, the technique must be capable of resolving information from composite materials. Although a seemingly obvious constraint this must be borne in mind as although many existing NDE methods have been successfully applied to metallic materials they cannot all be universally applied to composite materials. Composite materials differ in two important areas: firstly, the physical properties such as thermal conductivity, acoustic attenuation, electrical resistivity and elastic behaviour are significantly different from metallic materials and this can affect the underlying physics which can dramatically change factors such as the resolution and sensitivity. Secondly, metallic structures are predominantly manufactured materials that above the microscale are homogeneous and isotropic in nature. Difficulties encountered in the detection of damage in composite materials arise from the inherent inhomogeneity and anisotropy of composite materials [38].

The mechanisms by which the NDE techniques extract data from components vary; therefore the following discussion splits the techniques into two broad groups for the purposes of comparison. These two groups are defined as *active* and *passive*, where these two categories are defined relative to the state of the structure at the time of the test, i.e. a technique in the *passive* set would collect data with a sensor from a dormant structure or unloaded structure. The *active* techniques however require the structure to be excited in some manner and the subsequent response to be recorded with a sensor.

The first techniques that will be reviewed fall into the *passive* group, whereby a sensor is applied to the structure and information regarding the structure is collected. The *passive* techniques that will be reviewed are:

i. Visual
ii. Ultrasound
iii. Radiography
iv. Infra-red Thermography (IRT)
v. Mechanical

The review of *active* techniques covers the manner and reason by which the structure is excited and the subsequent level of information that can be gathered from the structure. The six techniques reviewed here are:

i. Strain gauge
ii. Holography
iii. Shearography
iv. Electronic Speckle Pattern Interferometry (ESPI)
v. Digital Image Correlation (DIC)
vi. Thermoelastic Stress Analysis (TSA)
vii. Vibration Based Methods (VBM)
viii. Acoustic Emission (AE)

Inevitably there is some overlapping between the two groups and these will be discussed during the review of the technique.

2.5 Passive techniques

2.5.1 Visual

Visual techniques are the simplest form of NDE and rely merely on the visual observation of the component to detect gross imperfections or defects. It forms one of the most widely used forms of inspection [16] due to its cost and ease of use. Visual techniques have found acceptance as they are non-invasive and the operator can scan the entire structure as long as the surface is clean and well illuminated. The most recent Airbus, the A380, is certified for flight by the European Aviation Safety Agency (EASA) using visual techniques that account for 80 – 90 % of the inspection routines [39]. Defects causing deformations of the surface modify the way in which the surface reflects ambient light and in order that visual techniques detect damage these changes must be recognised by the operator. There is a low assurance of sub-surface defects being identified and it has been estimated that visual techniques provide only a 10 % detection rate [40]. The reliance of visual techniques is based on the assumption that critical damage mechanisms result in visible surface deformations. This may be true for gross damage but resolution of visual techniques is not defined so the extent to which surface observations can resolve subsurface defects is unknown.

Visual inspection techniques are therefore qualitative and provide no quantitative results to the reliability of the structure [41] and any conclusions drawn from the visual inspections is based only upon the intuition of the inspector. Therefore the technique can only provide level *i*) damage detection and crucially cannot provide data on the remnant life.

2.5.2 Mechanical

Mechanical or '*tap*' testing is a common and inexpensive form of inspection where the operator introduces a pressure wave into the specimen, typically by *tapping* the surface with a hammer-like tool [42]. Damage detection is reliant on the pressure wave having a constant velocity in a given substance; therefore a change in the acoustical impedance (due to damage) results in a change in the sound (indicating a discontinuity with reference to an undamaged area) that can be discerned by the operator. As the variation in the sound response must be perceived by the operator the technique is reliant on the judgement of the operator to characterise the response to that achieved from a sound area [42]. Developments in the technique have resulted in specially designed receivers to analyse the sound and compare the response with defect free parts. This can help to

automate the process but it is still inherently reliant on the interpretation of the recorded sound. Erroneous data can result from damaged areas such as a crushed sandwich structure core, or an adhesive-filled area of core being mistakenly identified as an undamaged area [16] where no distinct difference can be perceived in the acoustic impedance. The technique has found application as a primary method in the detection of disbonds or for the detection of separations between layers of laminated structures [42], and through thorough analysis the technique has been shown to be effective in the detection of; *i*) crushed core or debonds in sandwich panels and *ii*) impact damage and delimitations in composite structures [42].

Limitation to the extent of damage detection is evident, for in order that the detection of delaminations be successful the geometry of the damage must be approximately 25 mm or greater in diameter and be located less than 1 mm below the surface [16]. Due to the inadequacies presented, further inspection is warranted before conclusive results to the type and extent of damage can be made [16].

The mechanical and visual methods of inspection presented rely on damage identification to be inferred by observing the effect of damage remotely from the surface of the structure. Improvements on the detection of sub-surface anomalies are possible in the following three methods of inspection: ultrasound, radiographic and thermal techniques.

2.5.3 Ultrasound

Ultrasound methods rely on the wave propagation principles presented through tap testing. They however benefit from the ability to record the time taken to transmit and receive a higher frequency sound wave. This allows the quantification of the damage position through the thickness (again assuming the velocity of the sound is constant) [16]. As a result of this, ultrasound techniques are widely used to locate internal and size defects in materials [42]. Ultrasonic inspection has been used to detect flaws, bond failures, and porosity [42]. The greatest difficulty in investigating composite materials lies in the fact that the sound attenuates more quickly in composites than traditional materials. Furthermore, sound attenuation is more dramatic in a damaged material than in the same undamaged structure [43]. Thus this attenuation limits the depth to which damage detection is reliable. Although the damage may be located and the extent of the damage size assessed the flaws are only identifiable as inhomogeneities against a homogeneous background and provide no information relating to the type or criticality of the damage on the structure.

Traditional ultrasound techniques require contact to be made with the area being inspected to ensure signal propagation between the transducer and the observed component. This resulted in ultrasonic inspection being characterised as providing slow point-by-point inspection rates as the application of couplant restricted the area and speed of cover. To some extent this negated the ability of ultrasound to locate and size damage as it is not practical to scan the entire component. Recently ultrasound laser based applications avoid the need for contact; however the effective result of an ultrasonic test is still heavily dependent on subject surface condition, direction and acoustic impedance.

2.5.4 Radiographic

Radiographic techniques allow the detection of defects that alter the absorption rates of radiation introduced into the component. Subsurface anomalies can be visualised through the measurement of the intensity of a monochromatic beam (such as X-rays) transmitted through a structure, and deviations in the recorded intensity are a result of absorption at damage sites. A specific area is targeted and, as with ultrasonic testing, the time involved to obtain results limits the full-field capability and as such it is only sensible to apply it to flaws with *a priori* knowledge of their location. However, using Fluoroscopic radiography [44] means real time data can be obtained allowing for a scan of a component. However this method is restricted by a lower resolution.

The Radiographic technique requires access to both sides of the component and this is a major drawback in the application to in-service components. It does however overcome one of the drawbacks of ultrasonic testing as it is effective for complex geometries [44]. Further limitations include the sensitivity of the relative position of the scanning probe to the damage orientation and if not optimal can result in flaws being undetected. Radiographic imaging does offer a range of benefits including the ability to image sub-surface defects [45] and this capability extends to the detection of areas with porosity, water entrapment, crushed core, cracks and resin rich or starved areas. However, in highly multilayered structures such as composites, the X-ray path is often scattered due to the anisotropic and heterogeneous nature of the material and hence it is difficult to obtain consistent results. The technique has “Health and Safety” implications arising from the use of X-ray radiation, which impinges further on its applicability in the field.

2.5.5 Infra-red Thermography

IRT techniques observe a structure using an IR detector and therefore offer a non-contacting, full-field technique in a portable system. The sensitivity is determined by the thermal resolution of the IR detector and the spatial resolution by the number of pixels incorporated on the IR array and subsequently the stand-off distance and infra-red optics. Although IRT has the potential to rapidly scan large areas of complex structures locating areas of concern, limited quantitative interpretation can be derived from this data. The methods by which IRT can be applied to structures result in an overlap between the *passive* and *active* group division presented here.

Passive IRT is concerned with the interpretation of the thermal signature of a structure where abnormal temperature profiles indicate a potential problem. Using the IR detector focussed on the structure under investigation alone the operator is made aware of temperature differences observed with respect to a reference (or *hotspots*) that may indicate the presence of a sub-surface defect [46]. *Active* IRT [46] subjects the structure to a pulse of energy (hence Pulse Thermography) whereby the extent of damage will be measurable if the defect causes heterogeneity in the thermal properties. The subsequent analysis is reliant on the principle that the heat flow is altered by the presence of damage. Improvements in computing power have permitted the development of a technique referred to as Pulse Phase Thermography (PPT) [46, 47] which enhances the quantitative aspect of the technique. The PPT technique allows the further enhancement of the thermal data observed, as it analyses variations in the transmitted signal for attenuation and lag with respect to other points across the structure. PPT is not mature but has been applied to simple damage assessment applications [48]. As the technique is reliant on the variation in the thermal properties due to damage, it is therefore applicable to internal defects in composites such as delaminations, debonding or foreign objects found within laminates. Extensive field studies have been performed that enable qualitative results to be obtained for simple 2D structures [48]. With processing such as PPT defect depth can be revealed but yields insufficient data to definitively assess the effect of the damage on the integrity of the structure. Without substantial modelling of expected heat flux through the structure advanced methods of IRT such as PPT are limited to close to surface sub-surface anomalies in simple components [48]. This is likely to change as computing power increases to accurately model heat flux in three dimensions. The results achievable with both IRT approaches highlights to engineers' possible areas of concern but allow no further assessment to be made to the effect of the anomaly detected on the structure.

In summary *passive* techniques are characterised by the ability to highlight anomalies against homogeneous background, but as the structure is not loaded it is not possible for any of the techniques to impart any information regarding the affect of the damage on the stress state of the structure and thus its future integrity. Furthermore, this pattern recognition style of approach is heavily dependent on the interpretation of the results. The majority of composite structures incorporate some form of secondary stiffening material, fixing or a change in stacking though the structure. The analysis of an apparent anomaly must be made with reference to the subsurface that for clear reasons may not be visible at the time of inspection. This issue can introduce errors that can be classified in two categories: *i*) *false-positive* which is attributed to an indication of damage when none is present and *ii*) *false-negative* when there is no indication of damage when damage is present [14]. The occurrence of the first type is a nuisance but does not suffer the clear safety issues presented if the latter type occurs. The overriding benefit however is a result of the *passive* nature and the simplicity of experimental set-up that this enables; this is of advantage to the application of NDE to in-service maintenance of composite components where data can be obtained practically instantaneously from *in situ* examinations.

2.6 Active techniques

The *active* methods of assessment grouped here differ in the manner in which data can be collected with respect to the state of the structure at the time of the test. They all require the structure to be *excited* or *loaded* in some manner in order that data can be extracted at two or more points within the working range of the structure. This group is further split into three sub-sections relating to the extent of the structure that is observed:

i. Local: Strain gauge techniques
ii. Full-field: TSA, Holography, Shearography, ESPI, DIC
iii. Globally: VBM, AE

2.6.1 Strain gauge

The electrical resistance strain gauge is the most widely used device for experimental stress analysis [44] and provides the strain over the contact footprint of the gauge and as such the strain on the surface assuming the gauge is perfectly bonded to the structure. As a flaw in an object usually induces strain anomalies both surface and therefore internal flaws can be inferred; the resolution will be limited if the internal flaws are very far from the surface [49]. The issue of depth resolution may be overcome by using different strain

sensors such as optical fibres [50] which can be embedded in composite materials [50] and unlike surface mounted gauges embedded gauges monitor internal strain development *in situ*. The most popular type of optical fibres strain sensors make use of fibre Bragg gratings in silica fibres. The structural integrity of the structure may be obtained by applying a load and observing the corresponding stiffness response of the structure by recording the strain for the applied load. To make the best approximation to the structural integrity the loading is applied in a manner commensurate with that encountered in service. The technique has the potential to provide information on the remaining life of the component through changes in the measured strain. Passively the strain gauge will identify any gross deformation, as a departure from the zero strain recorded at the initial fitment. Once mounted or embedded strain gauges are permanent features of the structure. This produces two conflicting situations continual real time monitoring is enabled but the structural response may be modified by the addition of the gauge. Although the strain behaviour may be monitored for deviations as a result of damage it is not possible to identify the damage type or extent. Using electrical resistance strain gauges for damage analysis in composite materials presents a significant challenge due to the temperature dependence of electrical resistance strain gauge measurements, where temperature variations in the order of 30 ˚C are possible at damage sites (see Chapter 5). Temperature variations may be compensated for using a dummy gauge; however, the inhomogeneous distribution and magnitude of the heating effects may make correction difficult (Chapter 5). Furthermore, a major limitation is found in the limited resolution obtained from strain gauges and is ultimately limited by the spatial positioning or location of the gauges on or within the component.

2.6.2 Holography, Shearography & ESPI

These three techniques are full-field mapping methods that dispense with the resolution limitations and contact difficulties encountered by strain gauge techniques. Surface measurements are required from the deformed and undeformed structure; the loading of the structure to accomplish this is commonly achieved by stressing the structure through pressure, vacuum, thermal, acoustical or vibrational excitation methods [49, 51]. Importantly any movement of the structure during the data capture can degrade the quality of analysis as the fringe patterns are corrupted; isolating tables are required to ensure that any movement of the surface of the structure is that induced by the applied stress alone. At the present time this requirement precludes taking the techniques out of the laboratory environment. Holography is a surface *deformation* mapping method where holograms recorded from the deformed and undeformed component [52] are analysed, and the superposition of these two images creates a fringe pattern that

indicates the surface deformation. Variation in the deformation from that expected indicates some variation in the structure's compliance and indicates some form of damage is present. A development of Holography is the ESPI [52] technique that benefits from the capability to display the correlation fringes in real-time on a TV monitor without the need of photographic processing or optical filtering. A further optical technique is Shearography [49] which provides the surface *strain* directly and does not suffer from signal degradation (due to vibration) to the same extent as Holography or ESPI. The fringe pattern produced can be extremely complex, and it is questionable whether it is possible to detect all of the important defects with reliability and repeatability. Localisation, the extent and the characterisation of damage are again dependent on the interpretation of surface strain maps. However, it has been reported that it is possible to achieve damage detection by processing the fringe pattern which represents loci of surface strains. Verification of this capability has been demonstrated for delamination damage and cracks as a result of impact damage in GRP by comparison with ultrasound tests [52]. Damage has been classified using this technique but quantitative data relating the damage severity has not been forthcoming. Although large areas of composites and sandwich materials have been inspected at a rate of 20 metres per hour [16] it is not rational to scan entire structures using this technique looking for possible areas of damage (depicted as anomalies in the recorded fringe pattern) and the technique is better suited to damage with *a priori* knowledge of the location [53]. In general these techniques are limited by size, cost, complexity of the equipment, and the difficulties of taking the technique out of the laboratory.

2.6.3 Digital Image Correlation

DIC tracks the movement of an applied surface pattern during loading. This is achieved by analysing the displacement of surface patterns within the discretised interrogation windows of the whole image [54]. Therefore, this technique is dependent on the application of a suitable pattern to the surface which has been cited as the most important factor in determining the quality of the results obtained by DIC [55]. Commercial systems obtain full-field data using a charge coupled device (CCD) camera (i.e. non-contacting) and can resolve to a high accuracy of 40 μm [56]. Three dimensional data can be produced by using two CCD's focussed on a specific point on the structure from different directions. At the present time there is limited literature reporting the use of DIC for the study of composite materials; however, an example of its application to the investigation of the macro and mesoscale strain of glass fibre reinforced polymer (GFRP) has been presented by Godara and Raabe [57]. Godara and Raabe used DIC to assess the surface stress heterogeneity of a multilayered cross woven

laminate; the contrast pattern required being applied with a fine black coloured acrylic resin spray. DIC shows good potential as a strain analysis technique but its unproven application to composite materials as a damage assessment procedure is of concern.

2.6.4 Thermoelastic Stress Analysis

TSA [21] is a technique that provides data that can be related quantitatively to the stress state on the surface of a component. This is achieved by using sensitive equipment capable of recording small changes in temperature due to the thermoelastic effect [20, 21] that occur as a result of the application of a load to the component. Using an IR detector for these temperature measurements the technique is non-contact and developments in the equipment available have improved the ability to capture full-field stress data in real-time. The thermal and spatial resolution is determined by the IR detector and the optics. The latter can be adjusted with the use of various IR lens, and studies reported in literature indicate the spatial range achieved: from an area 3 mm x 3mm [58] to complex structures 3000 mm long [59] made possible by combining data sets in a post processing procedure. One of the primary requirements and challenges in applying the technique is that the structure must be cyclically loaded within the elastic limit of the material and at a suitable rate to achieve adiabatic conditions. Furthermore, the emissivity of the surface must be uniform and relatively high in order that IR measurements may be made [60]. The emissivity is of little concern to polymer based composites as in general polymers have a high emissivity in the IR range [61]. Although TSA has many advantages, some further important factors must be considered with regard to the application of the technique for analysis of composite materials; these are detailed in Chapter 3.

As with all the surface measurement techniques discussed it may be possible to infer the effect of subsurface damage from the observation of surface strains. The data can be processed to provide information as to the level of damage within the component (i.e. flaws that create strain concentrations and thus reduce the strength of the component). TSA has been applied to the study of composite materials [24] and it has been reported that the technique has been validated against normalised surface stress data from finite element analysis models [36]. Damage evolution has been monitored in composite materials [62]; damage mechanisms such including split plies [63] and impact damage [64] have been cited to cause discernible change in the thermoelastic signal. Through the quantification of surface stress levels estimates as to the residual safe working capability of the structure should be possible in terms of the ratio between the current working stress and the yield stress of the component.

2.6.5 Vibration Based Methods

Whereas sonic resonance and ultrasonic methods interrogate the component passively at a specific site for changes in the response to an input, VBMs aim to analyse the response of a structure globally to an input. As such the technique is specific to the component under test and analysis is dependent on the global response to structural change within the material. Vibration-based NDE methods [65] use the observed change in natural frequency, and thorough assessment of Eigen-parameters between an initially undamaged structure and the latter damaged structure to provide the basis for a damage indicator. Combining mathematical models of a structure under test in conjunction with advanced analysis of the changes in natural frequencies through the application of neural networks have provided some evidence to determine the location and size of damage [66]. However, attempts to quantify damage are not robust and limited evidence has been presented displaying the ability to characterise damage. Predictions to the extent or effect of damage on the residual life of a component from VBM results are not evident. The practicalities of the technique require that the response to an input are observed [67], and it is posited that this could be achieved through surface displacement measurements and would be acquired using one of the variety of surface strain measurement techniques discussed. The structure must be excited in order that the modal characteristics of the structure are generated; methods of generating this in a service structure have not been reported to date.

2.6.6 Acoustic Emission

The physical manner in which the AE [68] method works precludes a *passive* inspection routine as the structure must be loaded and indeed must be subject to the occurrence of damage mechanisms to trigger. Therefore the goal of any AE system is to be incorporated within a structure and to provide the continual monitoring of it and in essence 'listen' for acoustic signatures which indicate damage occurrence. An acoustic emission is a naturally occurring phenomenon within materials; transient elastic waves that are produced from a sudden strain energy release, resulting from microstructural changes, which propagate and are recorded at surface mounted transducers. Strain energy release may occur from damage mechanisms observed in composite degradation such as cracking, dislocation motion or the formation or collapse of internal voids. It has been reported that damage types can be evaluated to a certain extent and with analysis the technique will to some degree differentiate between defects such as delamination and fibre breakages [69]. However, great skill is required on the part of the operator to

interpret the collected data from the structure and to relate it objectively to possible damage sources [70]; and this is hampered as a consequence of operational noise that can swamp data collection. The application of AE to damage in composite materials is not developed, however it has been hypothesised that if data collected can be analysed efficiently and the appropriate signs be identified AE would provide a method of monitoring damage. Locating the damage source in a composite material is theoretically possible using an array of sensors. Location of the source is dependent on the propagation of the wave being fully understood. As with the ultrasound techniques this is complex in orthotropic materials due to the attenuation of the wave and the orthotropic nature in which a wave travels from the source. Further assessment techniques would be subsequently required as AE does not provide information regarding the size or shape of the defect. The ability to continually monitor structures for damage occurring has benefits in terms of the reduction in effort required to identify if and where damage has occurred. Both the AE and VBM techniques differ from the other assessment techniques described as they provide a monitoring technique rather than a tool for non-destructive damage assessment.

The major benefit of the *active* techniques reported here is their ability to provide data that is linked to the stress state in the component that to some extent consequently enables a quantitative estimation to residual life measurements to be made. However, the complexities of a dedicated test environment in which the structure can be loaded incur difficulties.

2.7 Critical analysis of existing techniques

From the review of the 11 selected techniques it is evident the variety of information that can be obtainable is extensive and varied. It is therefore important to analyse and critically assess the suitability of these techniques; this will be achieved by assessing them against the criteria stipulated in Section 2.4. A summary of the findings is shown in Table 2.1.

Table 2.1. Inspection method applicability comparison

Technique	**(*i*)**	**(*ii*)**	**(*iii*)**	**(*iv*)**	**(*v*)**	**Surface / Internal**	**Contact / Non-contact**	**Local / Full-field / Global**
Passive								
Visual	×	×	✓	×	×	*Surface*	*Non-contact*	*Full-field*
Ultrasound	×	×	✓	✓	×	*Internal*	*Couplant*	*Local*
Radiographic	×	×	✓	✓	×	*Internal*	*Non-contact*	*Full-field*
IRT	×	✓	✓	✓	×	*Surface*	*Non-contact*	*Full-field*
Sonic resonance	×	×	✓	✓	×	*Internal*	*Contact*	*Local*
Active								
Strain gauges	×	×	✓	×	✓	*Surface*	*Contact*	*Local*
Holography/ Shearography/DIC	×	×	✓	×	×	*Surface*	*Non-contact*	*Full-field*
TSA	×	×	✓	✓	✓	*Surface*	*Non-contact*	*Full-field*
VBM	✓	✓	×	×	×	*Both*	*Both*	*Global*
AE	✓	✓	×	×	×	*Both*	*Contact*	*Global*

Key	**Description**		
(*i*)	Detect damage remotely	(*iv*)	Characterise damage type
(*ii*)	Localise damage	(*v*)	Residual life prediction
(*iii*)	Extent of damage		

This review of the available NDE methods has allowed a comparison to be made to gauge the applicability of the various techniques to provide a means with which to meet the identification and characterisation levels introduced in Section 2.4. To further hone the suitable methods the following discussion appraises the techniques against the requirements.

VBM, AE and strain gauges all meet the first two requirements with the ability to detect and localise damage. However, with strain gauges an entire component cannot be monitored, and resolution is limited to the local area surrounding the gauge. Full coverage would require large numbers of gauges, data processing and the attachment of the gauge would provide some artificial stiffening of the component. The measurement of the full-field strain is more suited to the Holography, Shearography & ESPI techniques, but these have not been demonstrated robustly out of the lab. Although providing a global analysis of a structure, VBM suffers from instability due to factors such as environmental conditions causing a change in the component stiffness. AE

combines the benefits of the VBM and strain gauges methods, in as much as a global analysis can be achieved regardless of the material condition. A full coverage can be achieved with sensors spaced across the component surface. However, difficulties in localising damage to a specific point on the structure have been identified in anisotropic materials. A nuance with all of these methods is the requirement for the component to be under load for readings to be made. Inspection using radiography or ultrasonic methods involves precise scanning over large areas as the techniques are typified by providing a small scanning area which is not effective in covering large areas of the structure to locate damage. Furthermore, they offer the ability to highlight anomalies in the structure that may be distinguished against a homogeneous background but do not provide information on the stress distribution in the structure and cannot directly provide a means of relating the collected data into final component failure. Thermography offers a technique for broad area inspection that has the potential to significantly reduce the inspection time. Again thermography techniques do not provide information on the stress in the structure and further challenges include the achievable penetration through the thickness [48] that may need to be investigated. Whilst to some extent radiography and IRT methods can provide information to analyse the extent of the damage apparent, they do not offer information to enable a judgement to be made as to the effect of the damage on the remaining strength of the component. The strain gauge and TSA measurement techniques have been shown to provide the opportunity for this. As discussed the optical strain techniques are less robust and the strain gauge is spatially limited when compared with TSA and in addition they are sensitive to small movements and vibration. Therefore, the only realistic proposition for full-field stress in complex regions is TSA. Studies to identify the effect of damage on the residual strength have been reported in literature [60], [71, 72]. Furthermore, the advantage of TSA is that the component is loaded and therefore stresses similar to those encountered in service can be generated to reveal critical flaws. TSA does not provide a technique that lends itself to damage location however and it is evident to achieve a complete damage assessment strategy a combination of techniques must be used. A complementary technique is required for damage localisation.

In view of the importance of being able to assess composite structures for damage, very few studies have been dedicated to the stress analysis in the actual component subject to damage. Of the conventional NDE techniques none offer a direct measure of the surface stresses in a full-field manner. An assessment approach is proposed based on TSA and complemented with an IRT technique, PPT. The combination of the two techniques described is a novel approach in the field of damage assessment in composite materials and it is envisaged that it will provide the means for assessment of composite materials

subject to damage. Accepting the reality that no single method can provide all the necessary NDE information, effort is best placed to integrate these two methods. The advantage of these specific methods is that both techniques can be achieved using a single IR device and the differences in data collection would provide a level of overlap which would undoubtedly enhance the reliability [16] and detection ratio. The remainder of this thesis will address the application of TSA to composite materials, addressing the challenges in applying the techniques discussed to enable a damage analysis procedure to be developed.

TSA falls into the group of active techniques and therefore requires the structure to be loaded for measurements to be made as a stress change is required to generate a response. The work presented in this thesis is restricted to the application of TSA to the laboratory environment where this change is applied using a standard test machine. To develop TSA into a fully fledged NDE technique is highly desirable but requires significant advances and verification of new loading methods. Developments of the DeltaTherm software do show developments in this direction and it is envisaged that thermoelastic data may be collected using random input stresses in the future. This would permit, for example, the vibrations that are normally present in service (e.g. vibrations due to engine operation) to enable *in situ* measurements to be made. Further possibilities may include the use of an impact with instrumented hammer and measuring the transient impact and response.

Chapter 3

Current status of the theory and application of TSA to orthotropic composite components

3.1 Introduction

In the previous chapter TSA was identified as having the potential as a damage analysis technique for composite structures. The technique has been applied to a variety of composite structures such as Paynter and Dutton's [59] work on large-scale wind turbine blades and Dulieu-Smith *et al.* who studied the stress distributions in a marine tee joint [25] for design optimisation purposes. To provide a background, this chapter begins by reviewing the fundamental elasticity theory for orthotropic bodies and how this is related to the thermoelastic theory.

The application of TSA to composite components is described, with emphasis on the hardware used in the experimental work described in this thesis. A review of the thermoelastic studies to date on composite materials is provided, in particular those subject to damage, highlighting the inadequacies of some of the existing approaches with respect to obtaining quantitative data from a composite structure. The aim of this chapter is to examine the necessary considerations to enable quantitative damage analysis of orthotropic composite structures and therefore define where further development of the theory and methodology is required.

3.2 Thermoelastic theory for orthotropic bodies

The thermoelastic effect [73] results from a reversible conversion between mechanical deformation and thermal energy in an elastic solid. The theoretical treatment of this phenomena for a single element was first made available in 1853 by Thomson later Lord Kelvin [73]. The basic thermoelastic relationship for the temperature change, ΔT, is caused by a change in the stress state in a linear elastic, homogeneous solid. So that the thermoelastic theory can be applied to FRP structures it is essential to understand the nature of stresses developed in orthotropic laminated materials. The properties of an orthotropic material are directional [1] and therefore it is necessary to define the reference axes of a laminated structure. Figure 3.1 represents the surface and second ply of a laminated composite material. The fibre orientation indicated by the parallel lines, in this configuration there are three reference axes, defined as follows:

i. in the individual plies (blue arrows), relative to the fibre directions, denoted by the subscripts 1 and 2 (for TSA the surface ply is most important),

ii. in the laminate (red arrows), relative to the direction of the principal stress, denoted by the subscripts x and y,

iii. in the laminate (black arrows), relative to the laminate principal material directions, denoted *L* and *T* (this allows the global mechanical response of the material to be included in the assessment of the thermoelastic response).

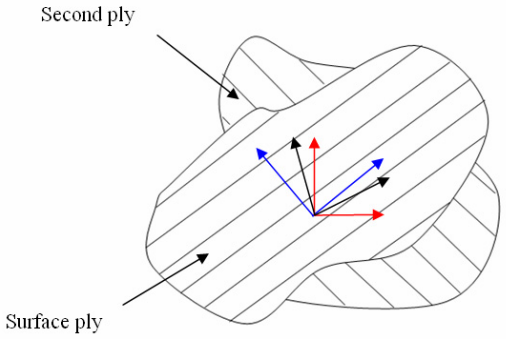

Figure 3.1. Material reference axes defined for two lamina plies of a laminate

In TSA the measurement is taken from the surface ply and therefore the reference axes used in the following treatment are those of the surface ply (1 and 2). To understand the elastic behaviour of anisotropic materials the starting point is to consider the three dimensional stress-strain systems acting on a point and express these as tensors. This three dimensional stress system acting at a point in a continuum is shown in Figure 3.2.

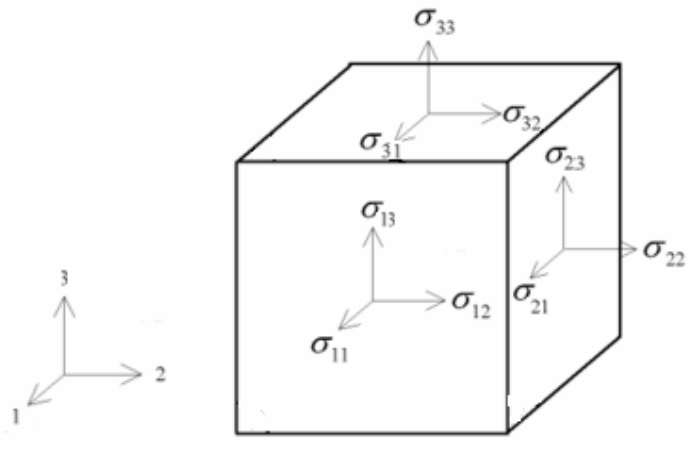

Figure 3.2. State of stress at a point

In tensor notation the stresses, due to the application of a mechanical load, acting on the point are expressed as:

$$\sigma_{ij} = \begin{bmatrix} \sigma_{11} & \sigma_{12} & \sigma_{13} \\ \sigma_{21} & \sigma_{22} & \sigma_{23} \\ \sigma_{31} & \sigma_{32} & \sigma_{33} \end{bmatrix} \tag{3.1}$$

where σ_{11}, σ_{22} *and* σ_{33} are the direct stresses and $\sigma_{12}, \sigma_{21}, \sigma_{13}, \sigma_{31}, \sigma_{23}$ *and* σ_{32} are the shear stresses.

The system shown in Figure 3.2 is assumed in a state of mechanical equilibrium and consequently $\sigma_{12} = \sigma_{21}, \sigma_{13} = \sigma_{31}$ *and* $\sigma_{23} = \sigma_{32}$. Similarly the strain tensor acting on the point of interest can be expressed as:

$$\varepsilon_{ij} = \begin{bmatrix} \varepsilon_{11} & \varepsilon_{12} & \varepsilon_{13} \\ \varepsilon_{21} & \varepsilon_{22} & \varepsilon_{23} \\ \varepsilon_{31} & \varepsilon_{32} & \varepsilon_{33} \end{bmatrix} \tag{3.2}$$

where $\varepsilon_{11}, \varepsilon_{22}$ *and* ε_{33} are the direct stresses and $\varepsilon_{12}, \varepsilon_{21}, \varepsilon_{13}, \varepsilon_{31}, \varepsilon_{23}$ *and* ε_{32} are the shear stresses.

The second order tensor stress and strain terms introduced in Equations (3.1) and (3.2) are related by the elastic properties of the material in question. In simple elastic uniaxial systems this relationship follows Hooke's law; in orthotropic systems this relationship is more complex:

$$\sigma_{ij} = C_{ijkl}\varepsilon_{kl} \tag{3.3}$$

where $\left[C_{ijkl}\right]$ is the stiffness matrix and involves a combination of Young's modulus and Poisson's ratio.

Similarly a matrix can be created to express the strain-stress terms:

$$\varepsilon_{ij} = S*_{ijkl}\,\sigma_{kl} \tag{3.4}$$

where $\left[S*_{ijkl}\right]$ is the compliance matrix and is the inverse of the stiffness matrix.

The compliance and stiffness terms are fourth order tensors and to be completely characterised require 9 x 9 matrices with an associated array of 81 elastic constants. As the point of interest is assumed to be in mechanical equilibrium it is possible to equate many of the variables (suffix pairs) due to symmetry. This enables a contracted notation to be developed that reduces the characterisation to 36 elastic constants. The relationship between the conventional tensor relationship and the contracted notation is defined in Table 3.1.

Table 3.1. Stress and strain tensor suffix notations

Full notation	11	22	33	23, 32	31, 13	12, 21
Contracted notation	1	2	3	4	5	6

In order that the stress and strain tensors acting on a point can be directly related through the 6 x 6 stiffness and compliance matrices the conventional manipulation is to express the stress and strain tensors using the contracted notation as follows:

$$\begin{bmatrix} \sigma_{11} & \sigma_{12} & \sigma_{13} \\ \sigma_{21} & \sigma_{22} & \sigma_{23} \\ \sigma_{31} & \sigma_{32} & \sigma_{33} \end{bmatrix} = \begin{bmatrix} \sigma_1 \\ \sigma_2 \\ \sigma_3 \\ \tau_4 \\ \tau_5 \\ \tau_6 \end{bmatrix} \tag{3.5}$$

$$\begin{bmatrix} \varepsilon_{11} & \varepsilon_{12} & \varepsilon_{13} \\ \varepsilon_{21} & \varepsilon_{22} & \varepsilon_{23} \\ \varepsilon_{31} & \varepsilon_{32} & \varepsilon_{33} \end{bmatrix} = \begin{bmatrix} \varepsilon_1 \\ \varepsilon_2 \\ \varepsilon_3 \\ \gamma_4 \\ \gamma_5 \\ \gamma_6 \end{bmatrix} \tag{3.6}$$

where the shear stress and strain terms are notated τ and γ respectively.

Therefore in the case of an *anisotropic* material, the stress-strain relationship has the following form:

$$\begin{bmatrix} \sigma_1 \\ \sigma_2 \\ \sigma_3 \\ \tau_4 \\ \tau_5 \\ \tau_6 \end{bmatrix} = \begin{bmatrix} C_{11} & C_{12} & C_{13} & C_{14} & C_{15} & C_{16} \\ C_{21} & C_{22} & C_{23} & C_{24} & C_{25} & C_{26} \\ C_{31} & C_{32} & C_{33} & C_{34} & C_{35} & C_{36} \\ C_{41} & C_{42} & C_{43} & C_{44} & C_{45} & C_{46} \\ C_{51} & C_{52} & C_{53} & C_{54} & C_{55} & C_{56} \\ C_{61} & C_{62} & C_{63} & C_{64} & C_{65} & C_{66} \end{bmatrix} \begin{bmatrix} \varepsilon_1 \\ \varepsilon_2 \\ \varepsilon_3 \\ \gamma_4 \\ \gamma_5 \\ \gamma_6 \end{bmatrix} \tag{3.7}$$

By consideration of energy conservation in the system further symmetries are evident [1] that demonstrate that the stiffness and compliance matrices are symmetrical. Therefore for a general *anisotropic* body there are 21 independent elastic constants (from the 36 apparent in Equation (3.7)). For an *orthotropic* laminate system (with three mutually perpendicular planes of material symmetry) the stress-strain relationships are developed in the same manner as above but the number of independent elastic constants can be reduced to nine. This is possible by considering the laminate when the reference material axes are coincident with the planes of material symmetry (i.e. a *specially orthotropic* laminate). In this case there are no interactions between

i. the normal stresses σ_1, σ_2, σ_3 and shear strains γ_4, γ_5, γ_6, i.e. normal stresses acting along principal material directions produce only normal strains,
ii. the shear stresses τ_4, τ_5, τ_6 and normal strains ε_1, ε_2, ε_3, i.e. shear stresses acting on principal material planes produce only shear strains,
iii. the shear stresses and shear strains on different planes; i.e. shear stress acting on a principal plane produces shear strain only on that plane.

The stress-strain relationship can be therefore be characterised by nine independent constants as:

$$\begin{bmatrix}\sigma_1\\ \sigma_2\\ \sigma_3\\ \tau_4\\ \tau_5\\ \tau_6\end{bmatrix}=\begin{bmatrix}C_{11} & C_{12} & C_{13} & 0 & 0 & 0\\ C_{12} & C_{22} & C_{23} & 0 & 0 & 0\\ C_{13} & C_{23} & C_{33} & 0 & 0 & 0\\ 0 & 0 & 0 & C_{44} & 0 & 0\\ 0 & 0 & 0 & 0 & C_{55} & 0\\ 0 & 0 & 0 & 0 & 0 & C_{66}\end{bmatrix}\begin{bmatrix}\varepsilon_1\\ \varepsilon_2\\ \varepsilon_3\\ \gamma_4\\ \gamma_5\\ \gamma_6\end{bmatrix} \tag{3.8}$$

The symmetry of the elastic constants allows the stiffness matrix to be simplified about the leading diagonal of the matrix and this is demonstrated by the symmetry of the suffices in Equation (3.8). The strain-stress relationship for an orthotropic material is similarly derived using $[\varepsilon_i]=[S^*_{ij}]\ [\sigma_j]$.

Composite laminates are predominately used in the form of a thin sheet loaded in the plane of the laminate. Composite laminae can therefore be considered in a plane stress condition, i.e. all stress components in the out-of-plane direction are equal to zero, i.e. $\sigma_3 = \tau_4 = \tau_5 = 0$. Therefore, Equation (3.8) further reduces to:

$$\begin{bmatrix}\sigma_1\\ \sigma_2\\ 0\\ 0\\ 0\\ \tau_6\end{bmatrix}=\begin{bmatrix}C_{11} & C_{12} & C_{13} & 0 & 0 & 0\\ C_{21} & C_{22} & C_{23} & 0 & 0 & 0\\ C_{31} & C_{32} & C_{33} & 0 & 0 & 0\\ 0 & 0 & 0 & C_{44} & 0 & 0\\ 0 & 0 & 0 & 0 & C_{55} & 0\\ 0 & 0 & 0 & 0 & 0 & C_{66}\end{bmatrix}\begin{bmatrix}\varepsilon_1\\ \varepsilon_2\\ \varepsilon_3\\ \gamma_4\\ \gamma_5\\ \gamma_6\end{bmatrix} \tag{3.9}$$

Matrix expansion of Equation (3.9) gives:

$$\sigma_1 = C_{11}\varepsilon_1 + C_{12}\varepsilon_2 + C_{13}\varepsilon_3 \tag{3.10}$$

$$\sigma_2 = C_{12}\varepsilon_1 + C_{22}\varepsilon_2 + C_{23}\varepsilon_3 \tag{3.11}$$

$$0 = C_{13}\varepsilon_1 + C_{23}\varepsilon_2 + C_{33}\varepsilon_3 \tag{3.12}$$

Noting that $\gamma_4 = \gamma_5 = 0$ the shear stress is expressed as:

$$\tau_6 = C_{66}\gamma_6 \tag{3.13}$$

By rewriting Equation (3.12) in terms of ε_3 and substituting this expression into Equations (3.10) and (3.11) the first principal stress can be expressed as:

$$\sigma_1 = C_{11}\varepsilon_1 + C_{12}\varepsilon_2 - C_{13}\left[\frac{1}{C_{33}}(C_{13}\varepsilon_1 + C_{23}\varepsilon_2)\right] \tag{3.14}$$

Factorising (3.14) in terms of the direct strains allows Equation (3.14) to be rewritten as:

$$\sigma_1 = \left[C_{11} - \frac{C_{13}}{C_{33}}C_{13}\right]\varepsilon_1 + \left[C_{12} - \frac{C_{13}}{C_{33}}C_{23}\right]\varepsilon_2 \tag{3.15}$$

The bracketed terms can be simplified by using the reduced stiffness terms where $Q_{ij} = C_{ij} - \frac{C_{i3}C_{j3}}{C_{33}}$ (i,j = 1, 2, 6). The reduced stiffness terms are derived from the manipulation of the compliance terms with consideration to a loaded uniaxial laminate as detailed in full by Daniel and Ishai [1], and are defined as follows:

$Q_{11} = E_1 \big/ (1 - \nu_{12}\nu_{21})$, $Q_{22} = E_2 \big/ (1 - \nu_{12}\nu_{21})$, $Q_{12} = \nu_{21}E_1 \big/ (1 - \nu_{12}\nu_{21}) = \nu_{12}E_2 \big/ (1 - \nu_{12}\nu_{21})$ and $Q_{66} = G_{12}$

The components of the stiffness matrix (Q_{ij}) are dependent on the Young's modulus of the material and the Poisson's ratio in the direction of interest. The substitution of the reduced stiffness terms simplifies (3.15) as follows:

$$\sigma_1 = Q_{11}\varepsilon_1 + Q_{12}\varepsilon_2 \tag{3.16}$$

The same expansion is carried out for the second direct and shear stress relationships as follows:

$$\sigma_2 = C_{12}\varepsilon_1 + C_{22}\varepsilon_2 - C_{13}\left[\frac{1}{C_{33}}(C_{13}\varepsilon_1 + C_{23}\varepsilon_2)\right] \tag{3.17}$$

$$\sigma_2 = \left[C_{12} - \frac{C_{23}}{C_{33}}C_{13}\right]\varepsilon_1 + \left[C_{22} - \frac{C_{23}}{C_{33}}C_{23}\right]\varepsilon_2 \tag{3.18}$$

$$\sigma_2 = Q_{12}\varepsilon_1 + Q_{22}\varepsilon_2 \tag{3.19}$$

Finally for convenience the shear stress in Equation (3.13) can be expressed as follows

$$\tau_6 = C_{66}\gamma_6 = Q_{66}\gamma_6 \tag{3.20}$$

Therefore Equation (3.9) is simplified for an *orthotropic* material in the form:

$$\begin{bmatrix}\sigma_1\\ \sigma_2\\ \tau_6\end{bmatrix} = \begin{bmatrix}Q_{11} & Q_{12} & 0\\ Q_{12} & Q_{22} & 0\\ 0 & 0 & Q_{66}\end{bmatrix}\begin{bmatrix}\varepsilon_1\\ \varepsilon_2\\ \gamma_6\end{bmatrix} \tag{3.21}$$

Following the same principles the strain compliance matrix can be expanded to provide:

$$\begin{bmatrix}\varepsilon_1\\ \varepsilon_2\\ \gamma_6\end{bmatrix} = \begin{bmatrix}S^*_{11} & S^*_{12} & 0\\ S^*_{12} & S^*_{22} & 0\\ 0 & 0 & S^*_{66}\end{bmatrix}\begin{bmatrix}\sigma_1\\ \sigma_2\\ \tau_6\end{bmatrix} \tag{3.22}$$

where the compliance terms are expressed as:

$$S^*_{11} = \frac{1}{E_1},\ S^*_{22} = \frac{1}{E_2},\ S^*_{12} = \frac{-\nu_{12}}{E_1} = \frac{-\nu_{21}}{E_2},\ \text{and}\ S^*_{66} = \frac{1}{G_{12}}.$$

The stress and strain state due to the application of a mechanical load acting on a point in equilibrium has been defined for an orthotropic material system by Equations (3.21) and (3.22). For TSA the reversible temperature induced strain that occurs as a consequence of the application of thermal energy must be included. The temperature variation will result in a thermal strain that is a function of the coefficient of thermal expansion of the material and the temperature change experienced. Including the thermal strain the stress-strain-temperature relationship may be generalised for an orthotropic body using the expression for the stress tensor (Equation (3.21)) as:

$$\sigma_i = \sum_{i=1}^{6} Q_{ij}\left(\varepsilon_j - \alpha_j \Delta T\right);\ i, j = 1,.....,6 \tag{3.23}$$

where α_j are the coefficients of linear thermal expansion.

Similarly the strain-stress-temperature relationship can be expressed as:

$$\varepsilon_i = \sum_{j=1}^{6} S^*_{ij}\sigma_j + \alpha_i \Delta T \; ; \; i, j = 1,.....,6 \, , \tag{3.24}$$

The basic thermoelastic relationship between the stress change and the accompanying temperature change, ΔT, is derived from the laws of thermodynamics [21, 74] in the form:

$$\Delta T = -\frac{T}{\rho C_\varepsilon} \sum_i \frac{\partial \sigma_i}{\partial T} \varepsilon_i + \frac{Q^*}{\rho C_\varepsilon}, \text{ with i } = 1,\ldots,6 \tag{3.25}$$

where T is the absolute temperature, C_ε is the specific heat at constant strain, Q^* is the heat input, ρ is the mass density, σ_i is the stress change tensor and ε_i is the strain change tensor.

The initial development of Equation (3.25) is based on the fundamental laws of thermodynamics and is therefore valid for *isotropic* or *anisotropic* materials. As the work in this thesis is concerned with orthotropic materials, Equation (3.25) will be developed into a working equation for thermoelastic studies of orthotropic composite laminates. This is approached in two steps: firstly, the stress variables are defined as given in Equation (3.23) and secondly, the strain terms are defined as given in Equation (3.24). The treatment is based on the work of Stanley and Chan [21] that deals with isotropic bodies; in their later 1988 paper [24] on orthotropic bodies only part of the treatment was presented. As the focus of this thesis is to develop and apply the theory for laminated composites a detailed presentation of the background theory is provided in the following, much of which has not been covered elsewhere.

Expansion of Equation (3.23) provides the stresses acting on the point of investigation:

$$\begin{bmatrix} \sigma_1 \\ \sigma_2 \\ \tau_6 \end{bmatrix} = \begin{bmatrix} Q_{11} & Q_{12} & 0 \\ Q_{12} & Q_{22} & 0 \\ 0 & 0 & Q_{66} \end{bmatrix} \begin{bmatrix} \varepsilon_1 - \alpha_1 \Delta T \\ \varepsilon_2 - \alpha_2 \Delta T \\ \gamma_6 - \alpha_6 \Delta T \end{bmatrix} \tag{3.26}$$

Expansion of this for the tensor components 1, 2, and 6, as defined for an orthotropic solid, defines the direct stresses and shear stress terms:

$$\sigma_1 = Q_{11}(\varepsilon_1 - \alpha_1 \Delta T) + Q_{12}(\varepsilon_2 - \alpha_2 \Delta T) \tag{3.27}$$

$$\sigma_2 = Q_{12}(\varepsilon_1 - \alpha_1 \Delta T) + Q_{22}(\varepsilon_2 - \alpha_2 \Delta T) \tag{3.28}$$

$$\tau_6 = Q_{11}(\gamma_6 - \alpha_6 \Delta T) \tag{3.29}$$

So that stress terms can be substituted into Equation (3.25) in the partial derivatives must be obtained. To do this the usual approach is to assume that the elastic constants and therefore the reduced stiffness values (Q_{ij}) are independent of temperature. Over the small reversible temperature range expected by the thermoelastic effect this is valid for most materials. It is however necessary to make a judgement to the expected variation in elastic properties encountered during the testing of composites (this is discussed fully in Chapter 5). Results provided by Aiello and Ombres [75] observed only a four percent variation in the Young's modulus over a 50 K temperature rise for an E-glass epoxy FRP similar to that used in the experimental work of this thesis. Therefore making this assumption here provides no grounds for concern. Differentiating Equations (3.27) – (3.29) with respect to temperature and neglecting the small temperature dependence of the elastic constants, gives the partial derivatives for the three components of the stress tensor:

$$\frac{\partial \sigma_1}{\partial T} = -Q_{11}\alpha_1 - Q_{12}\alpha_2 \tag{3.30}$$

$$\frac{\partial \sigma_2}{\partial T} = -Q_{12}\alpha_1 - Q_{22}\alpha_2 \tag{3.31}$$

$$\frac{\partial \tau_6}{\partial T} = -Q_{66}\alpha_6 \tag{3.32}$$

The next variable in the thermoelastic relationship (Equation (3.25)) are the strain terms; the orthotropic strains are defined as:

$$\begin{bmatrix} \varepsilon_1 \\ \varepsilon_2 \\ \gamma_6 \end{bmatrix} = \begin{bmatrix} S^*_{11} & S^*_{12} & 0 \\ S^*_{12} & S^*_{22} & 0 \\ 0 & 0 & S^*_{66} \end{bmatrix} \begin{bmatrix} \sigma_1 \\ \sigma_2 \\ \tau_6 \end{bmatrix} + \Delta T \begin{bmatrix} \alpha_1 \\ \alpha_2 \\ \alpha_6 \end{bmatrix} \tag{3.33}$$

Expansion of Equation (3.33) provides:

$$\varepsilon_1 = S^*_{11}\,\sigma_1 + S^*_{12}\,\sigma_2 + \alpha_1 \Delta T \tag{3.34}$$

$$\varepsilon_2 = S^*_{21}\,\sigma_1 + S^*_{22}\,\sigma_2 + \alpha_2 \Delta T \tag{3.35}$$

$$\gamma_6 = S^*_{66}\,\tau_6 + \alpha_6 \Delta T \tag{3.36}$$

Further consideration of the working principles of a laminate system it follows that for a specially orthotropic laminate then for $j \geq 4$, α_j equals zero [24]. Noting this simplifies Equations (3.32) and (3.36); substituting Equations (3.30) – (3.32) and (3.34) – (3.36) into Equation (3.25) the following expression for the temperature change can be derived:

$$\begin{aligned}\Delta T = \frac{T}{\rho C_\varepsilon}\{&\left(-Q_{11}\alpha_1 - Q_{12}\alpha_2\right)\left(S^*_{11}\,\sigma_1 + S^*_{12}\,\sigma_2 + \alpha_1 \Delta T\right) + \\ &\left(-Q_{12}\alpha_1 - Q_{22}\alpha_2\right)\left(S^*_{21}\,\sigma_1 + S^*_{22}\,\sigma_2 + \alpha_2 \Delta T\right)\} + \frac{Q^*}{\rho C_\varepsilon}\end{aligned} \tag{3.37}$$

To further simplify, the next step is to derive a relationship between C_ε and C_p (the specific heat at constant pressure). This relationship between C_p and the specific heat at constant volume is [76]:

$$C_p - C_v = T\left(\frac{\partial P}{\partial T}\right)_v \left(\frac{\partial V}{\partial T}\right)_p \tag{3.38}$$

and introducing C_ε requires that the density be included as follows:

$$C_p - C_\varepsilon = -\frac{T}{\rho}\left(\frac{\partial \sigma_i}{\partial T}\right)\left(\frac{\partial \varepsilon_i}{\partial T}\right) \tag{3.39}$$

The negative sign arises in Equation (3.39) because a body under positive pressure reacts with a negative stress (i.e. a compression).

Again, assuming the elastic constants are temperature independent over the temperature range of interest here, the bracketed strain derivatives in Equations (3.39) can be presented as:

$$\frac{\partial \varepsilon_1}{\partial T} = \alpha_1 \tag{3.40}$$

$$\frac{\partial \varepsilon_2}{\partial T} = \alpha_2 \tag{3.41}$$

and by substituting the previously derived values for $\left(\partial\sigma_i \big/ \partial T\right)$, the following expression is obtained from Equation (3.39) for the relationship between C_ε and C_p:

$$C_p - C_\varepsilon = -\frac{T}{\rho}\left\{ Q_{11}{\alpha_1}^2 + 2Q_{12}\alpha_1\alpha_2 + Q_{22}{\alpha_2}^2 \right\} \tag{3.42}$$

To obtain ΔT in terms of C_p some simplification is necessary. By making the substitution $x = \left(-Q_{11}\alpha_1 - Q_{12}\alpha_2\right)\left(\alpha_1\right) + \left(-Q_{12}\alpha_1 - Q_{22}\alpha_2\right)\left(\alpha_2\right)$ simplifies Equation (3.42) to:

$$C_\varepsilon = C_p - \frac{Tx}{\rho} \tag{3.43}$$

If now $y = \left(Q_{11}\alpha_1 + Q_{12}\alpha_2\right)\left(S_{11}\sigma_1 + S_{12}\sigma_2 + \alpha_1\Delta T\right) + \left(Q_{12}\alpha_1 + Q_{22}\alpha_2\right)\left(S_{21}\sigma_1 + S_{22}\sigma_2 + \alpha_2\Delta T\right)$ then Equation (3.37) becomes:

$$\Delta T = -\frac{T}{\rho C_\varepsilon} y + \frac{Q^*}{\rho C_\varepsilon} \tag{3.44}$$

Expanding Equation (3.44) in terms of the specific at constant pressure provides:

$$\Delta T = -\frac{Ty}{\rho}\frac{1}{\left(C_p - Tx \big/ \rho\right)} + \frac{Q^*}{\rho}\frac{1}{\left(C_p - Tx \big/ \rho\right)} = \frac{Q^* - Ty}{\rho C_p - Tx} \tag{3.45}$$

A further two substitutions; $a = \left(Q_{11}\alpha_1 + Q_{12}\alpha_2\right)$ and $b = \left(Q_{12}\alpha_1 + Q_{22}\alpha_2\right)$, results in $x = a\alpha_1 + b\alpha_2$, that further enables y to be expressed as:

$$y = a\left(S^*_{11}\,\sigma_1 + S^*_{12}\,\sigma_2 + \alpha_1\Delta T\right) + b\left(S^*_{21}\,\sigma_1 + S^*_{22}\,\sigma_2 + \alpha_2\Delta T\right) \tag{3.46}$$

$$y = a\left(S^*_{11}\,\sigma_1 + S^*_{12}\,\sigma_2\right) + b\left(S^*_{21}\,\sigma_1 + S^*_{22}\,\sigma_2\right) + \Delta Tx \tag{3.47}$$

Substituting the above development of y into Equation (3.45) for the temperature change provides:

$$\Delta T = \frac{Q^*}{\rho C_p - Tx} - \frac{Ta\left(S^*_{11}\,\sigma_1 + S^*_{12}\,\sigma_2\right)}{\rho C_p - Tx} - \frac{Tb\left(S^*_{21}\,\sigma_1 + S^*_{22}\,\sigma_2\right)}{\rho C_p - Tx} - \frac{T\Delta Tx}{\rho C_p - Tx} \tag{3.48}$$

$$\Delta T\rho C_p - Tx = Q^* - Ta\left(S^*_{11}\,\sigma_1 + S^*_{12}\,\sigma_2\right) - Tb\left(S^*_{21}\,\sigma_1 + S^*_{22}\,\sigma_2\right) - T\Delta Tx \tag{3.49}$$

$$\Delta T = \frac{Q^*}{\rho C_p} - \frac{T}{\rho C_p} z \tag{3.50}$$

where $z = \left[a\left(S^*_{11}\,\sigma_1 + S^*_{12}\,\sigma_2\right) + b\left(S^*_{21}\,\sigma_1 + S^*_{22}\,\sigma_2\right)\right]$.

Expanding z with the a and b substitutions and simplifying produces:

$$z = \left(Q_{11}\alpha_1 + Q_{12}\alpha_2\right)\left(S^*_{11}\,\sigma_1 + S^*_{12}\,\sigma_2\right) + \left(Q_{12}\alpha_1 + Q_{22}\alpha_2\right)\left(S^*_{21}\,\sigma_1 + S^*_{22}\,\sigma_2\right) \tag{3.51}$$

Expanding this equation and factorising the principal stresses and coefficient of thermal expansion terms provides z in terms of the reduced stiffness and compliance terms as:

$$\begin{aligned} z = {} & \alpha_1\sigma_1\left(Q_{11}S^*_{11} + Q_{12}S^*_{21}\right) + \alpha_1\sigma_2\left(Q_{11}S^*_{12} + Q_{12}S^*_{22}\right) \\ & + \alpha_2\sigma_1\left(Q_{12}S^*_{11} + Q_{22}S^*_{21}\right) + \alpha_2\sigma_2\left(Q_{12}S^*_{12} + Q_{22}S^*_{22}\right) \end{aligned} \tag{3.52}$$

Expanding the reduced stiffness terms into terms of Young's modulus and the Poisson's ratio terms, Equation (3.52) results in the elimination of the Young's modulus terms and the following expression:

$$\begin{aligned} z = {} & \alpha_1\sigma_1\left[\frac{1}{1-\nu_{12}\nu_{21}} - \frac{\nu_{12}\nu_{21}}{1-\nu_{12}\nu_{21}}\right] + \alpha_1\sigma_2\left[\frac{\nu_{12}}{1-\nu_{12}\nu_{21}} - \frac{\nu_{12}}{1-\nu_{12}\nu_{21}}\right] \\ & + \alpha_2\sigma_1\left[\frac{\nu_{21}}{1-\nu_{12}\nu_{21}} - \frac{\nu_{21}}{1-\nu_{12}\nu_{21}}\right] + \alpha_2\sigma_2\left[\frac{-\nu_{12}\nu_{21}}{1-\nu_{12}\nu_{21}} + \frac{1}{1-\nu_{12}\nu_{21}}\right] \end{aligned} \tag{3.53}$$

Inspection of the bracketed terms in Equation (3.53) shows that they are either one or zero so that:

$$z = (\alpha_1\sigma_1 + \alpha_2\sigma_2) \tag{3.54}$$

Substituting z back into Equation (3.50) provides an equation for the change in temperature in terms of T, C_p, ρ, α, σ and Q as follows:

$$\Delta T = -\frac{T}{\rho C_p}(\alpha_1\sigma_1 + \alpha_2\sigma_2) + \frac{Q^*}{\rho C_p} \tag{3.55}$$

The second term in Equation (3.55) incorporating the heat transfer term, Q^*, is assumed negligible (with regard to the value of the first term) and for the purposes of TSA and to-date in most thermoelastic work the heat transfer term has been neglected. In order that this assumption is valid it is necessary to cyclically load the component at such as rate to achieve a *pseudo-adiabatic* state, whereby there is no measurable attenuation of the thermoelastic signal due to heat transfer. Therefore the relationship derived by Stanley and Chan [24] for the temperature change for an orthotropic material has been derived and is expressed as follows:

$$\Delta T = -\frac{T}{\rho C_p}(\alpha_1\Delta\sigma_1 + \alpha_2\Delta\sigma_2) \tag{3.56}$$

In [24] Equation (3.56) was validated using two types of composite component. In the validation on an orthotropic composite cylinder loaded in compression, the laminated nature of the material was set aside as the component was symmetrically wound. This means that the stress in each ply was equal and a simple force over area formulation for the applied stress in the laminate was valid. Potter [77] proposed a theory that took into account the laminate behaviour in terms of the strain. Potter's theory accounted for the variation in stress ply-by-ply but was not developed into a general theory. In Chapter 4 a general strain based theory is developed from Equation (3.37).

In isotropic materials the coefficient of thermal expansion is directionless therefore $\alpha_1 = \alpha_2 = \alpha$; making this substitution into Equation (3.56) allows the familiar thermoelastic equation presented in Stanley and Chan's original work [21] to be obtained:

$$\Delta T = -KT\Delta(\sigma_1 + \sigma_2) \tag{3.57}$$

where K, the thermoelastic constant [23], is given by:

$$K = \frac{\alpha}{\rho C_p} \tag{3.58}$$

K is crucially important in any attempt to obtain stress data from measured temperature changes. It is evident that the larger K is then, certainly, the larger will be ΔT, the value the thermoelastic signal relies on. However, the temperature change associated with typical stress changes in materials under test are only of the order of 0.01 - 0.1 °C, therefore extremely sensitive equipment is essential for quantitative work. Table 3.2 lists the typical material values and calculates K, the thermoelastic constant.

Table 3.2. Material properties [23]

Material	α $\left(10^{-6} C^{-1}\right)$	C $\left(Jkg^{-1}\circ C\right)$	E (GPa)	ν	K $\left(10^{-6} MPa^{-1}\right)$
Duralumin	22.5	873.6	73	0.345	9.20
EN1A	12.6	475	207.1	0.28	3.39
Epoxy	35	1040	2.8	0.37	28.76
Pyrex	3.2	940	70	0.2	1.42

The relatively high K value for epoxy materials is of benefit to TSA of epoxy based composite structures and is a further incentive to further develop the technique. Regardless of this however it is still necessary to accurately discern very small temperature variations. In the practical application of TSA this is achieved using an IR photon detector as described in the following section.

At this stage it is worthwhile discussing the adiabatic assumption and neglecting the Q^* term in Equation (3.55). Bakis and Reifsnider [78] investigated the influence of material inhomogeneity and anisotropy using carbon fibre reinforced plastics. They also investigated the limitations of Equation (3.56) in terms of the adiabatic assumption made in its development. It was found that the thermoelastic response was affected by a number of factors, which included the volume fraction, the thermoelastic properties of the micro-constituent materials, the orientations of the laminae within the laminate, and the orientation of the lamina on the surface. For composite materials it was suggested that the non-adiabatic behaviour in carbon fibre reinforced polymer (CFRP) laminates could be due to heat transfer between the fibre and matrix or caused by viscoelastic

effects. The former was discounted by Wong [79] for fibres of diameter ≈7 μm which is typical for composite laminates. Wong discussed the effects of non-adiabatic conditions on the thermoelastic signal recorded from the specimen surface due to heat transfer at large stress gradients, such as those experienced between plies orientated at different angles in a laminate. A lumped approach was presented and it was shown that the temperature gradients between the fibres and the surrounding matrix, generated by the thermoelastic effect, presents such high values as to provoke an almost instantaneous heat transfer by conduction. Resulting in a very rapid thermal equilibrium where there is no difference in the temperature changes observed in the fibres and the matrix. In order that this assumption is maintained the loading frequency must be considered in testing and the range between 5 – 30 Hz was demonstrated to be adequate. Experimental work was later carried out using glass reinforced epoxy composites by Cunningham *et al.* [36] who demonstrated that the adiabatic assumption is valid from 1 Hz to 15 Hz, this was verified for a range of laminate stacking sequences. The material used throughout the experimental work of this thesis is identical to that used in reference [36]. Therefore the neglection of the heat transfer term in Equation (3.55) is valid. It is clear for some laminated materials higher frequencies may be required to achieve adiabatic conditions but for polymer based composites a loading frequency of 30 Hz is adequate. This is achievable with standard test machines. Therefore the work in this thesis assumes that the stress-induced temperature change, ΔT, occurs adiabatically throughout.

3.3 Measurement of ΔT using an infra-red photon detector

The first documented measurement of ΔT, due to the thermoelastic effect, was achieved by Belgen [80] who used a single-point radiometer. The radiometer provided a non-contacting means of obtaining ΔT by measuring the radiant flux from the component. In the current work two TSA systems manufactured by Stress Photonics, the DeltaTherm 1000 [81] and 1400 are used to record the thermoelastic data. Both of these systems incorporate a Focal Plane Array (FPA) infra-red (IR) detector which is enclosed in a cold shield of Liquid Nitrogen. The DT1000 (Figure 3.3a) and DT1400 (Figure 3.3b) both incorporate Indium Antimonide (InSb) *staring* detector arrays being 128 x 128 or 256 x 256 respectively. The *staring* facility allows data to be continuously collected over the entire field of view producing a full-field image. The signal is digitally processed at a rate of 146 Hz, providing almost instant thermoelastic data acquisition. This provides the opportunity to monitor damage growth and to assess damage at representative loads in real time in the actual component [64]. The thermal resolution of the DeltaTherm

1400 system is 2 mK [82], which produces a stress sum resolution of 0.25 MPa for an epoxy component at room temperature.

a) b)

Figure 3.3. DeltaTherm 1000 and 1400 respectively

The IR detector is focused on the component under examination using an IR lens. The lens type and the detector stand-off distance dictates the field of view. The lens attached to both systems in Figure 3.3 is a 25 mm lens and is used in all the experimental work presented in this thesis.

The ability to record the ΔT associated with the thermoelastic effect via a non-contacting device is possible because any solid with a temperature above 0 K will emit energy in the form of electromagnetic radiation/thermal radiation at its surface [83]. Increasing the bulk body temperature will increase the quantity of heat transferred by thermal radiation. By tracking the amount of energy emitted in the form of electromagnetic radiation accurate temperature measurements are made by means of the IR thermography [84]. In TSA systems the IR photon detector is used, these detectors are made from a semiconductor material that is sensitive to photon flux [85]. The output voltage from the detecting system is digitally processed to produce what is known as the thermoelastic signal, S, which is linearly related to the temperature change on the material surface. Since the magnitude of the useful signal is very small, a special technique for noise rejection and correlation is used to process the analogue detector output signal into the digital 'thermoelastic signal', S [81]. The experimental set-up is shown in Figure 3.4

which depicts *i*) the sub-systems used for collection and processing of the thermoelastic data using the DeltaTherm system and *ii*) how the DeltaTherm system interacts with the loading system.

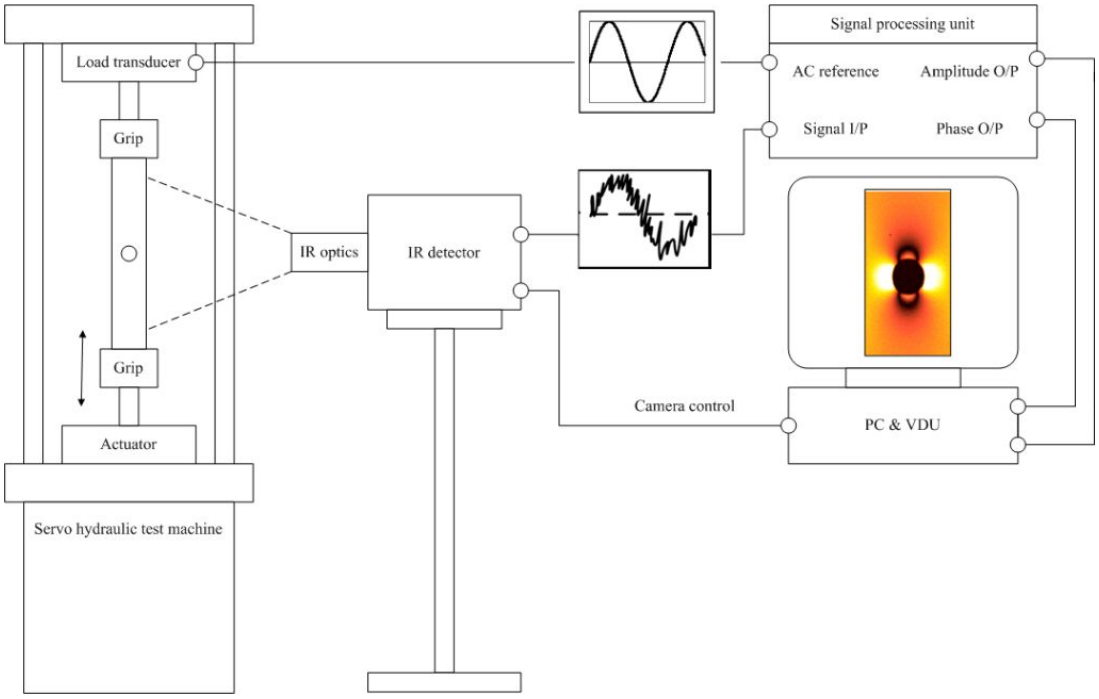

Figure 3.4. Experimental set-up including DeltaTherm sub-systems

The intensity of the photon collection defines the electrical signal output from the detector as the detector acts as a transducer turning a photon strike into a voltage signal. The spectral emissive power ($\Phi_{\lambda,b}$) for a blackbody in a hemisphere can be found using *Planck's law* [86], i.e.:

$$\Phi_{\lambda,b} = \frac{C_1}{\lambda^5 (\exp\left(C_2 / \lambda T\right) - 1)} \tag{3.59}$$

where C_1 is the first radiation constant = $2\pi c^2 h$ (h is Planck's constant, c is the speed of light and λ is wavelength), C_2 is the second radiation constant = ch/k (k is the Boltzmann constant).

It is possible to produce a finite integral to Planck's law (Equation (3.59)) if the integral is considered between zero and infinity and this provides the well-known fourth-power *Stefan-Boltzmann* relationship for evaluating the radiant emittance over all wavelengths Φ_b as follows:

$$\Phi_b = 2\pi c^2 h \int_0^{\infty} \frac{d\lambda}{\lambda^5 (\exp\left(ch/kT\lambda\right) - 1)} \tag{3.60}$$

letting $x = ch/kT\lambda$ allows the integration to be processed by substitution with respect to x. Thus, x must be rewritten to make λ the subject and subsequently differentiated with respect to x. i.e.: $\lambda = \frac{ch}{kTx}$, $\frac{d\lambda}{dx} = \frac{ch}{kTx^2}$ and $\lambda^5 = \frac{c^5 h^5}{k^5 T^5 x^5}$.

Substituting the relationship for λ^5 and the derivative of λ with respect to x into Equation (3.60) leaves:

$$\Phi_b = \frac{2\pi c^3 h^2 k^5 T^5}{c^5 h^5 kT} \int_0^{\infty} \frac{x^5 dx}{x^2 (\exp\left(ch/kT\lambda\right) - 1)} \tag{3.61}$$

and Equation (3.61) can be simplified to:

$$\Phi_b = \frac{2\pi k^4 T^4}{c^2 h^3} \int_0^{\infty} \frac{x^3 dx}{\exp(x) - 1} \tag{3.62}$$

It is the next steps where the integral in Equation (3.62), $I_s = \int_0^{\infty} \frac{x^3}{e(x) - 1} dx$, can be rewritten as a finite integral that allows Equation (3.60) to be evaluated. The integral, I_s, can be expressed as:

$$I_s = \int_0^{\infty} \frac{x^s}{e(x) - 1} dx = \int_0^{\infty} x^s e(-x) \sum_{n=0}^{\infty} e(-nx) dx \tag{3.63}$$

where:

$$I_s = s! \sum_{n=1}^{\infty} \frac{1}{n^{s+1}} \tag{3.64}$$

for s equal to 3, as in this case, the integral may be rewritten using the Riemann Zeta function [87] as:

$$I_3 = 6!\sum_{n=1}^{\infty}\frac{1}{n^4} = \frac{\pi^4}{15} \tag{3.65}$$

For other integrals of s, I_s may be written in the form: $I_s = s!\zeta(s+1)$ where $\zeta(x)$ is the Riemann Zeta function, which is available in mathematical tables for values of s [87]. The values that are used to present the theoretical basis to the application of IR detectors to TSA are tabulated in Table 3.3.

Table 3.3. Values of integrals I_s

s	I_s
2	2.4041
3	$\pi^4/15$

Using the integral in Equation (3.62) the radiant emittance can written as follows:

$$\Phi_b = \left(\frac{2\pi^5 k^4}{15c^2h^3}\right)T^4 \tag{3.66}$$

This result can be simplified by rewriting the right hand side of Equation (3.66) through the introduction of the *Stefan-Boltzmann* constant [76], B, as the bracketed term to give the well-known fourth-power *Stefan-Boltzmann* relationship for evaluating the radiant emittance over all wavelengths Φ_b as follows:

$$\Phi = BT^4 \tag{3.67}$$

Stanley and Chan [21] used the total radiant flux emitted from a surface to develop a working relationship for thermoelastic studies. It follows by differentiation of Equation (3.67) that the flux change, $\Delta\Phi$, resulting from a small change in the surface temperature, ΔT, is given by:

$$\Delta\Phi = 4\eta BT^3\Delta T \tag{3.68}$$

where η is the surface emissivity [83] which is important to consider in TSA [23] as it is probable that the surface will not behave like a blackbody (in the practical application of TSA it is usual that the surface is coated in a thin matt black paint layer to enhance and

standardise the surface emissivity; fortuitously the epoxy matrix in the laminates tested in this thesis provides sufficient emissivity to be tested as manufactured).

If the flux change is recorded by a linear detecting system, the thermoelastic signal will be proportional to the change in temperature and therefore it follows from Equation (3.56) that the change in the principal material stresses is given by:

$$S = -4R^{*}\eta B\rho C_{p}T^{4}\left(\alpha_{1}\Delta\sigma_{1} + \alpha_{2}\Delta\sigma_{2}\right) \tag{3.69}$$

where R^{*} is some detector response factor for the operating system.

Grouping the variables before the bracket on the right-hand side of Equation (3.69) as those dependent on the material under test and the settings of the detector system as the revised calibration constant for orthotropic materials, A^{*}, provides the general thermoelastic relationship for orthotropic materials:

$$A^{*}S = \left(\alpha_{1}\Delta\sigma_{1} + \alpha_{2}\Delta\sigma_{2}\right) \tag{3.70}$$

However, in this treatment Stanley and Chan [24] neglected the fact that an IR detector used is a photon detector and not a Bolometer. In a similar manner it is possible to obtain a discrete equation for the number of photons (N_b) emitted by an object at a specific temperature by dividing the energy in each wavelength interval by the energy carried by each photon. To evaluate the relationship for a general case the photon flux can be derived for the total number of photons per unit area and time by producing a closed form integral of the equation for spectral radiant emittance [86] again this is only possible by considering the wavelength range between zero and infinity, as follows [86]:

$$N_{b} = \int_{0}^{\infty} \frac{2\pi c}{\lambda^{4}\left(\exp\left(hc/\lambda kT\right) - 1\right)}\partial\lambda \tag{3.71}$$

The integration is possible using the substitution method and the subsequent derivatives presented for Equation (3.61) is repeated to provide Equation (3.71). Noting that here λ is raised to the power four in this case the λ terms can be rewritten for this derivation as:

$$\lambda^{4} = \frac{c^{4}h^{4}}{k^{4}T^{4}x^{4}} \tag{3.72}$$

Substituting into Equation (3.71) leaves:

$$N_b = \frac{2\pi c k^4 T^4}{c^4 h^4} \frac{ch}{kT} \int_0^\infty \frac{x^4}{x^2(\exp(x)-1)} dx \tag{3.73}$$

which again can be simplified and rewritten to make use of the Riemann Zeta function:

$$N_b = \frac{2\pi k^3 T^3}{c^2 h^3} \int_0^\infty \frac{x^2 dx}{\exp(x)-1} \tag{3.74}$$

The integral, in Equation (3.74), may be evaluated in a similar manner to that used previously, where *s* is taken as two. Therefore the integrand may be expressed as using the Riemann function for 2 as detailed in Table 3.3, incorporating the finite value for the integral into the equation leaves:

$$N_b = \frac{2\pi k^3 T^3}{c^2 h^3} (2.4041) \tag{3.75}$$

this formulation again allows the substitution of the *Stefan-Boltzmann* constant to provide the following relationship between the number of photons incident and the surface temperature:

$$N_b = \frac{0.370B}{k} T^3 \tag{3.76}$$

The quantity $0.370B/k$ = 1.52 x 10^{15} photons s^{-1} m^{-3} sr^{-1} K^{-3} and can be regarded as the *Stefan-Boltzmann constant for photodetectors* [88]. Denoting the constant for photodetectors as B', Equation (3.76) simplifies to:

$$N_b = \eta B' T^3 \tag{3.77}$$

The relationship presented in Equation (3.77) shows that when considering the entire electromagnetic spectrum the total number of photons increases with the cube of the absolute temperature whilst the radiant emittance over the entire spectrum increases with the fourth-power of absolute temperature. The relationship for the number of photons (N_b) emitted from a surface as derived above and presented in Equation (3.77) has been

used by other researchers attempting to relate the photon flux to the thermoelastic signal. In work presented by Enke *et al*. [89] this was presented to model the Stress Pattern Analysis by measurement of Thermal Emissions (SPATE) [85] (the commercial predecessor to the DeltaTherm) Cadmium Mercury Telluride (CMT) detector's response to the absolute temperature but it cannot be correct as the SPATE system does not operate over the entire spectrum but is limited to the 8 – 12 μm window. It is impossible to derive a closed form relationship, as presented for the radiant emittance or photon flux above, for practical narrow band IR detectors as the Riemann Zeta function that enabled the integration is only valid for integrals over the 0 - ∞ range. Therefore it is necessary to consider other mathematical methods to express the relationship between the spectral radiant power and the absolute temperature between the wavelength limits of the IR detector of interest; this is considered in Chapter 5.

The characteristic plot of $\Phi_{\lambda,\, b}$ against wavelength is illustrated in Figure 3.5 and shows the energy radiated for a given temperature. Two areas of interest are illustrated; these are the operating spectrums of the DeltaTherm system (DT1000 and DT1400) and the SPATE system [85]. The operational ranges of these two systems are in the 2 - 5 μm and 8 - 12 μm range respectively. A further line is plotted which indicates the maximum spectral radiant emittance for a blackbody at various temperatures; it can be shown that $\Phi_{\lambda,b}$ has a maximum, λ_{max}, which can be calculated from *Wien's displacement law* [86]. For a specimen with an absolute temperature of 293 K, λ_{max} occurs at 9.89 μm; within the operating range of the SPATE detector.

From inspection of the five temperature profiles depicted in Figure 3.5 it can be seen that the $\Phi_{\lambda,\, b}$ is a function of the absolute temperature of the body. Therefore, an increase in the absolute temperature will result in a greater photon flux for a given mechanical deformation and will therefore have an affect on the thermoelastic signal recorded. In work by Quinn [90] the DeltaTherm system was shown to be sensitive to the absolute temperature to a greater extent than the SPATE system. This is as a result of the behaviour of Planck's law between the differing operating wavelength ranges of the detectors. The reason that the SPATE system is less sensitive to an absolute temperature changes is that the spectral emissive power is closer to the maximum level which results in the isotherms being closer together which means for a given temperature rise the $\Phi_{\lambda,\, b}$ will change to a lesser extent.

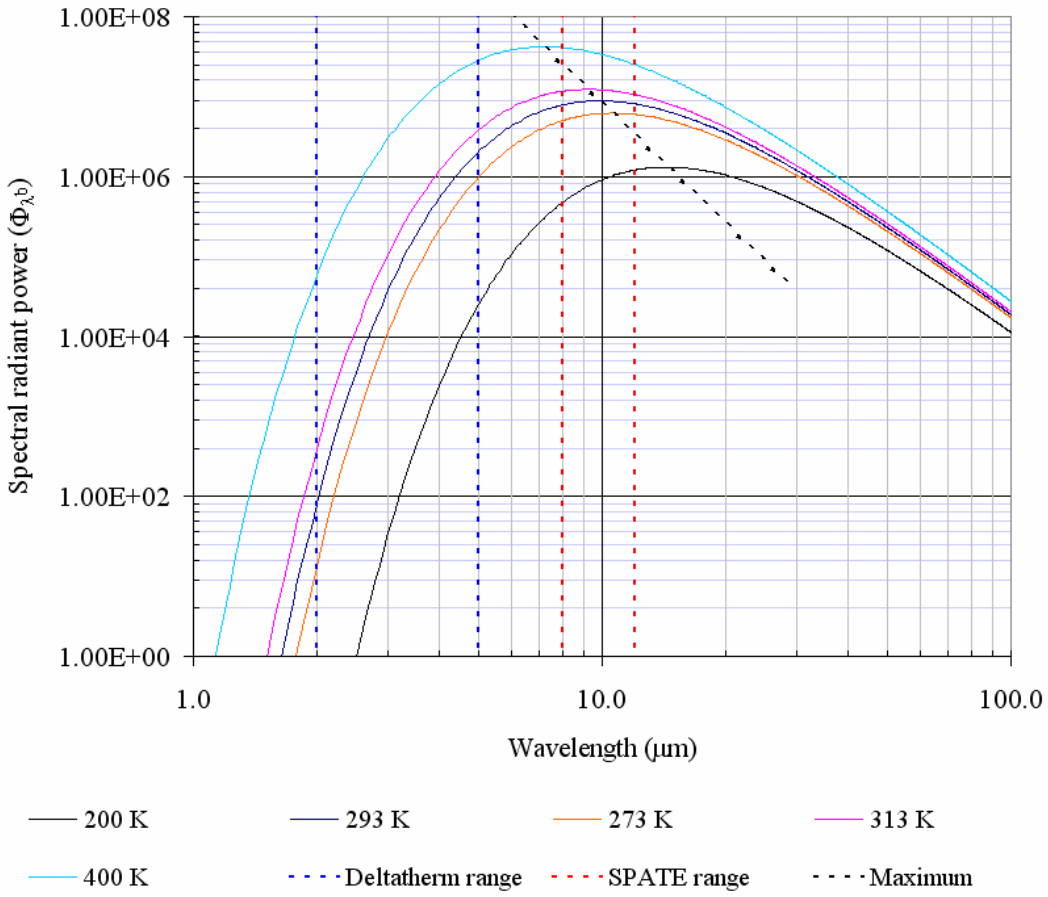

Figure 3.5. Spectral emissive power of a blackbody

The effect of the absolute temperature on the thermoelastic signal was acknowledged by Ometron who marketed the SPATE system. A correction factor, R, was developed and accounted for any departure from the absolute temperature at which the stress calibration took place. Work by Fulton [91] with the SPATE observed that the correction factor was closely related to a ratio of the absolute temperatures at the time of test and calibration raised to a power index of three as defined by the SPATE manual [92] and Enke [89].

Although the calibration constant A^* for orthotropic materials has been calculated for some special cases [21, 25, 93], in these studies no compensation was made for changes in surface temperature as the temperature effect was deemed negligible. However, preliminary work [94] that characterised the effect of temperature on the DeltaTherm thermoelastic signal theoretically showed that the power law could be as great as 11. Due to this large power index in the current thesis a primary objective is to develop a temperature correction procedure that will de-couple the effect of absolute temperature on the recorded signal and thus enable quantitative stress analysis to be undertaken over a range of absolute surface temperatures. The manner by which variation in the absolute temperature may occur over the course of a TSA study can be divided into two groups:

i. variation in the environmental conditions,

ii. viscoelastic behaviour of the specimen.

Temperature variations due to environmental conditions are self explanatory, however temperature changes as a consequence of the viscoelastic properties of FRPs under a load justifies further discussion. When damage evolves in FRPs viscoelastic heating occurs at the damage site. As polymers are generally good insulators the heat is not dissipated quickly and 'hot-spots' form on the surface of the material. Such temperature rises have been reported during testing of composite materials [36, 59, 71, 72, 95, 96]. The temperature rise is attributed to internal heat generated during the fatigue loading of composites and results from viscoelastic heating, the relative movement of the individual plies, and from interlaminar friction. Localised temperature rises occur with a higher intensity in composite materials at damage sites, such as at crack tips. The extent of the heating is explored further in Chapters 5. As the calibration constant includes the absolute temperature (from Equation (3.69)) it follows that A^* would have to be recalculated for any change in the absolute temperature. As temperature may vary point-by-point it is not effective to incorporate the temperature correction into the calibration constant. Instead it is intended that the increase in thermoelastic signal due to temperature will be corrected point-by-point. To understand how these temperature variations will affect the behaviour of the spectral radiant power (as provided by Planck's law) a treatment is devised in Chapter 5 that takes into account the operating wavelength of the detector. A numerical study is carried out to derive a power law relationship in Chapter 5. To verify this relationship an experimental programme of validation is provided in Chapter 6. Once the effect of temperature on the signal can be predicted it will be possible to develop a correction procedure that can be incorporated in the processing of the thermoelastic data before it is analysed; the manner in which this will be applied is also developed in Chapter 6.

3.4 Methods for calibrating the thermoelastic data

The purpose of calibrating the thermoelastic signal is to enable the full-field data to be quantitatively processed to obtain values to the stress and strain on the surface of the component. Calibration routines are evident for isotropic materials whereby a calibration constant may be incorporated into Equation (3.57) in a similar fashion to that discussed for the development of Equation (3.70) as follows:

$$AS = \alpha \Delta(\sigma_1 + \sigma_2) \tag{3.78}$$

where A is the isotropic calibration constant.

The isotropic calibration constant may be calculated by one of the three principal techniques as presented by Dulieu-Smith [22], as follows:

i. direct calibration, using properties of the IR detector, system variables, specimen surface emissivity and the thermoelastic constant of the specimen material,
ii. calibration against measured stress,
iii. calibration against calculated stress.

Calibrating the thermoelastic signal using method *i*) requires values for both the material and detector properties. This presents significant challenges with the DeltaTherm system as it has not been radiometrically calibrated and therefore values for the detector properties are not available. Furthermore, this method is not regarded as accurate and Brown [97] estimates that error, due to inaccuracies in the properties, to be as high as 20%. In the latter two calibration routines an independent value of the stress is required via *ii*) a measured stress or *iii*) a calculated stress. This can be achieved by using electrical resistance strain gauges, where the gauges are attached to an area producing a uniform signal. The sum of the principal stresses can be determined using the strain measurements and Hooke's law; however, values for the material's Young's modulus and Poisson's ratio are required; inaccuracies result from the use of incorrect material values, errors in the gauge factors or incorrect thermoelastic measurements from the sensor area. The third method can be achieved by calculating the stress from a well defined known stress field, i.e. a bar loaded in simple tension.

Unfortunately calibration of orthotropic materials cannot be as simply approached, there are two significant factors that add to the complexity: firstly, the principal stresses cannot be directly calculated from measured strain inputs or calculated without significant analysis of the material properties, geometry and loading and secondly, due to the manufacturing routes typical of FRP composite components an isotropic resin-rich layer of varying thickness is present on the surfaces observed by TSA.

Equation (3.56) provides the thermoelastic response for an orthotropic material, however it is not clear if the source of the thermoelastic signal originates from the resin-rich layer or the surface ply. An investigation by Dunn [98] with a series of experiments was carried out where the effects of thermal conduction on the thermoelastic response of CFRP laminates were investigated. The results demonstrated the effect of the surface

epoxy layer on the thermoelastic response; whereby the removal of the layer resulted in markedly different results and adiabatic range. In a study of the effect of ply lay-up on the thermoelastic response by Cunningham *et al*. [63] the results showed that the resin-rich layer plays an important role. They concluded that the thermoelastic response obtained from a component with a resin-rich layer is a function of the global stiffness of the laminate. A similar finding was made by El-Hajjar and Haj-Ali [99], they proposed a method to measure the surface strain on a pultruded composite component by taking advantage of an in-plane isotropic surface layer with the assumption that the surface layer is responsible for the thermoelastic response. Work by Pitarresi *et al.* [61] and Barone [100] who studied woven composite material concluded that the thermoelastic response was generated by strain transfer into the resin-rich surface layer. Later work by Pitaressi *et al.* [61] compared ratios of the thermoelastic signal recorded from various laminates to values generated by a revised thermoelastic formulation to include the resin material properties which provided promising but not conclusive results. Although there has been some continued effort there is no clear and definitive proof to signify that the thermoelastic signal recorded is generated from the epoxy region. The source of the thermoelastic response is a key point of the thesis and an investigation into this is described in Chapter 4.

Aside from the resin-rich layer the increased complexity of calibrating orthotropic over isotropic materials primarily lies in the manner in which the surface stresses are incorporated in Equation (3.70). Whereas the thermoelastic relationship for isotropic materials (Equation (3.78)) is a function of the stress sum, the thermoelastic relationship for an orthotropic body (Equation (3.70)) cannot be simply considered as a function of the stress components alone. The homogeneity of an isotropic material allows the singular coefficient of thermal expansion to be grouped as a common factor for both the principal material stress components. This it is not possible with orthotropic materials as the directionality of the coefficient of thermal expansion terms must be included in relation to the stress components acting in that direction. This complication was overcome in a procedure that enabled orthotropic calibration which was reported in [25, 93] for the study the stress distribution of a composite tee joint assembly using TSA. The purpose of the work was to validate finite element analysis models and hence the requirement to calibrate the thermoelastic data. The method presented involved a reworking of Equation (3.70) [23], so that the thermoelastic response from an orthotropic material could be expressed in terms of stress as follows:

$$\Delta\sigma_1 + \frac{\alpha_2}{\alpha_1}\Delta\sigma_2 = \frac{A*S}{\alpha_1} = A**S \tag{3.79}$$

In this approach A** can be determined by loading a sample of the material in a manner that the stress transverse to the major principal material direction, σ_2, is zero. Subsequently the ratio of the coefficients of thermal expansion can be obtained by loading a sample so that σ_1 is zero.

In [25] the required stress states were obtained from two representative blocks of the material that could be loaded in tension and compression in order that σ_1 and σ_2 could be assumed zero. A further attempt was made to calibrate the thermoelastic signal [36] from specimens loaded in tension, the calibrated thermoelastic data was compared against finite element analysis but a 25 % difference was reported. Review of the stress state reported, using laminate theory, demonstrated that σ_2 was incorrectly assumed to be zero in the cross-ply laminate to the detriment of the accuracy of calibration constant. The results presented in [25, 36, 93] show that calibration is possible for orthotropic materials but it is clear that the process is complex.

The calibration routine is laden with possible sources of error due to the complexities of creating calibration specimens that allow for the surface stresses to be calculated. The surface stress can be calculated but this operation is beset with difficulties unless the component is of a simple geometry, and the material properties and loading regimes are well known. The difficulty arises in obtaining the stress generated in the surface ply and the resin-rich layer as it is dependent on the architecture of the composite construction, i.e. the stacking sequence of the laminae that form the laminate. If the elastic properties of the lamina, the thickness of the manufactured ply and the loads are known it is possible to calculate the stress in the surface lamina or the resin-rich layer in a uniaxial stress field. The calculations are further dependent on material properties that may not be available. It is evident that there is no generic calibration procedure for orthotropic materials and the ability to calibrate the thermoelastic signal into engineering units is a vital component of this research and will provide a useful tool for TSA studies. The lack of a calibration routine has resulted in thermoelastic data being reported in uncalibrated units or normalised against baseline data for example in the observation of a wind turbine blade model [59]. Therefore an objective of the present work is to devise a general calibration routine for orthotropic composite laminates based upon laminate strains rather than the surface lamina stresses. The alternatives to applying a stress based calibration routine are discussed in Chapter 4 where Equation (3.56) is developed in

terms of strain and is used for a basis for calibration. This has benefits for multi-directional composite laminates as the strain is constant (unlike the stress) through the thickness of a multidirectional laminate and can be measured using extensometers or strain gauges. This dispenses with the discussed difficulties presented in obtaining a value to the stress sum in orthotropic materials. In [36, 61, 77, 99] strain formulations are used to assess the thermoelastic response for specific materials, but the issue of calibration is not addressed. With an appropriate calibration routine it will be possible to obtain the strain in orthotropic composites subject to damage and calculate full-field quantitative results.

3.5 Thermoelastic studies of composites subject to damage

It has been reported [101] that the complexities of the anisotropic behaviour of composites and the effect of temperature on the thermoelastic signal (as Sections 3.2 and 3.3 discuss) has been a contributing factor to the lack of quantitative TSA studies of composite structures. It is envisaged that the development of a strain calibration routine coupled with a means to correct for surface temperature increases will facilitate quantitative analysis. To illustrate the potential of the thermoelastic technique as a means of damage analysis, the following section reviews the relevant literature to date. Further to the principles introduced in Chapter 1 and the defect, damage, fault hierarchy developed in Chapter 2, this section reviews how damage in composite materials have been studied by analysing the thermoelastic response from the structure or component.

As discussed in Chapter 2 TSA has been predominantly applied in the laboratory environment to suit the testing equipment required. As such the components tested have primarily been test coupons or scale models with damage that is introduced artificially. In reviewing the literature it is evident that the damage has been initiated in different ways and can be grouped into the five following subgroups:

i. seeded flaws
ii. static overload
iii. fatigue
iv. impact damage

For that reason this review is divided into subsections according to the above classifications of damage initiation. The focus of this thesis is damage caused by fatigue however, it is important to review literature on other types of damage initiation as these

will provide useful working methodologies, analysis techniques and highlight short comings that may benefit the present work.

3.5.1 Seeded damage

The introduction of a known quantity of seeded damage during manufacture removes the need to locate the damage. The depth, orientation, size and to a certain extent the type and severity of damage can be controlled so that study can quantify the effect of the damage on the thermoelastic signal alone.

Cunningham *et al.* [63] demonstrated certain types of seeded damage could be identified using TSA with the DeltaTherm 1000 system. Two damage types seeded in the composite laminate during manufacture were investigated: delamination and fibre-breakage. The damage was introduced using Polytetrafluoroethylene (PTFE) patches to model delamination and by cutting transversely across single lamina to model fibre and matrix breakage. Two batches of specimens were manufactured from an epoxy pre-impregnated T300 carbon fibre and E-glass both consisting of 13 plies in a 0/90˚ cross-ply configuration The cut lamina were located at different positions through the laminate stack thickness in both the 0˚ and 90˚ plies. The PTFE patches were placed between the first and second, third and fourth, fourth and fifth and sixth and seventh plies from the observed surface at different positions. The specimens were cyclically loaded at 62 ± 62 MPa at 10 Hz and the thermoelastic data collected. At the position where the fibres were cut in the 0˚ plies there was a change in the thermoelastic signal which was attributed to the 'fibre-breakage'. The 0˚ plies in a cross-ply lamina are the predominant load bearing plies and as such the cutting of the fibres ('fibre-breakage') reduces the load bearing capacity and therefore influences the stress distribution. The cut matrix in the 90˚ plies do not affect stress distribution in the specimen greatly and caused no discernible deviation in the thermoelastic data at their location. The delamination effect did not change the thermoelastic response. The paper concluded that TSA could not detect sub-surface damage from delaminations when the component is in uniaxial tension, although no confirmation was made on whether the insertion of PTFE had resulted in a real delamination.

In a similar manner to Cunningham *et al.* [63], Paynter *et al.* [59] introduced a seeded damage patch in a laminated structure. In this case the structure was a model wind-turbine blade and represented a much more complex component than that which had been studied previously. The 4500 mm long blade was constructed with a glass / polyester outer skin reinforced in the centre with a foam sandwich core. The seeded flaws were introduced using peel ply at the manufacturing stage into the blade in pre-

determined positions. These were to simulate a shear web-disbond in the main structural spar and a delamination in the trailing edge. The effect of heating on the thermoelastic signal was acknowledged and to avoid heating the blade was cyclically *loaded* at a reduced level for TSA measurements using the DeltaTherm. This also limited the physical movement of the blade maintaining the component surface within the focal range of the detector. The damage areas were all identified by deviations in the thermoelastic signal; however when the electronic processing unit of the DeltaTherm was supplied with a reference signal equal to twice the load frequency clear identification of significant subsurface damage was identified. Both the root delaminations and the trailing edge crack were apparent and furthermore the noise in the signal was reduced. This is clearly an important finding, although the reasons for the improved damage identification were not made clear in the paper.

As the thermoelastic signal is a function of the stress state on the specimen surface any irregularity in the geometry will be observed from the stress pattern obtained. Although not purposefully introduced (as seeded damage) TSA has been shown to emphasize defects or damage that has occurred during manufacture. In [25] it was shown that manufacturing anomalies such as asymmetry in the structure and the presence of voids were clearly manifested in the thermoelastic data from composite tee joints. The load path was modified by these inconsistencies and could be explicitly defined by the thermoelastic data recorded with the SPATE. Whilst not pure damage these inconsistencies result in a faulty structure. Variations in the manufacture from that envisaged at the design of a model wind turbine-blade [95] were also highlighted from thermoelastic results reported by Hahn *et al*. The stress concentrations apparent in the structure could not be predicted by finite element models as the numerical models were reliant on the product representing perfectly the design. It was commented that the thermoelastic results could be used to modify the numerical models. The size of the component meant that successive data from the DeltaTherm had to be remodelled into the full section during post-processing stages.

3.5.2 Static overload

The brittle nature of the reinforcing constituents of FRP composite laminates results in sudden degradation to failure when loaded beyond their design limits. Static overload has been used as a means to introduce damage into a component. An example of this was presented in the work of El-Hajjar and Haj-Ali [102], who examined a composite structure that was formed by the bolting together of two ‘L’ shaped components. The components were manufactured from FRP pultruded material; pultrusion is a manufacturing route where fibre reinforcement is continually layered through a matrix.

The structure was loaded with a monotonic displacement until damage was detected by a rapid decrease in the load carrying capacity. Following damage the specimens were *loaded* cyclically at 5 Hz and TSA data was recorded using the DeltaTherm. From the thermoelastic results recorded an asymmetric stress distribution was observed (due to unanticipated bending of the structure) and delamination also was detected as a localised change in the thermoelastic signal.

TSA was used by Mackin and Purcell [96] to track the effect of crack propagation on the stress distribution of ceramic matrix composites (CMCs). Test coupons were manufactured from 0/90˚ laminated plates with notches cut into the side (with a root radius of 500 microns). The damage was initiated by applying high tensile load to the coupon, at regular intervals the coupons were unloaded and a SPATE 9000 system measured the thermoelastic signal by loading the specimens at 10% of their elastic limit at 10 Hz (it was reported that AE was used to monitor if further damage was propagated during the thermoelastic measurements). The low cyclic load was applied to avoid damage propagation during the long TSA data collection times. The effect of heating caused by interlaminar friction was acknowledged but neglected as it was deemed negligible due to the low loading. A stress concentration factor (*SCF*) was calculated using thermoelastic data at the damage site and normalising this with data from the far-field (where it was said the damage did not have any effect on the stress state and therefore the thermoelastic signal). It was concluded that as the damage accumulated the *SCF* decreased and served as a indication of stress redistribution away from the notch tip.

Mackin and Roberts [62, 71] continued the work by Mackin and Purcell [96] on a variety of CMCs including woven and UD lay-ups. The specimens were manufactured and tested in a similar manner with a double edge-notch. At each stage however two sets of thermoelastic data were recorded; as the DeltaTherm was used the authors were confident further damage would not progress during the data collection. It was discussed that the purpose of the two tests was to observe the stress distribution at a low *load* and later to increase the cyclic *load* amplitude so that the DeltaTherm produced a larger thermoelastic signal to observe the damage mechanisms at a commensurate fatigue load. In both scenarios and through-out the testing a constant cyclic *load* was applied to the specimens whilst the thermoelastic data was collected even though it was acknowledged damage was propagating between the notches. At the higher cyclic load there was significant heat generation; the heat generation was assumed to be created by a dissipative mechanism due to friction created at the sliding interfaces of the fibres. The areas subject to damage could be identified as ‘hot-spots’ and were used to locate

damage. Again a *SCF* was calculated that was factored by the growth of the notch across the specimen width. It was demonstrated that there was a reduction in the stress concentration at the notch as damage propagated vertically and effectively blunted the notch tip. The effect of the damage on the stress distribution could be analysed in greater depth due to the improved full-field resolution.

3.5.3 Fatigue damage

A study by Cunningham *et al.* [103] characterised damage in a UD GFRP component with a central circular hole using DeltaTherm. The hole was used as a damage initiator and a damaging fatigue load was applied to the specimen of 10 ± 8 kN at 15 Hz. Cracks were observed to propagate from the hole as a result of longitudinal splitting parallel to the fibres. Thermoelastic and thermal images were recorded at the fatigue *load* to monitor damage propagation. The uncalibrated thermoelastic signal was normalised with data from an undamaged area. The cracks grew by approximately 5 mm and then stopped propagating, the fatigue load was maintained and after a period of 74 minutes the thermoelastic signal was again recorded. Although the fatigue cracks had not grown there were changes in the thermoelastic signal. It was surmised that the changes in the signal from the beginning to the end of the test could not be attributed to damage evolution. The results show that considerable viscoelastic heating had taken place with time and that the thermoelastic data was significantly affected by this increase in temperature. It was considered that the heating at the cracks was caused by friction due to crack-face rubbing and local viscoelasticity due to the damage modifying the material properties. It was suggested a possible solution would be to use the DeltaTherm thermal data to map the temperature and then use this to correct the thermoelastic data and hence separate the heating effect from any change in the stresses (to obtain a measure of stress changes caused by the damage alone).

Uenoya and Fujii [104] presented a simple approach that examined thermoelastic data before and after damage initiation. The work was carried out on two carbon-fibre (T300-B) woven specimens with a circular hole at the centre of the specimen. The damage was introduced in two manners by the application of an interrupted static load and in tension-tension fatigue. The thermoelastic the data was obtained using a JEOL JTG-8010 system whilst the specimens were loaded with a constant cyclic *load* at 5 Hz. The data was presented as the change in the thermoelastic signal between these two states. The coupons were tested at a *load* corresponding to 14-15 % of the static tensile strength at a frequency of 5 Hz. The damage was noted to change the stress distribution recorded and this was concluded to have been caused by damage propagation, the stress concentration at the hole was reported to diminish.

The effect of hygrothermal ageing on the structural properties of a sandwich construction composite marine tee joints was examined by Dulieu-Barton *et al.* [93]. Three joints were used in this work and were each subjected to a specific routine in order that the effect of ageing on the load bearing capacity could be assessed; an unaged and unloaded joint was used as a thermoelastic baseline for the results. Thermoelastic data was recorded from the specimens at two stages during the ageing (after 60 and 144 days), after these periods of ageing one of the specimens was subjected to a fatigue load, one was statically loaded and the other was left unloaded. It was necessary for the components to dry before thermoelastic data could be recorded. The calibration of the components was not possible as it was suggested that the material properties would be altered by the ageing. The difficulties in calibrating the thermoelastic data resulted in the results being normalised against the unaged joint which was tested at the same time (to avoid environmental variations in the analysis of the results). The thermoelastic data was collected using a DeltaTherm with the components *loaded* at 8 Hz. The results from the aged components (subject to the three fatigue routines) indicate a reduction in the thermoelastic signal in the outer quadriaxial skins of the structure; this was attributed to the fact that their load bearing capability was reduced due to ageing. The work showed the potential of TSA in the evaluation of complex aged structures.

3.5.4 Impact

The poor mechanical performance of the matrix material in composite components to impact can results in damage initiation through the thickness of a laminate. Several studies have been presented where a specimen is impacted to initiate damage and thermoelastic data collected from the damage area to assess the effect on the stress distribution. Dulieu-Barton and Chapman [105] carried out a study on impact damaged sandwich specimens, constructed from a Coremat non-woven foam core and a single ply of 0/90˚ E-glass plain weave mat skin. The specimens were subjected to controlled levels of impact damage produced by using a simple gravity drop hammer, mounted with a wedge shaped and ball-end impactor. It was not the purpose of the study to investigate the propagation of the damage through fatigue and after impact the specimens were cycled with deliberately low amplitude to avoid damage accumulation and growth during the one-hour thermoelastic scan using the SPATE system. A further precaution to avoid damage accumulation was the 10 Hz loading frequency, it was commented that ideally the frequency would have been maintained above 20 Hz however, as the SPATE could not be collect data in a real time this would have resulted in a further 100,000 fatigue cycles during the data collection. Appropriately and importantly a cyclic *displacement* was applied during the thermoelastic data collection

as it was noted that the damage would decrease the stiffness of the specimen; applying a constant load would result in a larger strain for the same given load in the damaged component. This was essential as thermoelastic readings from the damaged specimens were normalised against the signal from the undamaged specimen (before impact); this ratio was defined as a damage parameter. The thermoelastic results showed that the average reading from the damaged specimens was greater than that for the undamaged specimens. The reasoning for this was posed as likely due to increases in stress adjacent to the impact as a result of reduction in the specimen cross-sectional area. It was concluded that the results demonstrated that a damage parameter based on purely the average signal would not be adequate as manufacturing variations were noted to cause more variation than the damage and analysis of the thermoelastic signal must be made to assess the point-by-point signal variation.

A further investigation of impact damaged woven GRRP composites was completed by Santulli *et al.* [64], using the DeltaTherm system. The test specimens were 10-ply woven mats and were manufactured from an E-glass resin composite. The specimens were impacted with a range of energies and the damage was located using radiographic C-scan data as in some of the cases no visible surface damage was present. The improvements in data collection and processing offered by the DeltaTherm meant that the amplitude of the cyclic *load* was not restricted by the length of the data collection. The reduced data collection time signalled to the authors that damage studies in composite materials is more realistic and has introduced the possibility of 'real time' monitoring of damage growth. To avoid variation between the specimens the signal from each section of the structural unit in the damaged region was normalised by dividing it by the appropriate average reading taken from the undamaged region. The readings were compared and it was demonstrated that the thermoelastic signal level increases with damage severity. A notable feature of this work was that the damage was mainly sub-surface and the effect of the damage caused sufficient surface stress redistribution to be observed in the thermoelastic data. The impact damage disrupted the regular pattern of the data obtained from the undamaged regions and gave a good indication of the damage location.

Horn *et al.* [71, 72] presented an approach to estimate the residual lifetime of impact damaged composites on a case-by-case basis. The samples were long fibre glass polyurethane composites manufactured in a variety of lay-up configurations. Damage was initiated by subjecting a range of specimens to a range of impact energies that resulted in surface cracking and delamination. Following impact the specimens were subjected to a fatigue load until failure. The cyclic *load* was applied at a reduced level

(from that of the fatigue routine) during the capture of the TSA data using a DeltaTherm; a ratio of the thermoelastic data at the damage site to that at away from the damage was used to obtain a *SCF* (in a similar manner to earlier work by the authors [96]). In an attempt to assess the effect of the damage on the integrity of the specimen the stress applied to the specimen was multiplied by the *SCF* to obtain a 'modified-stress' due to the damage. It was proposed that this value could then be used as the stress variable on an *S-N* curve (obtained from tensile tests of undamaged specimens of the same material in question) to account for the influence of damage raising the stress locally and reducing the structural longevity. The results demonstrated that this procedure provides conservative estimates of the residual lifetimes following impact. The effect of local heating at the damage site on the stress calculations was not discussed and could account for the conservative values of *SCF* obtained from the TSA technique.

3.5.5 Summary

From the review of the literature it is evident that TSA has been used for damage evaluation on a variety of composite components. The information in Table 3.4 presents a summary of this information. Within the summary table the specific specimen details such as lay-up, material and any geometrical details are reported. The TSA system, the cyclic load and frequency applied are provided along with the reported effects of temperature on the thermoelastic signal. The manner in which damage is initiated and the type of damage identified is reported. Finally it is detailed whether the thermoelastic signal is calibrated and if the signal recorded is used to provide a parameter pertaining to the residual life.

The significance of absolute temperature variation was discussed in a number of papers but no definitive solution was proposed; the manner in which the effect was approached was dealt with in a number of manners:

1. the cyclic load applied was purposefully low to avoid viscoelastic heating
2. the effect was neglected
3. it was acknowledged but could not be quantitatively assessed

None of these methods provide a robust manner by which the effect of temperature on the thermoelastic signal can be assessed. The first method [59, 62, 71, 105] is preventative but cannot guarantee that heating will not occur and also does not account for any fluctuation in the ambient temperature. In some of the literature the effect of temperature on the signal was not commented [96, 99, 104] and could account for some of the unanticipated trends in the thermoelastic data that were observed. The remaining

papers [36, 63] acknowledged the effect of temperature and it was concluded that this prohibited even a qualitative analysis with the DeltaTherm [103]. These outcomes highlight the need for a correction procedure; such a procedure has not been devised for the DeltaTherm system and it is essential that such a process is implemented to achieve robust analysis of thermoelastic data. This process is investigated in Chapters 5 and 6.

Table 3.4. Summary of damage literature

Ref.	Material	Lay-up	Notch	Damage initiated	System	TSA load	Freq. (Hz)	Temp.	Damage identified	Cal.	Residual life
[63]	GFRP CFRP	0/90˚	No	Seeded	DT.	62 ± 62 MPa	10	3	'Fibre breakage'	No	No
[59]	GFRP	Various	No	Seeded	DT.	1.3 ± 1.35 kN		1	Shear web disbond	No	No
[25]	GFRP	Woven & CSM	No	Delamination	SPATE	1.7 ± 0.7 kN	8	2	Stress redistribution	Yes	No
[95]	GFRP	Unspecified	No	Fatigue	DT.	Unspecified		1	Stress redistribution	No	No
[102]	FRP	Pultrusion	No	Static overload	DT.	1.8 ± 1.3 kN	5	2	Delamination	No	No
[96]	CMC	0/90˚	Edge	Static overload	SPATE	10% elastic limit	10	2	Stress redistribution	No	No
[62, 71]	CMC	0/90˚& UD	Edge	Static overload	DT.	10% elastic limit	10	1 / 3	Stress redistribution	No	No
[36]	GFRP	UD	Hole	Fatigue	DT.	10 ± 8 kN	10	3	Longitudinal splitting	Yes	No
[104]	GFRP	Woven	Hole	Fatigue	JEOL	15% elastic limit	5	2	Stress redistribution	No	No
[93]	GFRP	Various	No	Ageing	DT.	-6.4 ± 3.4 kN	8	2	Stress redistribution	No	No
[64]	GFRP	Woven	No	Impact	DT.	105 ± 35 MPa	5 - 30	1 / 3	Subsurface damage	No	No
[105]	GFRP	0/90˚	No	Impact	SPATE	0.6 ± 0.4 kN	10	2	Stress redistribution	No	No
[71, 72]	GFRP	Various	No	Impact	DT.	1.5 ± 1 MPa	10	1 / 3	Cracking	No	Yes

The issue of calibrating the thermoelastic data to obtain stress or strain data from composite materials subject to damage was only approached in one paper where the thermoelastic signal was assumed a function of the resin-rich layer [36]. The calibrated thermoelastic signal was compared with finite element analysis results and whilst the stress profile was similar the results did not correlate well. The remaining papers were split into those that calculated a ratio of thermoelastic signal from the site of damage and that from the far-field to obtain a stress concentration factor and the remainder analysed the uncalibrated data alone. Whilst the latter two methods provide an indication of a stress concentration factor it cannot provide information as to residual life. It is apparent that the ability to verify the source of the signal and subsequently calibrate would provide a benefit to these types of study. A calibration routine that expresses the thermoelastic signal recorded from orthotropic materials in terms of strain is provided in Chapter 4.

The purpose of these studies was to introduce some form of damage in the composite laminate and consequently assess the redistribution of stress using TSA. As damage initiation is expected to cause some variation in mechanical performance it is expected that the behaviour of the laminate under load will change. Because TSA requires the specimen under test to be cyclically loaded consideration must be made to the degradation of mechanical properties of the composite under investigation as this will have consequences on the choice of cyclic load applied in the test routine. Aside from work by Dulieu-Barton and Chapman [105] which acknowledged the importance of considering the reduction of stiffness during damage propagation, the majority of the literature reported that a constant load was applied during the collection of thermoelastic data. If the stiffness degradation is not considered at the time of test this complicates the comparison of successive data sets due to the fact that as the material degrades a constant load would result in a greater strain per load. This is not ideal as it will complicate the analysis of data from damaged materials and the signal change will be a function of stress redistribution due to damage and strain applied. It is prudent to consider the loading regime and this is covered in Chapter 7.

The purpose of the work reported in this thesis is to enable a composite subject to damage to be assessed using the thermoelastic data as a damage indicator. Of the 15 topical papers reviewed and summarised in Table 3.4 it is evident that although there has been significant TSA effort in the field the results presented have remained largely phenomenological. Predominantly the effect of damage has been observed in a qualitative sense pertaining to an indication of the trend of the stress concentration and distribution, e.g. [96, 105]. The results presented where damage was seeded in the

laminate demonstrate that fibre breakage [63] and to an extent sub-surface defects [59] can be defined by TSA. Whilst these studies provide confidence in the ability of the technique to discern damage they do not provide evidence of developing the capability of damage assessment or residual life. The majority of the work presented in the last five years has incorporated the DeltaTherm which has been shown [36, 62, 93] to provide an increased opportunity to assess damage propagation at periodic intervals through the fatigue life of a component. However, the progression to quantitative analysis and residual life estimations has been largely elusive. Nevertheless, there is an indication of the potential; Horn *et al*. [71, 72] presented a method whereby the residual fatigue lifetime could be assessed on a case-by-case basis. It was suggested that the effect of impact could be assessed by using *S*-*N* type curves obtained from equivalent undamaged specimens. The thermoelastic data was proposed to redefine the stress variable of the *S*-*N* curve to allow for the damage. The *S* data would be 'modified' to take into account the increased stress at the damage site. The 'modified' stress would be calculated by multiplying the applied stress to the component by the *SCF* at the damage site (the *SCF* would be calculated by taking a ratio of the thermoelastic signal at the damage site and the far-field signal away from the damage). The results were described as conservative and were reliant on numerous sets of test data for the specific material under test. The discrepancies in the results may be accounted for as it is evident allowance was not made for the effect of heating at the damage site and the effect of damage on the degradation of the mechanical properties during the application of a cyclic load.

In all cases where it is the primary objective to assess the damage the thermoelastic signal is used in the uncalibrated form. By calibrating the thermoelastic data it would be possible to obtain strain data that could be used for refining or comparison with existing failure theories such as those described by Daniel [1] or provide a route for and the potential to develop a new damage assessment procedure based on the thermoelastic response. As the TSA technique can collect data from the actual structure under fatigue type loading a clear benefit of using a calibration strategy would be to link the thermoelastic response with failure.

3.6 Development of application of TSA to composites

The thermoelastic theory has been presented in full with respect to the stress state of a loaded orthotropic body. The manner and theory in which thermoelastic data can be obtained in a non-contact manner using IR equipment has been reported and the equipment used in this thesis, the DeltaTherm, was introduced. The theoretical derivation of the spectral radiant emittance presented from Planck's law provides the background and understanding of how non contacting measurements of the thermoelastic effect can be made. The characteristics of Planck's law and its dependence on absolute temperature were discussed with respect to the impact this has on using an IR detector to record the thermoelastic response.

The literature dedicated to using TSA for composite materials subject to damage was reviewed and although it has been demonstrated to be a functional technique for experimental stress analysis in a wide range of engineering applications it is clear that the application of TSA for quantitative damage analysis of composite materials is not straightforward. Firstly, a means of interpreting and calibrating the thermoelastic signal in terms of strain is required so that TSA can provide real-time information on the resultant integrity of the component. Calibration will permit the stresses and strains at the damage site to be understood and hence allow an informed decision to be made to the residual life of the component. Secondly, the issue of the sensitivity to temperature requires a manner in which the signal can be analysed for stress alone. Thirdly, the manner in which damage affects the behaviour of the component under load has not been well documented and it has been established that the change in the elastic properties must be taken into consideration when applying the cyclic load.

The review provided in this chapter has enabled the development of a 'road map' of parameters that need to be considered and their effects resolved in order to establish a damage assessment scheme based on TSA. These are as follows:

1. A calibration routine for obtaining the strains in composite materials is not available and is therefore developed in Chapter 4.

2. A means of correcting for temperature variation based on the performance of an InSb detector operating in the 2 – 5 μm range must be established; this is done in Chapters 5 and 6.

3. A damage assessment methodology that encompasses the details highlighted in the summary of the current literature so that a residual life estimate is possible is described in Chapter 7.

4. TSA is not a rapid inspection tool so a means of localising damage in specimens is required, particularly if the damage is sub-surface. Initial work in Chapter 8 will show that PPT is suitable for this.

Chapter 4

A generalised approach to the calibration of orthotropic materials for TSA

4.1 Introduction

The purpose of thermoelastic calibration is to enable full-field thermoelastic data to be quantitatively processed to obtain stress and strain values. Once a calibration constant has been defined for a given material system and DeltaTherm set-up, subsequent thermoelastic data can be manipulated to provide engineering values. As TSA can be applied to any structure (undergoing cyclic loading) complex stress distributions can be evaluated. As TSA obtains data from the component's area of interest the results are not dependent on the inaccuracies incurred through numerical modelling that may include; material variation, deviations in the geometry or structure or changes in the loading regime to highlight a few non trivial problems. The difficulties encountered in modelling the effect of damage (discussed in chapter 2) due to the redistribution of stress add yet more modelling complications that only serve to support the application of TSA.

The subject of calibrating the thermoelastic signal and specifically calibrating orthotropic materials was approached in Chapter 3. The accepted methods of calibrating the thermoelastic signal - direct calibration using the properties of the TSA system and material properties, against measured stress and calculated stress on the surface were reviewed with respect to the DeltaTherm system and orthotropic materials as required in

this thesis. The fact that the DeltaTherm system is not radiometrically calibrated precludes calibration in the first manner. Consequently calibration is limited to the latter two manners using the relationship presented in Equation (3.70) that at present is regarded as the basis for thermoelastic studies of orthotropic materials. As Equation (3.70) has been developed in terms of the surface stresses it is necessary to obtain values of these in order that A^* can be evaluated for a given material and thermoelastic settings. It is however feasible to calculate the direct stresses in laminated composite materials by applying CLT [1]; provided the elastic properties of the lamina, the thickness of the manufactured plies and the loads are known. It is usual that a simple representative laminate is loaded (in a manner which provides the necessary variables to calculate the surface stress) and the thermoelastic signal measured from an area of uniform signal. For this defined state it is possible to obtain a value for A^*, which can be used accordingly in later thermoelastic studies of similar materials where it is not possible to accurately analyse the surface stress due to geometry or loading complexities.

It is evident that this can provide a route to calibration but is laden with possible sources of error due to estimates of material properties in the calculations that are used to evaluate the stress state in the surface ply. The chapter focuses on the development of a calibration approach that is based on formulating Equation (3.70) in terms of strain. The advantage of working in terms of strain is twofold: firstly the strain is constant through the thickness of an intact multidirectional laminate and secondly, the strain can be measured directly using experimental methods such as extensometers or strain gauges. This method would provide a direct approach to calibration and allow TSA to be applied in a straightforward manner to a general composite structure. One important consideration to be tackled in the calibration routine is the effect of the resin-rich surface layer, present in composite laminates due to the nature of the manufacturing processes. In Chapter 3 this was shown to have an affect on the thermoelastic response.

The development of the strain based calibration routine will approached by firstly revisiting the thermoelastic theory and in particular studying the manner in which the orthotropic relationships can be expressed in terms of strain rather than stress. With a thermoelastic equation in terms of strain it will be possible to validate the approach using a variety of multidirectional laminates constructed from layers of unidirectional (UD) pre-impregnated glass fibre reinforced epoxy. These are made into a series of standard tensile specimens with similar surface ply properties but with different global stiffness and Poisson's ratio values and importantly it will be possible to both measure and calculate the principal strains on the surface to relate to the thermoelastic signal recorded from the specimens. As the stress state may be obtained for these simplified

samples it will also be possible to compare the results in the traditional formulation. Therefore through the substitution of known values it will be possible to calculate A^* for the material system using three approaches:

i. using Equation (3.70) and *calculating* the surface ply or resin-rich layer *stresses* with CLT [1],
ii. *calculating* the laminate *strains* using CLT [1], and
iii. *measuring* the laminate *strains*.

As described it will be necessary to develop a new thermoelastic formulation to enable methods (*ii*) and (*iii*) to be assessed, the background theory for this being provided in the next section of this chapter. In validating the values of A^* it is demonstrated that the response from the test specimens is not from the orthotropic surface ply but from the thin (25 μm) surface resin layer. Experimental evidence is provided that confirms the findings of the earlier work [61, 63, 99, 106] in a quantitative manner. The existence of the resin-rich surface layer significantly simplifies matters and it is shown that the material used in the work throughout this thesis can be considered 'thermoelastically isotropic' but 'mechanically orthotropic'.

4.2 Theory

Here the theory is developed in terms of strain instead of stress; two of the three stress/strain systems that were introduced to describe the reference axes of an orthotropic are used in the following development; relative to the fibre directions, denoted by the subscripts 1 and 2, and relative to the laminate principal material directions, denoted L and T (this allows the global mechanical response of the material to be included in the assessment of the thermoelastic response). The development of the strain relationship stems from Equation (3.37); Q^* is neglected to give:

$$\Delta T = -\frac{T}{\rho C_\varepsilon}\{(Q_{11}\alpha_1 + Q_{12}\alpha_2)(S^*_{11}\,\sigma_1 + S^*_{12}\,\sigma_2 + \alpha_1\Delta T) + (Q_{12}\alpha_1 + Q_{22}\alpha_2)(S^*_{21}\,\sigma_1 + S^*_{22}\,\sigma_2 + \alpha_2\Delta T)\} \tag{4.1}$$

The bracketed terms that appear in Equation (4.1) that group compliance and stress terms are introduced into the derivation as strain change tensors, Equation (3.33), and therefore can be replaced by the principal strain terms as follows:

$$\Delta T = -\frac{T}{\rho C_\varepsilon}\{(Q_{11}\alpha_1 + Q_{12}\alpha_2)\Delta\varepsilon_1 + (Q_{12}\alpha_1 + Q_{22}\alpha_2)\Delta\varepsilon_2\} \tag{4.2}$$

It is now possible to develop a thermoelastic equation similar to that given by Equation (3.70) in terms of the lamina strains, and for convenience it is assumed that for a solid material C_p and C_ε are equal so that they can be grouped into the calibration constant A^* as follows:

$$A^* S = (\alpha_1 Q_{11} + \alpha_2 Q_{12})\Delta\varepsilon_1 + (\alpha_1 Q_{12} + \alpha_2 Q_{22})\Delta\varepsilon_2 \tag{4.3}$$

The strain in the surface ply fibre direction can be related to the strain in the laminate principal material directions (i.e. L and T directions) [1] with the expression:

$$[\varepsilon]_{1,2} = [T][\varepsilon]_{L,T} \tag{4.4}$$

where $[T]$ is the standard transformation matrix [1].

By substituting Equation (4.4) into Equation (4.3) a thermoelastic equation is obtained in terms of the laminate longitudinal, L, and transverse, T, strains, i.e.:

$$\begin{aligned} A^* S = \{&[(\alpha_1 Q_{11} + \alpha_2 Q_{12})m^2 + (\alpha_1 Q_{12} + \alpha_2 Q_{22})n^2]\Delta\varepsilon_L \\ &+ [(\alpha_1 Q_{11} + \alpha_2 Q_{12})n^2 + (\alpha_1 Q_{12} + \alpha_2 Q_{22})m^2]\Delta\varepsilon_T \\ &+ [(\alpha_1 Q_{11} + \alpha_2 Q_{12})mn - (\alpha_1 Q_{12} + \alpha_2 Q_{22})mn]\Delta\gamma_{LT}\} \end{aligned} \tag{4.5}$$

where $m = \cos\theta$ and $n = \sin\theta$ (θ is the angle between the axes of the surface ply (1, 2) and those of the laminate (L, T)). The expression given by Equation (4.5) is the basis for the calibration procedure. The equation can be simplified by judicious choice of stacking sequence, specimen geometry and loading configuration as shown in the next section of the chapter.

4.3 Calibration test specimens

The composite material used for the test specimens was 13 layers of a UD E-glass epoxy (SE84) pre-impregnated material supplied from SP (Structural Polymer) systems Ltd. The panels were consolidated under vacuum pressure for one hour and then cured for four hours at a temperature of 80 ºC (Details of the lay-up procedure are given in Appendix A; this pre-preg. manufacturing route is identical throughout the thesis). After curing, end tabs strips were bonded to both sides of the panel using an adhesive film. Five panels were made with different stacking sequences, as detailed in Table 4.1. The tabs were manufactured of the same material with a $[0]_{17}$ lay-up. The tabs were tapered at an angle of 15˚, which provided a 15mm scarf. The end tabbed panels were then cut into tensile type test specimens of the configuration shown in Figure 4.1. The specimens were 40 mm wide and had an approximate gauge length and thickness of 180 mm and 3.5 mm respectively. The laminate plates, from which the specimens were cut, were manufactured individually and the slight variations in the finished geometry of the specimens were measured. The thickness and gauge length of the specimens, which are important metrics in the subsequent analysis of the laminates, are given in Table 4.1. Figure 4.2 shows a micrograph of a section, as indicated in Figure 4.1. The surface resin-rich layer is clearly visible and is approximately 25 μm thick.

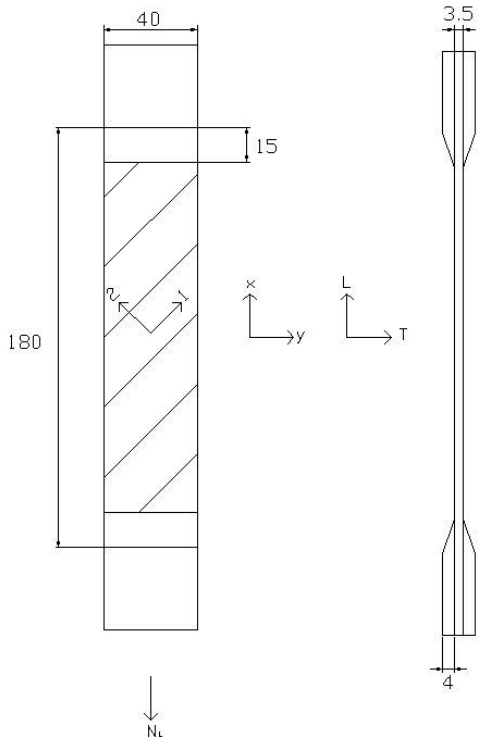

Figure 4.1. Laminate schematic (*Dimensions in mm*)

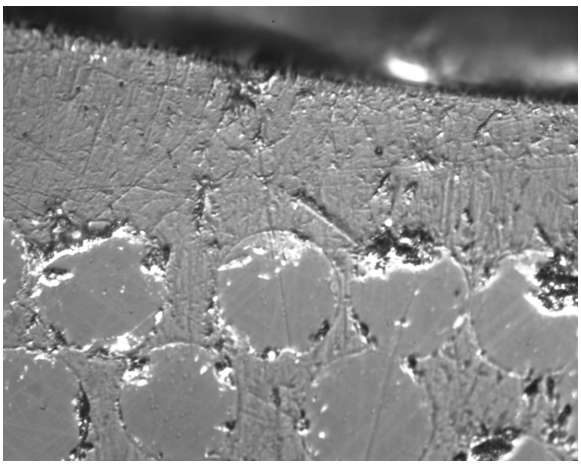

Figure 4.2. Micrograph of UD laminate cross section

In Figure 4.1 a 45^o surface ply is shown. The surface ply axes (1, 2), laminate axes (L, T) and principal stress axes (x, y) are also shown in Figure 4.1 The specimen loading is also provided in Figure 4.1. The five laminate configurations given in Table 4.1 are denoted as follows: 'UD' for a *unidirectional laminate* i.e. all plies in the longitudinal direction, 'Mixed' for a laminate with only two transverse plies and a longitudinal surface ply, '0/90' for a *cross-ply laminate* with a longitudinal surface ply, '90/0' for a *cross-ply* laminate with a transverse surface ply and '±45' for an *angle-ply* laminate with a surface ply at 45^o to the longitudinal direction. The UD, Mixed and 0/90 specimens were manufactured to allow thermoelastic analysis of specimens that have the same surface properties and different mechanical properties. The 0/90 and 90/0 specimens allowed evaluation of materials that have different surface properties but similar mechanical properties. The angle-ply laminate, i.e. ±45, was included as it has a finite laminate shear strain. In all cases the principal stress axes (x, y) are coincident with the laminate axes (L, T), i.e. the first principal stress direction is always the laminate longitudinal direction.

To obtain the calibration constant, A^*, from the test specimens described above using Equation (4.5), it is necessary to derive equations for each specimen that are functions of the laminate principal strains. In a tensile test specimen the transverse strain in the laminate is related to the longitudinal strain by $\varepsilon_T = -\nu_{LT}\varepsilon_L$, where ν_{LT} is the laminate major Poisson's ratio. Therefore it is possible to eliminate ε_T from Equation (4.5) for a tensile specimen (with the exception of the ±45 specimen) and express A^* as a function of the longitudinal strain alone. The orientation of the surface ply fibre direction is relative to the longitudinal laminate axes, and denoted as θ (Figure 4.1). The UD, Mixed and 0/90 laminates have a surface fibre direction coincident with the laminate axes and as such θ is equal to zero. Therefore the calibration equation for these three

laminates is identical and involves only the m^2 term given in Equation (4.5). The 90/0 has a surface fibre direction orientated at 90˚ to the laminate longitudinal axes and as such the calibration equation is a function of only the n^2 terms in Equation (4.5). For angle ply laminates such as the ±45, where the direction of the surface fibre orientation is somewhere between 0˚ and 90˚, the calibration equation is a product of both the m^2, n^2 and mn terms, meaning that the shear term γ_{LT} is retained. It is important to note that the strain terms, ε_L, ε_T and γ_{LT}, in the equations given in Table 4.1 are, by strain compatibility, constant through the thickness of the laminate. In Table 4.1 the expressions are provided for A^* for each of the specimens. The last row in Table 4.1 gives the calibration constant based on the response from the resin-rich layer for each of the specimens and varies only with ν_{LT}.

Table 4.1. Laminate notation, geometry, stacking sequence and thermoelastic calibration constant

Notation	Thickness (mm)	Gauge length (mm)	Stacking sequence	Calibration constant
UD	3.5	181	$[0]_{13}$	$A^* = \{[(\alpha_1 Q_{11} + \alpha_2 Q_{12}) - \nu_{LT}(\alpha_1 Q_{12} + \alpha_2 Q_{22})]\Delta\varepsilon_L\}/S$
Mixed	3.56	183	$[(0_6,90,0,90,0_6]$	$A^* = \{[(\alpha_1 Q_{11} + \alpha_2 Q_{12}) - \nu_{LT}(\alpha_1 Q_{12} + \alpha_2 Q_{22})]\Delta\varepsilon_L\}/S$
0/90	3.55	182.5	$[(0/90)_3,0, (90/0)_3]$	$A^* = \{[(\alpha_1 Q_{11} + \alpha_2 Q_{12}) - \nu_{LT}(\alpha_1 Q_{12} + \alpha_2 Q_{22})]\Delta\varepsilon_L\}/S$
90/0	3.561	179.5	$[(90/0)_3,0, (0/90)_3]$	$A^* = \{[(\alpha_1 Q_{12} + \alpha_2 Q_{22}) - \nu_{LT}(\alpha_1 Q_{11} + \alpha_2 Q_{12})]\Delta\varepsilon_L\}/S$
± 45	3.587	182	$[(+45/-45)_3,45, (+45/-45)_3]$	$A^* = \{((\alpha_1 Q_{11} + \alpha_2 Q_{12}) + (\alpha_1 Q_{12} + \alpha_2 Q_{22}))(\Delta\varepsilon_L + \Delta\varepsilon_T) + (((\alpha_1 Q_{11} + \alpha_2 Q_{12}) - (\alpha_1 Q_{12} + \alpha_2 Q_{22}))\gamma_{LT})\}/2S$
Resin-rich layer	As specimens above	As specimens above	As specimens above	$A^* = \left[\left(\frac{\alpha_R E_R}{1-\nu_R}(1-\nu_{LT})\right)\Delta\varepsilon_L\right]\Big/S$ where α_R is the coefficient of thermal expansion of the resin-rich layer, E_R is the Young's modulus and ν_R the Poisson's ratio of the resin-rich layer

To calculate the calibration constant, A^*, from each specimen type given in Table 4.1 a test programme was devised to gather the required data in the two manners described in the introduction; experimentally using measured values and numerically using calculated values. A^* was also calculated for each laminate using the traditional stress formulation as given by Equation (3.70). For all cases the thermoelastic signal, S, was recorded from each laminate. Once the full compliment of terms on the right-hand side of the equations have been determined the calibration constant, A^*, can be evaluated. By inspection of Equation (3.56) and Equation (3.70) it can be seen that A^* is a function of the density and the specific heat only. If the same detector is used, the same surface preparation is carried out and the temperature remains constant then A^* is independent of the surface ply orientation. Therefore each of the equations given in Table 4.1 should yield the same value of A^*. Likewise, A^* obtained from the stress formulation should be identical to that obtained from the strain formulations provided in Table 4.1.

4.4 Derivation of the parameters for calibration

4.4.1 Loading regimes

The test specimens were loaded in an Instron 8802 test machine and subject to cyclic loading at a frequency of 10 Hz; it has been shown [63] that this frequency was sufficient to generate adiabatic conditions in the test specimens. The experimental test set-up is illustrated in Figure 4.3.

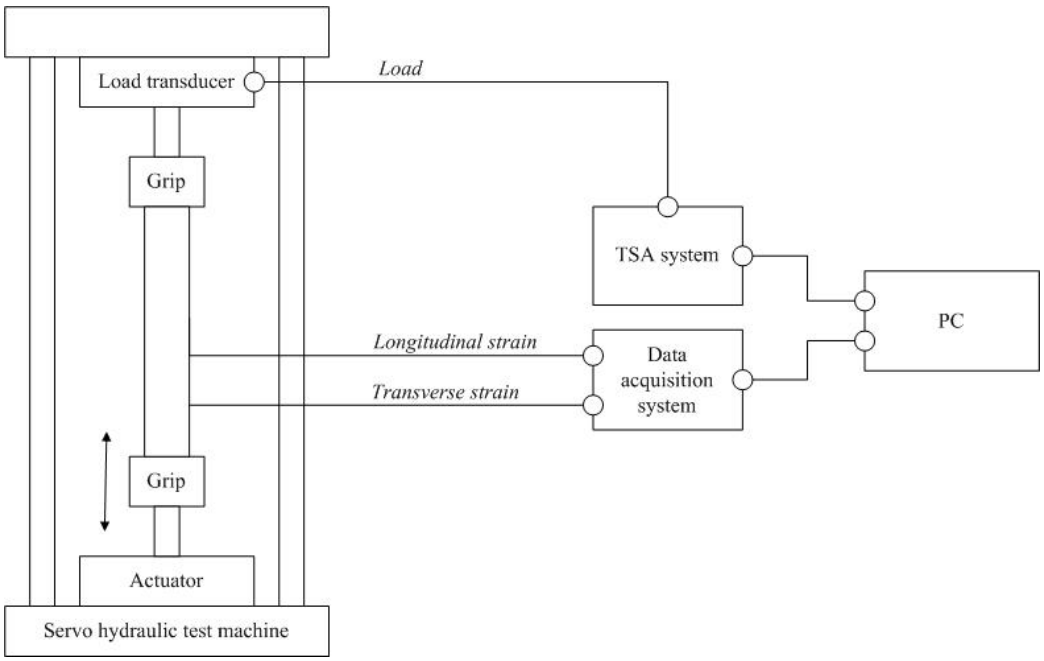

Figure 4.3. Experimental test set-up

Two data sets were generated: one where the load range was constant and one where the displacement range was constant for each of the five test specimens. This was achieved by altering the method of loading the test specimens; the first set was obtained in load control where each of the laminates was stressed with a *constant load* of 8 kN and the second set was obtained by in displacement control applying a *constant displacement* to the laminates of 0.44 mm. The variation in strain for the specimens loaded with a constant load would be expected to vary to a significant degree due to the variation in laminate stiffness, whereas the specimens loaded with a constant displacement would be expected to provide constant strain values. The displacement resulting from the constant applied load of 8 kN and the load resulting from the constant applied displacement of 0.44 mm were also recorded at the time of the test and are provided in Table 4.2.

Table 4.2. Loading regimes

Laminate index	Constant load (8 kN)	Constant displacement (0.44 mm)
	Displacement range (mm)	Load range (kN)
UD	0.32	10.99
Mixed	0.34	10.40
0/90	0.44	8.00
90/0	0.48	7.48
± 45	1.2	3.28

4.4.2 Material properties

In order to evaluate A^* from the equations in Table 4.1 it is necessary to establish the properties for the laminate constituent material and resin-rich layer. The laminate constituent material properties can be divided in two categories: *i*) those relating to the surface lamina, i.e. α_1, α_2, Q_{11}, Q_{22}, and Q_{12}, are surface ply properties in the principal material directions and *ii*) those relating to the global behaviour of the laminate, in this case, ν_{LT}.

The mechanical properties required for the calculation of the reduced stiffness terms, (namely E_1, E_2, G_{12}, ν_{12} and ν_{21}) and the major Poisson's ratio value, ν_{LT}, were obtained from experimental studies of UD test specimens. In order to determine these values it was necessary to obtain the orthogonal strains from two UD laminates loaded in tension. The first laminate had its fibres orientated longitudinally, i.e. at 0˚ and the second with the fibres orientated transversely, i.e. at 90˚. Long gauge extensometers were used in preference to strain gauges to obtain a strain value from the mid section of the specimen and not a localised area corresponding to the foot print of the strain gauge. The results

were obtained from the average of three laminates. From the first test, i.e. with the fibres parallel to the first principal stress, the applied direct stress over the laminate cross section can then be calculated, as the cross-sectional area in the free length of the coupon is known. From this stress data and the measured longitudinal strain it is possible to calculate the Young's modulus in the fibre direction. The major Poisson's ratio value could then be determined from the ratio of the longitudinal to transverse strain. The second tension test was carried out with the second laminate, i.e. with the fibre direction perpendicular to the first principal stress direction. With this information the Young's modulus in the direction transverse to the fibres was calculated in a similar fashion and subsequently the minor Poisson's ratio calculated, from the two moduli and major Poisson's ratio values. The material properties for the laminate are given in Table 4.3. The values used for the calculation of Q_{11}, Q_{22}, and Q_{12} were obtained from these properties as the material properties will be the same for a lamina as the laminate. The shear modulus and the coefficients of thermal expansion are detailed in Table 4.3 and were taken from values presented in literature and manufacturer's data [1, 85, 107]. Material properties for the epoxy layer are given in Table 4.4; the elastic properties were taken as identical to those obtained from a transversely loaded UD laminate.

Table 4.3. UD E-Glass/epoxy material properties

Longitudinal Young's modulus, E_1	36.8 GPa (Measured)
Transverse Young's modulus, E_2	8.4 GPa (Measured)
Shear modulus, G_{12}	3 GPa [1]
Major Poisson's ratio, ν_{12}	0.25 (Measured)
Minor Poisson's ratio, ν_{21}	0.05 (Measured)
Coefficient of thermal expansion, α_1	$6\times10^{-6}/\,°C$ [85]
Coefficient of thermal expansion, α_2	$35\times10^{-6}/\,°C$ [85]

Table 4.4. Epoxy material properties

Young's modulus, E_R	8.4 GPa
Poisson's ratio, ν_R	0.25
Coefficient of thermal expansion, α_R	$35\times10^{-6}/\,°C$ [85]

The major Poisson's ratio, ν_{LT}, for each of the test specimens is required for the strain calibration equations, in Table 4.1. The major Poisson's ratio, ν_{LT}, can be calculated for each of the test specimens using CLT with the geometry, stacking sequence, ply orientation and ply material properties. The calculation of Poisson's ratio also enables the Young's moduli values for each of the test specimens to be evaluated. Whilst these values are not explicitly required for the thermoelastic calibrations given in Table 4.1

they have been calculated so that the CLT results can be compared against experimentally determined values, and thus provide a confirmation of the CLT values (see Table 4.5). The experimental results, for the laminate elastic properties, were obtained in an identical manner to those described to obtain the material characteristics of a UD lamina (see above). A typical stress strain plot recorded from a 0/90 laminate is shown in Figure 4.4 and provides the experimental value for the Young's moduli.

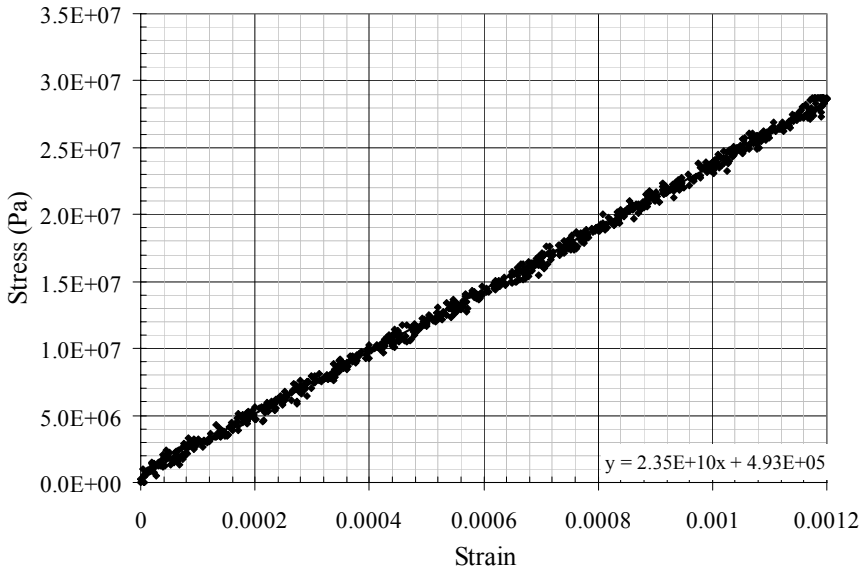

Figure 4.4. Stress strain plot for 0/90 laminate (*Indicating E_L*)

The experimental Poisson's ratio was determined from the ratio of the longitudinal to transverse stain. These strain values are plotted in Figure 4.5 again for a 0/90 laminate.

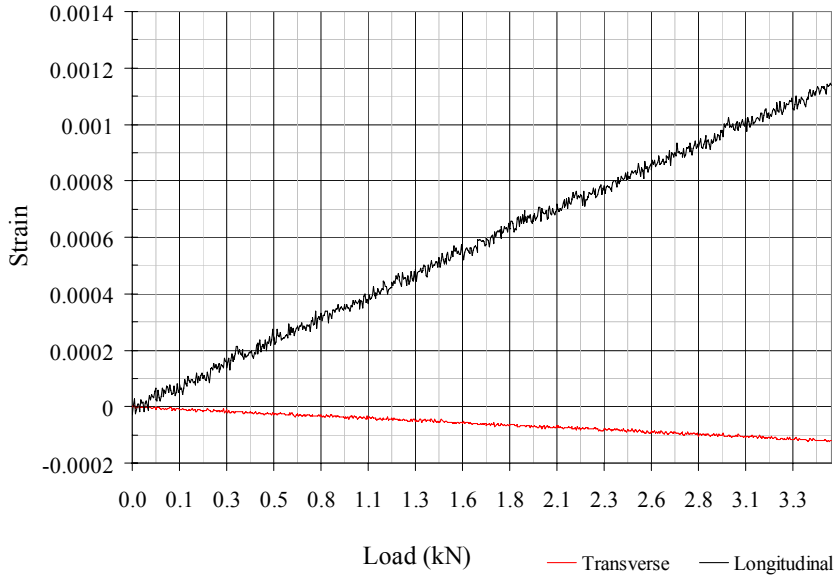

Figure 4.5. Longitudinal and transverse strain for 0/90 laminate

The full set of results for the ν_{LT} and E_L values for the test specimens are given in Table 4.5 (the first two rows of data repeat the results obtained previously for the two UD laminates tested). There is good agreement between these sets of data, giving confidence in the CLT methodology and the stress and strains derived from this (see below), as well as validating the calculated elastic properties for each laminate.

Table 4.5. Laminate properties

Specimen	CLT		Experimental	
	Young's modulus, E_L (MPa)	Poisson's ratio, υ_{LT}	Young's modulus, E_L (MPa)	Poisson's ratio, υ_{LT}
UD	36.8	0.25	36.8	0.25
90	8.4	0.05	8.4	0.05
Mixed	33.6	0.16	31.9	0.14
0/90	24.5	0.096	23.5	0.099
90/0	22.2	0.087	20.9	0.083
± 45	9.2	0.60	9.0	0.49

The major Poisson's ratio for the ± 45 was calculated as 0.60 using CLT; it is possible [107] for orthotropic materials the range of Poisson's ratio extends beyond 0.5 (the limited expected for isotropic materials) and as such is a feasible value.

4.4.3 Calculation of strains and stresses

The remaining unknown terms are the laminate strains, surface ply stresses and thermoelastic signal. The stresses, $\Delta\sigma_1$ and $\Delta\sigma_2$, are calculated using CLT [1] whilst the strains, $\Delta\varepsilon_L$, $\Delta\varepsilon_T$ and $\Delta\gamma_{LT}$ are also calculated using CLT and obtained experimentally. It is possible to predict the mechanical properties of a composite laminate and subsequently the expected strains and stresses for a given loading arrangement if the lamina material properties, geometry, orientation and the laminate stacking sequence are known using CLT. CLT is used here to provide strain, stress and laminate Poisson's ratio values to substitute into the strain and stress calibration equations. The CLT calculations required for each of the test specimens are repetitive in nature, so a computational procedure was developed to calculate the behaviour, as detailed by Daniel and Ishai [1]. The material properties and geometries required for these calculations follow those previously obtained and are provided in Table 4.1 - Table 4.4.

To obtain the laminate strains resulting from the applied load range, the relationships between the externally applied loads and the resulting strains are as follows:

$$\begin{Bmatrix} \Delta N_L \\ \Delta N_T \\ \Delta N_{LT} \end{Bmatrix} = [A] \begin{Bmatrix} \Delta \varepsilon_L^0 \\ \Delta \varepsilon_T^0 \\ \Delta \gamma_{LT}^0 \end{Bmatrix} + [B] \begin{Bmatrix} \Delta k_L \\ \Delta k_T \\ \Delta k_{LT} \end{Bmatrix} \tag{4.6}$$

where ΔN_L is the range of axial load calculated as the plane load per unit width assumed to act at the laminate midplane, ΔN_T is the range of transverse load, ΔN_{LT} is the range of the shear load, [A] is the extensional stiffness matrix and [B] is the coupling stiffness matrix [1]. $\Delta \varepsilon_L^0$, $\Delta \varepsilon_T^0$ and $\Delta \gamma_{LT}^0$ are the range of midplane strain due to the applied loading range and Δk_L, Δk_T and Δk_{LT} are the midplane curvatures due to the applied load range.

In the tests the loading is applied in the axial direction alone and therefore ΔN_T and ΔN_{LT} are equal to zero. The [*A*] and [*B*] matrices were calculated from a combination of the lamina thickness, location within the laminate relative to the laminate midplane, and the reduced stiffness of the ply (i.e. *Q*) in the direction of loading. From Equation (4.6) it is therefore possible to derive the required values for the laminate strains in the *L* and *T* directions to input into the calibration equations in Table 4.1; these are provided in Table 4.6 and Table 4.7 for the load and displacement control tests respectively.

The strain values derived from Equation (4.6) are transformed so that they are expressed relative to the principal surface ply fibre directions. Then the surface stress range in the principal fibre directions (i.e. 1 and 2) can be obtained using the orthotropic stress-strain relationship presented in Equation (3.21). The stresses in the surface ply in the direction of the principal material axes are provided in Tables 5 and 6 for load and displacement control respectively.

4.4.4 Measurement of laminate strain

During testing the applied displacement and load were recorded during both the displacement and load control tests. Therefore using the gauge length of the specimen it is possible to estimate the strain in the specimens. However, this proved inaccurate due to the scarf of the end tab protruding beyond the gripped tab area, as shown in Figure 4.2. As all the tabs were of a UD configuration, the stiffness did not match the specimens (apart from the UD), so the strain in the specimens could not be accurately

determined from the applied displacement. Therefore the laminate applied strain ranges ($\Delta\varepsilon_L$ and $\Delta\varepsilon_T$) were measured using a dynamic extensometer. The measured laminate applied strain is recorded in Table 4.6 and Table 4.7 for load and displacement control respectively and it can be seen that these values correlate well with those calculated using CLT.

Table 4.6. Applied stress and strain values for the load control tests

Laminate	Method	UD	Mixed	0/90	90/0	±45
Orthotropic surface						
$\Delta\sigma_1$ (MPa)	CLT	57.2	63.8	87.8	-3.06	41.9
$\Delta\sigma_2$ (MPa)	CLT	0	1.29	3.07	20.6	12.3
Resin-rich layer						
$\Delta\sigma_x$ (MPa)	CLT	13.2	15.0	20.9	23.0	46.8
$\Delta\sigma_y$ (MPa)	CLT	0	1.29	3.22	3.78	-19.7
Laminate						
$\Delta\varepsilon_L$	CLT	0.00155	0.00173	0.00238	0.00262	0.00577
$\Delta\varepsilon_T$	CLT	-0.000389	-0.000278	-0.000224	-0.000223	-0.00352
$\Delta\varepsilon_L$	Measured	0.00155	0.00179	0.00231	0.00252	0.00603
$\Delta\varepsilon_T$	Measured	-0.000373	-0.000251	-0.000228	-0.000209	-0.00352

Table 4.7. Applied stress and strain values for the displacement control tests

Laminate	Method	UD	Mixed	0/90	90/0	±45
Orthotropic surface						
$\Delta\sigma_1$ (MPa)	CLT	78.6	83.0	87.8	-2.86	17.2
$\Delta\sigma_2$ (MPa)	CLT	0	1.64	3.07	20.2	5.02
Resin-rich layer						
$\Delta\sigma_x$ (MPa)	CLT	17.9	19.5	20.9	21.6	18.0
$\Delta\sigma_y$ (MPa)	CLT	0	1.68	3.22	3.53	-7.6
Laminate						
$\Delta\varepsilon_L$	CLT	0.00214	0.00225	0.00238	0.00245	0.00237
$\Delta\varepsilon_T$	CLT	-0.000534	-0.000362	-0.000224	-0.000209	-0.00144
$\Delta\varepsilon_L$	Measured	0.00219	0.00222	0.00235	0.00241	0.00215
$\Delta\varepsilon_T$	Measured	-0.000527	-0.000311	-0.000232	-0.000200	-0.00105

The stiffening effect of the scarf is demonstrated in Table 4.7 where it can be seen that the $\Delta\varepsilon_L$ values are not constant for the same applied displacement. Clearly taking the 0.44 mm displacement value and dividing by the gauge length would produce larger values of $\Delta\varepsilon_L$ than reported in Table 4.6 and Table 4.7. From the stress data shown in Table 4.6 and Table 4.7 it is evident that in the Mixed, 0/90 and 90/0 there is a finite

transverse stress in the specimens. This occurs as a consequence of the traction imposed by the mismatch in the Poisson's ratio ply by ply. The finite transverse stress value is significant as it is a multiplied by α_2 in Equation (3.70), and α_2 for a glass epoxy laminate is in the order of six times greater than α_1 (see Table 4.3).

4.4.5 Thermoelastic signal

The last variable required to determine A^* is the thermoelastic signal, S. To record the thermoelastic signal from each of the test specimens each specimen was loaded as described in Table 4.2 at a frequency of 10 Hz. The DeltaTherm 1000 system was used to collect the thermoelastic data. A 25 mm IR lens was used so that the detector was positioned at a stand-off distance of 500 mm from the specimen surface to achieve a full-field of view of the entire test specimen. The specimen surface, from which the thermoelastic signal was recorded, was left in the manufactured state and unpainted as the epoxy surface provides a sufficiently high emissivity for thermoelastic studies. Inspection of the thermal data recorded simultaneously with the thermoelastic data showed no thermal variations between the test specimens during the tests so it was not necessary to correct the thermoelastic signal for temperature variations [26] (A detailed discussion of the temperature correction routine is provided in Chapter 5 and 6). The thermoelastic signal recorded from both test regimes are detailed in uncalibrated A/D units in Table 4.8 for the load and displacement control tests. The data had coefficients of variation in the range 4.5 % to 7.9 %. It can be seen from Table 4.8 that neither a constant applied load nor a constant applied displacement result in a constant thermoelastic signal. In general the thermoelastic signal magnitudes follow the order of the laminate longitudinal stiffness given in Table 4.5, with the exception of the ± 45. This is because the surface ply axes are not coincident with the laminate axis and demonstrates that even in simple specimens careful analysis of results is required.

Table 4.8. Thermoelastic signal, S

Laminate	UD	Mixed	0/90	90/0	±45
S (load)	585 ± 7.3 %	765 ± 4.7 %	1136 ± 4.5 %	1189 ± 5.8 %	1105 ± 5.8 %
S (displacement)	845 ± 7.4 %	999 ± 4.9 %	1136 ± 4.9 %	1169 ± 5.7 %	460 ± 7.9 %

4.5 Validation of calibration routine

Using either the calculated or measured data it is now possible to obtain A^* from the three approaches described; *i*) using the calculated surface ply *stresses* given in Table 4.6 and Table 4.7 and applying Equation (3.70), *ii*) using the calculated laminate *strains*

given in Table 4.6 and Table 4.7 and applying Equation (4.5) and *iii*) using the measured laminate *strains* and applying Equation (4.5). The values for A^* derived for each approach are listed in Table 4.9 for the constant load tests and Table 4.10 for the constant displacement tests. In Table 4.9 and Table 4.10 values of ν_{LT} calculated from CLT were used in rows *i* and *ii* and measured values of ν_{LT} were used in row *iii*. The value of A^* obtained using the orthotropic surface ply properties has an average value of 0.589 ± 4.3 % and 0.578 ± 3.6 % for the constant load and constant displacement tests respectively. Assuming that the resin-rich layer is the source of the thermoelastic signal A^* has an average value of 0.753 ± 2.4 % and 0.778 ± 4.3 % for the constant load and constant displacement tests respectively. (It should be noted that the values of A^* presented in Table 4.9 - Table 4.10 are not absolute and are specific to the DeltaTherm 1000 system and the settings used in this work.)

Table 4.9. A^* derived for orthotropic surface ply properties (Constant load)

		UD	Mixed	0/90	90/0	±45
i)	(MPa/°C)	0.587	0.558	0.560	0.597	0.603
ii)	(MPa/°C)	0.586	0.558	0.559	0.597	0.602
iii)	(MPa/°C)	0.594	0.595	0.539	0.576	0.604

Table 4.10. A^* derived for orthotropic surface ply properties (Constant displacement)

		UD	Mixed	0/90	90/0	±45
i)	(MPa/°C)	0.558	0.556	0.559	0.569	0.595
ii)	(MPa/°C)	0.560	0.557	0.559	0.568	0.597
iii)	(MPa/°C)	0.569	0.558	0.558	0.560	0.614

Table 4.11. A^* derived for isotropic resin-rich layer properties (Constant load)

		UD	Mixed	0/90	90/0	±45
i)	(MPa/°C)	0.790	0.745	0.743	0.788	0.858
ii)	(MPa/°C)	0.781	0.743	0.744	0.790	0.798
iii)	(MPa/°C)	0.791	0.791	0.717	0.762	0.821

Table 4.12. A^* derived for isotropic resin-rich layer properties (Constant displacement)

		UD	Mixed	0/90	90/0	±45
i)	(MPa/°C)	0.741	0.742	0.743	0.752	0.791
ii)	(MPa/°C)	0.745	0.741	0.744	0.751	0.775
iii)	(MPa/°C)	0.758	0.742	0.742	0.741	0.804

A^* is a function only of the specific heat and density of the material and not dependent on the orthotropic properties of the laminate. Therefore the fact that the A^* values are in

close agreement does not completely validate the theory presented here and does not identify if the signal response is from the resin-rich surface layer or the orthotropic surface ply. A further important feature is the difference between the values of $(\alpha_1 Q_{11} + \alpha_2 Q_{12})$ and $(\alpha_1 Q_{12} + \alpha_2 Q_{22})$ that appear in Equation (4.5). For this material $(\alpha_1 Q_{11} + \alpha_2 Q_{12})$ equals 0.298 and $(\alpha_1 Q_{12} + \alpha_2 Q_{22})$ equals 0.311. Clearly the difference between the response of the 0/90 and 90/0 specimen will be very small as indicated in Table 4.9 and Table 4.10. The values of $(\alpha_1 Q_{11} + \alpha_2 Q_{12})$ and $(\alpha_1 Q_{12} + \alpha_2 Q_{22})$ for the isotropic resin material are equal at 0.392. The difference between this value and that obtained for the orthotropic material of approximately 0.30 accounts for the factor of 25% difference between the two sets of A^* values.

To identify the source of the thermoelastic signal with certainty it was necessary to derive a value of ΔT to ascertain if it is the orthotropic surface ply or resin-rich layer that provides the response. The DeltaTherm system is not radiometrically calibrated, therefore it is impossible to determine an absolute value of the thermoelastic temperature change as given by Equation (4.3). It was necessary to use an IR system that is radiometrically calibrated and as such capable of resolving the temperature change associated with the thermoelastic response. Here a Cedip Silver IR system, with a temperature resolution of 17 mK was used to obtain ΔT. The data required to evaluate ΔT directly is given in Table 4.13. For the orthotropic material; the specific heat, C_p, value was obtained from [108] and the density was measured [63]. The equivalent data for the epoxy material was obtained from literature [109]. Table 4.14 and Table 4.15 provides calculated and measured ΔT values using both the isotropic resin-rich layer and the orthotropic surface ply. The temperature of specimen surface remained constant through the testing and at a value of 291 K.

Table 4.13. Properties of resin-rich layer and orthotropic surface ply

Material property	Epoxy	GRP
Epoxy specific heat, C_p (J/kgK)	1040	882
Epoxy density, ρ (kg/m^3)	1170	1846

Table 4.14. Thermoelastic temperature change obtained for resin-rich layer

Test method		ΔT (°C)				
		UD	Mixed	0/90	90/0	±45
Load	Calculated	0.110	0.136	0.202	0.224	0.227
	Measured	0.10	0.13	0.18	0.21	0.25
Displacement	Calculated	0.150	0.177	0.202	0.210	0.093
	Measured	0.14	0.17	0.19	0.19	0.09

Table 4.15. Thermoelastic temperature change obtained for orthotropic surface ply

Test method		ΔT (°C)				
		UD	Mixed	0/90	90/0	±45
Load	Calculated	0.061	0.076	0.113	0.126	0.122
	Measured	0.10	0.13	0.18	0.21	0.25
Displacement	Calculated	0.084	0.099	0.113	0.123	0.050
	Measured	0.14	0.17	0.19	0.19	0.09

It is evident from Table 4.14 and Table 4.15 that the measured thermoelastic response is that of the resin-rich layer and not that from the orthotropic surface ply, as the measured ΔT values are in close agreement with those calculated using material properties. This indicates that any composite material with a resin-rich layer of 25 μm or greater can be treated as 'thermoelastically isotropic'. However the material construction, i.e. the stacking sequence must be considered in any analysis and must be considered as 'mechanically orthotropic'. Therefore a calibration routine must be devised that accounts for the mechanical orthotropy of the material, without the need to know the material properties laboriously derived in Section 4.4. Moreover this routine must be based on a strain measurement, rather than calculating the stress in the resin-rich layer. Such a calibration constant using a simple tensile specimen would be as follows:

$$\frac{\Delta\varepsilon_L\left(1-\nu_{LT}\right)}{S}=\frac{A^*\left(1-\nu_R\right)}{\alpha E_R}=B^* \tag{4.7}$$

Table 4.16 gives the B^* values for each test specimen and it can be seen the value is constant for the UD, Mixed, 0/90 and 90/0 the value is 0.191 ± 0.47%. It can be seen that the ±45 is about 20% greater than the other values. The explanation for this may result from discrepancies in the properties used for the ±45; from Table 4.5 it can be seen that there is a difference between the calculated and measured values and also the shear modulus was obtained from literature sources.

Table 4.16. B^* values for each test specimen

		UD	Mixed	0/90	90/0	±45
B^*	Constant load	0.199	0.197	0.191	0.194	0.232
B^*	Constant displacement	0.191	0.185	0.189	0.188	0.227

Having derived B^* it is now possible to relate the sum of the principal strains to the thermoelastic signal as follows:

$$\Delta\varepsilon_L + \Delta\varepsilon_T = B^* S_c \tag{4.8}$$

If the material is thermoelastically orthotropic for lay-ups where the principal material axes and the surface ply axes correspond it is possible to use the following equation to obtain:

$$\frac{\Delta\varepsilon_L\left(\left(\alpha_1 Q_{11} + \alpha_2 Q_{12}\right) - \nu_{LT}\left(\alpha_1 Q_{12} + \alpha_2 Q_{22}\right)\right)}{S} = A^* \tag{4.9}$$

Clearly it is not possible to manipulate Equation (4.9) to give a simple expression that relates the strain to the thermoelastic signal. In cases when $\nu_{LT} \to 0$, e.g. cross ply laminates it would be possible to neglect the second bracketed term in the numerator of Equation (4.9) as in these cases the transverse strain is small. In other cases it is necessary to measure both the longitudinal strain and the transverse strain and know the material properties given in Equation (4.9), so the calibration would determine A^* only.

For all other surface ply configurations a specific calibration routine must be developed that accounts for the shear in the laminate. As all the materials used in this thesis have a resin rich layer the calibration constant has been calculated for the various detector settings used in this thesis and is collated in tabulated form in Appendix B.1.

A strain calibration routine has been developed using 'Matrix laboratory' (MATLAB) that manipulates the uncalibrated thermoelastic signal (S) by the strain calibration constant (B^*) to produce full-field strain sum plots. The MATLAB process was designed to extract the thermoelastic data from files saved as American Standard Code for Information Interchange (ASCII) text files from the DeltaTherm operating software (Deltavision) and be processed retaining the full-field capability (i.e. 128 x 128 and 256 x 256 data matrices corresponding to the DeltaTherm 1000 and 1400 system respectively). After calibration a further algorithm has been devised that applies a software header and footer to the calibrated data set so that it could be reformatted and reviewed in the Deltavision software and exported to a spreadsheet or graphing application for analysis. The MATLAB code for the software header and footer is provided in Appendix C.1 and the calibration code in Appendix C.2

4.6 Conclusions

The motivation for the work presented in this chapter was to develop a calibration routine so that quantitative strain values can be obtained from thermoelastic readings from a general composite structure. The traditional stress based calibration routine is dependent on knowledge of the stresses in the surface lamina, which for a general composite laminate is not straightforward and must be calculated using CLT that necessitates an accurate knowledge of the material properties, geometries and loading. The chapter has shown that obtaining the relevant material properties requires extensive experimental characterisation of the material properties.

The strain calibration routine presented has been verified by both measurement and calculation of the strain applied against the traditional stress based calibration method. The effect of varying the laminate's global mechanical properties has been incorporated into the development of the calibration approach and the dependent variables are included in the calibration procedure. The subsequent applicability to specimens with a variety of stacking sequences has also been approached. The comparison of the calibration constant generated by the three methods displayed a good correlation and provides assurance in the application of this new calibration method.

A new calibration constant, B^*, that is valid for specimens with a resin-rich layer based on an isotropic thermoelastic response from specimens that are mechanically orthotropic has been developed. All the specimens used in this thesis have a resin-rich layer and therefore this approach is applied throughout. Therefore this new measured strain calibration routine will be used in the experimental work in the following chapters to

quantitatively calibrate thermoelastic results from composite laminates subject to damage.

A further calibration constant for specimens without a resin-rich surface layer that are mechanically and thermoelastically orthotropic would be required. The simplifications possible by considering the isotropic nature of the resin would not be possible and the full complement of orthotropic properties would be required. Therefore calibration would be specific to each specimen and the mechanical properties would be required to calculate Equation (4.5). The work presented in this chapter has shown this is a feasible task.

The purpose of generating a thermoelastic calibration constant was described as providing a means of obtaining quantitative strain data from TSA. As the goal of this work is to analyse localised changes in strains due to damage the development of this calibration approach detailed here achieves a major objective in providing a methodology for thermoelastic damage assessment.

Chapter 5

A temperature correction methodology

5.1 Introduction

Following the work described in Chapter 3 it is evident that the key component in facilitating TSA is the IR detector. Equation (3.56) shows that the output from the detector, *S*, is dependent on both the surface stresses and the absolute surface temperature of the component under investigation. The purpose of this chapter is to provide a means of eliminating any effects of absolute temperature change on the thermoelastic signal so that the signal can be analysed in terms of the calibrated strain, hence linking the procedure detailed in Chapter 4 with the approach described in this chapter and Chapter 6. The temperature correction procedure entails separating the response that occurs as a consequence of changes in the absolute surface temperature from those related to the stress changes. Therefore a methodology is developed that provides *temperature corrected* thermoelastic data that is then calibrated in terms of strain.

As discussed in Chapter 3 it is the wavelength range of the IR system that dictates the extent to which the absolute temperature influences the thermoelastic signal. In an evaluation of the DeltaTherm [90] its sensitivity to absolute temperature variation was assessed in comparison to the SPATE system. As predicted by Planck's Law (see Chapter 3) the SPATE output was less sensitive to temperature change than that of the DeltaTherm.

The dependence of the thermoelastic signal on the specimen surface temperature recorded using the SPATE system was dealt with by using a manufacturer's calibration curve [92] that provided a temperature correction factor, R_{SPATE}. Where any temperature change would result in the R value deviating from unity and the associated thermoelastic data would be factored by this value during the calibration routine. It has been shown [91] that the temperature correction curve for the SPATE conforms very closely to the following relationship:

$$R_{SPATE} = (T_0 / T)^3 \tag{5.1}$$

where T_0 is the absolute temperature at which the detector was radiometrically calibrated.

The work in Chapter 3 shows that the relationship between the spectral radiant emittance and the surface temperature results in a function of T^3 and goes some way to explaining the cubic relationship given by Equation (5.1). Early work with the SPATE [110] demonstrated that the manufacturer's calibration curve (and hence the relationship derived in [91]) did not completely compensate for increases in surface temperature. However, it was commented [110] that the effect of temperature was minimal and was often well within the noise expected using the SPATE system and was thus largely ignored.

In Chapter 3 it is shown that the spectral radiant emittance is dependent on the operating wavelength range of the IR detector. SPATE operates in the 8 – 12 μm range and the DeltaTherm system operates in the 2 – 5 μm. range. The effect of these parameters is discussed in detail in Chapter 3. Results by Quinn [90] demonstrated that the effect of absolute temperature variations was not negligible when using the DeltaTherm and it was shown that a correction factor based on the entire wavelength range such as that given in Equation (5.1) is not sufficient. Whilst the inherent indifference to absolute temperature variations and the correction facility offered with the SPATE equipment couples to provide a system that is insensitive to temperature change, the DeltaTherm system offers benefits that far outweigh this feature. The principal disadvantage of SPATE was that it was a mechanical scanning device that collected IR data from a single detector [85], rather than a staring array system used by the DeltaTherm. The scanning method of data collection meant that a full-field stress contour map took 1-2 hours to produce with the SPATE system. The DeltaTherm detector array [111] simplifies the detector unit design and furthermore as the signal is processed digitally the

data collection time is reduced from hours to seconds. The ability for the DeltaTherm system to obtain thermoelastic data in near real-time is a major advantage for damage assessment and therefore it is essential to attack the challenge of temperature correction so that the system can be used generally. Therefore the purpose of this chapter is to establish the relationship between the thermoelastic signal and the surface temperature so a function similar to the form of Equation (5.1) is developed that can provide effective temperature correction for the DeltaTherm.

In the development of the correction factor for the SPATE it was assumed it would be applied globally to the entire data set as part of the calibration constant. Therefore if the temperature of the laboratory increased then the subsequent increase in temperature of the test specimen could be accounted for by a global temperature correction. However this approach is not suitable for thermoelastic studies of damage evolution. This was exemplified during damage analysis of a FRP laminate using the DeltaTherm system [36] where the thermoelastic signal was recorded to have increased by 20 % local to damage site where no discernible reason for change in the stress state was apparent. Interrogation of the corresponding thermal data showed a local temperature increase over the same time period and it was apparent that the signal increase was a function of the surface temperature observed. As the increase in the signal was restricted to a small area of the data it would not be correct to treat the entire data set for this temperature rise. It is therefore important that the temperature correction procedure is developed to be applied for the temperature increase at each pixel in the data array. In this chapter it is shown that the temperature increases during damage can far exceed those noted in [36] thereby providing further justification for the need for a temperature correction methodology.

There are a number of steps in the development of a revised correction factor: firstly, the relationship between the thermoelastic signal and the temperature must be defined and secondly, a means of measuring the absolute temperature must be devised. The first step is investigated in two manners: the expected rise in spectral radiant emittance is firstly characterised theoretically in this chapter by using Planck's law. In Chapter 6 the theoretical solution is validated against experimental data from the DeltaTherm system by noting the response of the output to changes in specimen surface temperature. The theoretical treatment of Planck's law devised here differs in an important manner to that presented in Chapter 3. It is not possible to produce a closed form relationship for the spectral radiant emittance between specific wavelength limits and as such it must be investigated in a numerical fashion. With regard to the second step (the measurement of the absolute surface temperature) it was suggested by Cunningham *et al*. [36] that the

DeltaTherm be used to obtain both the thermoelastic and thermal data. As the thermal data can be obtained simultaneously with thermoelastic data and is recorded point-by-point this would provide a means of measuring the surface temperature. As the DeltaTherm system is not radiometrically calibrated, the thermal data must be calibrated to obtain temperature data in Kelvin; a method for doing this is established in Chapter 6.

In this chapter the next section deals with the effect of temperature variations on the thermoelastic signal. A theoretical temperature correction approach is developed that accounts for this.

5.2 Temperature variation

Before the effect of temperature on the thermoelastic signal is investigated it is necessary to verify the extent of temperature rise expected and how this may occur. The manner in which variation in the absolute temperature may be experienced during damage analysis can be split into two major mechanisms:

i. variation in the environmental conditions,
ii. damage occurring in the FRP specimen.

Temperature variation due to environmental changes is self-explanatory, but the extent to which this may vary the absolute temperature of the component under test requires verification. The laboratory in which this work is conducted is not environmentally controlled and the data presented in Figure 5.1 illustrates the variation which can be expected day-by-day and subsequently hour-by-hour during a week in March.

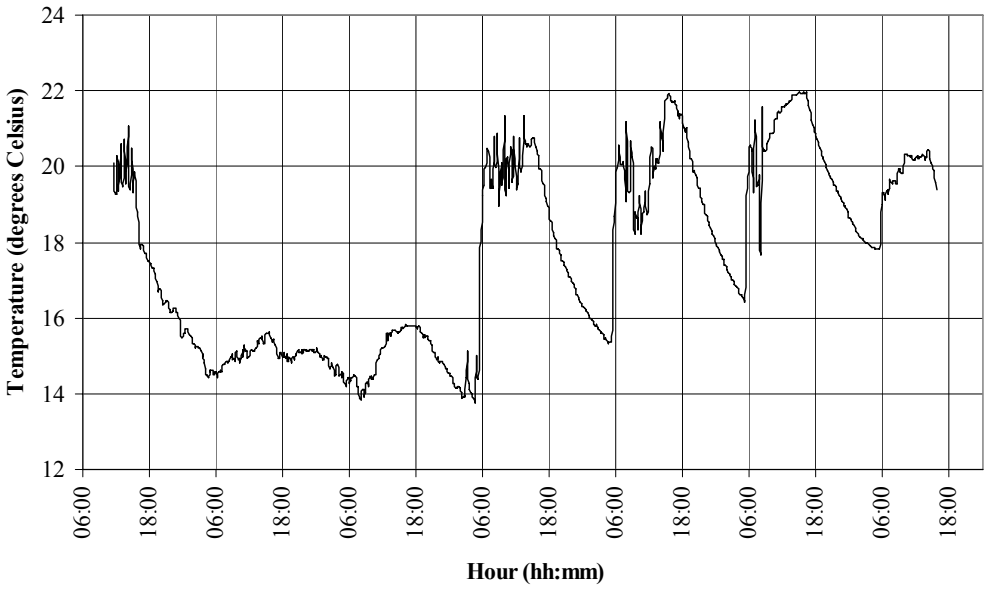

Figure 5.1. Variation in the ambient laboratory temperature

There is a maximum variation of 8 ˚C through the week and more importantly variations of 4 ˚C are experienced during the working day. It would be expected that the seasonal variation would exceed these two values by a factor of two.

Apart from ambient temperature variations the effect of temperature is compounded in the work presented in this thesis, by variations in temperature during testing of composite materials. Temperature variations have been reported by other authors during testing of composite materials and in particular at areas local to damage sites [59, 63, 71, 72, 95, 96]. This has considerable importance to the work presented in this thesis as it is the area local to the damage site that will be of interest when damage occurs as the stress is expected to redistribute around the damage site. Heat generated internally within a composite laminate undergoing a cyclic load has been reported [78, 112, 113]. Gamestedt *et al*. [112] cover heat dissipation in terms of dissipative fatigue mechanisms resulting in hysterisis losses. This loss gives rise to heat dissipation and a change in temperature of the material. Pye and Adams [113] also studied heat generation and propagation due to cyclic loading. They reported the correlation between the theoretical temperature rise expected against those gathered experimentally using an IR scanner. Reifsnider and Williams [114] measured heat emission from a rectangular boron-epoxy plate with a central hole and recorded a temperature increase of 36 K. Further testing by Bakis and Reifsnider [78] observed heat emission near damage regions of a graphite-epoxy laminate undergoing cyclic loading. Therefore it can be assumed that during fatigue testing of components at realistic load levels heat generation can be expected.

To ascertain the extent of heating that may be generated during fatigue loading of the composite materials used in this work a series of trials were undertaken. All of the test specimens used in this part of the work were manufactured in an identical manner to that reported in Chapter 4 and were of the same batch of SP Systems SE84HT E-glass pre-impregnated with an epoxy resin material and were loaded in the same manner using the servo-hydraulic test machine. As the specimens are made from a glass-fibre-epoxy material which has a low thermal conductivity it is expected that any heat generated will not be dissipated within a short space of time. A FLIR ThermaCAM SC 3000 [115] device was used to independently measure the absolute temperature of specimens during testing. The SC 3000 system incorporates a Quantum Well IR Photodetector (QWIP) FPA sensor system that operates at a wavelength of 8 - 9 μm [115]. As the FLIR system had been temperature calibrated this allowed full field temperature data to be recorded as the damage progressed.

The first test was carried out to observe the temperature rise expected on a specimen of similar design, manufacture and loading (8 ± 4 kN at 10 Hz) to those investigated in calibration studies in Chapter 4. The test specimen used was a $[(0/90)_3,0, (90/0)_3]$ and was loaded in the servo-hydraulic test machine and cycled for a period of just over 1 hour. The temperature profile (taken from the average of a vertical line along the specimen) of is shown in Figure 5.2. This provides a baseline that enables an estimation of the consequences of heat generation during 'standard' stress analysis type testing.

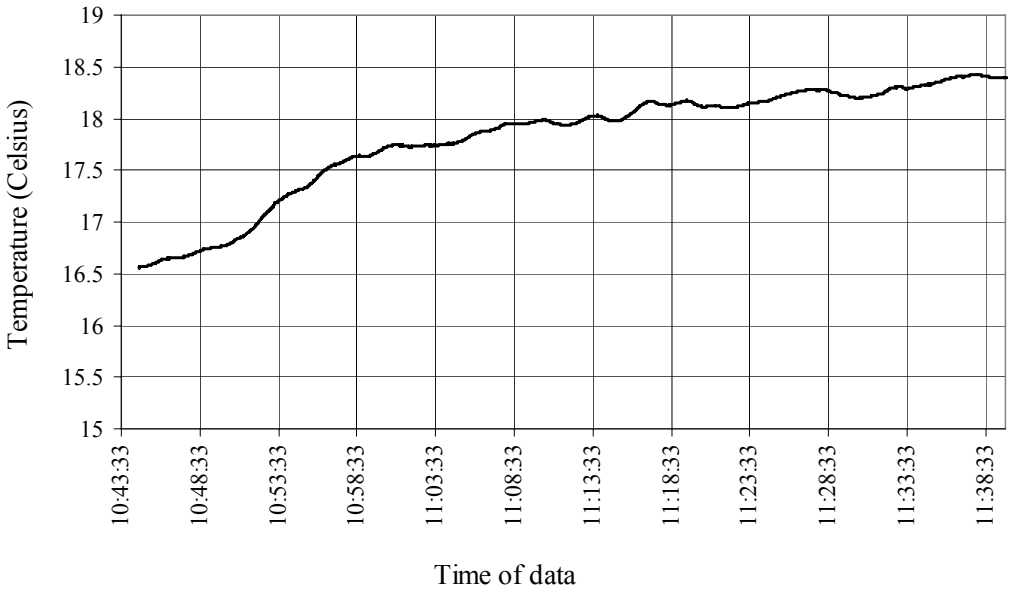

Figure 5.2. Variation in the 0/90 specimen maximum temperature

The average temperature over the first 10 minutes of the test shows a very small increase of 0.2˚C. This result demonstrates that during the cyclic loading of composites at a load level sufficient to promote a measurable thermoelastic response the resulting surface temperature increase expected is negligible. This was an important consideration in the analysis of the data used in Chapter 4 and the data sets were checked for deviations in temperature across each specimen and between specimens. As no discernible variation in the temperature could be detected it was considered that the thermoelastic data was not affected by temperature. However, the temperature profile in Figure 5.2 does show some drift in the temperature profile after this initial period and after approximately a further 50 minutes of loading the temperature increases by 1.8˚C. The thermal profile from the entire specimen was investigated and it was evident that specimen surface temperature was not uniform and was hotter at the end gripped by the hydraulic actuator. The source of the temperature rise was attributed to the influence of the test machine hydraulic oil heating up during use. This adds a further issue to bear in mind with respect to the variation in temperature due to the ambient temperature local to the specimen. It should be remembered that thermoelastic data can be recorded in a matter of seconds so this period of loading would not be necessary if only one set of thermoelastic is required; nevertheless over longer period of loadings such as those expected with fatigue studies it will be fundamental part of the testing and must be considered.

The first example demonstrated the effect of both ambient heat and the temperature rise due to a modest loading that resulted in a general rise in the surface temperature. However, this only occurs if prolonged cyclic loading is used and is therefore not a consideration in standard stress analysis type tests. In contrast when damage evolves in FRPs heating occurs local to the damage site. As polymers are generally good insulators the heat is not dissipated quickly and ‘hot-spots’ form on the surface of the material. This phenomenon has been exploited in IRT inspections of composite components to locate damage, e.g. [48, 116]. The sensitivity of IR detectors allows small variations in absolute temperature to be discerned and in particular the high sensitivity obtainable by InSb detectors is beneficial to the accuracy of IRT analysis where the change in the *absolute temperature* is the observed variable. In TSA applications the sensitivity permits higher stress resolution but as the measured variable is *temperature change* to obtain thermoelastic data the sensitivity to change in absolute temperature is an unwanted effect. To obtain an insight to the temperature increase expected during damage a ± 45 laminate was subject to a fatigue load whilst thermal data was recorded. The temperature profile of this laminate is provided in Figure 5.3 at various stages through the fatigue life until failure.

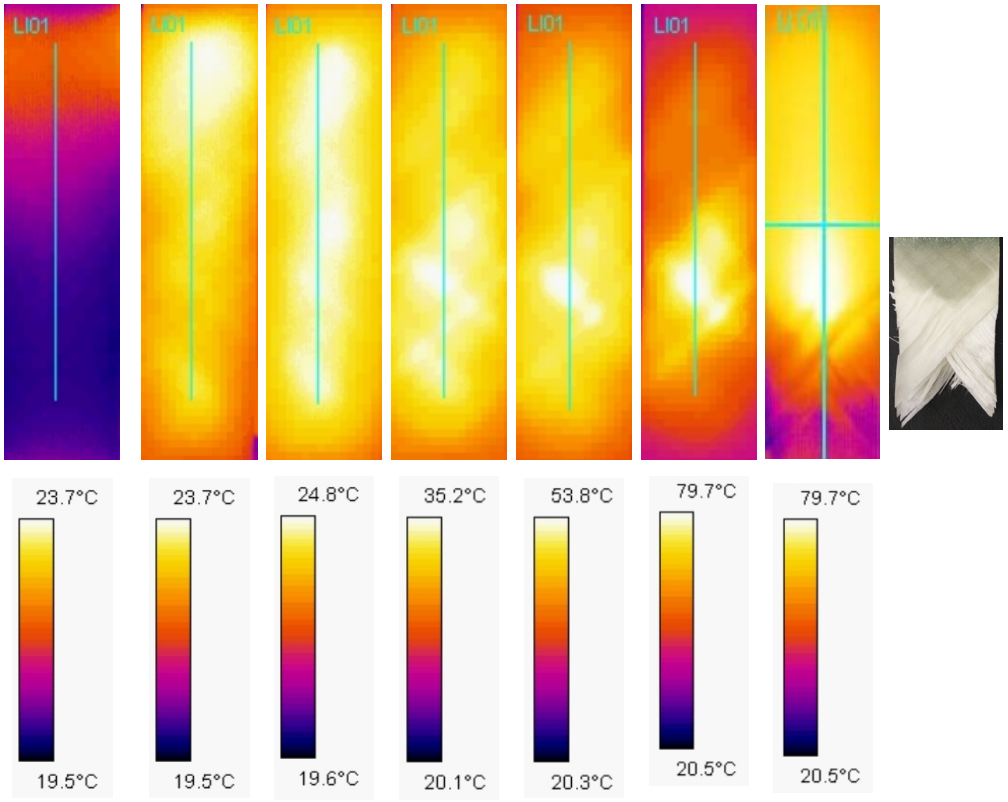

a) b) c) d) e) f) g) h)

Figure 5.3. Thermal distribution of a ± 45 GFRP coupon

The maximum temperature recorded from the line indicated (LI01 in Figure 5.3) is plotted in Figure 5.4. For the first 28 minutes of the test the specimen was cycled at 8 ± 6 kN at 10 Hz, the thermal images are illustrated in Figure 5.3a, b, c and d at times corresponding to the start of test, 1 minute, 2 minutes and 27 minutes after the start of the test respectively. The average temperature increase during this period was recorded as 6.7 ˚C. At 28 minutes from the start of the test the load was increased and cycled until failure. Figure 5.3e and f occur during the second period of fatigue at 43 and 51 minutes respectively and the final thermal image is captured immediately following the full failure of the laminate. At failure a maximum temperatures of 83 ˚C was evident Figure 5.3g, an increase of 50.7 ˚C, from the surface at the start of the test.

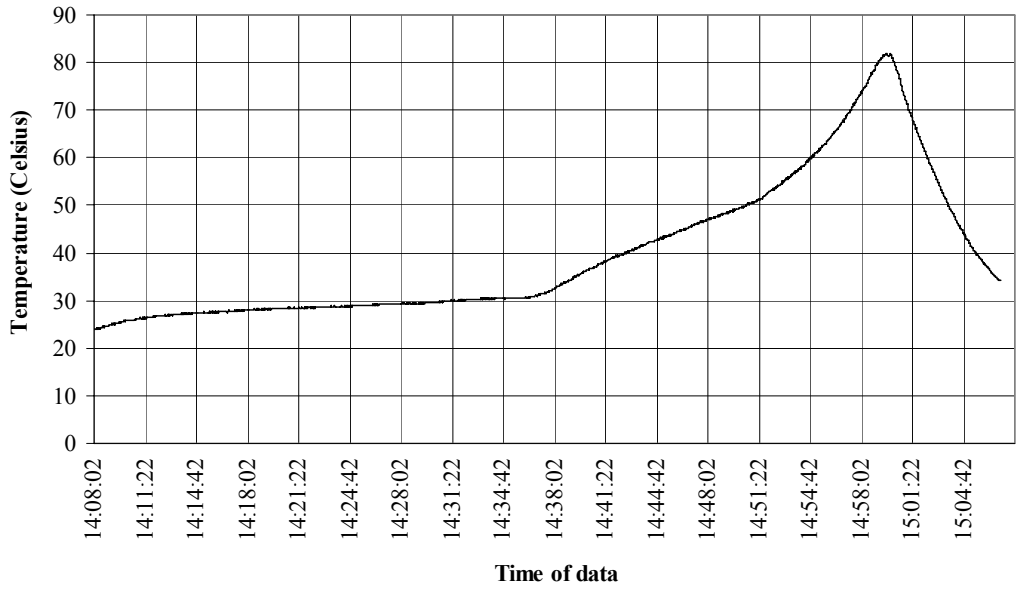

Figure 5.4. Variation in the ± 45 specimen maximum temperature

From Figure 5.3h the manner in which the laminate failed can be observed; as a consequence of matrix damage. Due to the angle ply stacking sequence there is a ply mismatch that generates interlaminar shear stresses whilst the laminate is loaded. It can be seen that this generates heat through the viscoelastic behaviour.

To continue the experimental work of Cunningham *et al.* [36] where heating, caused by the propagation of damage, was observed a test was devised that recreated their work. The test used a coupon of a similar construction to that used in [36] and was manufactured from 13 UD plies with an 8 mm diameter circular hole was cut in the centre of the specimen to act as an initiator for damage (see Figure 5.5).

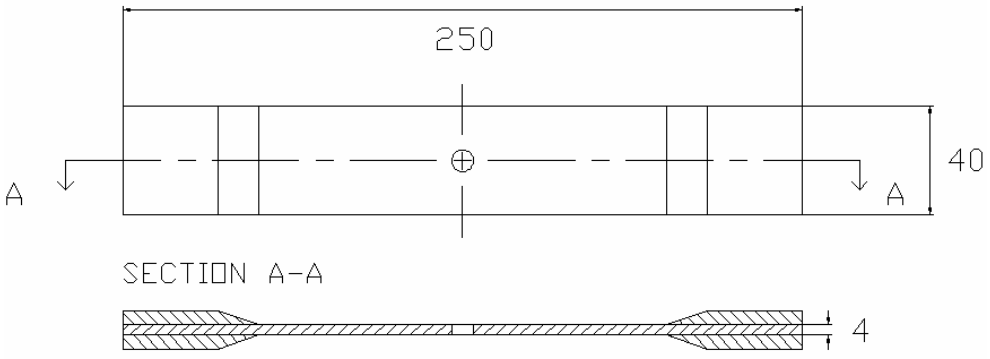

Figure 5.5. GFRP coupon

At a load of 8 ± 4 kN at 10 Hz, commensurate with that experienced under standard TSA conditions, the thermal distribution is shown in Figure 5.6 and plotted in Figure

5.7. An increase of 4.4 ˚C can be seen. Although no damage has initiated it is evident that some heat is generated due to the stresses at the hole.

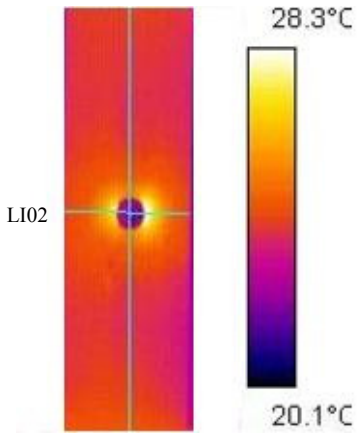

Figure 5.6. Thermal distribution of around a hole in a UD GFRP coupon

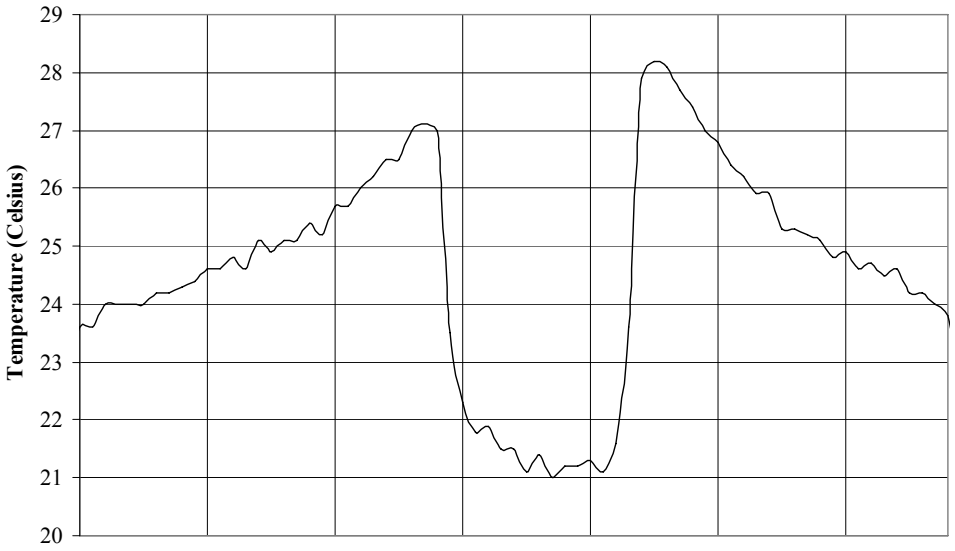

Figure 5.7. Variation in the temperature (*along line LI02 shown in Figure 5.6)*

To replicate the loading conditions reported in [36] the specimen was cycled at 10 ± 8 kN. Similar damage was observed to that reported by Cunningham *et al*. [36] and after 1000 cycles the maximum temperature at the site of the damage was 35 °C i.e. an average of 12 °C above ambient temperature. After this initial loading cycle the coupon was subjected to a cyclic load of 21 ± 11 kN at 5 Hz and cycled until gross failure of the component occurred. The results from the FLIR system are shown in Figure 5.8, and show a considerable change in the surface temperature of the component at the damage site throughout the tests.

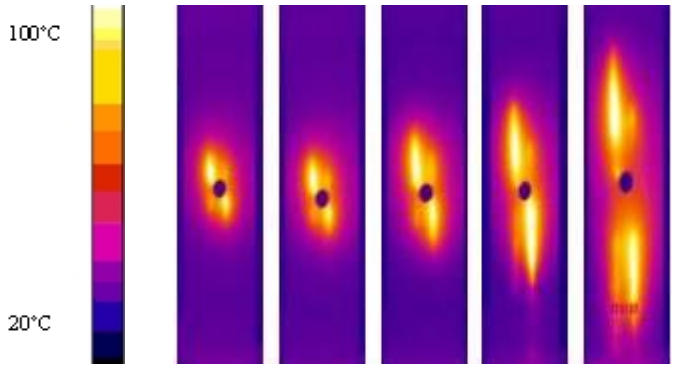

Scale (˚C) Temperature profile

Figure 5.8. Heating due to damaging fatigue cycle

In this type of coupon the damage evolves by matrix cracking, constrained in the transverse direction by the parallel fibres. After complete through thickness failure of the specimen the cyclic motion was continued so that frictional heating was promoted at the free surface damage sites. The evolution of the crack in the vertical direction can be followed by the temperature distribution through the specimen. The maximum temperature recorded from the specimen is given in Figure 5.9; interrogation of the data shows an increase of 76˚C. This level of heating far exceeds that caused by the effect of viscoelastic heating alone and must be attributed to the friction at the crack interfaces; although not relevant to TSA as the stress bearing capability of the coupon has been reduced to practically zero. However it should be considered that if temperature correction is not applied TSA would provide readings that indicate the specimen is still intact and carrying a stress. Therefore demonstrating that it is absolutely essential to have a temperature correction facility.

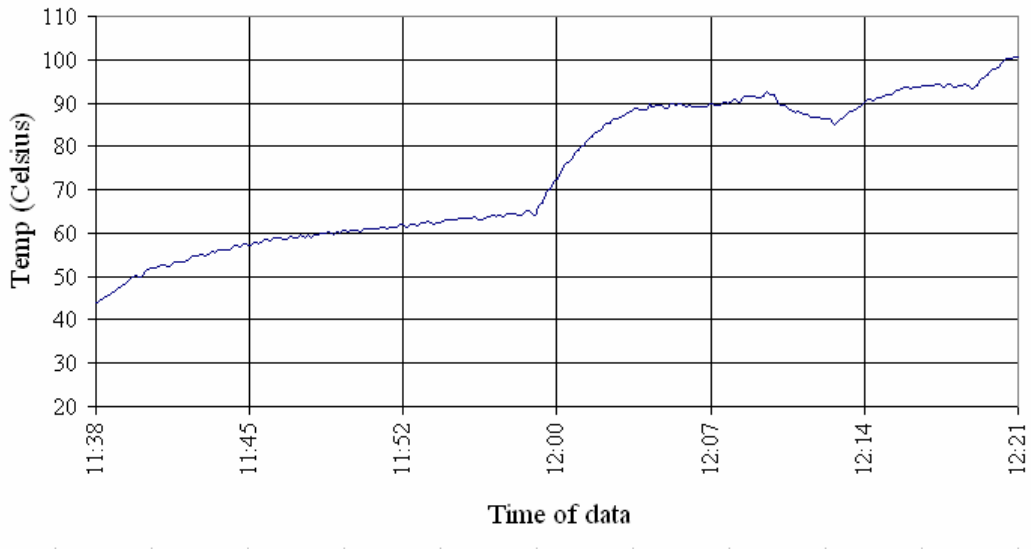

Figure 5.9. Maximum temperature recorded during fatigue

It cannot be assumed that change of the bulk temperature of a specimen is negligible either as a result of environmental changes or during the fatigue testing of composite materials. It has been shown that considerable heating is to be expected in the work described in this thesis that will significantly affect the thermoelastic response [63, 90]. Therefore a case for temperature correction has been made. Further, from Figure 5.3, Figure 5.6 and Figure 5.8, it is shown that the variation of temperature does not occur uniformly over the surface of the specimen and the correction must be provided for the temperature evident on a point-by-point basis and cannot be solved by simply applying a temperature corrected calibration constant. The theory that shows how an increase in the absolute temperature gives rise to an increased thermoelastic signal is provided in the next section and further demonstrating the sensitivity of InSb detectors to changes in absolute temperature.

5.3 Theoretical basis

In Chapter 3 a detailed description is provided of how the photon flux from the surface of the specimen is converted to a voltage output by the detector system and subsequently into the digital thermoelastic signal. This manipulation has been presented by previous researchers [21, 89]. However there is a significant omission in the treatments, as in all cases it is assumed that inputs from the entire electromagnetic specimen are collected by the photon detector. However this is not the case, as the SPATE system works over the 8 – 12 μm as it is a CMT device and the DeltaTherm works over the 2 – 5 μm as it is an InSb device. Therefore it is incorrect to integrate Planck's Law (see Equation (3.59)) over 0 - ∞, i.e. the entire electromagnetic spectrum. Only the operating wavelengths of devices should have been included in the integration. This methodology does not affect the previous TSA work reported in the literature in a detrimental manner assuming the absolute temperature does not alter or if calibration is carried out at a specific temperature. However, if temperature correction is required, simply using the $\left(T_0/T\right)^3$ as suggested in previous work is insufficient. This section of work demonstrates theoretically that in TSA the temperature correction index should be much greater than three.

As in Chapter 3 the number of photons per unit area and time is obtained by integrating Equation (3.71). However here the integration will be carried out over the operating wavelength band of the photodetector instead of the range zero and infinity. Evidently this will not yield the same result given by the formulation of Equation (3.77).

Mathematically it is not possible to integrate Equation (3.71) over a defined wavelength range and derive an expression that is simply a function of temperature (as in Equation (3.77)). For the purposes of this work, i.e. deriving a temperature correction factor, an expression that is just a function of temperature is desirable. An approximate approach is suggested for detectors where the response of the detector to temperature changes follows an approximate power law [84, 117, 118], i.e. $N_b \propto T^n$. Therefore it is possible to propose an equation that relates the surface temperature of a body to the total number of photons emitted over a particular wavelength range as follows:

$$N_{b_\lambda} = B'' T^n \tag{5.2}$$

where B'' is a constant that is dependent on the detector.

The index n can be evaluated by determining N_{b_λ} from Equation (3.71) by numerical integration over the wavelength of interest for a variety of temperatures. To obtain a numerical value of n is possible by taking logs of Equation (5.2) that yields a simple linear form between N_{b_λ} and T, i.e.:

$$\ln N_{b_\lambda} = \ln B'' + n \ln T \tag{5.3}$$

A plot of $\ln N_{b_\lambda}$ against $\ln T$ will be characterised by a linear relationship from which n can be determined from the slope of a plot and B'' can be derived from the intercept of the plot. To obtain values for N_{b_λ} for given temperatures a method to numerically integrate Equation (3.71) was developed. The numerical integration was preformed using a MATLAB procedure that was developed (Appendix C.3). The numerical integration was performed over the temperature range of 293 K to 323 K to cover the extent of temperature variation experienced in Section 5.2, the integration was performed three times over the wavelength ranges of interest:

i. 2 – 5 μm range (i.e. for the DeltaTherm system)
ii. 8 – 12 μm range (i.e. for the SPATE system)
iii. 1 – 1000 μm range (i.e. the *idealised* IR range)

The purpose of the second and third integrations were to firstly to assess the correction factor proposed by Ometron [92] for the SPATE system and secondly to verify the numerical integration and methodology provided accurate results as the value obtained

could be compared to that expected from the derivation of Equation (3.77). The values obtained were plotted and an example of the data produced is plotted in Figure 5.10 (for the DeltaTherm system), in all cases the correlation coefficient for the linear fit was 0.99.

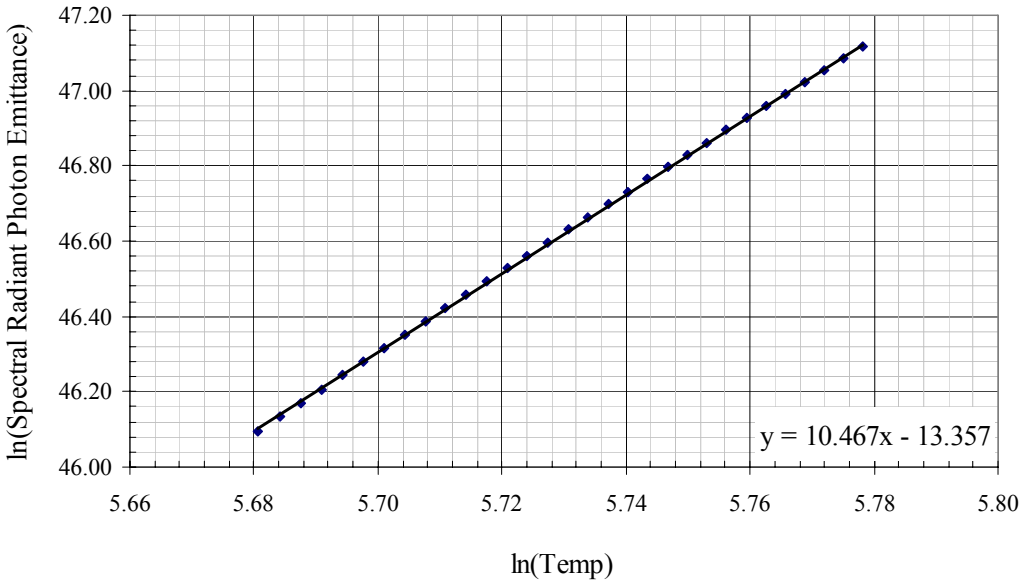

Figure 5.10. Numerically derived relationship for DeltaTherm

The procedure yielded results for *n* and the results are provided in Table 5.1

Table 5.1. Numerical integration

	Operation	Operating range (μm)	*n*
i	DeltaTherm	2 – 5	10.47
ii	SPATE	8 – 12	4.70
iii	Photon flux	1 – 1000	3.29

The results of the numerical integration would imply that Equation (5.1) should be rewritten as follows for the DeltaTherm system as:

$$R = (T_0 / T)^{10.47} \tag{5.4}$$

and correspondingly for the SPATE system:

$$R_{SPATE} = (T_0 / T)^{4.7} \tag{5.5}$$

There is a huge difference between Equation (5.1) and Equation (5.4), indicating that the DeltaTherm system is very sensitive to relatively small temperature deviations. A convenient approach described by Dreyfus [117] further corroborates this finding. The approach was developed as a coarse rule-of-thumb factor by considering the maxima of Planck's law with respect to the narrow spectral region (as the IR detectors used here). The approach can only be applied for a single wavelength and for the maximum at a single temperature; for the Planck's Law maximum at a temperature of 293 K and a wavelength of 5 μm (i.e. the DeltaTherm) *n* was calculated to be 9.89. As there was only 5.5 % difference between the numerical value and that predicted by the Dreyfus approach this provided confidence in the numerical integration and as such the sensitivity of the DeltaTherm. In real terms the power index of 10.47 is large, i.e. a 1 % variation in temperature would be expected to produce thermoelastic data that is 10.47 % greater or alternatively the thermoelastic data recorded from the ± 45 specimen whilst loaded at 8 ± 6 kN at start of the test would be 20 % lower than that recorded after 28 minutes and would require the corresponding thermoelastic data to be manipulated by a correction factor of 0.8.

There is an appreciable difference between the correction factor predicted by theory here and that offered for the SPATE (Equation (5.1)). As the correction factor provided by Ometron falls so closely to the variation expected by considering the full IR spectrum it is not clear whether the correction factor followed the conceived theorem reported in literature at that time (as discussed). The Dreyfus approach [117] applied to the DeltaTherm parameters is also valid for the SPATE operating range and by a similar method it was repeated for the wavelength of 10 μm. This provided a value of 4.94 for *n* within 5 % of that calculated numerically. Finally the relationship predicted for the photon flux where the power index was calculated to be 3.29 is within 8 % of that shown by the closed form integration.

Table 5.1 shows that the operating wavelength range has a large effect on the extent to which the change in absolute temperature will affect the spectral radiant emittance and in turn the thermoelastic signal produced. Ideally for TSA purposes the index *n* would be as low as possible to reduce the effects of temperature on the thermoelastic signal. However the sensitivity of the InSb detector discussed is of interest in the practical application of TSA and as such the peculiarities of behaviour must be accepted and subsequently quantified in use. In order that these theoretical findings can be compared and validated an experimental validation is required using data collected using the DeltaTherm system, as the lens and window used in the DeltaTherm detector will

attenuate the response, as will the specimen surface emissivity. Furthermore a means for experimental calibration based on the thermoelastic response is highly desirable as it is possible for the DeltaTherm operator to change the detector responsivity to suit the test conditions by adjusting an 'electronic iris'. The development of an experimental methodology may provide some information to the apparent difference between the SPATE theoretical *n* and that reported to provide a temperature correction factor by Ometron.

5.4 Conclusions

Variation in the absolute temperature of the surface investigated by TSA has an effect on the recorded thermoelastic signal. TSA studies have called for a procedure by which the effect of temperature can be quantified and removed. In the past this has not been a concern as with the operating parameters of the early commercial TSA system (SPATE) this effect was often considered negligible. However, the introduction of the DeltaTherm has been shown to magnify the effect of surface temperature to an extent where the thermoelastic measurements do not even have qualitative meaning. The change in sensitivity can be explained by consideration of the operating wavelengths of the IR detectors used by the two devices. The general relationship for Planck's law was derived in Chapter 3 and developed a relationship as a function of temperature. Historically this derivation was assumed to model the characteristics of the IR detector used in a TSA system. However this was not correct as they do not operate over the entire wavelength range. Therefore the purpose of this chapter was to extend this relationship to consider the operating wavelength of the IR devices and how in turn this changes the sensitivity to absolute temperature. A relationship has been developed that provides a power law relationship that can be used as the basis for temperature correction. Results demonstrated that the value of the power law index (and thus the temperature sensitivity) is specific to the operating wavelength range of the detector in use. The results generated compared well with a rule-of-thumb approach providing confidence in the methods. The extent to which temperature has an effect on the recorded thermoelastic signal was shown to be significant and warranted the concerns highlighted during early studies with the DeltaTherm. To ascertain the fit of the theoretical approach to that observed in experimental work the next step will be to derive the index, *n*, experimentally to account for the processing and optics encountered with the practical application of the DeltaTherm, and this is one of the aims of Chapter 6.

Chapter 6

Experimental derivation of the temperature correction parameters

6.1 Introduction

The purpose of this chapter is to define an experimental means to calibrate the relationship between the material temperature and the thermoelastic signal from the DeltaTherm system so that the signal may be corrected to allow for a surface temperature rise. This chapter presents the design of devices for the experimental derivation on the index *n* given in Chapter 5. The methodology for applying the temperature correction factor is devised, so that it can be applied in a full-field point-by-point manner. A validation of the methodology is carried out using artificially heated metallic and FRP components subjected to a constant stress range, hence demonstrating that the stress change can be decoupled from the effects of temperature variations in a typical component.

As discussed temperature variations may be experienced due to a number of different mechanisms during testing because of the practical constraints of the test procedure. Some examples of these are described in the chapter and it is shown that the temperature correction methodology can successfully eliminate the effect of variations in the surface temperature resulting from the test procedure. Finally a damaging composite is

examined and it is shown that applying the methodology reveals details of the stress field resulting from the damage, which would have been otherwise masked by a temperature increase resulting from localised heating at the damage site.

The DeltaTherm system has the advantage that it can collect both thermal and thermoelastic data simultaneously. This means that the absolute temperature given in Equations (5.4) can be measured at the same time as collecting the thermoelastic data and hence provides the basis for a full-field point-by-point temperature correction methodology that may be implemented automatically within the TSA system software. However, a complication is that the DeltaTherm system is not radiometrically calibrated, as the expectation in TSA is to derive a calibration constant either A or A^* experimentally [22, 93] and therefore a value of ΔT is not required. In order that T may be obtained in Kelvin the devices designed for obtaining the temperature correction are also used to calibrate the DeltaTherm thermal data. It should be emphasised at this stage that even if a system were to be available where calibrated temperature values could be obtained, Equation (5.4) remains valid so temperature correction is still necessary.

6.2 Experimental derivation of index *n*

It is possible to derive the temperature correction parameters, n and B see Equation (5.3), experimentally using a device that allows controlled temperature variations whilst experiencing cyclic stress. In previous work [119] such a calibration device was designed and some initial work was carried out to obtain the index n. The calibration device comprised an aluminium alloy cylinder, closed at either end with end caps (see Figure 6.1). The calibration device was a 101.6 mm diameter aluminium alloy cylinder tube with a wall thickness of 3 mm and a length of 200 mm. The cylinder housed an immersed heating element that was located at the base of the cylinder and could be controlled to raise the temperature of the water contained within the cylinder. To ensure adequate heat distribution within the cylinder, heat distribution was aided with a mechanically driven stirrer that promotes an even thermal distribution. The cylinder was loaded within the elastic region of the aluminium alloy using two ball bearings to maintain a uniaxial stress in the cylinder. The temperature of the free surface of the device was monitored using a single thermocouple, which was permanently attached to the cylinder. In this chapter the initial work carried out in [119] is revisited and n and B obtained over a much wider range of test variables.

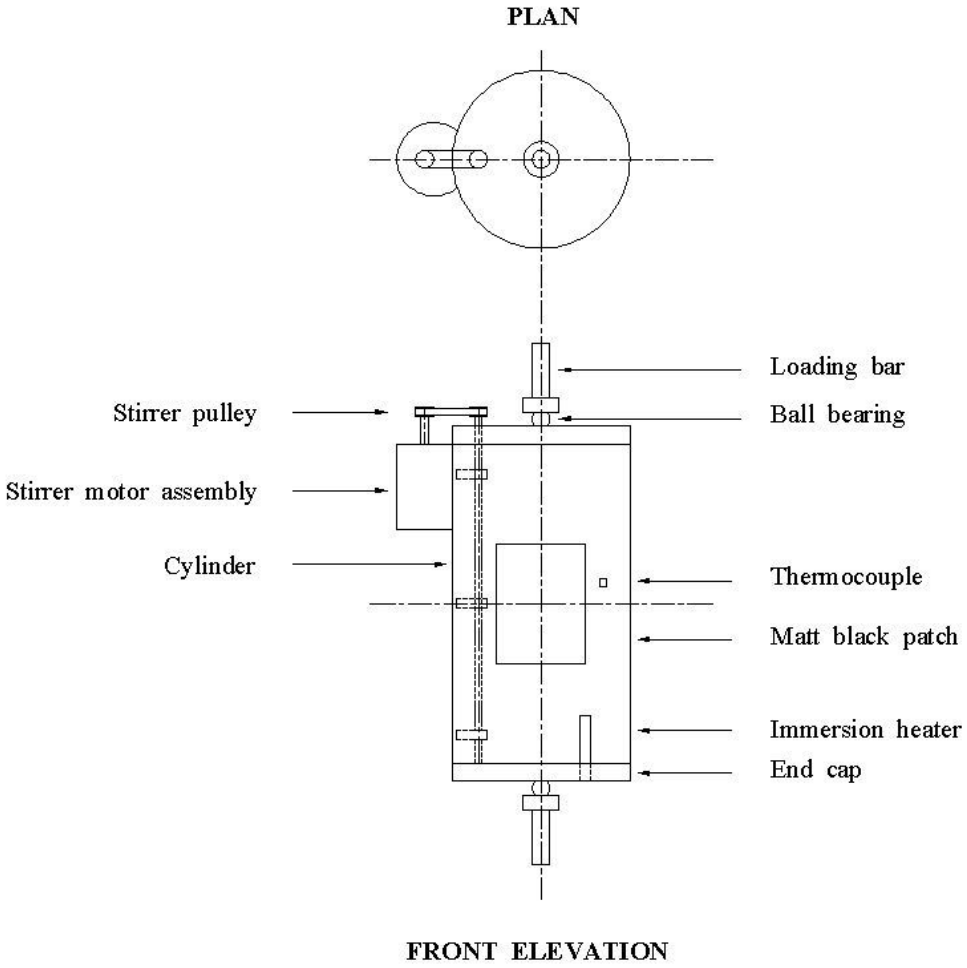

Figure 6.1. Calibration device.

To assess the effect of a change in material a further calibration device is also used in the current work: a FRP cylinder of identical dimensions to the aluminium alloy cylinder. The test procedure and loading levels were identical to that for the aluminium alloy device except the heating was achieved by pouring hot water into the cylinder and allowing the water to cool. As the FRP material was a good insulator, this approach allowed sufficient time to collect data in a controlled manner as the water cooled naturally. The aluminium alloy device was coated with two passes of Radio Spares matt black paint; the FRP device was not coated as the material has a high emissivity. As neither of the devices have an emissivity of unity, it is necessary to rewrite Equation (5.27) as follows:

$$N_\lambda = \eta B T^n \tag{6.1}$$

where η denotes the emissivity.

Differentiating Equation (6.1) with respect to T gives an expression for ΔT in terms of the photon count:

$$\Delta T = \frac{\Delta N_\lambda}{nBT^{n-1}\eta} \tag{6.2}$$

and assuming that the thermoelastic signal, S, is linearly related to ΔN_λ so that $S = Z\,\Delta N_\lambda$, where Z is detector response factor, the following relationship between ΔT and S is obtained as:

$$\Delta T = \frac{S}{nBZT^{n-1}\eta} \tag{6.3}$$

Substituting the above expression into Equation (3.44) gives:

$$\Delta(\sigma_1 + \sigma_2) = \left(\frac{1}{nBZT^{n-1}}\right)\left(\frac{1}{T\eta K}\right)S \tag{6.4}$$

where the first bracketed term on the right hand side of the equation is the detector responsivity [21].

Now it is possible to manipulate Equation (6.4) to derive n from the thermoelastic signal from a given detector. If $\Delta(\sigma_1 + \sigma_2)$, η and K are constant, i.e. for a test specimen subject to the same stress, then $\Delta(\sigma_1 + \sigma_2)(KnB\eta Z)$ can be defined as a constant, H, so that:

$$S = HT^n \tag{6.5}$$

The two calibration devices were used to compare values from different materials and surfaces. H is dependent on stress and material as well as surface condition therefore this will be different for the two specimens; however the index n is independent of specimen material and stress. To evaluate n a series of tests were carried out on each specimen over a range of temperatures (see Table 6.1). The different temperature ranges were chosen to assess repeatability. The temperature was changed in 0.5 K increments for the Duralumin specimen and in 2 K increments for the FRP specimen. Thermoelastic data was collected with two DeltaTherm systems (DeltaTherm 1000 (DT1000) and DeltaTherm 1400 (DT1400)); both systems were fitted with practically identical 25 mm IR lenses. The stress level was kept the same for all tests at 66.7 MPa. The loading

frequency was set to 10 Hz. The pixel integration time (electronic iris) that dictates the responsivity of the system was set so that the same value was used in all the tests. Thermoelastic data was averaged along the vertical centre line of the cylinder and ln$S$ plotted against ln$T$; five plots were obtained for each detector. The quantity n was derived from the slope of the plot and ln$H$ from the intercept (as illustrated by Figure 6.2); these are given in Table 6.1 along with the correlation coefficient.

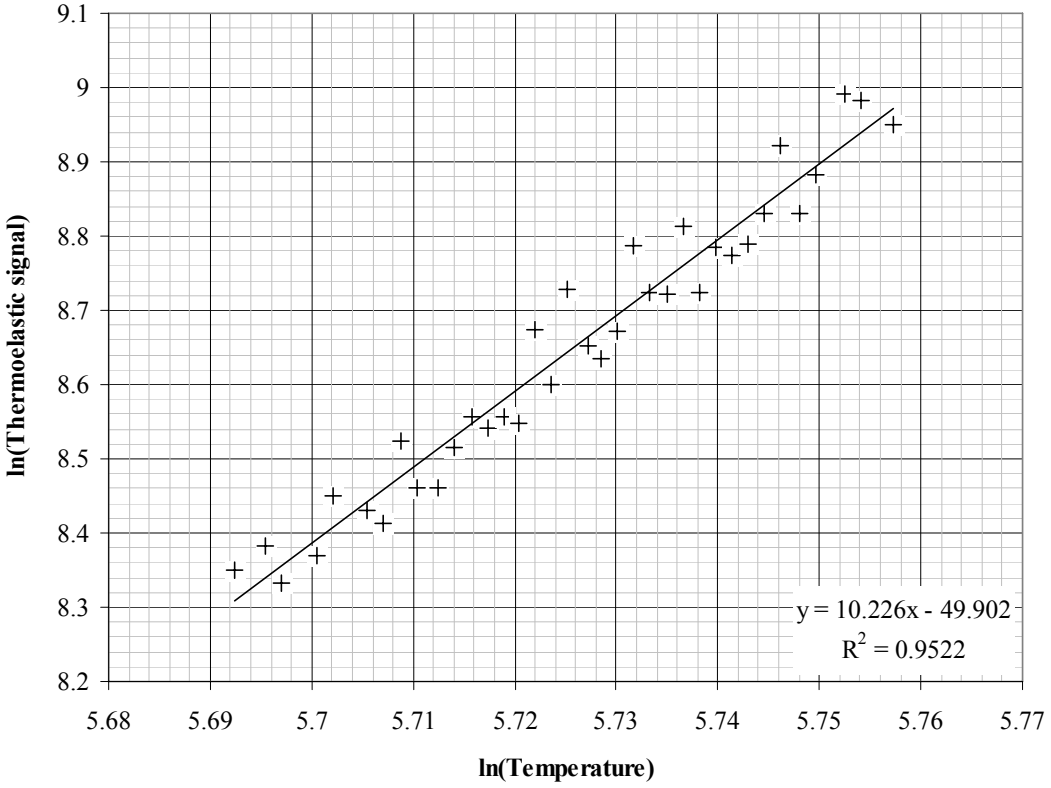

Figure 6.2. Sample experimental data plot

The value of n varied between 9.0 and 10.3 for the DT1000 and had an average value of 9.5 ± 4.9%. The value of n for the DT1400 varied between 9.4 and 10.2 and had an average value of 9.8 ± 3.9%. This clearly indicates that, as the detectors are both InSb and therefore operating in the same wavelength range, n is dependent only on detector operating wavelength and also that n is independent of the temperature ranges that would be used in practice. The value of n is less than that provided by the numerical study in Chapter 5. The reason for this is the optical system used in the DeltaTherm camera head. The average value of ln$H$ is -47.5 ± 5.7% and - 47.7 ± 4.8% for the DT1000 and DT1400 respectively. To check the dependence on frequency some tests were carried out at 5, 15 and 20 Hz; the results from these tests are also given in Table 6.1. There is very little difference between the values obtained for different loading frequencies, demonstrating that n is independent of the loading frequency. It is

noteworthy that the linear correlation coefficient (C.C.) for each plot was never less than 0.87. The value of *n* will be dependent on the electronic iris setting, as this changes the detector responsivity, and also on the optics used as different lens systems will affect the photon intensity.

Table 6.1. Derivation of index *n* for DeltaTherm system

Material	System	Temperature range (K)	Frequency (Hz)	*n*	ln*H*	C.C
Duralumin	DT1000	293 - 313	10	9.6	-48.0	0.91
Duralumin	DT1000	300 - 307	10	9.3	-46.3	0.93
GFRP	DT1000	293 - 330	10	10.3	-51.7	0.87
GFRP	DT1000	299 - 315	10	9.0	-44.3	0.98
GFRP	DT1000	289 - 327	10	9.5	-47.4	0.96
Duralumin	DT1400	295 - 308	10	9.4	-45.2	0.97
Duralumin	DT1400	295 - 317	10	10.2	-49.9	0.95
Duralumin	DT1400	294 - 320	10	9.8	-47.5	0.99
Duralumin	DT1400	294 - 328	10	10.2	-50.2	0.99
Duralumin	DT1400	295 - 317	10	9.5	-45.8	0.99
GFRP	DT1000	299 - 315	5	9.4	-46.7	0.99
GFRP	DT1000	293 - 330	5	9.5	-47.0	0.99
GFRP	DT1000	293 - 330	15	9.6	-47.8	0.99
Duralumin	DT1000	293 - 313	15	10.2	-52.2	0.99
GFRP	DT1000	299 - 315	20	9.3	-46.3	0.96

Archived data obtained by from Quinn [90] means it is also possible to compare the theoretical value obtained in Chapter 5 for the SPATE operating parameters with experimental data. This data was collected during a baseline evaluation between the newly introduced DeltaTherm and the SPATE system [90], and thermoelastic data was recorded to ascertain the comparative effect of temperature on the two systems. Thermoelastic data was recorded from a mild steel cylinder and the absolute surface temperature was measured from a surface mounted thermocouple. The temperature variation observed was as a result of variation in the ambient laboratory temperature alone. The raw data from the testing has been obtained and collated in a similar manner to that presented above. The value of *n* generated is listed in Table 6.2 for two sets of data, it should be noted the absolute temperature range is not as extensive as those encountered with the DeltaTherm set-up and a variation of 6 K and 4 K was recorded. The values of n_{SPATE} calculated were 5.1 and 4.0 and gave an average value of 4.55 ± 17.1 %. There is a larger scatter due to the smaller data set from which the plot and hence n_{SPATE} is extrapolated.

Table 6.2. Derivation of index n_{SPATE} for SPATE system

Material	System	Temperature range (K)	Frequency (Hz)	n_{SPATE}	ln$H$	C.C
Mild steel	SPATE	294 – 300	10	5.1	-23.4	0.96
Mild steel	SPATE	299 - 303	10	4.0	-17.0	0.96

The numerically obtained value for n_{SPATE} presented in Chapter 5 of 4.7 is in good agreement with the average of the experimentally derived value and provides a useful verification of the methods developed. The close agreement would also indicate that the power law presented in Section 5.3 is valid for the SPATE system which operates in the region of λ_{max} at room temperature. In the work presented by Fulton the correction factor power index provided by Ometron for the SPATE system was indicated to have a value of three. There is a difference of 33 % between the average experimental value of n_{SPATE} obtained from Quinn's data and the manufacturer's correction factor. This difference provides some explanation as to why work with SPATE [110] demonstrated that the manufacturer's calibration curve did not completely compensate for increases in surface temperature.

6.3 Calibration of thermal data

As described in the introduction, to obtain temperature values from the recorded DeltaTherm thermal data, a calibration procedure is required. The calibration was achieved in a similar manner to the procedure used to obtain n from the thermoelastic data using the devices described in the previous section. In this case the temperature is plotted against the DeltaTherm thermal reading to give a curve of the type shown in Figure 6.3, recorded from the FRP specimen using the DT1000 with an iris setting of 22 %. A 5^{th} order polynomial was fitted to the thermal data to provide a mathematical relationship between the thermal data and the temperature. The data had little scatter, the fifth order polynomial created by the line of best fit is given in Figure 6.3 had a correlation coefficient of 0.998. It should be noted that this curve is dependent on the material emissivity and is specific to the electronic iris setting of the system.

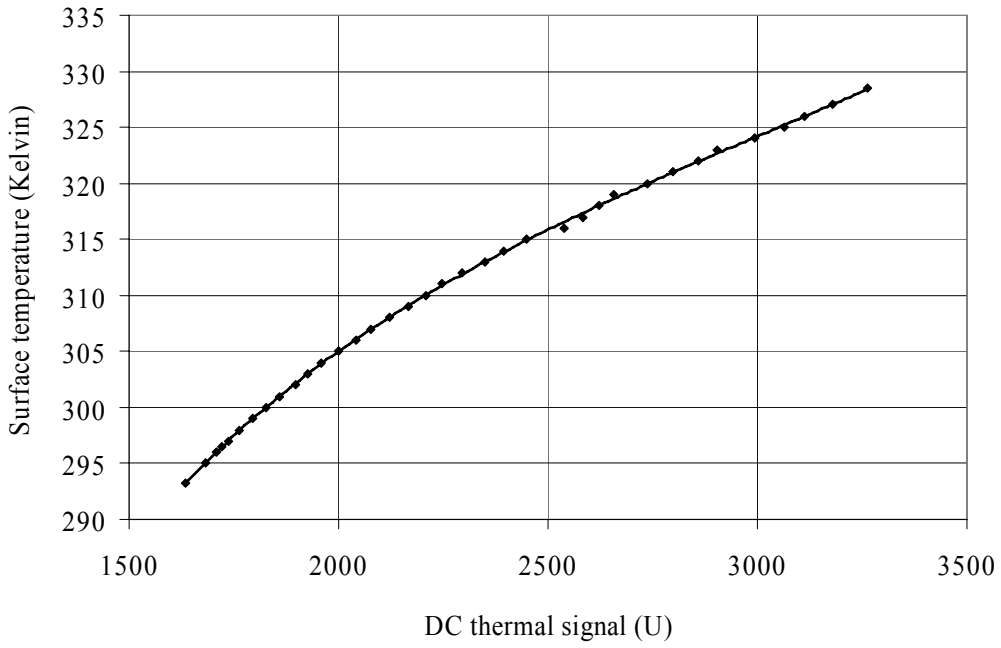

Figure 6.3. Surface temperature against uncalibrated DeltaTherm thermal data

In order to verify the calibration process, thermal data was captured at known temperature levels from a FRP coupon specimen. The coupon was heated from room temperature to 328 K with a hot air gun. Thermal data recorded was subsequently manipulated by the calibration polynomial which allowed a comparison against the known temperature. Figure 6.4 shows a plot of readings from a thermocouple against calibrated DeltaTherm thermal data, recorded with the DT1000 system at an iris setting of 22 %. The plot in Figure 6.4 shows that there is excellent agreement (the slope of the line is 0.98) between the readings from the thermocouple and the calibrated DeltaTherm thermal data demonstrating that this approach is valid for temperature calibration. The use of a thermocouple in this manner enables a validation of the thermal calibration process but is limited to a single point interrogation of the surface temperature and is accurate only to the ± 1 K specified by the thermocouple.

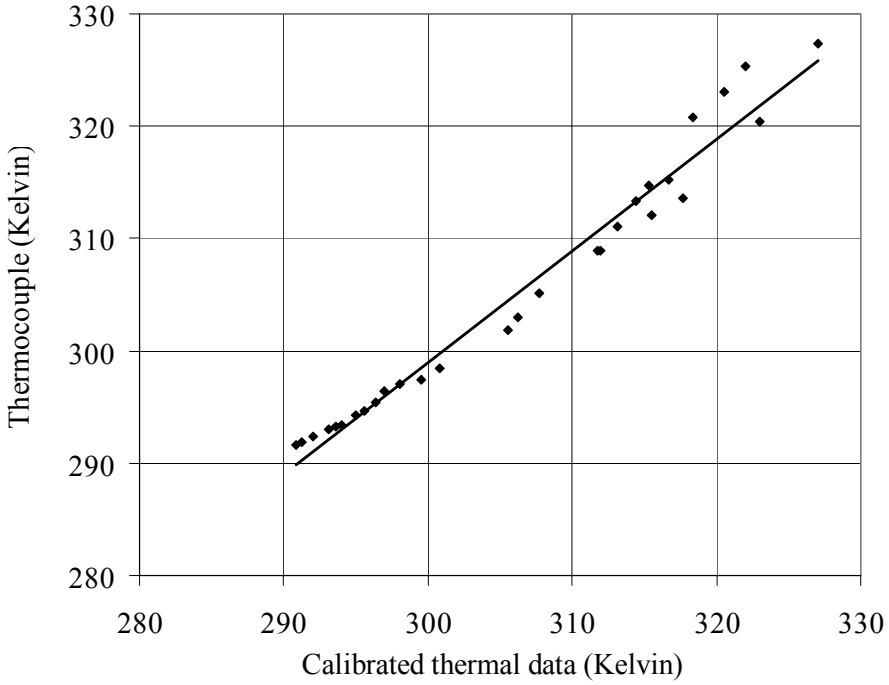

Figure 6.4. Comparison of single point thermocouple and calibrated thermal data

To validate the thermal calibration routine in a full-field manner the results from the DeltaTherm system were compared with results from a calibrated FLIR full-field IR thermography system, as used in Chapter 5. The full-field temperature calibration was carried out using a MATLAB code (Appendix C.4). In these tests, the surface temperature of a specimen was recorded using FLIR and the thermal data with the DeltaTherm equipment operated side by side. The test specimen was an aluminium alloy strip that was heated using a hot air gun. Figure 6.5 shows the temperature profile obtained along the centre line of the specimen for four temperature increments from the FLIR system and calibrated DeltaTherm thermal data. Comparison of the thermal data, in Figure 6.5, shows the full-field capability of the calibration routine. A direct comparison of a single point temperature reading from both systems is given in Figure 6.6 with the FLIR temperature reading plotted against the DeltaTherm reading over a range of 308 K to 321 K. There is almost exact agreement between the two systems with the linear correlation coefficient of the plot given as 0.99. As the thermal data is dependent on the DeltaTherm electronic iris setting, a library of polynomial equations (tabulated in Appendix B.2) has been created for the various operating settings and used appropriately in the following sections.

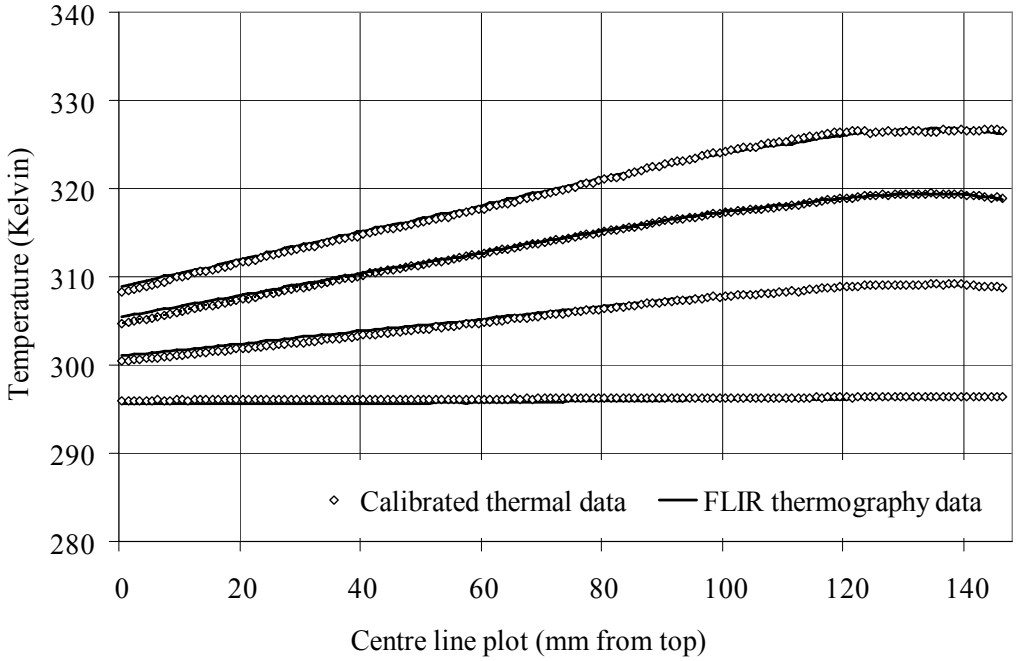

Figure 6.5. Comparison of full-field calibrated thermal and thermography

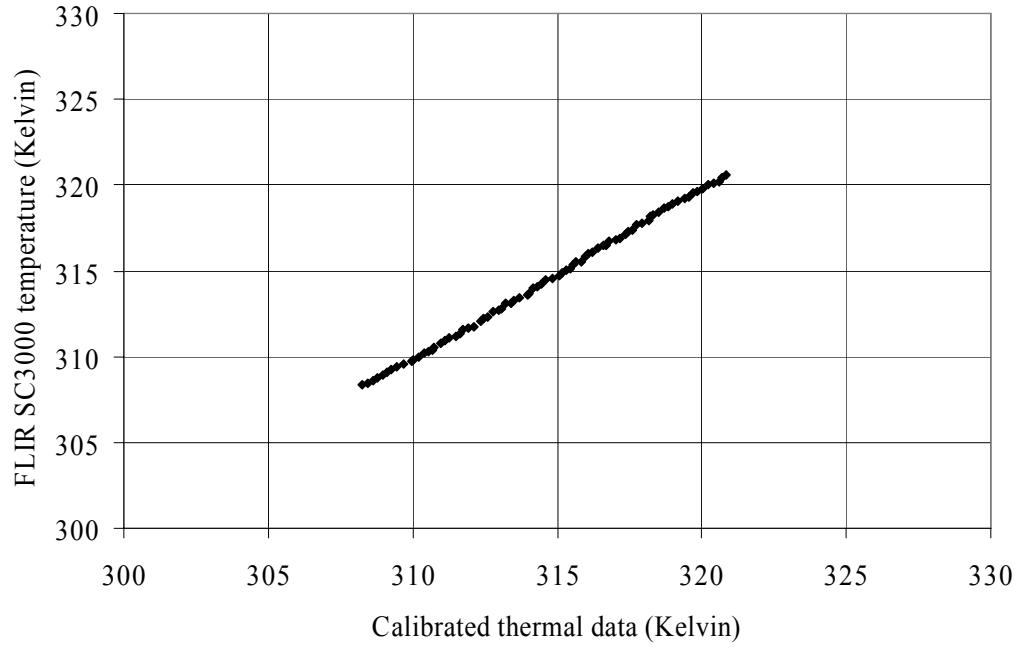

Figure 6.6. Relationship between single point calibrated thermal and thermography data

6.4 Temperature correction methodology

A means for temperature correcting the thermoelastic signal for increases in temperature has been devised. To implement this on full-field data it is necessary to create an algorithm to manipulate the data. This was done using MATLAB; a schematic of the

procedure is shown in Figure 6.7. The full-field nature of the data was retained, as the procedure processed the thermoelastic signal data set point-by-point. It should be noted that the corresponding thermal signal for each data point was obtained simultaneously by the system and calibrated to give an array of surface temperatures. At the start of a test series an initial data set is captured to provide thermoelastic data S_0, at a given temperature T_0 as shown in Figure 6.7. After a number of cycles more data is captured to give the modified thermoelastic signal field, S_m at the corresponding temperature field, T_m. The initial and modified thermal data are combined with the index n to give the correction factor R for each pixel in the array. Each element of the array of modified thermoelastic data, S_m, is then multiplied by the R value for the element to give the corrected thermoelastic signal S_c.

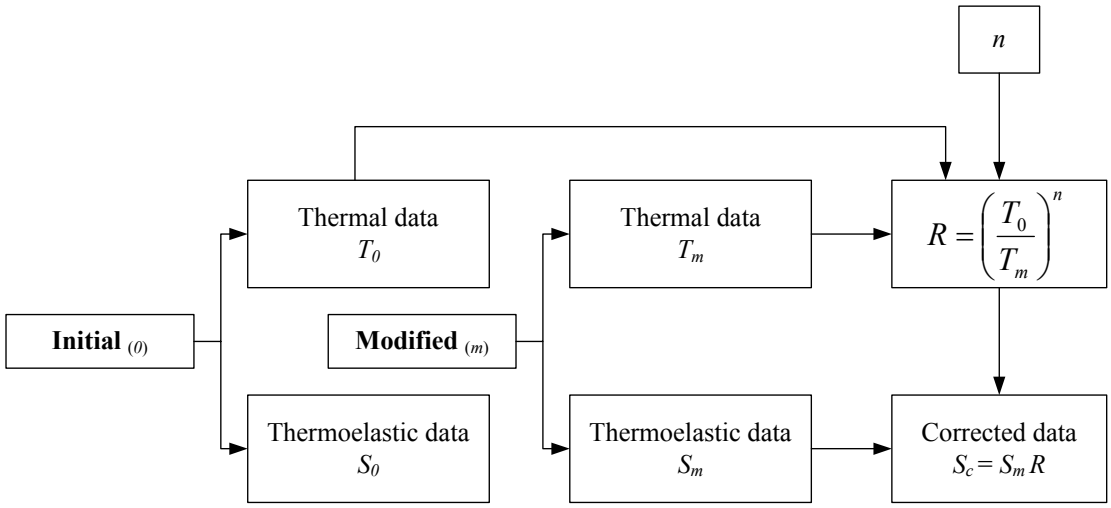

Figure 6.7. Schematic of temperature correction methodology

The processing algorithm was designed to take the data recorded by the DeltaTherm 1000 and 1400 and manipulate it to produce data that could be viewed and analysed through Deltavision, the software designed for the DeltaTherm system. Therefore the MATLAB process was designed to extract the required thermal and thermoelastic data from initial and modified data sets from Deltavision simple ASCII text files. Each data point was processed individually to give corrected data specific to the thermal and thermoelastic signal recorded at that data point (Appendix C.5). Post correction the software header and footer (Appendix C.1) was applied to the corrected data set so that it could be reformatted and viewed in the Deltavision software in an identical manner to the collected data, enabling a direct comparison between the three data sets.

6.5 Validation of temperature correction procedure

In this section two examples are described that illustrate instances where the test specimen or structure heats. The examples are such that they illustrate a global heating of the specimen and a localised heating of the specimen (both tests are carried out in load control so any heating of the specimen had no effect on the applied stress). The temperature change is corrected using the procedure described above and hence the procedure is validated.

In a non-climate controlled laboratory variations of 10 K or so may be experienced day-to-day as illustrated in Chapter 5. To simulate these conditions, a hot air gun was used to artificially heat the aluminium alloy strip used in the previous test. For comparative purposes the aluminium strip was cyclically loaded at a constant stress level throughout this test. Initial thermoelastic data (i.e. S_0) was captured with the strip at the laboratory temperature of 297 K, as shown in Figure 6.8. Subsequently and with no change to the experimental set-up the temperature of the strip was raised with a hot air gun to 309 K. At this elevated temperature the strip was allowed to stabilise and further thermoelastic data was captured, i.e. the S_m image in Figure 6.8. The data was then manipulated to give the corrected plot S_c which corresponds well with the original data. It can be seen in the S_m plot that the heating method resulted in a nonlinear temperature profile along the length of the specimen; however the full-field nature of the correction process eliminated this from the corrected data, S_c. To assess the accuracy of the process thermoelastic data was recorded from the vertical centre-line of the three images in Figure 6.8 and is shown in Figure 6.9, providing a direct comparison of the data-sets. Data from S_c although not equal to S_0 lies well within a 5% range which is considered as an acceptable experimental error.

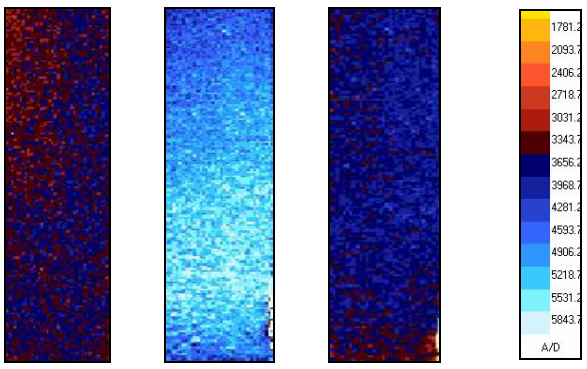

a) S_0 b) S_m c) S_c Scale (U)

Figure 6.8. Signal from heated aluminium specimen

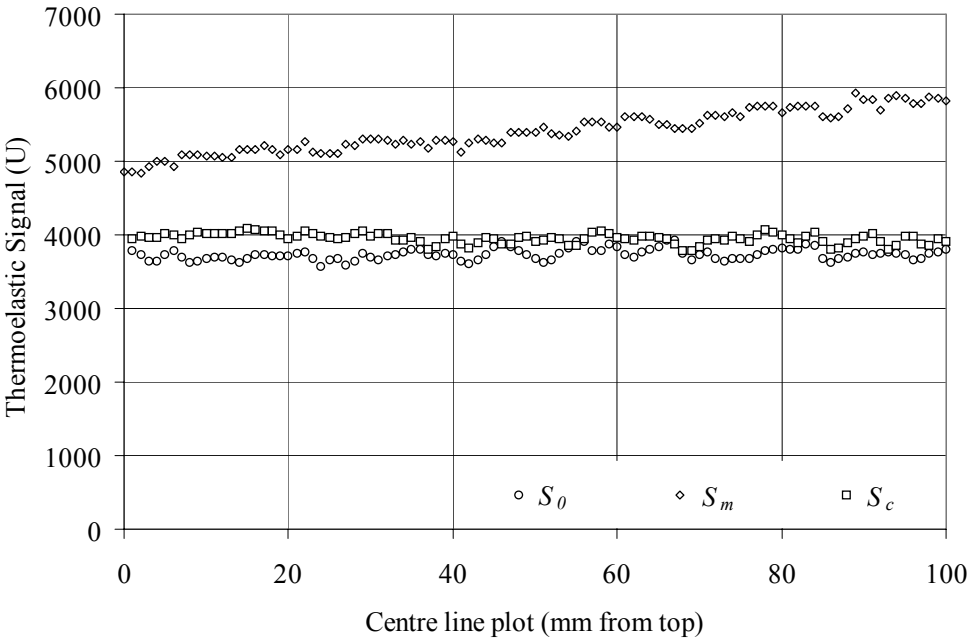

Figure 6.9. Line plot of corrected and uncorrected thermoelastic data.

The main purpose of the current work is to deal with localised heating as a result of the viscoelastic heating of a damaged composite specimen. The low thermal conductivity of reinforced polymers exacerbates the situation. To simulate a localised temperature rise the aluminium alloy coupon was loaded at 5 ± 3 kN with a constant cyclic stress. An electrical resistance heater patch was fixed to the rear of the coupon and provided a heat source to a small area of the coupon. The heat conducted to the front surface, which was observed by the DeltaTherm system. The recorded maximum temperature increase was 10 K. Figure 6.10 shows the sequence of S_0, S_m and S_c thermoelastic data. The S_c image shows the corrected data which has effectively reduced the effect of the thermal influence on the signal localised around the heater pad position. A line plot of the three data sets along the vertical centre line of the specimen is shown in Figure 6.11. The 10 K increase in temperature at the heater pad increases the thermoelastic signal by a factor of 50%. The correction procedure removes this and the plot shows S_c and S_0 data are in excellent agreement.

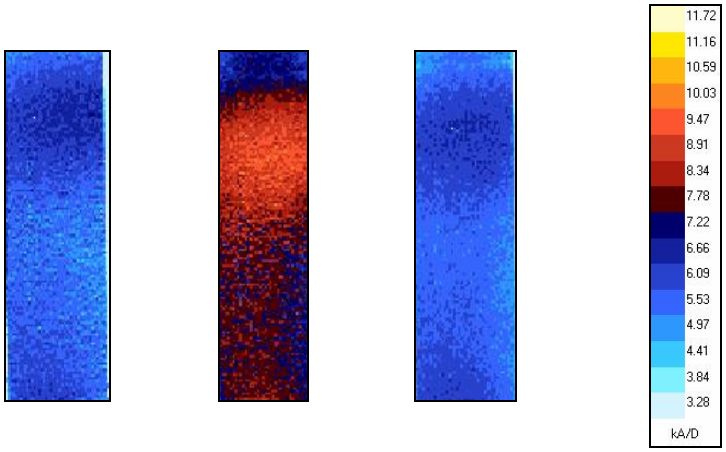

a) S_0 b) S_m c) S_c Scale (U)

Figure 6.10. Signal from aluminium specimen with localised heating

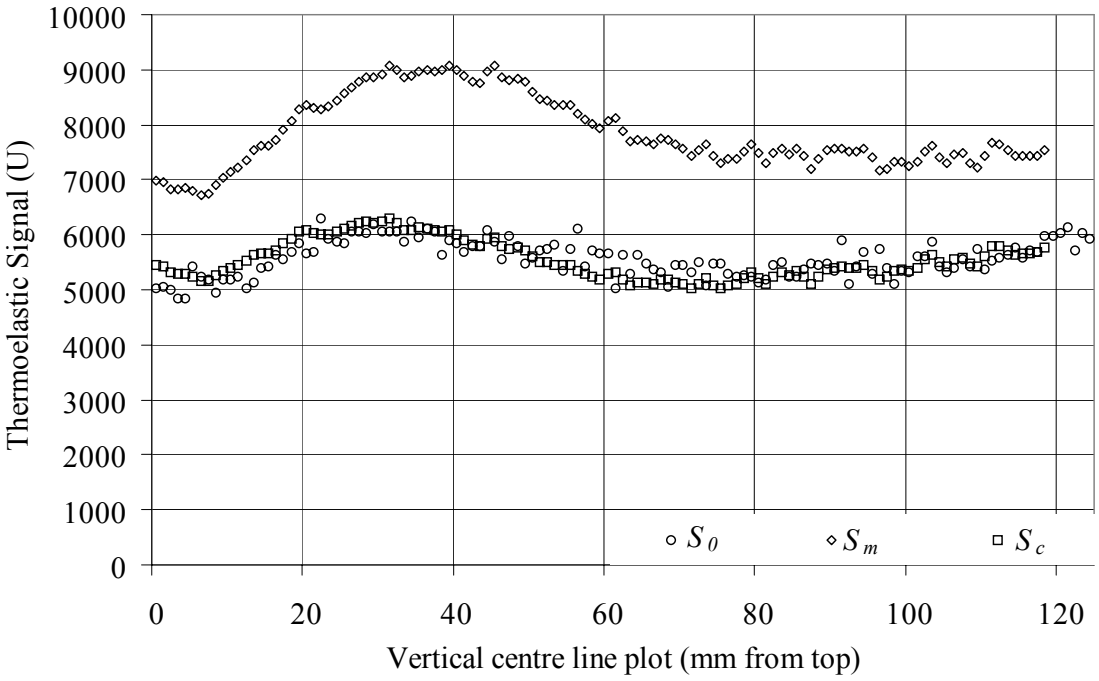

Figure 6.11. Line plot of corrected and uncorrected thermoelastic data

The above examples demonstrate how the thermoelastic data may be affected by thermal influences. The data is manipulated by the correction process to give S_c in each case, which returns to the initial level after correction. This demonstrates that any change in temperature can be decoupled from the effect of the stress change in the measured thermoelastic signal using the temperature correction methodology.

6.6 Practical applications of the temperature correction procedure

One of the governing assumptions for TSA is that all tests are carried out under adiabatic conditions [23]. In the majority of testing this necessitates the use of a servo-hydraulic test machine capable of cyclically loading a component. Prolonged use of such test equipment generates a substantial heat source due to the movement of the actuating hydraulic oil. A portion of this generated heat is dissipated by conduction to the gripping mechanism of the test machine, transferring heat to the specimen and raising its surface temperature. This is demonstrated by a simple test where a strip of aluminium alloy material was cyclically loaded under uniaxial tension in an Instron servo-hydraulic test machine. A full-field image of the thermoelastic signal at the start of the test is shown in Figure 6.12 as S_0. The specimen was cycled for approximately 5 hours and another image taken (see Figure 6.12), i.e. S_m. A non-uniform increase in temperature was experienced with the maximum increase of 5.5 K in the lower portion of the specimen nearest the actuating grip; this is mirrored in the thermoelastic data with the increase in the component surface temperature increasing the thermoelastic signal by 17%. The final image in Figure 6.12 is S_c, the corrected image, where it can be seen that the data is practically identical to that of the data at the start of the tests. A line plot along the centre line of the tensile strip was taken for each of the data sets shown in Figure 6.12 and given in Figure 6.13. The gradient in the S_m data is clearly shown and it can be seen that the signal has increased markedly. The correction routine removes the gradient and returns the signal to virtually the same magnitude as that obtained at the start of testing. Application of the temperature correction procedure in this context will be particularly important when monitoring long-term fatigue tests.

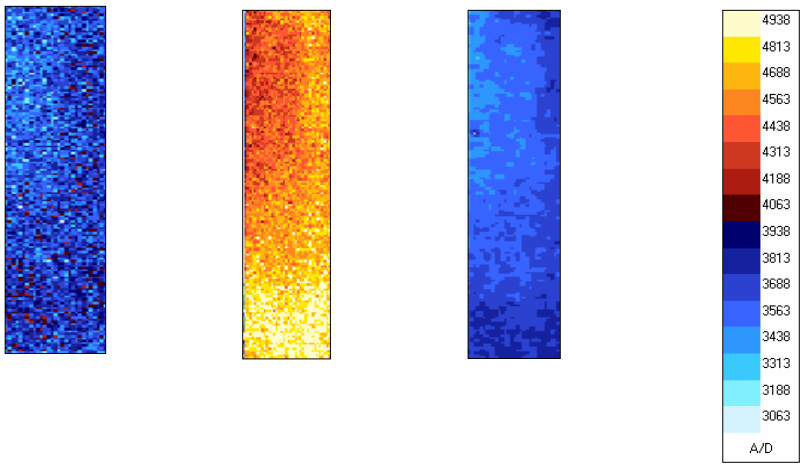

a) S_0 b) S_m c) S_c Scale (U)

Figure 6.12. Effect of thermal conduction from test machine on thermoelastic

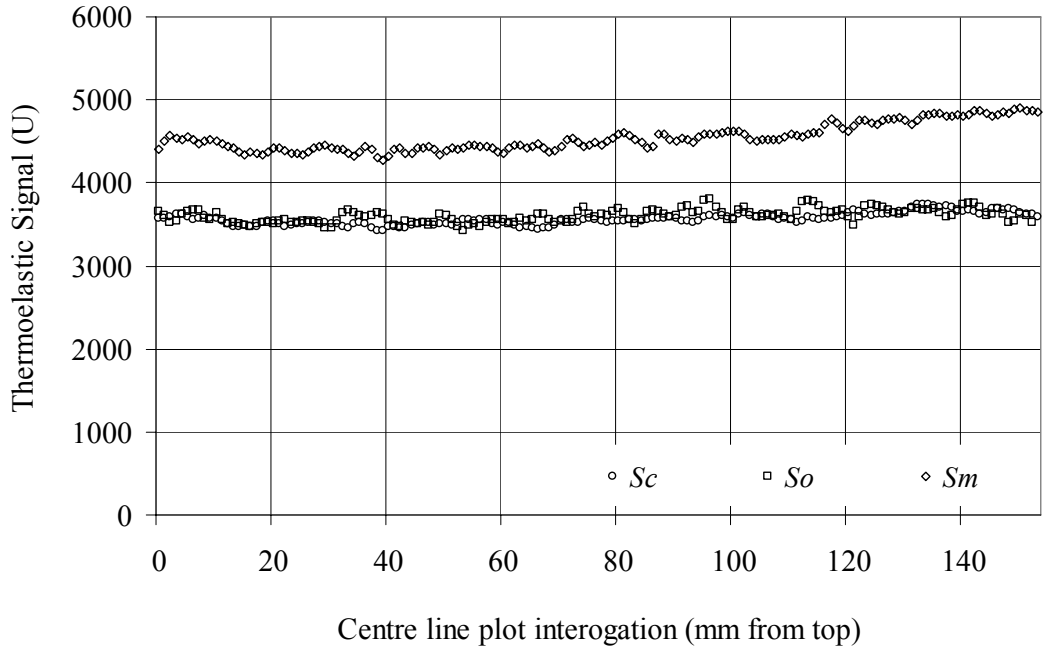

Figure 6.13. Line plot of corrected and uncorrected thermoelastic data

A further typical practical scenario occurs as a result of an inexperienced operator handling a low thermal conductivity material, such as a FRP. Figure 6.14 shows thermoelastic data from a FRP strip loaded in tension; the image to the left was taken five minutes after mounting the specimen in the test machine. While the increase in signal could be analysed as an area of a high stress area, inspection of the thermal image, shown in Figure 6.15, revealed a local temperature 'hot spot' at the corresponding position. The localised temperature increase was as a result of heat transfer from the operator's hand. This is illustrated clearly in Figure 6.15 where a calibrated thermal image is shown and it can be seen that the temperature increases locally by around 3 K. Therefore the initial image has already been 'modified' and is denoted, S_m in Figure 6.14. The low thermal conductivity of the material means that the temperature gradient remained for the entire test time. Instead of disregarding the data and repeating the test it was decided to apply the correction procedure. To do this it is necessary to obtain T_0. Therefore a point away from the influence of the operator's thermal input was chosen, as shown in Figure 6.15. This value was then used to create an artificial data set of constant thermal value which was then used as the baseline temperature input into the MATLAB correction program (Appendix C.5). This data-set can then be introduced as T_0 into the correction process. Figure 6.14 shows the corrected thermoelastic image, S_c, with the signal peak caused by the thermal input removed.

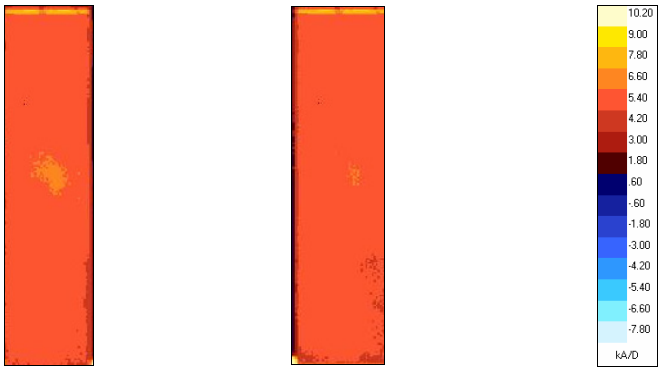

a) S_m b) S_c Scale (U)

Figure 6.14. Effect of localised temperature increase on signal

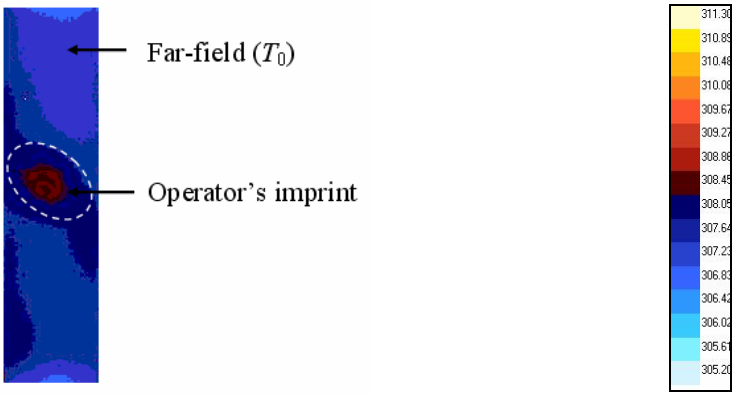

a) Temperature profile Scale (Kelvin)

Figure 6.15. Calibrated thermal data showing localised heating from operator's hand

A similar situation to the above arises if a strain gauge mounted on a specimen for calibration purposes. There will be a local heating when the gauge is excited and if the specimen is made from FRP the low thermal conductivity prevents the heat from dissipating and causes a localised increase in temperature in the neighbourhood of the gauge [36]. The temperature correction methodology could also be applied in these situations.

The two examples shown above clearly demonstrate that even in standard tests it may well be necessary to apply the temperature correction routine if accurate data is required for quantitative stress analysis. The two examples also illustrate the effectiveness of the correction routine.

6.7 Application to damaging FRP component

The work described in the two previous sections has shown that any change in the thermoelastic data resulting from a thermal input can be corrected for using the temperature correction procedure. The overall goal of this work is to be able to apply TSA to damaging composite components to identify the redistribution of the stress field caused by damage evolution. In this section the localised heating of a FRP specimen at a damage site is studied and the effect of temperature increase is decoupled from that of the stress changes. A UD specimen was manufactured in an identical manner to that described in Chapter 4 (and presented in Appendix A). An 8mm circular hole was introduced into the centre of the component (see Figure 6.16). The was cyclically loaded at 10 ± 4 kN in an Instron servo-hydraulic test machine. Initial thermal, T_0, and thermoelastic, S_0, data using the DeltaTherm 1000, at the same load and at 10 Hz, were collected from the vicinity of the central hole before the loading was increased to 10 ± 8 kN so that damage was initiated as cracks emanating from the hole in the direction of the fibres (see dotted lines on Figure 6.16). The load level was maintained whilst the crack propagated through the thickness of the laminate and grew vertically above and below the hole. The crack initiation and growth provided both a stress change and a heat source. Heat was generated locally at the damage site due to frictional heating at the newly created crack faces. The loading was reduced to the initial level and again the thermal, T_m, and thermoelastic, S_m, data were again recorded. The stress in the coupon was redistributed due to the damage transferring the stress to the undamaged portion of the coupon.

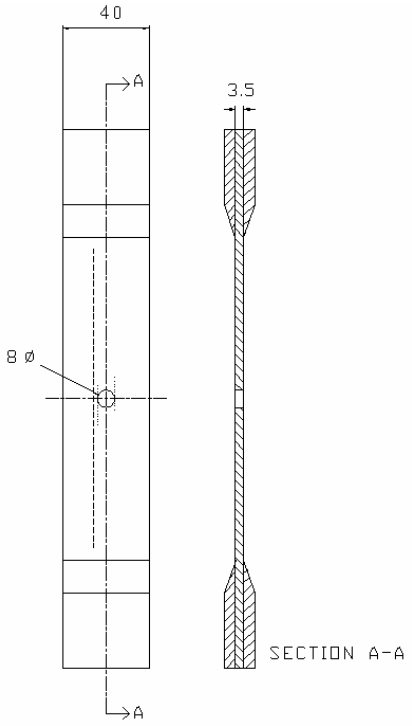

Figure 6.16. UD FRP test coupon

The sequence of S_0, S_m and S_c thermoelastic data are shown in Figure 6.17 and the corresponding thermal data for T_0 and T_m in Figure 6.18. At the damage site the temperature rise of 3 K is evident through the comparison of T_0 and T_m in Figure 6.18. The effect of the thermal increase is evident in the data plots in Figure 6.19 (data interrogation lines taken along the dashed line as shown on Figure 6.16), the maximum signal reduced by 10 % after correction. Uncovering this 10 % reduction would enable a quantitative analysis and prevent a conservative design. The change in stress profile and the residual difference from the corrected thermoelastic data, S_c, and S_0 can be attributed to the change in the stress field caused only by the redistribution of stress around the damaged areas.

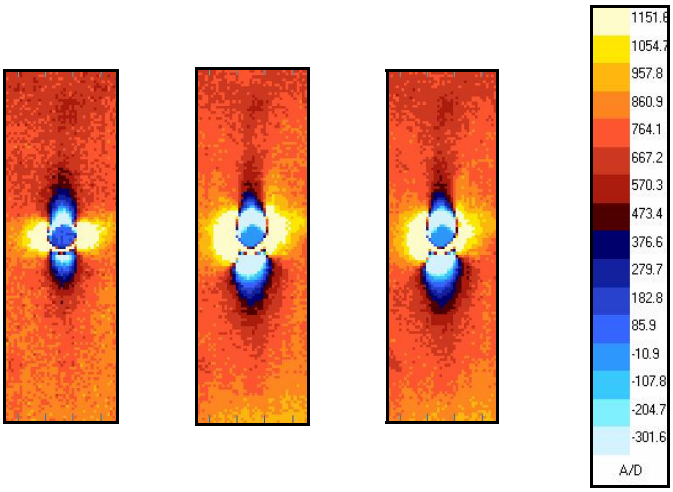

a) S_0 b) S_m c) S_c Scale (U)

Figure 6.17. Thermoelastic data from damaging FRP coupon

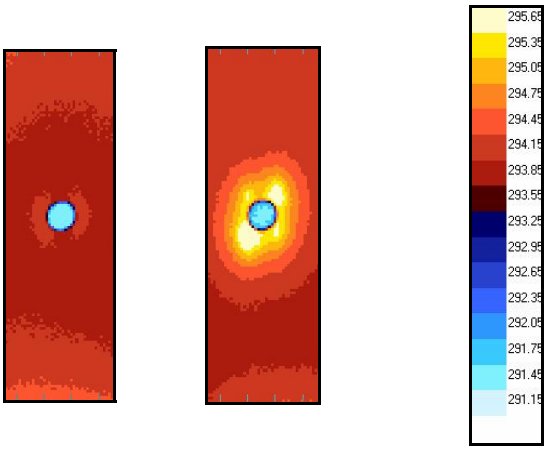

a) S_m b) S_c Scale (Kelvin)

Figure 6.18. Thermal data from damaging FRP coupon

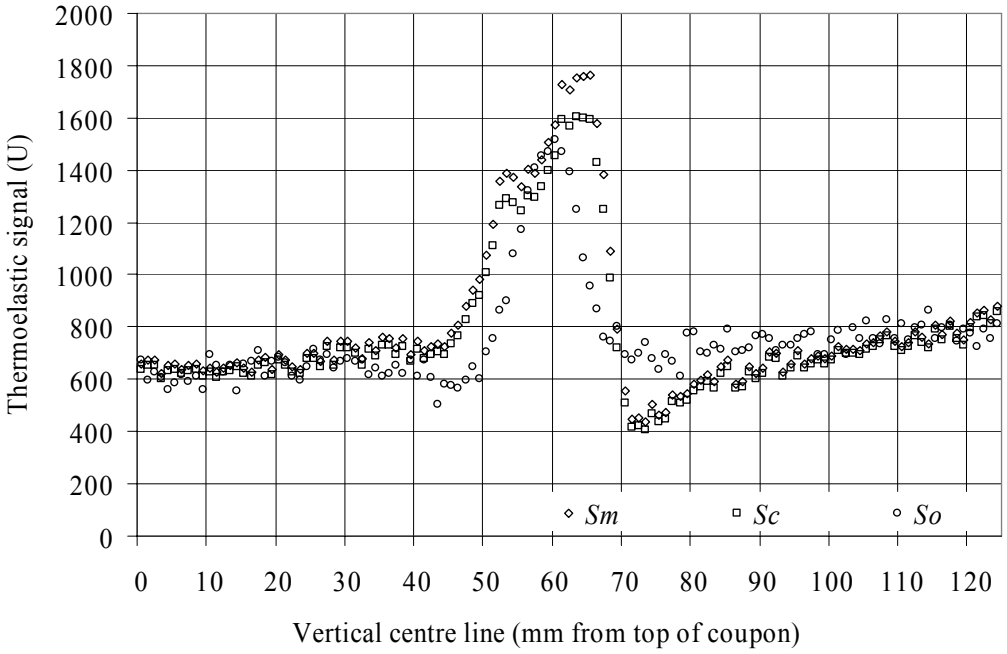

Figure 6.19. Comparison of corrected and uncorrected data from damaging FRP coupon

6.8 Conclusions

A correction process is presented by which surface temperature variations due to localised heating may be understood, quantified and eliminated. Following the theoretical development of the methodology in Chapter 5 an experimental verification is presented in this chapter. This has been possible using a device and a test procedure that have been designed to provide values of the power law index *n*. The comparison of the theoretical and experimental values derived showed a good correspondence.

To enable the correction factor to be applied in practice surface temperatures must be obtained simultaneously with the thermoelastic signal, a routine to calibrate the thermal data obtained from the DeltaTherm system was devised; this was validated successfully against both thermocouple and calibrated full-field temperature data.

A correction process algorithm was designed that incorporated the correction factor into a process that enabled a point-by-point full-field manipulation of the thermoelastic data by applying the correction factor function at each pixel.

The correction process was validated using aluminium specimens subject to an artificial temperature increase whilst experiencing a constant cyclic stress, and the effect of the artificial temperature rise was eliminated by the correction procedure. It has also been

demonstrated that the procedure can be used to eliminate errors due to temperature rise that can be expected during standard testing.

The application of the procedure has been demonstrated on a damaging composite coupon, where temperature changes were evident in the neighbourhood of the damage site, permitting the data to reveal the thermoelastic signal resulting from the stress redistribution caused by the damage.

The development of a temperature correction methodology provides confidence that localised heating may be understood, quantified and eliminated during the analysis of the thermoelastic data presented in this thesis. It must be anticipated that localised temperature variation and the resultant influence on the thermoelastic signal will be prevalent during the fatigue of FRP composite laminates. The relevance of the temperature correction procedure and the results presented have wide application for TSA using the DeltaTherm in situations other than where the absolute surface temperature can be guaranteed to be constant throughout the testing. It is also expected that the theoretical methods presented are applicable to IR detectors operating at different wavelength ranges (as used in commercial systems other than the DeltaTherm) and could form the basis of a similar approach if required.

Chapter 7

TSA of composite materials subject to fatigue damage

7.1 Introduction

From the identification of TSA as a suitable damage assessment technique in Chapter 2, the following chapters have introduced and discussed TSA, developed a generalised strain based calibration routine for thermoelastic data recorded from composite laminates and devised a manner in which the effect of the absolute surface temperature can be corrected. Without these procedures it is not possible to attempt to analyse thermoelastic data in a quantitative manner to assess the effect of damage in a composite component. In this chapter a methodology is developed that incorporates these procedures into a damage assessment procedure in a manner which is summarised on the flow diagram shown in Figure 7.1.

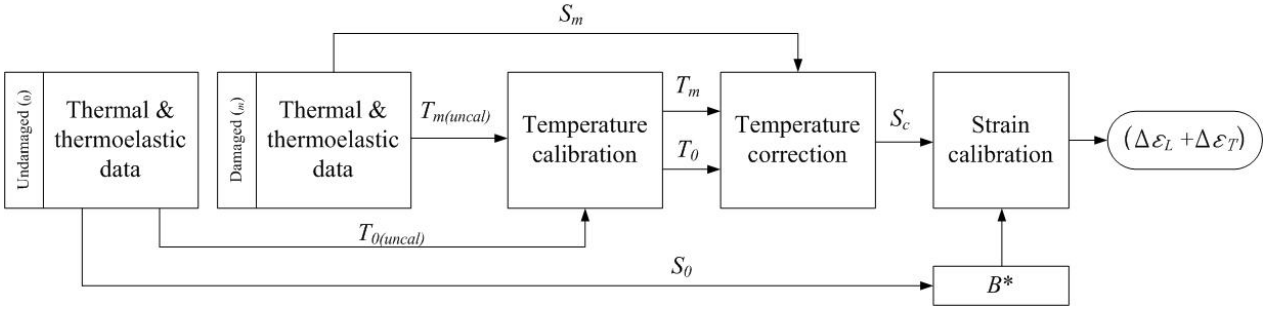

Figure 7.1. Damage assessment procedure

The procedure shown in Figure 7.1 is implemented using MATLAB programs (Appendix C.1 - 5) that are applied to the data array obtained from the DeltaTherm software and presents the output in a full-field manner. Firstly thermoelastic data, S_0, and absolute temperature, T_0, are obtained from the undamaged specimen. The S_0 data is used to obtain the calibration constant B^* and the T_0 data is used as the baseline for the temperature correction. After some form of damage the thermoelastic data, S_m, and the temperature, T_m, are obtained. S_m is corrected and a data set is obtained that is temperature corrected in a point-by-point fashion. The S_c output is then strain calibrated using Equation (4.8). The output of the procedure is a measure that is related to the strain sum change in the damaged component that occurs purely as a result of the stress distribution in the component.

In the application of this procedure to a component in service it would be expected that the damaged component would have been exposed to fatigue or in-service degradation due to impact or one of the many mechanisms described in Chapter 2. In the work presented in this thesis damage will be initiated and propagated artificially in laboratory conditions. Chapter 3 reviewed a number of methods in which damage has been introduced or initiated in composite structures during TSA studies, i.e. seeded, fatigue and impact. The real-time capability of the DeltaTherm (see Chapter 3) makes the system ideal for fatigue studies as data can be collected from the structure during the damage propagation. For this reason the damage assessment capability in this chapter will involve subjecting three specimens to a fatigue routine where damage will be initiated and propagated in a controlled manner by cyclically loading the specimens. The manner in which fatigue will be initiated will be split into two categories:

i. fatigue damage as a result of *in-plane* loading
ii. fatigue damage as a result of *out-of-plane* loading

The focus of this chapter will be damage initiation and propagation due to in-plane tension-tension fatigue loading of FRP tensile type coupons and Chapter 8 will present a method of out-of-plane loading a FRP laminate to propagate delamination damage. The manner by which the specimen is fatigued in this chapter is detailed in Section 7.3 and 7.4.

7.2 Test specimens

Three laminate panels were manufactured from 13 layers of UD E-glass epoxy material in an identical manner to the specimens described in Chapter 4. A ‘crossply’ (laminate

i)), a 'quasi-isotropic' (laminate *ii*)) and an 'angle-ply' (laminate *iii*)) panel were produced by orientating the pre-preg as specified in Table 7.1. The specimens that were cut from each panel were 40 mm wide and had an approximate length of 180 mm and thickness of 3.5 mm, as illustrated in Figure 7.2a. In specimens *i*) and *ii*) an 8 mm hole was introduced in the centre of the specimens as shown in Figure 7.2b. A modified drill bit that minimised tearing of the surface plies was used to produce the holes.

Table 7.1. Test specimens

Laminate	Lay-up	Laminate type	Illustration
i)	$[(0/90)_3, 0, (90/0)_3]$	Crossply	Figure 7.2b
ii)	$[(0, \pm 45, 90)_{2s}]$	Quasi-isotropic	Figure 7.2b
iii)	$[(+45/-45)_3, 45, (+45/-45)_3]$	Angle-ply	Figure 7.2a

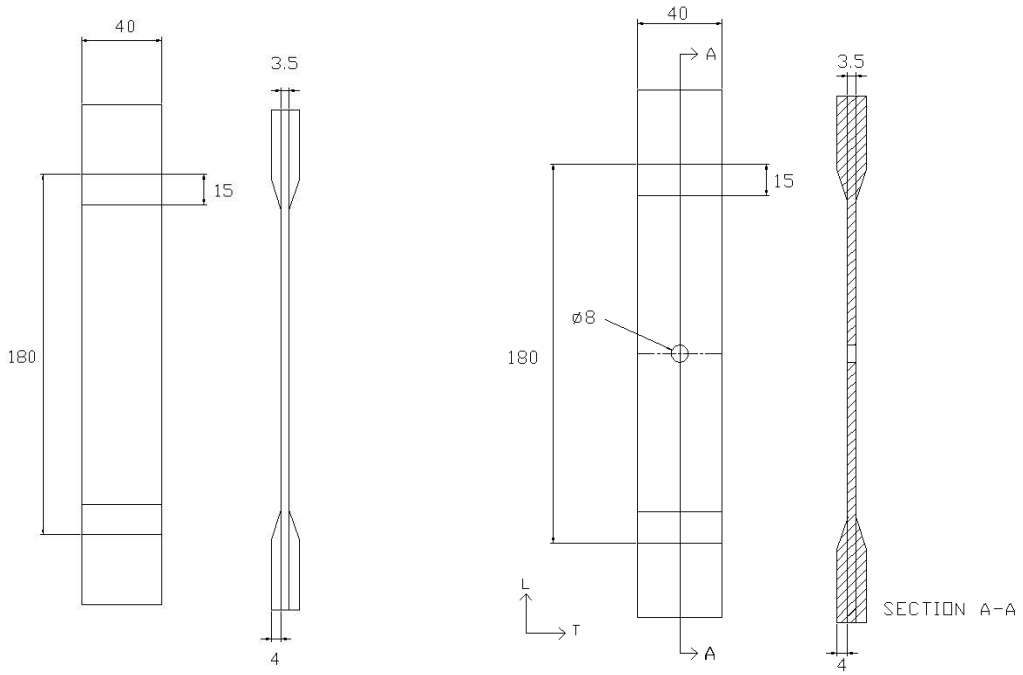

a) b)

Figure 7.2. Specimens (*Dimensions in mm*)

7.3 Damage evolution

The three laminate types were chosen so that different damage mechanisms could be obtained during fatigue loading. The damage progression expected for these laminates have been characterised in the literature using conventional non-destructive techniques such as radiography or microscopic examination of surface replicas [120]. In a crossply test laminate (i.e. *i*)) the dominant damage mechanism is matrix cracking caused by the large mismatch of mechanical properties between the layers [121]. The damage takes the form of small longitudinal cracks in the transverse ply and splits in the longitudinal ply

between the fibre and the matrix. It is often assumed that the cracking spans either the width or the length of the plate. However, transverse cracking only occurs where the applied strain exceeds the failure strain of the matrix material [122]. The quasi-isotropic type *ii)* configuration was chosen as crossply laminates are not extensively used in engineering applications. Quasi-isotropic laminates such as type *ii*) are more widely used [123] and the damage mechanisms are well known [120, 121, 124]. The stress field in a multidirectional laminate is more complicated than crossply laminates as there are three stresses to consider ply-by-ply, but the damage evolution is more progressive as the stress discontinuities ply-by-ply are less severe. However, matrix cracking occurs in the off axis plies and delaminations develop in a similar manner to those in cross ply laminates. The third angle-ply laminate is used to produce specimens that are loaded in the direction of bisectors of reinforcement angles. In this configuration all the laminae in the stack will experience an almost identical stress field [125]; the only difference is the direction of the shear stresses. Therefore in-plane failure can initiate in any lamina with equal probability with matrix crack accumulation occurring parallel to the fibre direction [112, 126, 127]. In the laminates it is expected that the damage will accumulate and cause stress transfer to the remaining intact plies until a stress state is generated that causes gross failure of the laminate through the failure of the fibre or matrix across the width of the test specimen.

To illustrate how the stacking sequence influences the damage initiation it is necessary to investigate the stress field generated when the laminates are loaded. It is necessary to make the assumption that the laminate is perfectly bonded (i.e. the strain longitudinally and transversely is constant through the thickness) and the laminate is in equilibrium [1]; this allows the stress state generated in the plies of the laminate to be understood and subsequently how the stress state initiates damage.

The manner in which damage propagates is first considered for the laminates were there is a large Poisson's ratio mismatch between the 0˚ and 90˚ plies (i.e. laminate *i*) and to an extent laminate *ii*)). The dominant damage mechanism here is matrix cracking caused by the large mismatch of mechanical properties between the layers [121]. The matrix cracking is initiated as when a crossply laminate is under an axial tensile stress, σ_L, all plies will strain equally (by virtue of load sharing). However as described when acting independently the 0˚ and 90˚ plies would undergo different longitudinal and transverse deformations as a consequence of their different major Poisson's ratio value (see Chapter 4) and this deformation is depicted for a single ply in Figure 7.3a and b respectively. However, when the 0˚ and 90˚ plies are bonded together in a laminate they will experience the same transverse strain Figure 7.3e. This generates interlaminar shear

stresses, τ_{ZT} , which in the transverse direction tend to expand the 0˚ and compress the 90˚ plies in the laminate. This shear stress varies between the two opposing free-edges of a laminate as illustrated in Figure 7.3c and d. The effect of strain compatibility in the longitudinal direction has the effect of developing a large strain in the 90˚ plies.

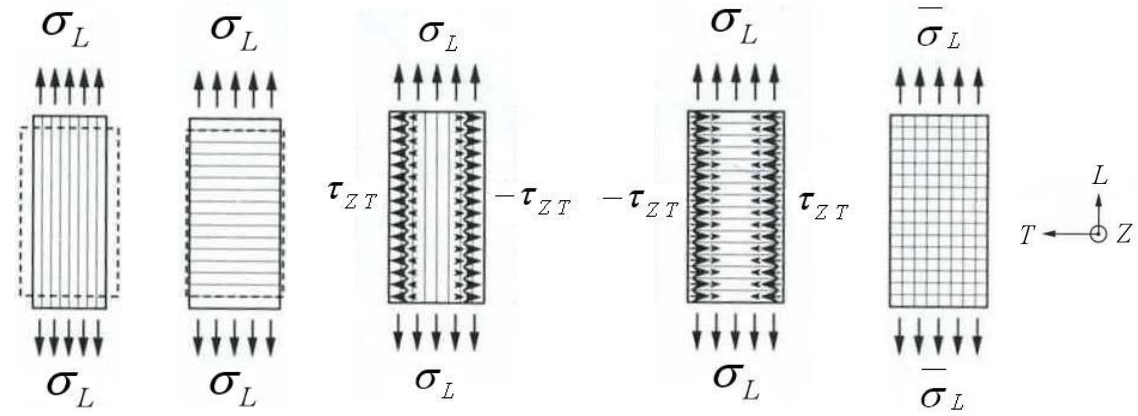

a) Ply 1 (0˚) b) Ply 2 (90˚) c) Ply 1 (0˚) d) Ply 2 (90˚) e) Laminate f) Axes

Figure 7.3. Stress state in a crossply laminate under axial tension

The imposed strain in the 0˚ and the 90˚ plies in the bonded laminate in the transverse and longitudinal direction respectively (over that which would be observed in a single unbonded ply) results in matrix damage; cracks in the 90˚ ply and splits in the 0˚ ply between the fibre and the matrix. Further damage propagates as a result of this damage mechanism as delamination initiates where these two mechanisms intersect in a laminate stack [128]. As a consequence of the shear stress state developed by the mismatch in ply stiffness a complex three dimensional stress state is developed to equilibrate the stress acting within the laminate. In crossply laminates the finite in-plane transverse stress and shear stress reduce to zero at the free edge causing a finite through-thickness direct stress within the laminate [1], as shown (for half the laminate width) in Figure 7.4. This stress system acts within one laminate thickness, *t*, of the free edge and results in undesirable large stress gradients.

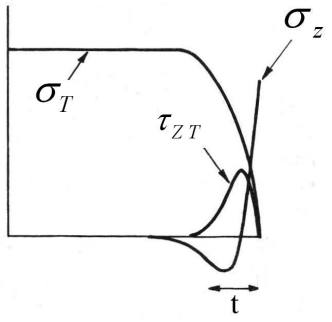

Figure 7.4. Edge effects due to Poisson's ratio mismatch

The plies orientated at ± 45˚ in the quasi-isotropic and the angle ply laminates promote a different detrimental stress field that can again be explained by assuming there is a perfect bond between each ply and the laminate is in equilibrium. The manner in which an angle ply laminate generates interlaminar shear stresses is again due to the interaction of the directionality of the mechanical properties in the differently orientated plies. A single angle ply lamina under a tensile axial stress will undergo shear deformation according to the off-axis orientation as shown in Figure 7.5a and b. When bonded in a laminate an interlaminar shear stress, τ_{ZL}, acts to equilibrate this shear strain generated by the opposing plies as shown in Figure 7.5c and d. The shear stress, τ_{ZL}, produces a moment which is further equilibrated by an intralaminar shear stress, τ_{LT}.

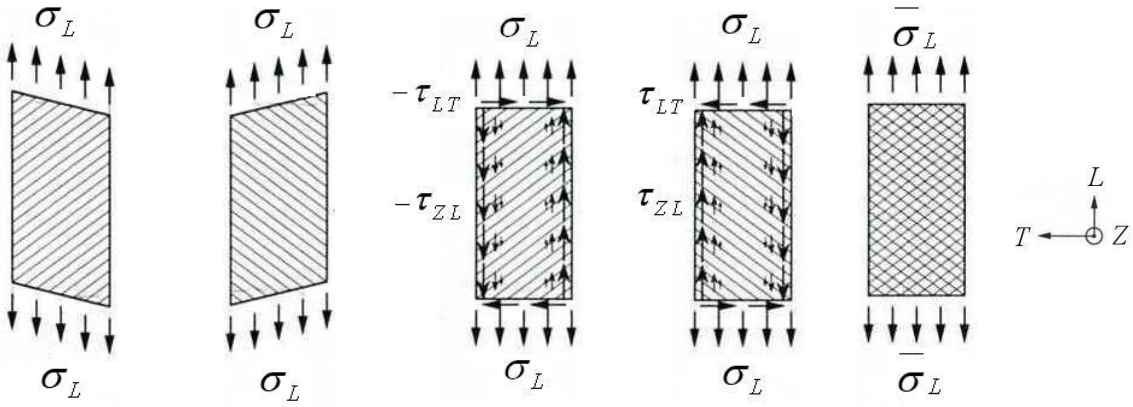

a) Ply 1 (+45˚) b) Ply 2 (-45˚) c) Ply 1 (+45˚) d) Ply 2 (-45˚) e) Laminate f) Axes

Figure 7.5. Interlaminar and intralaminar shear stresses in an angle ply laminate

This shear coupling developed is illustrated for half the laminate width in Figure 7.6. In the type *i*) and *ii*) laminates the large through thickness direct stress at the edges will tend to *peel* successive plies and result in delamination at the ply interfaces. In the type *iii*) and also in the type *ii*) the stress state will tend to shear the successive plies. The ability to withstand these circumstances are dependent on the strength of the matrix and thus damage will be initiated below the expected failure strength of the fibre reinforcement. Therefore the edge stresses will initiate localised matrix cracking damage and will tend to propagate into the laminate under the fatigue loading. The magnitudes of the stresses generated at the free edges are a function of the in-plane stresses and therefore will be accentuated in areas of higher in-plane stress. The type *i*) and *ii*) specimens both contain a hole and it is expected that damage will initiate from the free edge at the hole boundary as a result of the stress concentration.

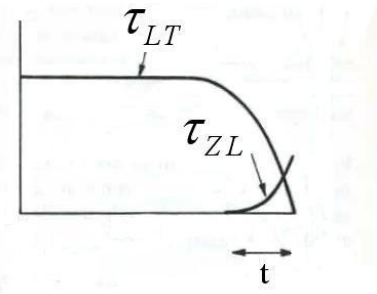

Figure 7.6. Edge effect due to shear coupling mismatch

The anisotropic stress concentration around discontinuities in composite components can be obtained from a consideration of anisotropic elasticity theory for infinite and homogeneous plates [123]. For finite width specimens experimental observation of the stress and strain concentration factors have been developed for typical composite laminates [1, 123]. For the two specimens with holes it is possible to estimate the influence of the hole in damage accumulation. In the type *i*) specimen the stress gradient is high at the hole boundary and a stress concentration of approximately 5 has been obtained for a boron reinforced epoxy laminate [1]. The stress distribution around a hole in a type *ii*) laminate has been shown to be similar to that of an isotropic plate [1] and the stress concentration for a glass-epoxy laminate has been demonstrated experimentally to be approximately 3.5 [123]. The strength reduction as a consequence of the introduction of a hole is a function of the radius; for the 8 mm hole in the type *ii*) laminate a reduction of 40 % of the strength should be expected [1].

The introduction of a hole in angle ply laminates does not produce the same magnitude of stress concentration as in the type *i*) and *ii*) laminates due to a lower ratio between the longitudinal and transverse stiffnesses. In the first two examples it is anticipated that damage would propagate from the hole notch. The hole is a high stress concentration area with the associated free-edge complexities and as such is the prime area at which the damage assessment can be targeted. However, a known initiation site is uncommon in laminated composite structures and the study in the ± 45 exemplifies why a full-field assessment is required. Therefore it was decided to test the angle ply specimen without a hole and without any known damage or weaknesses.

In all the laminates it is expected that the damage will accumulate and cause stress transfer to the remaining intact plies until a stress state is generated that causes gross failure of the laminate through the failure of the fibre or matrix across the width of the test specimen.

7.4 Application of TSA and fatigue loading

The effect of damage propagation, such as those discussed above, on the mechanical properties of a test specimen must be a major consideration when specifying the cyclic load required for TSA. Of the 15 papers reviewed in Chapter 3 (where TSA was used to study damage in a composite laminate) all but one used a constant load to cyclically load the specimen. However during damage propagation it is expected that the elastic properties of the material will change [31]. The upshot of this is that during the collection of thermoelastic data at various stages through the fatigue life the laminate strain cannot be assumed to be constant if the same cyclic load is applied throughout. Therefore, if the loading routine does not consider this the thermoelastic results collected at a damage site will be a function of any strain redistribution due to damage compounded with a global strain increase due to the application of a constant cyclic load. To illustrate the extent of the stiffness reduction possible in a GFRP laminate, an observed failure test of a $[90_3/0]_s$ GFRP laminate recorded a stiffness reduction of 45 % [31]. If TSA was recorded from this specimen at stages through the fatigue life and a constant cyclic load had been applied the stiffness reduction would have approximately had a two fold increase on the thermoelastic signal due to the loading condition alone. It is therefore crucial to consider the stiffness degradation in the test routine.

To characterise the expected stiffness degradation on a specimen representative of those used in this thesis, a full-failure test was performed on a 90/0 crossply E-glass epoxy FRP specimen (identical in design and manufacture to those detailed in Chapter 4) to failure. The damage expected was transverse cracking in the 90˚ plies. The method in which the mechanical properties for varying levels of damage was achieved by loading the specimen quasi-statically with increasing load increments at five kN intervals; after the application of each load increment the load was removed and the mechanical performance of the coupon was assessed by taking the secant modulus. Also at each load step the laminate was illuminated with white light from the rear of the specimen and the transverse cracking that had propagated could be observed visually from the front surface. The cracking evident can be seen as dark horizontal lines in the images in Figure 7.7 (obtained using a digital camera). The images presented illustrate the matrix cracking at the start of the test Figure 7.7a and at two later stages in the load history Figure 7.7b and c. To calculate the effect of the damage on the mechanical performance the Young's modulus was plotted with comparison to the crack density against the applied stress and is shown in Figure 7.8. It can be seen that the Young's modulus decreased by 16 % during the test, in a trend that followed the crack density. The crack density and resulting decrease in modulus rises markedly above 200 MPa before the

crack density plateaus as the applied stress reaches the ultimate failure stress of the laminate.

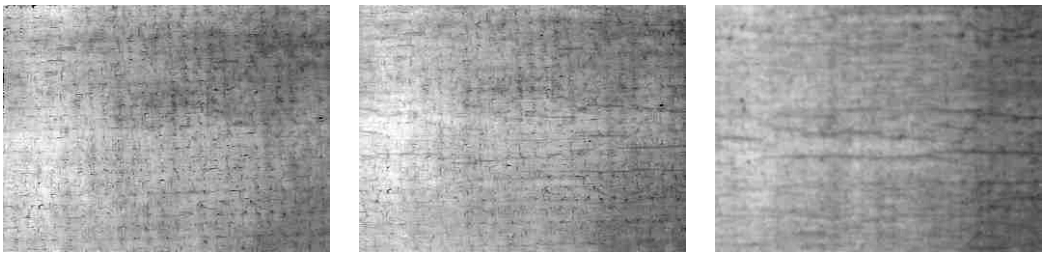

a) 0 MPa (0 kN) b) 286 MPa (40 kN) c) 429 MPa (60 kN)

Figure 7.7. Visual inspection of transverse cracking in 90/0 GFRP specimen

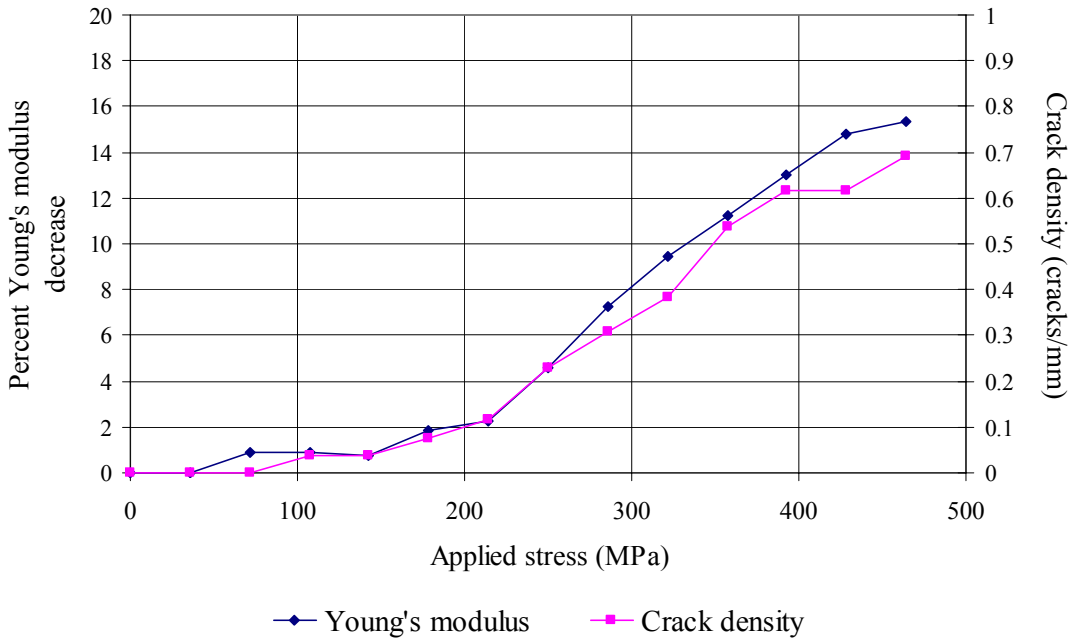

Figure 7.8. Behaviour of Young's modulus and crack density with stress applied

The effects of damage on the stiffness, as illustrated briefly above, have not been well integrated into documented TSA studies where in the majority of cases a constant load has been applied to the component during damage propagation [36, 64, 71, 72, 96, 104, 105]. To ensure that the readings obtained from TSA are as a result of the stress/strain redistribution due to the damage alone (not the applied load), it is proposed to apply a *constant cyclic displacement* to the test specimens to maintain a uniform level of strain in the laminate. This means that as the material elastic properties deteriorate (particularly the longitudinal modulus) the load applied reduces in proportion to the reduction in the stiffness.

It has been shown that the method of loading is important during the collection of thermoelastic data and for similar reasons of stiffness degradation it is also important to consider the method of applying fatigue to a laminate. In laboratory based tests, fatigue can be applied by constant load cycling and constant displacement cycling. In [129] differences in the stiffness degradation rates for constant load and constant displacement fatigue routines were discussed. In constant displacement cycling as damage propagates a lower load is progressively required to deform the sample, consequently as the stress applied to the sample is progressively reduced, the amount of deterioration per cycle decreases. Therefore, in a constant displacement fatigue tests, the stiffness reduction occurs quickly at first and then reduces. Conversely in load controlled fatigue the effective stress increases as damage accumulates and the fatigue life will be considerably lower [130]. As a consequence of this situation it has been shown [125] that it is almost impossible to fail angle-ply specimens in fatigue by applying a constant displacement. In light of these findings it was decided to carry out the fatigue routine in this chapter by applying a constant load throughout the fatigue life.

To initiate and propagate damage a method is needed to apply fatigue in the laboratory to the specimens. In the current work it was planned to use an Instron 8802 servo hydraulic test machine. These machines have the limitation that for large displacements only low frequencies can be applied. To assess the loading that could be generated by the test machine it was necessary to obtain the performance envelope for the machine, which is provided by the manufacturer and is shown in Figure 7.9.

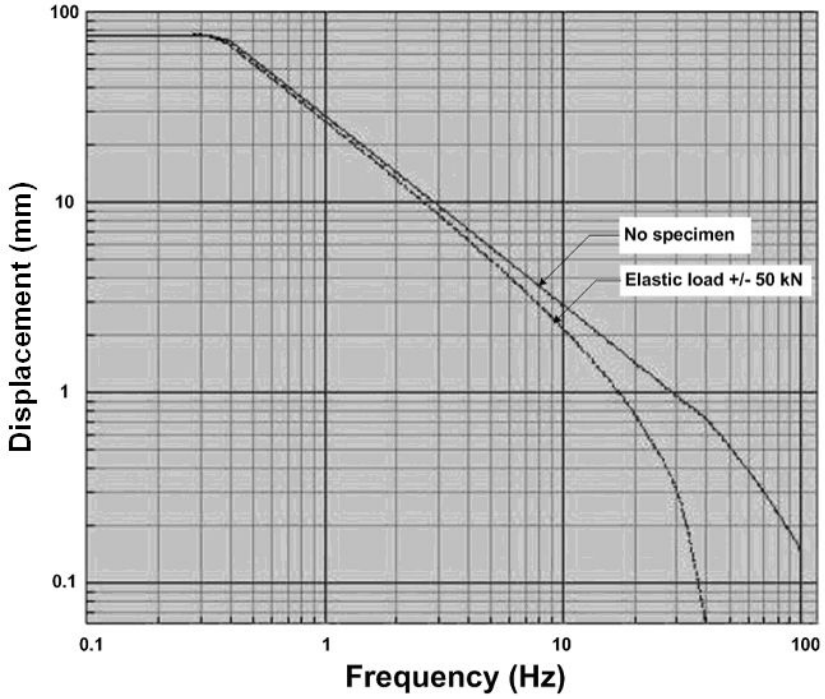

Figure 7.9. Performance envelope for Instron 8802 servo-hydraulic test machine [131]

Cunningham *et al*. [36] demonstrated that a cyclic load of at least 10 Hz must be applied to achieve adiabatic conditions for the type of specimen used in this thesis. Analysis of the plot in Figure 7.9 shows that the unloaded system can achieve a displacement of 3 mm at a rate of 10 Hz. Preliminary tests loading a UD E-glass epoxy FRP specimen in the test machine showed that a displacement amplitude of 1.5 mm at 10 Hz was the practical limit of the system in order that an accurate and repeatable cyclic displacement could be achieved. The requirement to provide a constant strain throughout the life of the specimen has been discussed in this section and therefore it is considered prudent to keep the displacements well within this limit when performing TSA. As a result of these findings it was decided that the specimens should be fatigued under load control with a low frequency. For the TSA studies the control would be reverted to position control and applying lower amplitude and therefore achieving the necessary 10 Hz frequency. The cyclic loads applied in fatigue and during TSA to the three specimens are detailed in the following section.

7.5 Loading procedure

To establish the effect of the damage from the specimens at stages during their fatigue life a test procedure was developed as shown in Figure 7.10. Starting with the virgin test specimen the elastic properties of the specimen are obtained, the thermal and thermoelastic data are then obtained followed by the application of a fatigue load that results in damage. The procedure is repeated and results in a number of 'fatigue steps' being applied to each specimen that could be related to life of the specimen.

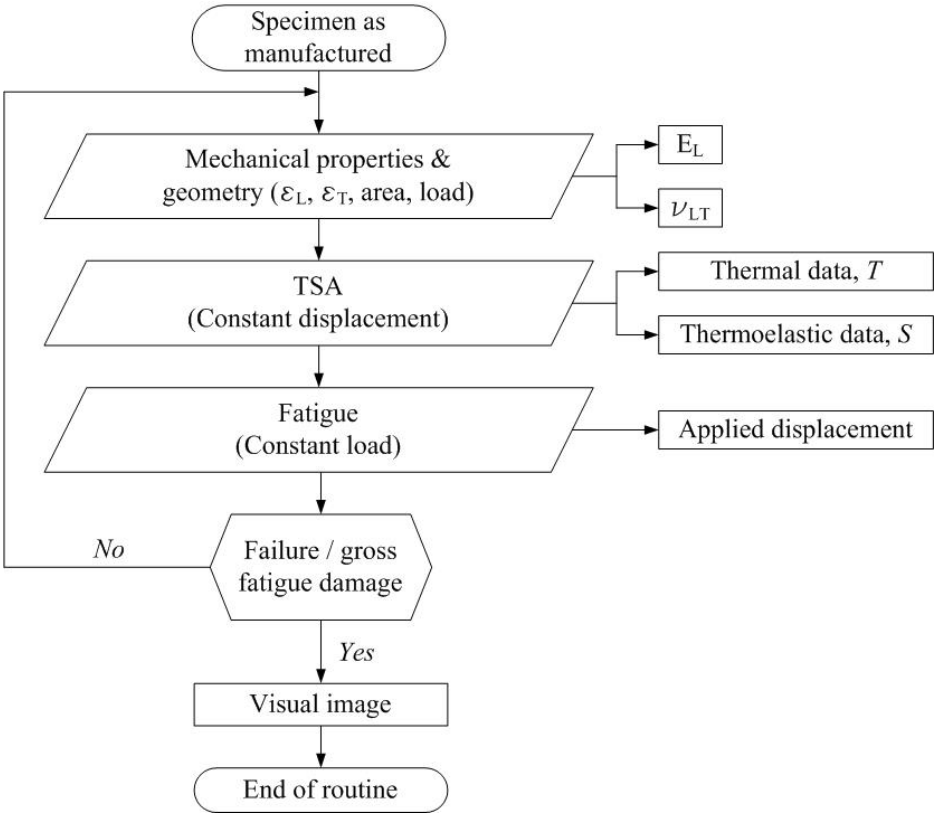

Figure 7.10. Fatigue test method

At the start of each step the longitudinal and transverse stains were recorded from a quasi-static tension test over a 0 to 5 kN range with a ramp-rate of 1 kN/min. The longitudinal to transverse strain ratio will enable the major Poisson's ratio to be calculated for use in the calibration procedure. The load applied during the quasi-static test was used to obtain that the global secant Young's modulus, E_L, for the specimens. The purpose of calculating the modulus was to provide a metric with which to compare the TSA data by establishing the residual stiffness of the specimens after N cycles. The extensometers, used to obtain the strains, remained attached to the specimen during the TSA constant displacement testing to obtain the longitudinal strain change, $\Delta\varepsilon_L$, to monitor the strain during the collection of the TSA data.

The thermal, T, and thermoelastic, S, data were recorded using a DeltaTherm system with a 25 mm lens that meant the detector was positioned at a stand-off distance of 500 mm from the specimen surface to obtain a full-field of view the specimen. The S and T data are the inputs for the thermoelastic procedure illustrated in Figure 7.1. The specimen surface, from which the thermoelastic signal was recorded, was unpainted and left in the manufactured state as the epoxy surface provides a sufficiently high emissivity for thermoelastic studies [23]. Glass/epoxy is transparent, so a visual inspection of the specimen can provide an insight into the types of damage occurring in the specimens. Figure 7.10 shows the visual inspection taking place at the end of the procedure when

gross damage had evolved. The visual inspection was made by using a macroscope and illuminating from the underside of each specimen. It should be noted that in practice this would not be possible as in-service structures would normally be coated in an opaque finish.

Table 7.2 provides the applied displacements used in the TSA data collection, the fatigue load used to produce the damage and the number of fatigue steps to produce gross damage; each fatigue step comprised of 3000 cycles.

Table 7.2. Cyclic loading

Specimen	TSA		Fatigue			
	Displacement	Frequency	Load	Frequency	Cycles	Number of steps
i)	0.167 mm	10 Hz	14 ± 12 kN	2 Hz	3000	17
ii)	0.178 mm	10 Hz	12 ± 11 kN	2 Hz	3000	17
iii)	0.44 mm	10 Hz	8 ± 6 kN	2 Hz	3000	10

7.6 Crossply

The strain sum distribution recorded at the start of the test, at fatigue step 14 and from the final data set is shown in Figure 7.11a, b and c respectively. The strain sum data presented in Figure 7.11 shows the strain field for the width of the specimen with the vertical axis centred on the hole and extending 30 mm either side of the centre.

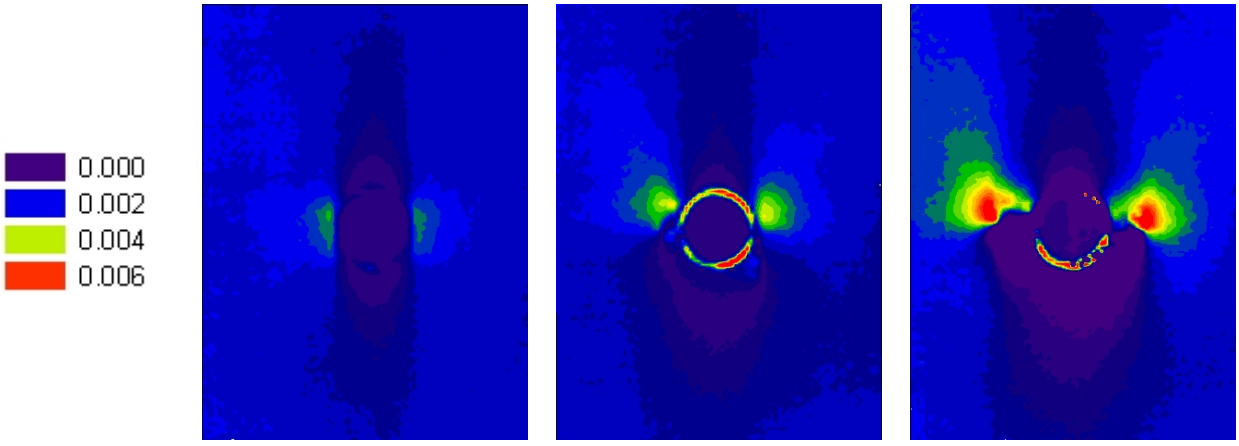

Figure 7.11. Strain sum in crossply

The maximum temperature variation during the collection of the thermoelastic data was 12 K, the temperature distribution is shown in Appendix D (for Steps 1, 14 and 16).

The data shown as red around the hole in the image given in Figure 7.11b and c occurs as a consequence of the test specimen motion, this is a known phenomenon in TSA and is most pronounced at edges. The effect of motion causes the thermoelastic signal to 'blur'. Observation of the affected area through the fatigue history shows motion becomes more of an issue as the stiffness reduces local to the hole. A robust method of compensating thermoelastic data for motion is not available at present and therefore in this work it is ignored as the only significant effects are restricted to the vicinity of the hole edge.

To inspect the damage propagation that has caused the redistribution of strain around the hole the specimen was imaged using a macroscope and the result is shown in Figure 7.12. As predicted the fatigue loading has initiated localised damage around the hole. The mismatch in the Poisson's ratio between the 0˚ and 90˚ produce an interlaminar shear which produces strains sufficient to cause cracking of the epoxy matrix. There is matrix cracking in the transverse plies where the matrix cracks (the short dark horizontal lines in the image) appear to be restricted to the areas of the specimen subject to a tensile strain. Longitudinal splits have occurred in the 0˚ plies, running vertically and parallel with the 0˚ fibres; these are most severe at the edge of the hole. The dark areas with diffuse edges between the longitudinal splits indicate delaminations. As the concentration of matrix cracking increases to a saturation point, for a constant loading (fatigue) scenario, the stress is redistributed at the local level into the unbroken constituents. In the crossply laminate this means transfer of the stress into to the 0˚ ply. As there are large stress concentrations at the hole, of the order of 5 in crossply (see above), fibre breakage is initiated at the edge of the hole. Although not visible in the image shown in Figure 7.12, fibre breakage occurred in the form of cracks extending (in a discontinuous manner) from the hole towards the edge of the specimen; the positions of the cracks are marked with a dotted line in Figure 7.12. A comparison of the line of the cracks with the TSA data shown in Figure 7.11, shows that the strain has redistributed as a consequence of the cracks and the strain 'concentration' has move to the tip of the crack. A more detailed examination of the localised data is provided later in the chapter. Prior to this a comparison of the global response of the specimen to that of the strain sum derived by the TSA is made.

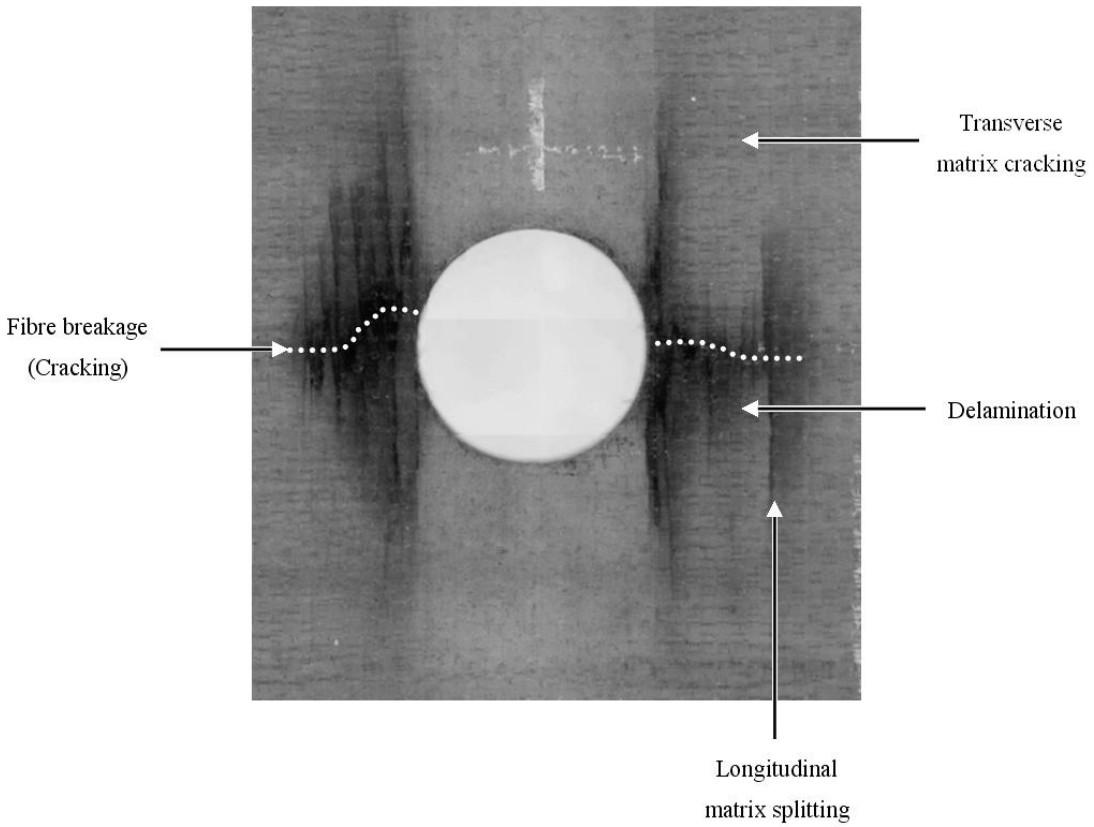

Figure 7.12. Macroscope image of damage in crossply

To make a concise global comparison of all of the collected thermoelastic data an analysis routine was developed so that strain sum was analysed at each stage of the fatigue loading. Three metrics were established: the percentage of the image area that gave a strain sum of greater than 0.001, the percentage of the image area that gave a strain sum of less than 0.001 and the maximum strain sum. The lower image area metric provides an indication of the reduction in strain in certain areas as the load carrying capacity reduces; the upper limit provides an indication of the strain redistribution as a result of the damage. The expectation is that these two metrics will change at the same rate. This data is plotted in Figure 7.13 along with the percentage decrease in the measured Young's modulus of the specimen.

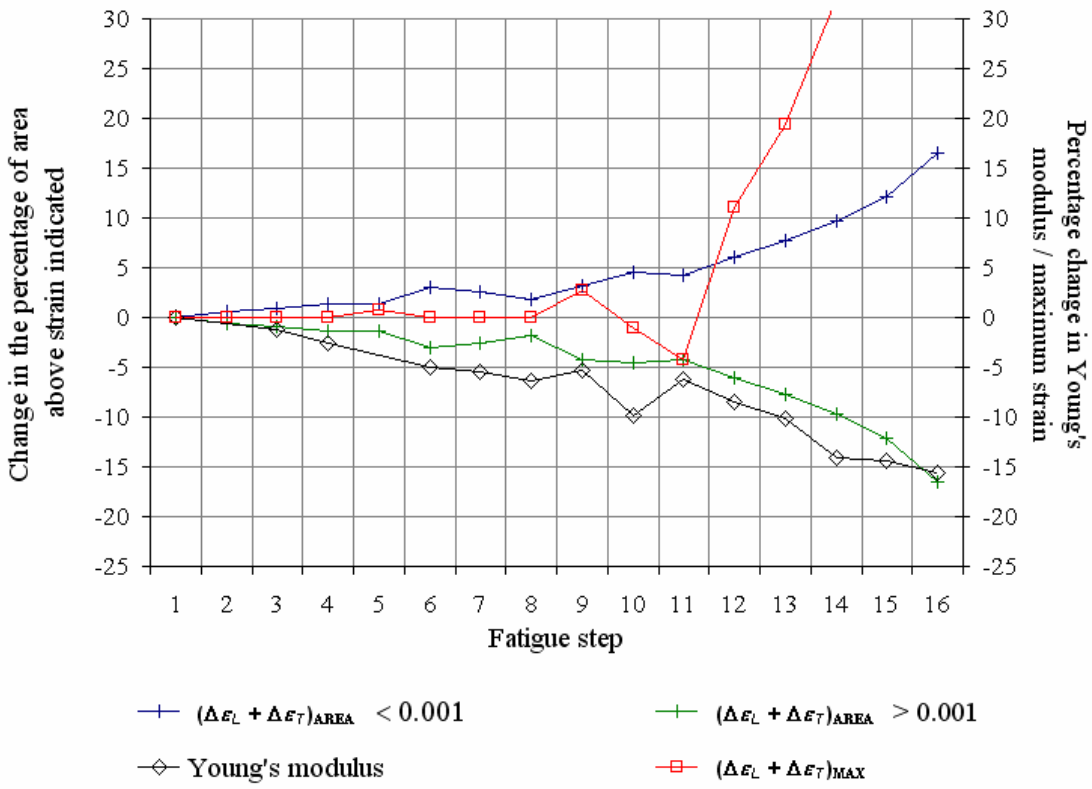

Figure 7.13. Strain metrics and mechanical properties for crossply

Figure 7.13 shows that in the early stages of the fatigue loading (up to step 8) the decrease in Young's modulus is more rapid than the strain redistribution indicated by the TSA data. In fact there is no change in the maximum strain until fatigue step 8. This is because transverse matrix cracking is occurring in the 90˚ plies only during these fatigue steps. As little of the stress is carried by these plies it has a small effect on the global strain and has a less pronounced effect on the strain sum data collected by the TSA; this was noted by Cunningham *et al*. [63] who showed that simulated cracks in transverse lamina in crossply could not be detected in TSA data. Figure 7.14 shows a close up of the TSA data in the undamaged state and a close up of the macroscope image. Here it can be seen that the transverse matrix cracks are restricted to the areas of tensile strain observed in the undamaged TSA image (bounded by the dashed line).

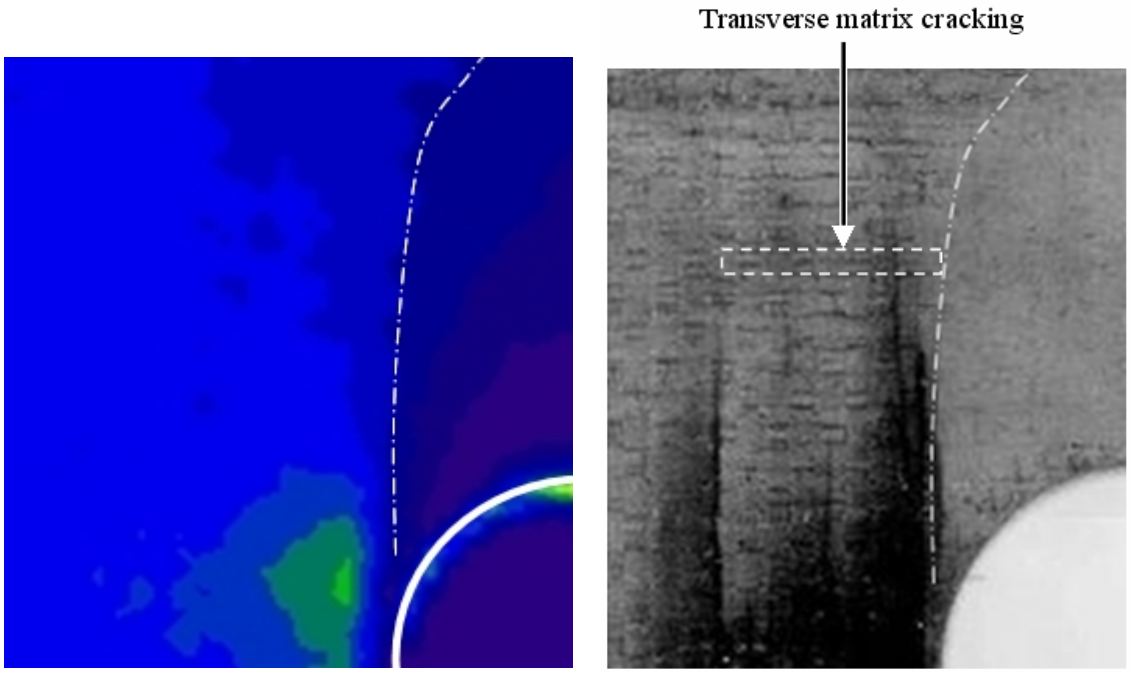

a) b)

Figure 7.14. Transverse cracking in crossply

Between fatigue steps nine and ten there is a large decrease in Young's modulus of 5 %. Inspection of the specimen revealed the initiation of breakage of the 0˚ fibres at the hole and explains the step change in stiffness at this stage. At fatigue step 9 there is a change in all three TSA strain data sets. At 9 there is an increase in the maximum strain and at 10 there is a decrease. Figure 7.15 shows the TSA data at steps 9 and 10. There is a large strain sum concentration at the hole edge at step 9 which is not evident at step 10. This clearly indicates that TSA is able to identify the imminent failure seen in the next fatigue step when the crack occurred. At fatigue steps 10 and 11 there is a reduction in the maximum strain followed by an increase at step 12. At step 11 the area metrics also start to increase/decrease more rapidly. At this stage more fibre breakage occurred and the crack in the specimen started to grow progressively. Figure 7.15c shows the strain concentration at the crack tip at fatigue step 13. The large changes noted in the TSA data are not present in the modulus data, which simply shows a steady decrease throughout the fatigue life. The TSA data is indicating that significant damage is present at step 9 and at step 12 failure is imminent. This section of work clearly shows that TSA data can be used as a damage assessment tool.

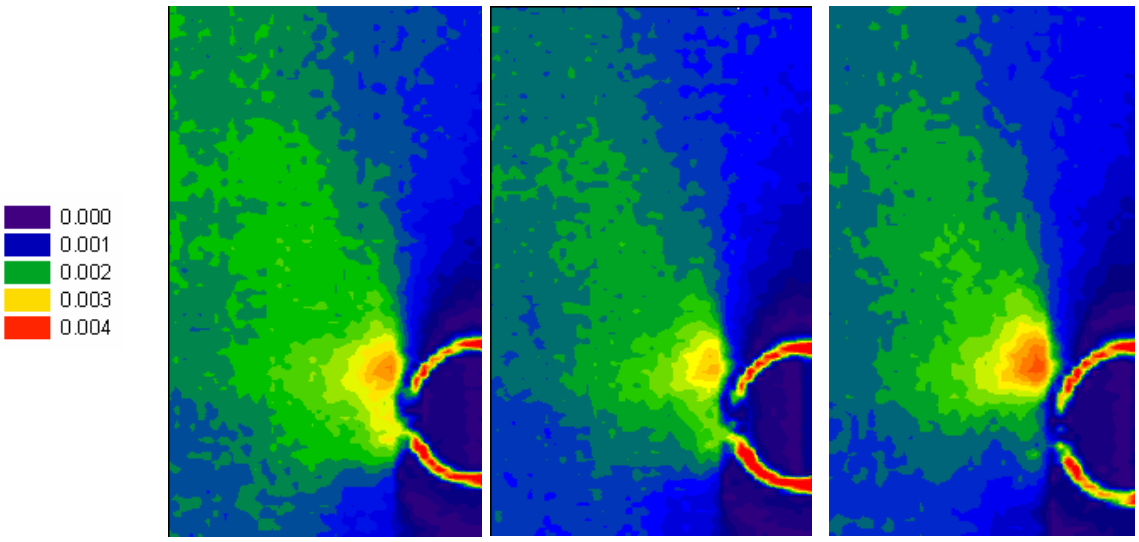

Figure 7.15. Strain sum evolution due to fibre breakage

7.7 Quasi-isotropic

The quasi-isotropic laminate was tested in an identical manner to the previous specimen. The strain sum data obtained from the TSA are shown in Figure 7.16 again for the beginning, middle and end of the fatigue damage process. The distribution on the surface shows that the strain concentration at the hole reduces as fatigue damage propagates within the laminate. In Figure 7.17 a macroscope image is shown from the end of the test. The Poisson's ratio mismatch between the four ply orientations has caused matrix cracking; this cracking is evident in Figure 7.17 in the +45˚ and -45˚ plies (the dark lines in the ±45˚ orientations) and also in the 0˚ plies as longitudinal splitting. (It is assumed transverse cracks have occurred in the 90˚ plies although these cannot be observed in the macroscope image.) It can be seen that there are delaminated areas around the hole; the delamination appears as the dark areas with diffuse edges. From inspection of Figure 7.17 it can be seen that the area of the delamination is bounded by the area of ±45˚ matrix cracking. The extensive delamination occurring in this laminate is a result of the shear mismatch between the plies (there is no shear mismatch in the crossply laminate). The axial loading develops an interlaminar shear stress that prevents the angle plies from deforming in opposing directions. In quasi-isotropic materials the stress concentration at the hole is less than that in the crossply. Therefore delamination occurs preferentially, instead of fibre breakage at the hole, as a result of the through-thickness direct stress. The delaminations result in a reduction in the load carrying capability and the strain concentration maxima occurring locally through the horizontal centre-line evident at the start of the test disperses and decreases during the test.

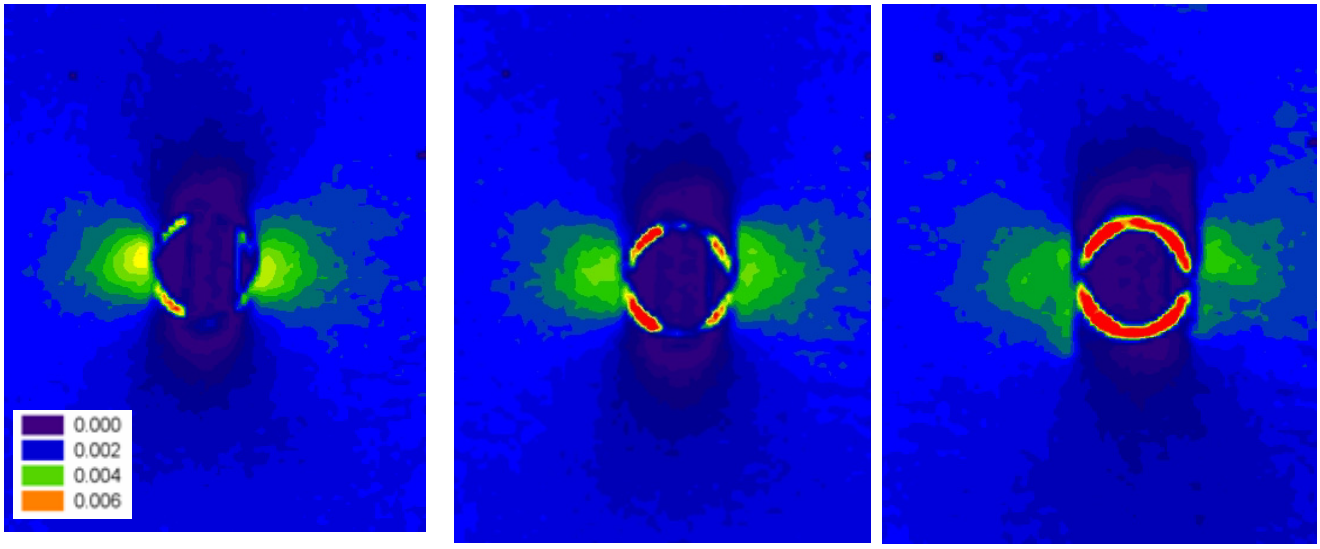

a) Step 1 (*Including scale*) b) Step 8 c) Step 16

Figure 7.16. Strain sum evolution in quasi-isotropic specimen

The maximum temperature variation during the collection of the thermoelastic data was 8 K, the temperature distribution is shown in Appendix D (for Steps 1, 8 and 16).

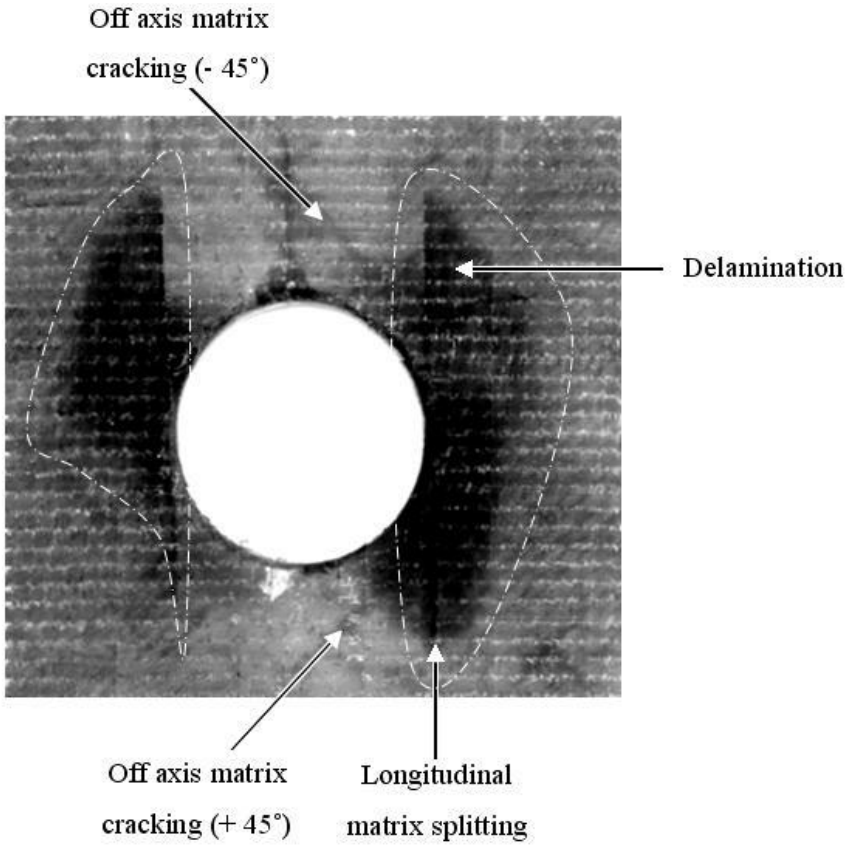

Figure 7.17. Macroscope image local to damage

Figure 7.18 shows the stiffness degradation in the component through the fatigue steps; both the Young's modulus and major Poisson's ratio decrease. This stiffness reduction is attributed to the cracking in the ±45˚ plies. The Poisson's ratio variation is slightly more complex; the decrease is interrupted at stages through the fatigue life. This can be attributed to an effect reported in [29] where longitudinal splitting had the effect of reducing the transverse stiffness of a laminate and in turn increasing the Poisson's ratio.

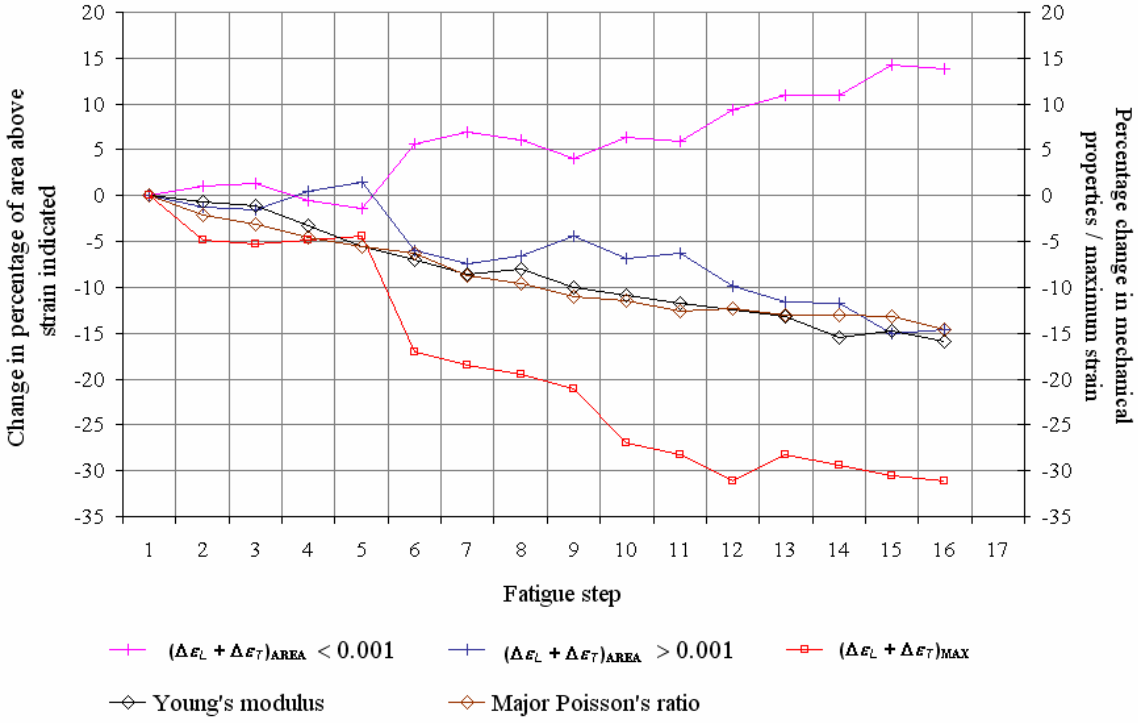

Figure 7.18. Strain metrics and mechanical properties for quasi-isotropic specimen

As with the crossply laminate it was decided to present the strain sum data in three forms: i.e. area of strain sum above 0.001, area below 0.001 and the maximum strain sum. The maximum strain sum decreases by 31% over the course of the fatigue steps. In Figure 7.18 it is evident that the TSA is insensitive to the early stages of fatigue. At fatigue step 5 there is a large change in the TSA data. The full-field strain sum data in Figure 7.19a and b shows fatigue steps 5 and 6. There is a clear reduction in the strain concentration as a result of the delamination and most importantly the occurrence of a longitudinal split at step 6. As with the crossply simply monitoring the elastic properties does not indicate the onset of the delamination, as the trend in this data is a steady decrease, even though a longitudinal split should cause an increase in Poisson's ratio. After the first split, which is clearly insufficient to case a major reduction in the load carrying capacity of the specimen, the TSA area data remains constant until step 11 when both data sets start to increase or decrease markedly. The maximum strain sum date shows a slight decrease up to step 9 and then another decrease at step 10 and then

remains constant. Figure 7.19c and d show the data at fatigue steps 11 and 12 with no discernable difference between the two. This work shows that when delamination damage is prominent the strain area metric provides a better damage indicator than the maximum strain sum data.

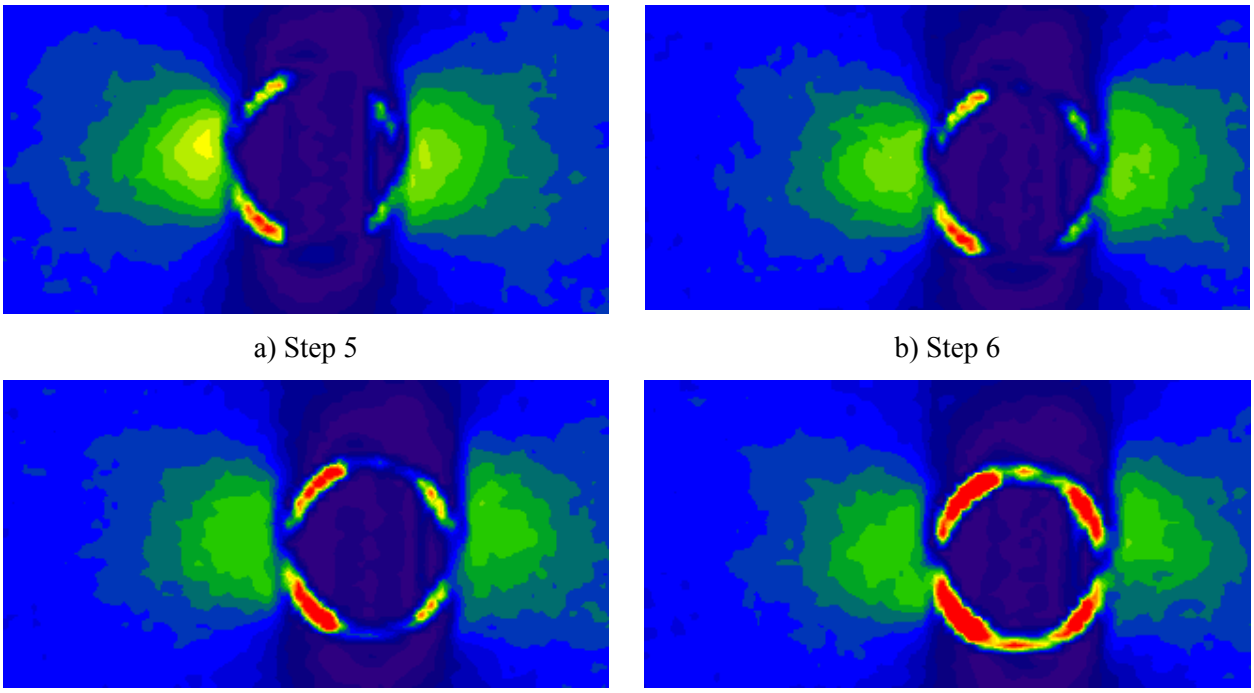

a) Step 5 b) Step 6

c) Step 11 d) Step 12

Figure 7.19. Strain evolution due to delamination

7.8 Angle ply

For the angle ply laminate the experimental set-up and the procedure was the same as the previous two specimen types. However to ensure the fatigue damage propagated to failure in a timely fashion, the fatigue load was set so it represented a substantial amount of the ultimate failure load of the coupon. The specimen was fatigue loaded over a series of 10 increments before gross failure occurred and prevented any further testing. Figure 7.20 shows the thermoelastic strain sum data obtained from the specimen at four load steps. Figure 7.20 a shows the first load step and it is clear that there is some initial damage in the specimen. It should be noted that the data shown was taken from the central area of the specimen and not close to either of the test machine grips. As the loading progresses the strain concentrations increase and the damage progresses. Figure 7.20e shows an optical image of the specimen in the failed condition and the position of the wires holding the two extensometers. In the TSA plots the data from the wires has been removed; this is evident in the plots of Figure 7.20a to d by the presence of discontinuities in the data.

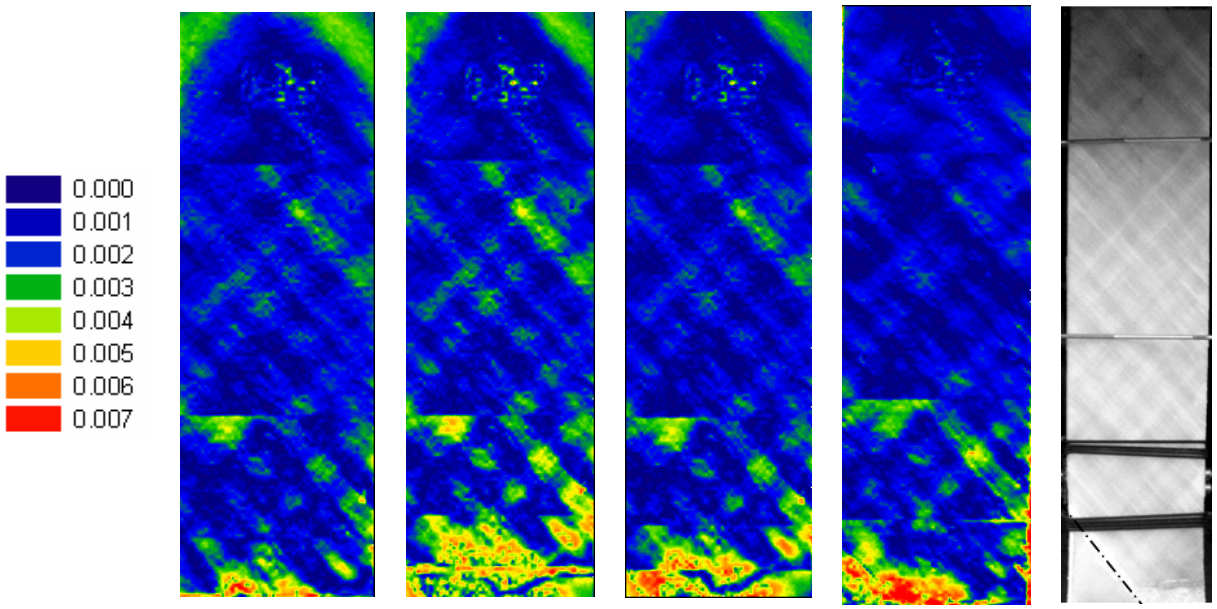

Figure 7.20. Strain sum evolution in angle ply

The maximum temperature variation during the collection of the thermoelastic data was 18 K, the temperature distribution is shown in Appendix D (for Steps 1, 3, 4 and 9).

Figure 7.20b, c and d shows distributed strain concentrations throughout the laminate corresponding to areas of matrix cracking. The matrix cracking is evident in the visual image of the surface of the component in Figure 7.20e, indicated by the lighter areas that follow the fibre direction. As the cracking accumulates less of the specimen is able to carry the load and this is evident in the increase in the darker areas in the TSA data. The growth of the darker areas corresponds to the progression of the matrix cracking between the fibres and evolves in the ±45 directions.

An identical procedure to that used in the previous two specimen types was used to produce Figure 7.21. Here the TSA area data shows a sharp increase/decrease between steps 3 and 4 and then returns to a nominally constant level. The maximum strain sum increases steadily throughout the fatigue steps, in much the same way as the modulus decreases. This indicates that TSA can monitor matrix cracking damage progression, but as the damage is distributed throughout the sample the strain changes do not provide such a clear indicator of gross failure as that seen with fibre breakage and delamination.

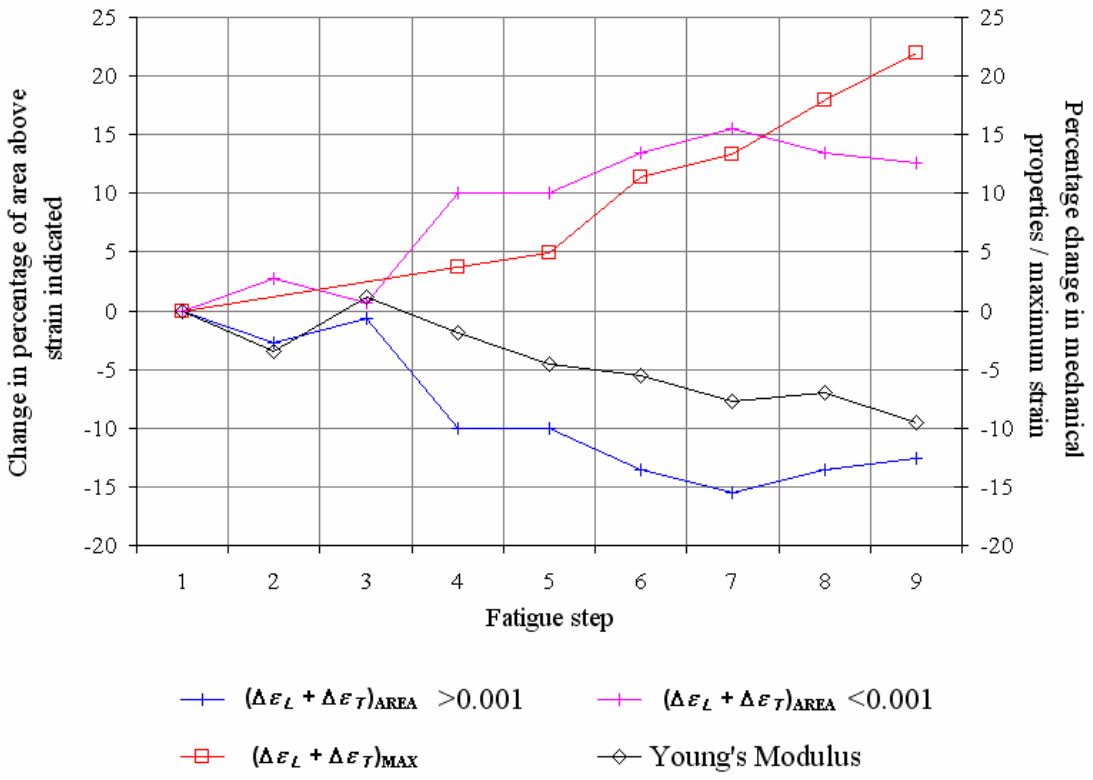

Figure 7.21. Strain metrics and mechanical properties in angle ply

To quantify how the strain has evolved over the course of the fatigue a 'damage analysis' macro has been developed in MATLAB (Appendix C.6) that provides a percentage change in the strain sum between undamaged and damaged data. The strain data is processed for each pixel, a threshold is set that accounts for noise in the data. If the change in the data is below the threshold the data from that pixel is rejected from the analysis. For pixels that are subject to a percentage change above the threshold the ratio of the strain in the damaged and undamaged state is calculated and displayed on a corresponding full-field plot. This process was carried out for the strain results from the type *iii*) laminate. The plots in Figure 7.22 demonstrate the distributed nature of the matrix cracking in the direction of the fibre axes. This clearly shows how the damage is increasing in the specimen without the distraction of the initial damage shown in Figure 7.20a and provides a means of visualising the damage extent and severity.

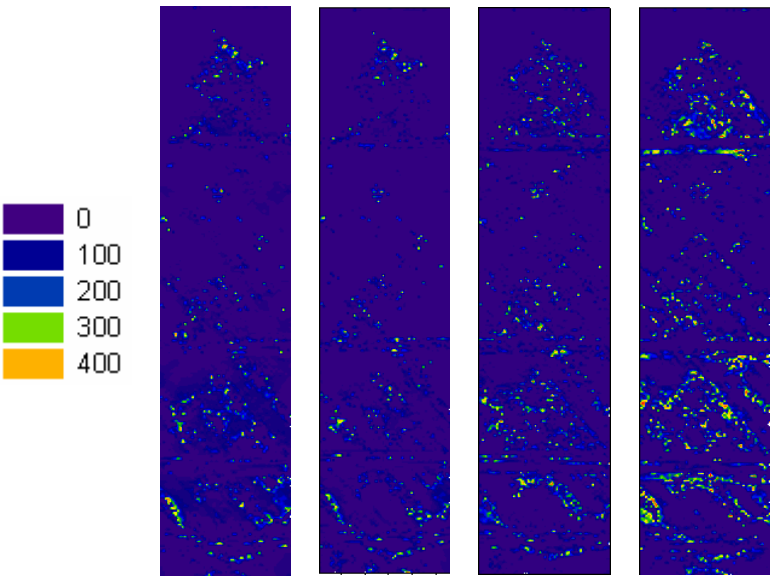

Scale (%) a) Step 3 b) Step 4 c) Step 7 d) Step 9

Figure 7.22. Full field damage map

7.9 Conclusions

It has been shown that TSA can be used in a quantitative manner to obtain the strain distribution in the neighbourhood of damage in laminated glass reinforced fibre composites. The damage types occurred together but specimens were designed so that a single damage type was the prominent cause of failure three types of damage have been studied:

1. Fibre breakage
2. Delamination
3. Matrix cracking

Damage metrics have been developed based on the thermoelastic response throughout the fatigue life. The experimental work described in the chapter has shown that these can be used as a damage indicator that is directly related to the level of fatigue damage that the specimen has been exposed to.

The work represents an important initial step in which a methodology for damage assessment has been established. The methodology using TSA accounts for changes in surface temperature due to damage evolution and incorporates a calibration procedure so that the data is presented in terms of strain.

Chapter 8

Subsurface delamination

8.1 Introduction

In Chapter 7 it has been shown that TSA can be used to assess damage at known locations, i.e. at a hole or in a small coupon type specimen. In reality subsurface damage occurs as a result of manufacturing defects and propagates into delamination. The purpose of this chapter is to assess the feasibility of using IR techniques to locate and assess damage.

To enable the provision of a complete damage assessment routine TSA must be integrated with complementary techniques in order that the five levels of damage identification (Chapter 2) are satisfied; the TSA approach lacks the capability to detect and localise damage in a straightforward manner. PPT is an IR technique that can locate internal damage (see Chapter 2). It is intended that PPT will form the basis of an anomaly detection routine that would be performed over the structure in order that areas of damage are identified. If the PPT results show any concern it is proposed to apply TSA.

Figure 8.1 shows a flow diagram of the complete IR damage assessment approach. For all components it is necessary to collect TSA data in the undamaged state; this is stored until it is required. Periodically throughout the structure's life, it is inspected using PPT.

If damage is apparent then the TSA damage assessment routine is applied. The assessment decides if the component can continue in service, i.e. is the reduction in quality or performance (see Chapter 2) acceptable. If the reduction in quality or performance is such that it is considered a fault (see Chapter 2) then a repair can be carried out and then the structure returned to service. At this stage it may be prudent to assess the quality of the repair using TSA. It is clear that this approach requires periodic inspection and does not provide an alert that damage is present. A means of incorporating this will be discussed in Chapter 9.

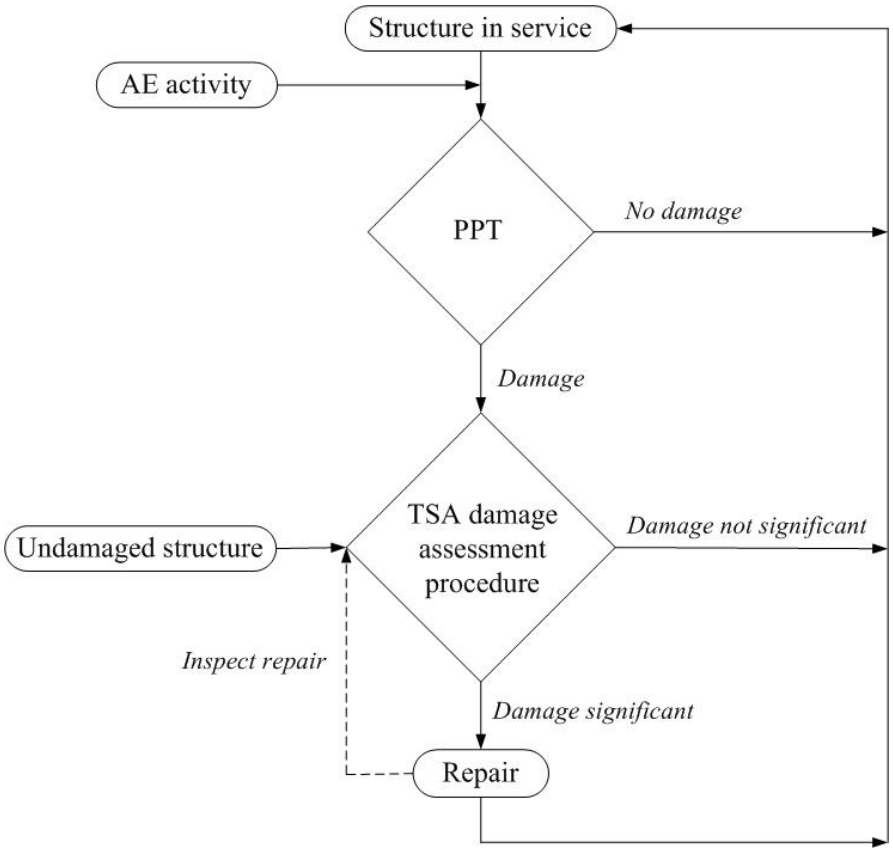

Figure 8.1. IR damage assessment method

In this chapter the proposed technique is applied to GFRP specimens that have internal delaminations. The delaminations are grown in a controlled manner in a specially designed rig. The rig and specimen design is described in detail. A brief overview of the PPT technique is provided. PPT and TSA are applied to the damaged component and through comparison of the visual extent of the delamination (possible with the glass epoxy constituents) the PPT results provide good indication to the spatial footprint of the delamination. The thermoelastic results provide a measure of the strain redistribution due to the damage. The damage assessment visualisation procedure developed in Chapter 7 was applied and areas that caused gross damage were revealed.

8.2 Initiation and propagation of delamination damage

Interlaminar delamination has been developed during the in-plane fatigue testing, described in the previous chapter, but not in isolation to other damage. The ability to distinguish the effect of a delaminated area from thermoelastic data sets has not been reported. In work by Cunningham *et al.* [63] it was reported there was no discernible change in the thermoelastic signal around the seeded *delamination* when a GFRP specimen was loaded in tension. The seeded delamination took the form of a PTFE patch inserted during manufacture. Although this type of seeded damage has been used [132] the observations in [63] questions if this type of seeded damage would produce the desired effect. The inability to obtain a deviation in the thermoelastic data as a result of the pseudo delamination is a primary concern. There are two issues to consider: *i*) does the delamination cause a significant change to the surface stress or *ii*) does the patch have any effect on the integrity. Therefore, it was not possible to comment on the capability of TSA to detect delamination with any certainty. This provided the motivation for the design of a fatigue rig that could be used to initiate and propagate delamination through the debonding of two neighbouring plies within a laminate. With a laminate containing an actual delamination it would be possible to test the capability of TSA to resolve sub-surface damage.

The fatigue rig was based on a design reported [133] in which a rig was developed to propagate delamination damage to validate the use of radiographic methods. The purpose of the rig was to generate interlaminar shear between neighbouring plies within the laminate. In [133] the samples were of a small scale of the order of 60mm in length and 30mm in width and the fatigue rig was suitably sized to accept these specimens. In order that larger specimens could be investigated the design of the fatigue rig was scaled up. It was also decided to use a servo hydraulic test machine to apply the displacement therefore the design was altered in order that the rig could be mounted directly to the test machine as shown in Figure 8.2. It can be seen from Figure 8.2 that the free end of the laminate is deformed by the movement of the servo hydraulic actuator which does link to the test machine load cell. Consequently a cyclic displacement can only be applied not a cyclic load. The displacement is achieved though a roller which does not subject the laminate to a point load but generates a pure bending moment. The plan elevation in Figure 8.2 illustrates the clamped boundary condition designed in a half sine profile as suggested in [133]. The purpose of this clamp design is to generate higher levels of interlaminar shear in the central region of the laminate and helps initiates delamination

damage away from the free-edges. Further, this avoids peeling at the free-edges of the specimen and the arrangement ensures fatigue damage initiates along the centreline.

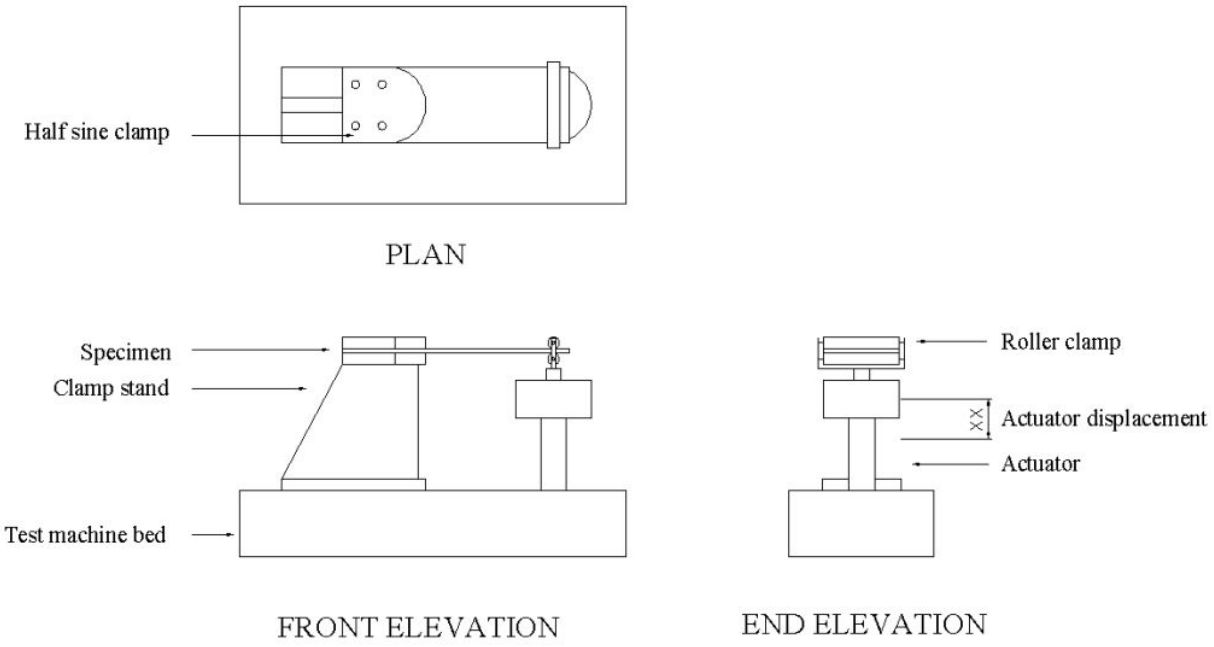

Figure 8.2. Fatigue rig in-situ on servo-hydraulic test machine

The laminate panels from which the specimens were cut were manufactured as in described in Chapter 4 but the specimens were 295 mm long by 100 mm wide and 1.5 mm in thickness. Various stacking sequences were manufactured, the purpose of these variations are described later. The clamped end was drilled to accept the clamp mounting bolts. Figure 8.4a shows a laminate in the undamaged condition. For reference Figure 8.4b shows a UD specimen with PTFE inserts as used in [63]. As the specimens are made of GFRP as in Chapter 7, it is possible to see the PTFE and also allows any damage to be visually observed in the specimen during fatigue.

The first laminate to be fatigue loaded was manufactured with a stacking sequence of $[0, 45, -45]_s$ and was subjected to 37800 cycles of fully reversed bending with a displacement amplitude of 30 mm at 1 Hz. Visual inspection of the specimen revealed delamination had propagated, the extent of the damage can be seen in Figure 8.4c and d. The visual images were obtained using a digital camera and illuminating the rear of the specimen. The delamination damage achieved can be appreciated when compared to the as manufactured laminate and the laminate with pseudo delamination inserts.

To reduce the number of fatigue cycles in which delamination may be initiated and propagated in laminates it was decided to manufacture specimens with stacking

sequences that generated a greater shear coupling ply mismatch. This was because it has been reported that the shear stress generated in angle-ply laminates can have a strong influence on delamination [134]. Using the material properties obtained in Chapter 4 it was possible to plot the shear coupling coefficient [107] specifically for the pre-preg material used in the specimens. The plot in Figure 8.3 shows this data for angles between ± 90˚ with respect to the 0˚ axis. The peak mismatch occurs when the plies are orientated at about ± 20˚. As expected there is no mismatch in the shear coupling coefficient for cross ply laminates (as discussed in Chapter 7) as the coefficient tends to zero when the plies are orientated at 0˚ and 90˚.

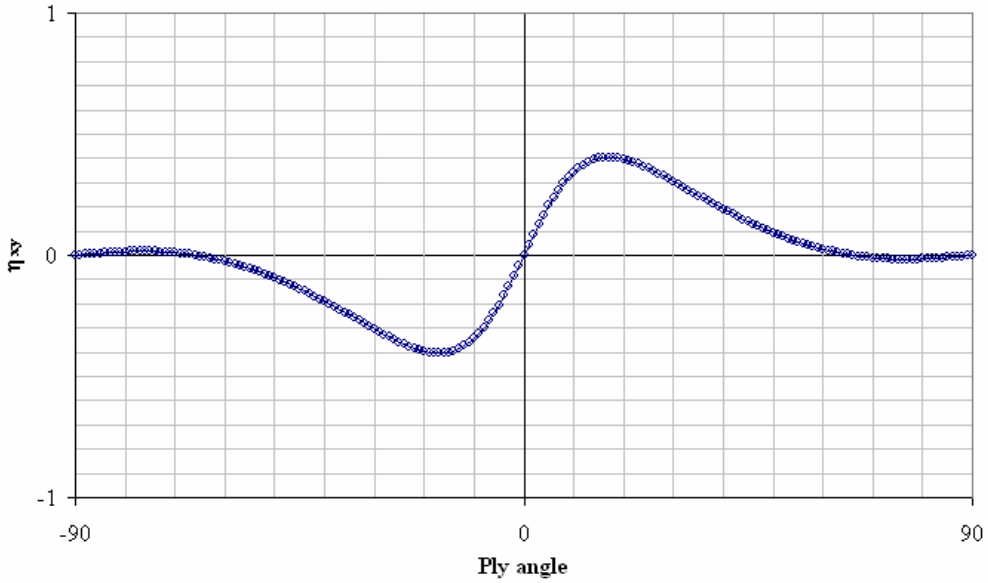

Figure 8.3. Mismatch due to ply orientations in laminate stack

Therefore a laminate was manufactured with a stacking sequence of $[0, 25, -25]_s$ and was subjected to 19600 cycles at 25mm displacement amplitude. The damaged laminate is shown Figure 8.4e and f and show that a significant delamination can be achieved over a much reduced fatigue period than that of the initial $[0, 45, -45]_s$ specimen. A further factor to consider is in Figure 8.4c, d, e and f surface cracking has occurred that is a result of the clamp corners causing damage to the surface plies. The clamp corners were rounded to prevent the surface damage.

The last laminate maintained the ± 25˚ angle plies within the laminate but they were separated by two 0 ˚ plies in the centre of the laminate which moved the angled plies away from the neutral axis of the laminate, resulting in a $[0, 25, -25, 0]_s$ laminate. The laminate was cycled for 19600 cycles again with 25 mm displacement amplitude. Figure 8.4g and h illustrate the delamination that was achieved. Inspection of Figure 8.4g and h (from the front and rear surface respectively) show that the delamination occurs at two

spatial locations through the laminate thickness; 1) between the first ± 25˚ laminae and 2) repeated between the second ± 25˚ laminae, i.e. between the 2nd and 3rd lamina and the 7th and 8th lamina from the surface ply.

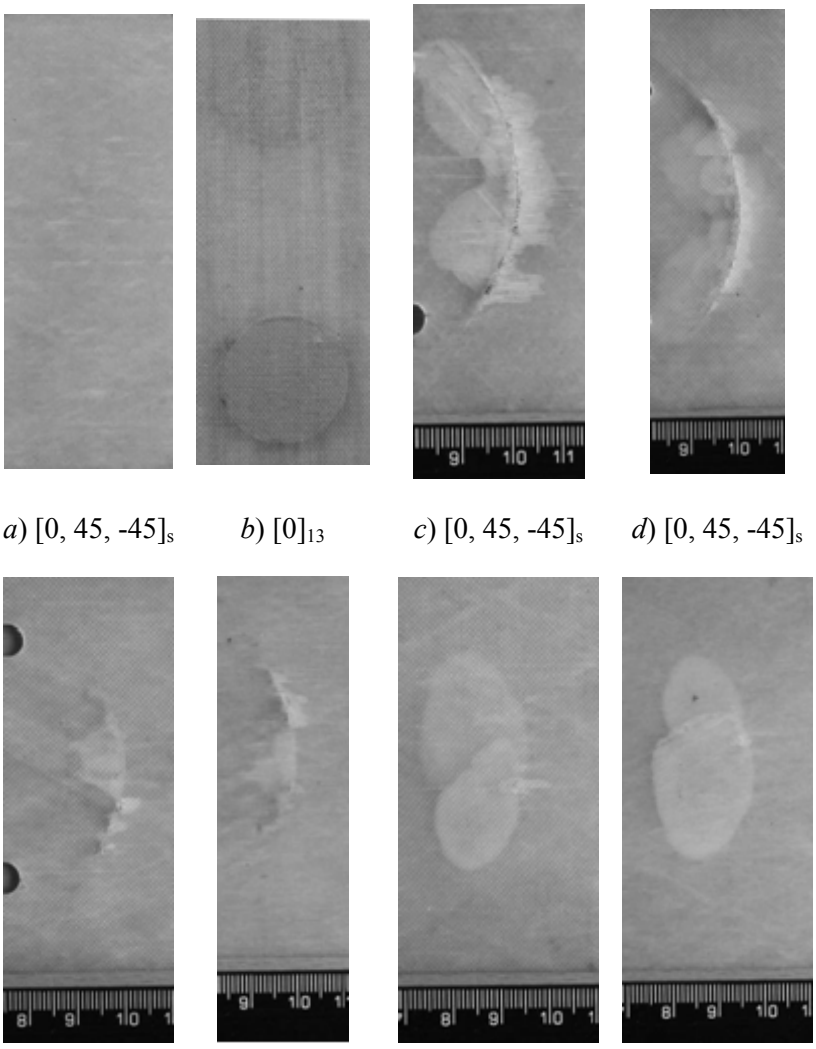

a) $[0, 45, -45]_s$ *b*) $[0]_{13}$ *c*) $[0, 45, -45]_s$ *d*) $[0, 45, -45]_s$

e) $[0, 25, -25]_s$ *f*) $[0, 25, -25]_s$ *g*) $[0, 25,-25, 0]_s$ *h*) $[0, 25,-25, 0]_s$

Figure 8.4. Delaminated GFRP specimens

8.3 Pulsed phase thermography

The delamination damage provided an excellent opportunity to assess PPT on subsurface damage, as it could be assessed against the visually observed position of the damage. PPT was introduced in Chapter 2; it is a relatively new approach that combines the traditional IRT techniques of pulse (PT) and modulated thermography (MT) [135]. It is a *passive* technique and therefore can be applied to large areas of in-service composite structures. Furthermore, it is relatively fast, so that inspections of large components can be carried out to pin-point areas of damage for further analysis. The experimental set-up

is shown in Figure 8.5 as no actuation of the specimen is required the set-up is simple and portable.

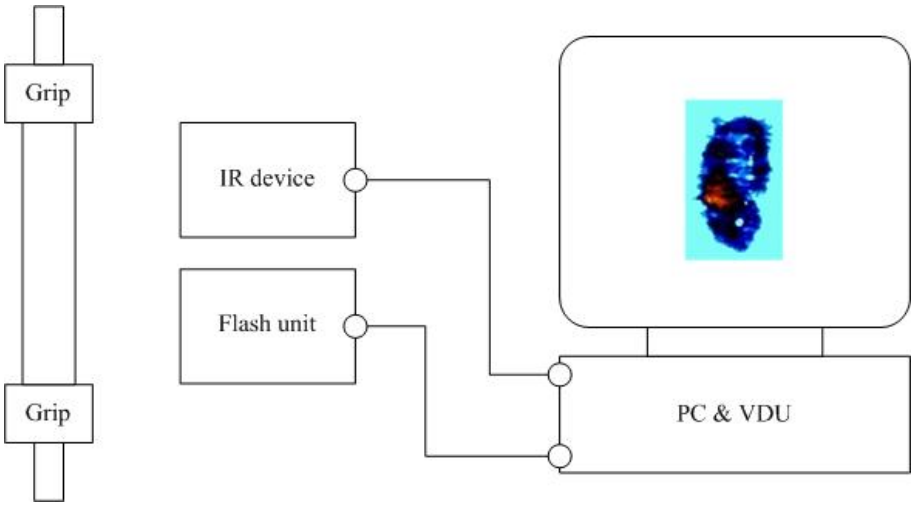

Figure 8.5. Pulse Phase Thermography operating schematic (*Reflection method*)

PPT offers benefits over the original IRT methods with improvement in contrast and analyses several frequencies in a single experiment. The theoretical background and initial tests using PPT were first reported in 1996 [135]; however, it is only in recent years that its potential as a tool for damage assessment has been cited [48]. As such it has not been developed into a mature technique, and the state of the art in terms of damage detection is not well established. Damage detection routines [48] have been performed on homogenous aluminium plates subject to gross defects (introduced as flat bottomed holes). Whilst it has been reported [48] that PPT has the potential to be applied to damaged composite structures the only reported studies have been restricted to the thermal modelling [136]. To the author's knowledge no experimental studies have been reported.

PPT is achieved by subjecting the structure under evaluation to a pulse of heat energy that propagates through the structure and subsequently analysing the thermal signature from the surface. A sequence of IR images is collected from the surface following the thermal pulse that captures the thermal decay *T(t)*. Mathematically the thermal pulse can be decomposed into a multitude of individual sinusoidal components [135] with various amplitudes and frequencies. The frequency content of these sinusoidal components, that diffuse through the structure and appear on the surface, can be obtained from the thermal images recorded using Fourier transformation analysis. The extraction and comparison of various specified frequency ranges, using a discrete one-dimensional Fourier transform at each pixel in the image, provides the basis for PPT. The frequency range analysed is dependent on the damage location and geometry within the specimen. The

output is provided in terms of the amplitude and phase of the frequency wave at the surface. The output is referenced relative to each pixel, at time *t*, in the field of view and as such no reference input is required but any change in transmission evident at the surface can be evaluated. Phase lag or attenuation, of the wave in question, at a pixel relative to another pixel will be evident in the analysis of the results. Any deviation in the phase or amplitude results is assumed to be apparent as a consequence of the specific diffusion path. The diffusion through the structure is influenced by the thermal conductivity, which will be modified at damage sites such as delaminated areas. Hence the heat diffusion through the damage will be modified and data from this region will have a different phase to that from undamaged material. Therefore, the damaged region will be revealed as a deviation in a phase plot. The use of deviations between data sets, or *novelty detection*, has been shown to provide a useful tool in damage identification [30].

As both PPT and TSA techniques require a sensitive IR device to record the thermal signature with time (the thermal decay and change respectively) it is possible that a damage assessment approach could be achieved using a single sensor; this would be beneficial for in-service applications and the combination of the two techniques would fulfil the five NDE criteria.

To establish the extent of the damage PPT was performed on the specimen at the end of the fatigue test routine, in reality this would determine the area that the TSA would be directed. The specimen was clamped in a vertical orientation and subjected to a metered thermal pulse using a Cullman camera flash unit positioned in contact with the rear surface of the specimen. A Cedip Silver 450M IR system was positioned 0.5 m from the front surface of the specimen and collected thermal data during the temperature decay from the surface. The basis of the set-up followed recommendations of Marinetti *et al.* [137]. The temporal information from the sequence of 500 thermal frames recorded was analysed for the frequency content of the constituent wave forms using a Fourier transform algorithm provided in the Cedip Altair software. The frequency range over which the analysis was carried out was between 0.1 and 1 Hz. The resolution of the results was determined by the frequency increment which was set at 0.09 Hz and thus provided 11 groups. The defect visible in Figure 8.6 is provided as a function of the phase difference of a 0.5 Hz frequency wave set. The defect is visible as a result of the modification of the diffusion path, due to the damage altering the thermal conductivity, from the energy source to the surface. (The delamination is essentially an air pocket and modifies the diffusion characteristics so that the damage could be visualised using the PPT technique). The phase reference is taken across the field of view with respect to the

defect area. The results of this are shown in Figure 8.6, it can be seen that they correlate well with the visual inspections in Figure 8.4. In all cases where delamination is present it can be seen that the PPT routine is capable of discerning the spatial extent of the subsurface damage.

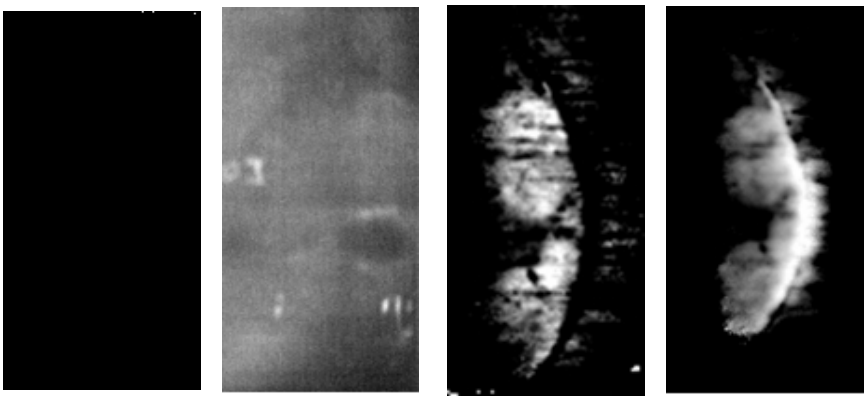

a) $[0, 45, -45]_s$ (No damage) b) $[0]_{13}$ (PTFE inserts) c) $[0, 45, -45]_s$ (Front) d) $[0, 45, -45]_s$ (Rear)

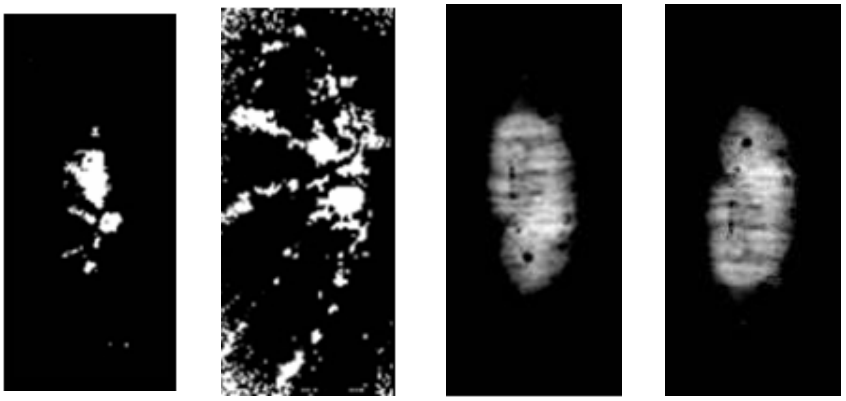

e) $[0, 20, -20]_s$ (Front) f) $[0,20,-20]_s$ (Rear) g) $[0, 25,-25, 0]_s$ (Front) h) $[0, 25,-25, 0]_s$ (Rear)

Figure 8.6. PPT results from delaminated specimens

The data shown in Figure 8.6g and h provide an interesting ability to observe the depth resolution of the PPT technique. The spatial distribution of the delamination can be observed in Figure 8.7a and c from the front and rear of the specimen respectively, the extents of the damage are bounded by the dashed white line. The delamination occurs at two positions through the laminate as dictated by the angle plies within the stacking sequence (which determine the initiation of the delamination).

Table 8.1. Ply stacking sequence and ply position from front surface

Ply number	1	2	3	4	5	6	7	8
Orientation	0	25	-25	0	0	-25	25	0

The delaminated area noted ‘1’ in Figure 8.7a occurs between the second and third plies and the area noted ‘2’ occurs between the sixth and seventh plies.

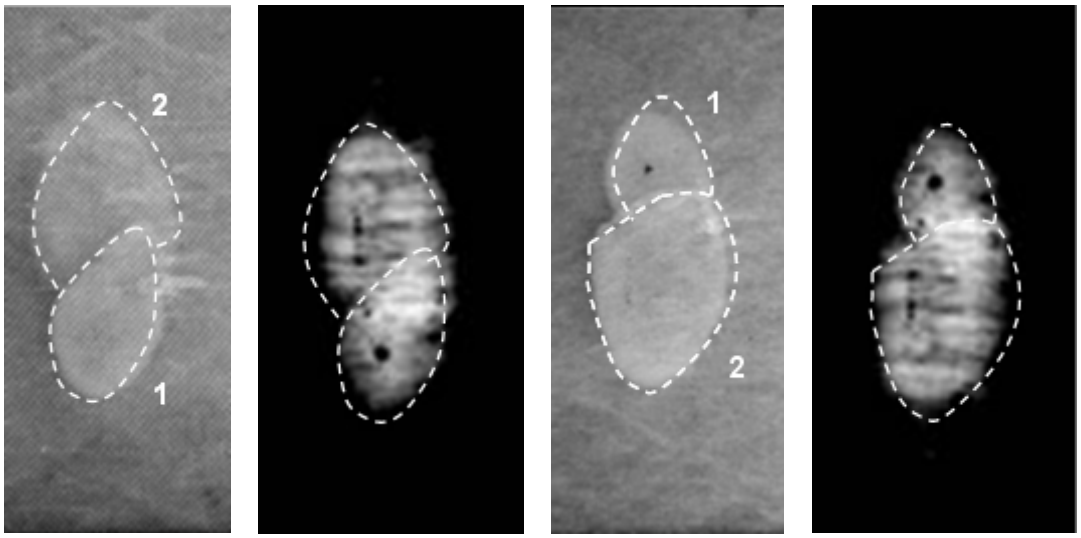

a) Visual front b) PPT front c) Visual rear d) PPT rear

Figure 8.7. Visual and PPT results from $[0, 25,-25, 0]_s$ delaminated specimen

It is possible to observe both areas ‘1’ and ‘2’ in the PPT data from both the front and rear of the specimen and thus illustrates that PPT is able to distinguish, in glass/epoxy specimens, this type of damage 6 plies from the surface which equates to a depth resolution of 1.5 mm using a simple camera flash unit to provide the heat pulse. As further specimens were not manufactured the maximum depth resolution could not be defined. However, using the fatigue routine described it would be possible to propagate delamination damage at differing depths through a laminate and define at what point the damage could no longer be detected. Furthermore, in the theoretical treatment of PPT it has been reported that it would be possible to make calculations to the depth of the defect [138, 139] this has not been carried out here and would be beneficial in future work. It should be noted the PPT has been verified with visual inspection for reasons and as discussed in Chapter 7 this would not be possible for in-service structures.

8.4 TSA damage analysis

It has been demonstrated that through consideration of the laminate stacking sequence and fatigue loading delamination damage can be reliably initiated and propagated in FRP laminates as required. In a similar manner to the damage assessment procedure introduced in Chapter 7 it was proposed to obtain thermoelastic data from the undamaged state and later from the damaged state. It was proposed that this would be achieved leaving the laminate in the fatigue rig (as Figure 8.2) and using the actuator

displacement to cyclically load the laminate. This introduces a challenge for the collection of thermoelastic data using the DeltaTherm as the laminate cannot be positioned directly in the field of view. The DeltaTherm system cannot be positioned above the fatigue rig as it must be maintained in a horizontal position due to the open storage of liquid nitrogen that is used to cool the IR detector. In [140] it was reported that a mirror could be used to collect thermoelastic data where a component was loaded horizontally; although a small reduction in the signal of 7.2 % was reported. As the attenuation is constant throughout the testing it could be incorporated in a calibration routine if necessary. The set-up for the fatigue rig is shown in Figure 8.8.

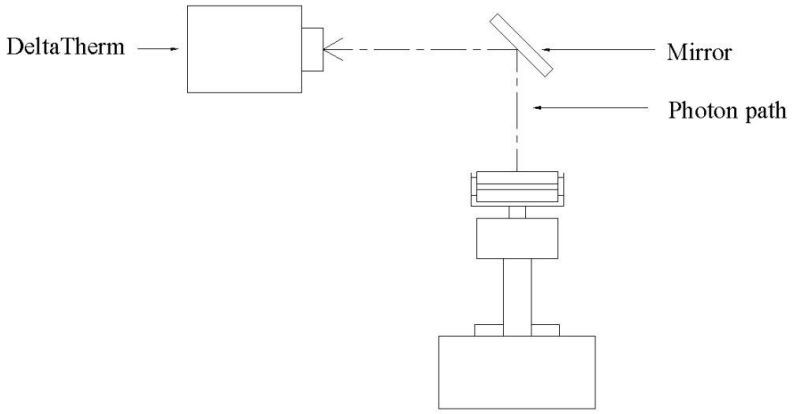

Figure 8.8. Method of TSA data collection from fatigue rig using in-situ mirror

The first laminate tested was the $[0, 25,-25, 0]_s$ specimen which was cyclically displaced at 1.3 mm at 10 Hz frequency and thermoelastic data collected. The expected stress distribution due to the clamping arrangement and the bending moment applied was clearly evident in the uncalibrated thermoelastic data however it was not possible to obtain thermoelastic results that indicated any deviation in the surface stress at the known location of the subsurface damage. Thermoelastic data was also collected from the $[0, 20, -20]_s$ and $[0, 45, -45]_s$ laminates (which had been delaminated) which were also loaded at the same amplitude and frequency; the thermoelastic data depicted the gross surface cracking but provided no further indication of the subsurface damage.

There are a number of reasons why the thermoelastic data did not display any variation in the signal around the delaminated area. Firstly, the delamination damage is located near the central axis of the laminate which under bending is a neutral axis and as such the damage may not effect the strain distribution within the laminate. Secondly, at 10 Hz the applied displacement amplitude was restricted to 1.3mm which may not cause sufficient strain within the laminate for the damage to modify the strain distribution at the surface. It may be possible to overcome both problems by manufacturing a thicker

laminate thereby allowing the angle plies to be moved further from the central axis and this would also result in a larger stress within the laminate for the achievable displacement amplitude at the required frequency. This potential solution is suggested for future work.

In response to the questions raised [63] during the attempt to observe pseudo delamination damage using TSA (discussed in Section 8.2) it was decided that a specimen could be fatigued in the rig and subject to TSA in uniaxial tension-tension loading. As the existence of delamination damage could be verified it would be possible to assess the response of TSA to delamination damage alone from a specimen subjected to a tensile load. To enable the specimen to be loaded between the grips of the servo-hydraulic test machine a narrower specimen of 45 mm width was manufactured. The specimen was subject to fatigue and TSA loading as detailed in Table 8.2.

Table 8.2. Cyclic loading

Specimen	TSA		Fatigue			
	Displacement	Frequency	Displacement	Frequency	Cycles	Number of steps
i)	0.167 mm	10 Hz	20 mm	1 Hz	6000	5

For consistency however the specimen was cyclically loaded using a constant displacement and this would allow for any unanticipated reduction in stiffness. Initial thermoelastic data was obtained before the specimen was fatigued and is shown in Figure 8.9a. Within the noise level expected the thermoelastic data recorded is uniform across the surface. The specimen was fatigued as detailed in Table 8.2 over 5 steps of approximately 6000 cycles or at a stage when it was evident that damage had visibly propagated. The data in Figure 8.9b, c, d and e show influence of the progression of the damage on the thermoelastic signal and compares to the damaged area seen in the visual image in Figure 8.9f which shows the damage evident at the end of the test.

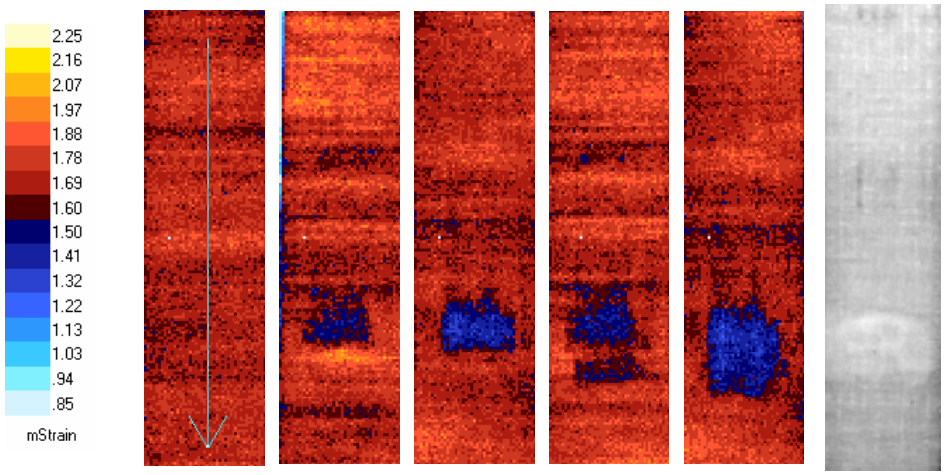

$(\Delta\varepsilon_L + \Delta\varepsilon_T)$ a) b) Step 1 c) Step 2 d) Step 3 e) Step 4 f) Visual

Figure 8.9. Thermoelastic signal from specimen through fatigue history

A line plot of the calibrated strain data (from the line indicated in Figure 8.9a) is plotted for each of the damage states in Figure 8.10. By comparing the plots from the damaged and the initial undamaged specimen it can be seen that there is a deviation between the pixels 81 to 111, which corresponds to the delaminated subsurface area. This deviation in strain demonstrates a reduction in the strain evident on the surface above the delaminated region. Immediately following the decrease in strain there is a sharp peak of strain at the delamination front. This behaviour is in agreement with work reported by Highsmith and Reifsnider [141] who used Moiré techniques to analyse strain around damage.

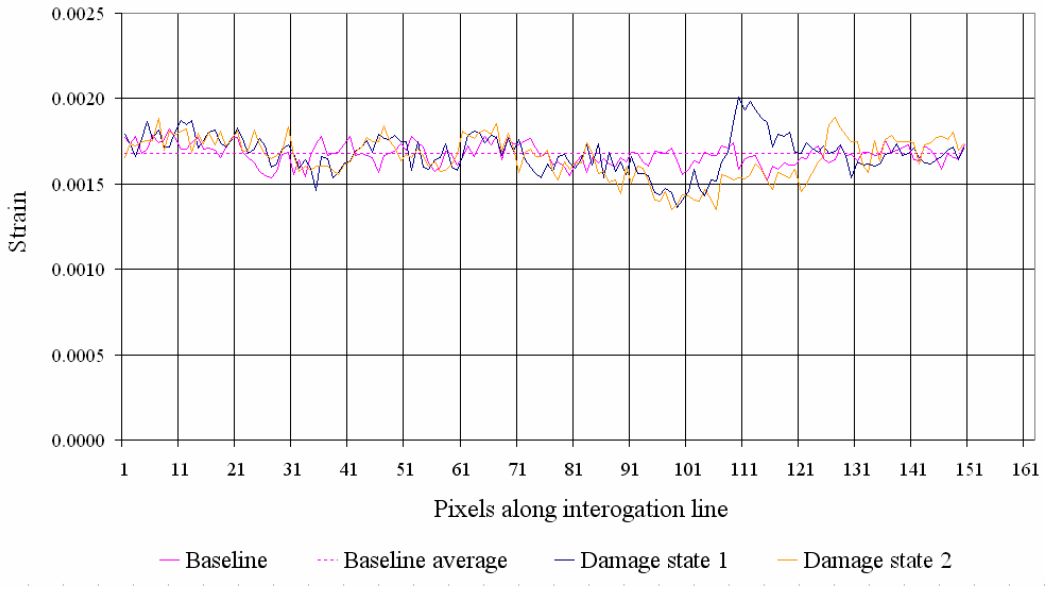

Figure 8.10. Comparison of thermoelastic signal from specimen

In a similar manner to the analysis of the strain sum data presented for the in-plane fatigue of the ±45 laminate in Chapter 7 the strain data for the delaminated specimen was analysed using the 'damage analysis' macro (as discussed in Section 7.8). Two data sets are compared; one from the step 1 (Figure 8.9b) and the other from the undamaged state (Figure 8.9a).

The results are shown in Figure 8.11; the full-field contour plot shows the regions that are affected by the subsurface delamination and in Figure 8.11b a line plot (as defined in Figure 8.9a) plots the data interrogated along the line. There are two regions of interest, from pixel 82 to 104, where the signal has increased/decreased significantly. Through the area corresponding to the delaminated region the signal is reduced by a factor of 0.8. At the delamination front there is a concentrated region of high signal 1.17 times greater than that recorded form the undamaged specimen. A further area of signal change has occurred due to the fatigue away from the delaminated area, this is located between pixels 19 to 27. This area corresponds to the section of the strip located between the rollers of the fatigue rig (Figure 8.2) where damage has also accumulated. The comparison of the thermoelastic data collected from the undamaged and damaged structure demonstrates the capability of TSA to provide information on strain redistribution caused by subsurface damage.

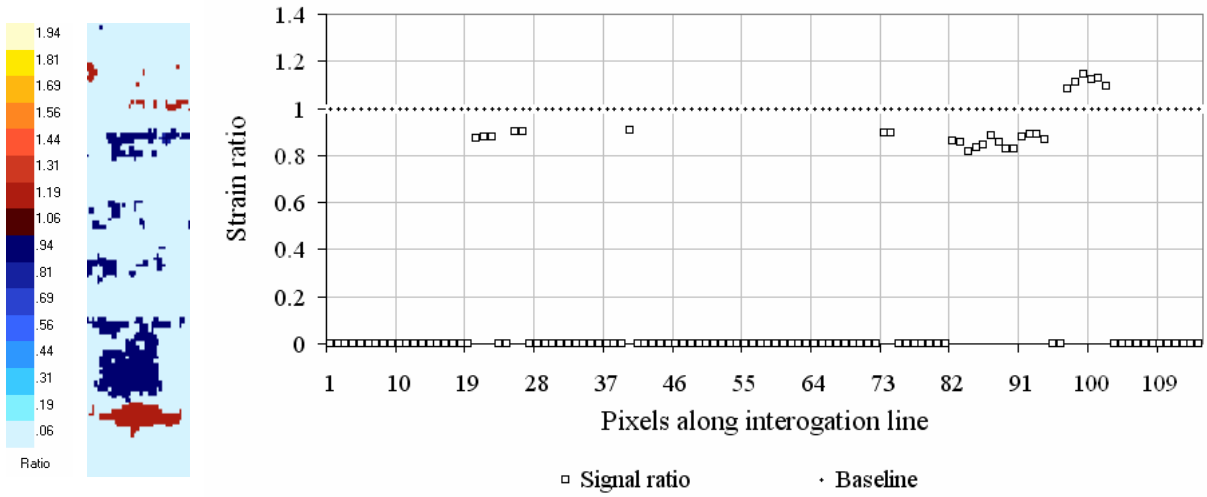

a) b)

Figure 8.11. Thermoelastic damage analysis ratio

8.5 Conclusions

A methodology has been presented to permit the integrity assessment of composite structure subject damage using two IR techniques to provide a non-contact, non-destructive and full-field damage assessment. This has been demonstrated on a GFRP specimen with delamination damage. A visualisation procedure highlighted the areas containing gross damage and has the potential to isolate regions were repair is necessary.

Chapter 9

Recommendations for future work and conclusions

9.1 Future work

The principal challenges formulated in the objectives of this thesis that allow the application of TSA to orthotropic materials in a quantitative manner have been achieved and incorporated into a methodology by which the technique can be applied to damaged composite components. The methodology has been demonstrated on GFRP laminates subject to fatigue damage and the results show that TSA has much promise in the area of damage assessment. During the experimental work it became evident that there were areas which through continued research would improve the technique and enable it to become more generally applicable. In the following section six topics are discussed that are recommended for future work.

9.1.1 Motion compensation

The thermoelastic data shown in Figure 7.11 was collected from a fatigue damaged specimen. At the hole boundary the thermoelastic data was blurred as a consequence of the test specimen motion during the cyclic loading. This is a recognised phenomenon in TSA and occurs near edges where the motion is such that data is collected from both the

ambient background and the component as the component strains between the extents of the peak and trough of the loading cycle. In these situations for each pixel that is projected onto an edge the differential between the specimen temperature and the ambient temperature is reported as ΔT rather than the temperature change expected from the thermoelastic effect. Therefore this data cannot be related to the change in the surface stresses. A robust method of compensating thermoelastic data for motion is not available for the DeltaTherm system at present and as such the data was presented with the effects of motion prominent at the hole. Although this has not caused any deficiency in the results or the analysis in this thesis it is expected that in a more general test, motion may obscure critical data. A method by which the motion may be compensated from the thermoelastic data is not a simple task. For example the expected strain around a discontinuity such as a hole is expected to vary in the longitudinal plane and therefore the motion will not be uniform. A technique is required that can compensate for both rotational and non-linear lateral motions.

9.1.2 Residual life measurements

The damage assessment routine presented in Chapter 7 and 8 have shown that TSA can be used in a quantitative manner to obtain the strain distribution in the neighbourhood of damage in laminated GFRP component. The damage metrics developed that were based on the thermoelastic response throughout the fatigue life can be used as a damage indicator; this is directly related to the level of fatigue damage. It would be interesting to incorporate the measurable redistribution of strain using TSA into strain based failure theories and therefore revise the strain inputs through the fatigue life to allow a more accurate analysis of the residual life to be achieved in a general sense for any component subject to a similar damage mechanism.

9.1.3 Depth resolution

TSA is a surface measurement technique and the ability to assess damage is reliant on the surface strain distribution being modified by the damage mechanism. It has been shown in Chapters 7 and 8 that both the subsurface and surface damage could be resolved in terms of strain changes. The delamination damage propagated in the uniaxial strip in Chapter 8 provided verification that subsurface damage (3 plies from the surface) caused sufficient surface strain distribution to be assessed through thermoelastic measurements. The ability to manufacture ‘delamination prone’ laminates and propagate delamination damage using the fatigue rig as detailed in Chapter 8 would provide the opportunity to assess the extent to which the subsurface damage could be analysed with

TSA. This would be possible by initiating delamination at various depths through a number of laminates which could be used in a thermoelastic benchmarking exercise. This information would enable the definition of the operational working parameters and sensitivity of the TSA technique.

9.1.4 Materials

All the FRP laminates used in Chapter 4 to 8 were manufactured from a single batch of SP systems E-glass epoxy material supplied in UD pre-preg form. This has maintained consistency through the analysis additionally the optical properties of the glass / epoxy constituents have provided the ability for damage to be visually observed for comparative analysis. The TSA technique however is not restricted to this material system and the theoretical derivations of the thermoelastic stress and strain formulations are applicable to orthotropic materials in general. The methods presented would be equally applicable to laminates with differing constituents including carbon fibre reinforced polymers (CFRP) which have application where a higher stiffness is required. However, developments in the manner in which fibre reinforcements are arranged within the lamina and the effect of this on the thermoelastic signal should be contemplated. In plain, satin or twill materials the reinforcing fibres are woven and results in the surface ply incorporating fibres both in the longitudinal and transverse orientation. It is likely that the thermoelastic analysis will be complicated as a uniform state of stress would not be expected across the surface.

To contend with different constituents and fibre patterns it would be useful to assess the effect on the thermoelastic signal in order that the TSA technique could be applied and analysed with certainty from a wide range of materials. It is envisaged that in a similar manner to strain calibration work presented in Chapter 4 that the majority of composite components will benefit from the resin-rich surface that provides an isotropic witness to the strain distribution from the surface ply which may ease the analysis.

A further material based consideration is the use of sandwich structures. Sandwich structures incorporate core material between two FRP skins; the purpose being two fold to increase the bending stiffness and provide improved shear strength. As the expected damage mechanisms differ in sandwich structures (i.e. debonding of the core and skin) it is possible that the method in which the component is loaded will need to be investigated. It is predicted to generate strain distributions the sandwich would have to be cyclically loaded with the structure subject to shear stress. Thereby in the vicinity of

the core debond it would be expected that shear load would be transferred to the composite skin which would be observed as a change in the strain.

9.1.5 Large structures

Using the assessment methodologies presented and following the verification of the TSA technique against a wide range of materials (as described above) its application to large representative structural components will be a possibility. Ideally this would be developed to the extent whereby TSA could be applied to structures outside of the laboratory; this introduces the conundrum of how to achieve the necessary cyclic loading. The technique of TSA is not alone in the requirement for the structure to experience a strain change to generate a response and it may be possible to use some of the proposed loading methods discussed during the review of the active assessment methods discussed in Chapter 2. These methods include pressure, vacuum or acoustical excitation that could be applied locally. There have also been developments in the DeltaTherm operating software which may provide alternatives to the application of a constant cyclic waveform to the component. It is envisaged that thermoelastic data may be collected using random input stresses in the future. This would permit, for example, the vibrations that are normally present in service (e.g. vibrations due to engine operation) to enable *in situ* measurements to be made. Further possibilities may include the use of an impact with instrumented hammer and measuring the transient impact and response. These would permit in-service analysis of components in a state of damage and timely assessment of the structural integrity. The development of these potential methods would be advantageous in the pursuit of applying TSA in a more rigorous and broad manner outside of the laboratory.

9.1.6 Continual monitoring

Whilst the prospects of a combined IR approach using PPT to direct TSA to areas of concern within a structure have been demonstrated the approach is largely restricted to off-line investigation where the component is periodically taken out of service for inspection regardless of the condition. For a structure in-service the cost implications of an off-line route of inspection are high as they necessitate a full sweep of the structure to locate any possible areas of concern (as discussed in Chapter 2). Operating damage assessment in this manner is not efficient and there exists an opportunity to detect damage onset and to move away from the reliance on periodic service intervals. To fill the gap of damage *detection* an on-line continual monitoring system would be beneficial; providing a signal to the operator at the onset of damage within a structure.

Ideally a sensing method would be incorporated within the structure and would remain dormant until a time where damage occurs above an acceptable threshold. These requirements outlined correspond to the potential capabilities of AE (introduced in Chapter 2) and it is a prospective candidate for such a method. The difficulties evident in pinpointing the source of the AE within an anisotropic 3D body require verification. However in the simplest form a network of sensors distributed through the structure would enable damage to be located to a smaller area of interest which could be later scanned using PPT. The anticipated assessment method is illustrated in Figure 8.1 whereby the AE precedes detailed PPT inspection and trigger an alarm for a PPT inspection to be carried out.

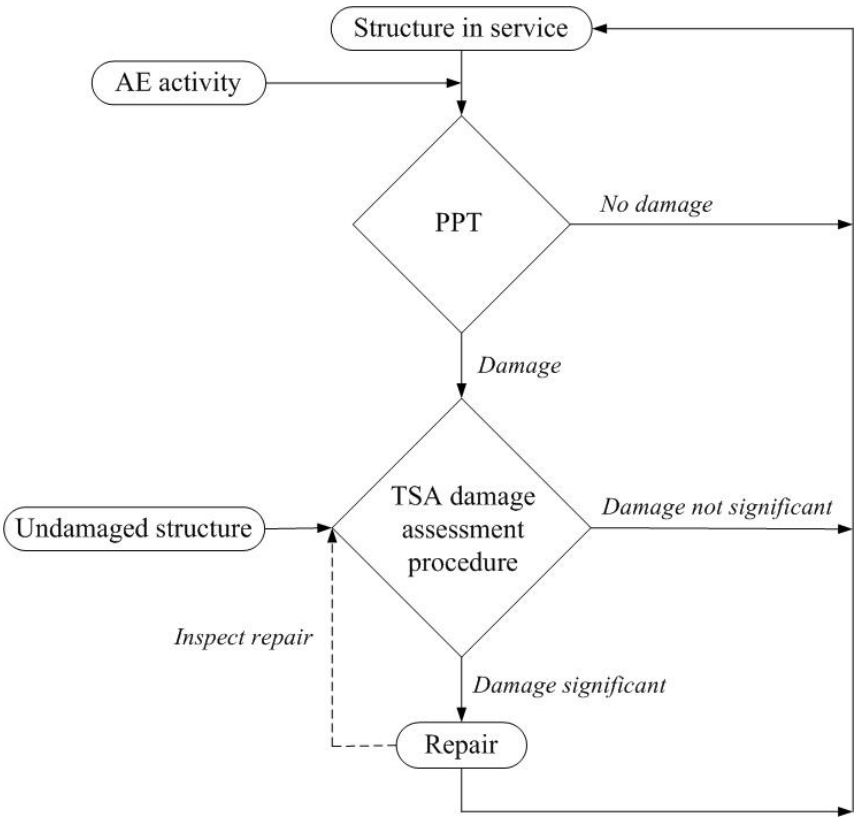

Figure 9.1. Modified damage assessment method

9.2 Conclusions

The development of the TSA damage assessment method for composite materials has been conducted with respect to specific stages that allow the effects of damage to be quantitatively analysed in terms of strain. These stages can be concluded as follows:

- Following the full derivation of the traditional thermoelastic theory for orthotropic bodies a calibration routine was developed so that quantitative strain values can be obtained from thermoelastic readings. A new strain calibration routine has been presented and verified. The calibration constant (B^*) is valid for specimens with a resin-rich layer and is based on an isotropic thermoelastic response from specimens that are mechanically orthotropic. As the goal of this work is to analyse localised changes in strains due to damage, the development of this calibration approach achieves a major objective in providing a methodology for thermoelastic damage assessment. Further, the strain calibration procedure presented will enable thermoelastic studies to be reported quantitatively and expand the application of TSA particularly in validation studies.

- Variation in the absolute temperature of the surface investigated by TSA has a significant effect on the recorded thermoelastic signal. It has been shown that the surface temperature will change during testing and without a suitable process to account for this the thermoelastic data cannot even be analysed in a qualitative manner. To overcome this problem a theoretical function has been developed that provides a power law relationship that can be used as the basis for temperature correction. This was achieved by consideration of Planck's law over the operating wavelengths of the DeltaTherm IR detector.

- The theoretical development of the temperature correction function was verified experimentally and accounted for the processing and optics of the DeltaTherm system. The correction process was validated on a variety of specimens subject to artificial and fatigue generated temperature increases. The development of a temperature correction methodology provides confidence that localised heating may be quantified and eliminated during the analysis of the thermoelastic data in damage studies. A methodology for applying the temperature correction procedure during post-processing of the thermoelastic data was devised. This involved the development of an algorithm that incorporated the correction factor in a point-by-point manipulation of the thermoelastic data at each pixel. This in

turn required the development of a method by which the thermal IR data from the DeltaTherm could be calibrated to Kelvin. This was achieved by developing a temperature calibration that was verified against radiometrically calibrated devices. The method and results presented highlight the need for the procedure to be applied to any thermoelastic data where the absolute temperature varies and thus has wider application in the analysis of TSA.

- The TSA technique has been applied to FRP composite components subject to fatigue damage using a damage assessment procedure. It has been shown that TSA can be used in a quantitative manner to obtain the strain distribution in the local to damage. Three types of damage have been studied: fibre breakage, delamination and matrix cracking. The damage types occurred together but specimens were designed so that a single damage type was the prominent cause of failure. Damage metrics have been developed that are based on the thermoelastic response throughout the fatigue life. The experimental work described in Chapter 7 has shown that these can be used as a damage indicator that is directly related to the level of fatigue damage that the specimen has been exposed to.

- An initial investigation on the possibility of combining TSA with a complementary IR technique (PPT) has been demonstrated in an IR damage assessment method. It has been shown that PPT can localise subsurface damage by providing the extent of damage spatially. The function of PPT in the method is to scan a component passively and on areas of concern highlighted use TSA to quantitatively assess the effect of the damage. The results collected were obtained from specimens that were delaminated in a purpose built fatigue rig. Thermoelastic strain data collected from a uniaxially loaded strip demonstrated the effect of the delamination on the strain distribution. A damage analysis macro provided a visual metric of the change in strain at the points of interest with respect to the undamaged specimen.

- The strain calibration and temperature correction methods that enable TSA to be applied quantitatively to damaged composite materials have not been accomplished prior to this work. The methods meet the objectives of the thesis and provide novel and vital methods applicable to TSA in general. The damage assessment methodology, that combines these methods, demonstrates the application of TSA to the damage assessment of composite materials.

References

1. **Daniel, I. M. and Ishai, O.**, *Engineering Mechanics of Composite Materials*. 1994: Oxford University Press.
2. **Dow, M. B.**, *The ACEE Program and Basic Composites Research at Langley Research Center (1975 to 1986)*. 1987, National Aeronautics and Space Administration: Hampton, VA.
3. **Harris, C. E., Starnes (Jr), J. H., and Shuart, M. J.**, *An assessment of the state-of-the-art in the design and manufacturing of large composite structures for aerospace vehicles*. 2001, Langley Research Center: Hampton, Virginia. p. 1-50.
4. **Cripps, R. M.**, Design and development of lifeboats - damage evaluation and repair of composite structures. *Applied Mechanics and Materials*, 2005, **3-4**, 3-8.
5. **Mouritz, A. P., Gellert, E., Burchill, P., and Challis, K.**, Review of advanced composite structures for naval ships and submarines. *Composite Structures*, 2001, **53** (1), 21-41.
6. **Ferabolia, P. and Masini, A.**, Development of carbon/epoxy structural components for a high performance vehicle. *Composites Part B: Engineering*, 2004, **35** (4), 323–330.
7. **Brøndsted, P., Lilholt, H., and Lystrup, A.**, Composite materials for wind power turbine blades. *Annual Review of Materials Research*, 2005, **35**, 505–538.
8. **Ramakrishna, S., Mayer, J., Wintermantel, E., and Leong, K. W.**, Biomedical applications of polymer-composite materials: a review *Composite Science Technology*, 2001, **61** (9), 1189-1224.
9. **Prince, K.**, Composites win over sports market. *Reinforced plastics*, 2002, **46** (9), 48-51.
10. **Ferguson, R.** *Large Scale Composite Testing at Airbus Filton Site*. In *2nd International Conference on Composites Testing and Model Identification*. 2004. Bristol, UK.
11. **Tserpes, K. I., Papanikos, P., Labeas, G., and Pantelakis, S.**, Fatigue damage accumulation and residual strength assessment of CFRP laminates. *Composite Structures*, 2004, **63** (2), 219–230.
12. **Ganguli, R., Chopra, I., and Haas, D. J.**, Simulation of helicopter rotor-system structural damage, blade mistracking, friction, and freeplay. *Journal of Aircraft*, 1998, **35** (4), 591-597.
13. **Boller, C.**, Ways and options for aircraft structural health management. *Smart materials and structures*, 2001 **10** (3), 432–440.
14. **Worden, K. and Farrar, C. R.**, An introduction to structural health monitoring. *Philosophical Transactions of the Royal Society A: Mathematical, Physical and Engineering Sciences*, 2007, **365** (1851), 303 - 315.
15. **Flynn, B. W., Bodine, J. B., Dopker, B., Finn, S. R., Griess, K. H., Hanson, C. T., Harris, C. G., Nelson, K. M., Walker, T. H., Kennedy, T. C., and Nahan, M. F.**, *Advanced technology composite fuselage – repair and damage assessment supporting maintenance*. 1997.

16. **Bar-Cohen, Y.**, Emerging NDE Technologies and Challenges at the Beginning of the 3rd Millennium - Part I. *NDT.net*, 2000, **5** (2)
17. **Li, H. C. H., Herszberg, I., Davis, C. E., Mouritz, A. P., and Galea, S. C.**, Health monitoring of marine composite structural joints using fibre optic sensors. *Composite Structures*, 2006 **75** (1-4), 321–327.
18. **Kessler, S. S. and Spearing, S. M.** *In-situ sensor-based damage detection of composite materials for structural health monitoring*. In *AIAA / ASME SDM Conference*. 2002.
19. **Birchon, D.**, *Non-destructive testing* 1975: Oxford University Press
20. **Pitarresi, G. and Patterson, E. A.**, A review of the general theory of thermoelastic stress analysis. *The Journal of Strain Analysis for Engineering Design*, 2003, **38** (5), 405-417.
21. **Stanley, P. and Chan, W. K.**, Quantitative stress analysis by means of the thermoelastic effect. *The Journal of Strain Analysis for Engineering Design*, 1985, **20** (3), 129-137.
22. **Dulieu-Smith, J. M.**, Alternative calibration techniques for quantitative thermoelastic stress analysis. *Strain*, 1995, **31** (1), 9-16.
23. **Dulieu-Barton, J. M. and Stanley, P.**, Development and applications of thermoelastic stress analysis. *The Journal of Strain Analysis for Engineering Design*, 1998, **33** (2), 93-104.
24. **Stanley, P. and Chan, W. K.**, The application of thermoelastic stress analysis to composite materials. *Journal of Strain Analysis*, 1988, **23** (3), 137-143.
25. **Dulieu-Smith, J. M., Quinn, S., Shenoi, R. A., Read, P. J. C. L., and Moy, S. S. J.**, Thermoelastic stress analysis of a GRP tee joint. *Applied Composite Materials*, 1997, **4** (5), 283-303.
26. **Dulieu-Barton, J. M., Emery, T. R., Quinn, S., and Cunningham, P. R.**, A temperature correction methodology for quantitative thermoelastic stress analysis and damage assessment. *Measurement Science and Technology*, 2006 **17** (6), 1627-1637.
27. **Worden, K. and Dulieu-Barton, J. M.**, An overview of intelligent fault detection in systems and structures. *Structural Health Monitoring*, 2004, **3** (1), 85-98.
28. **Suresh, S.**, *Fatigue of materials* 2ed. 1998, Cambridge: Cambridge University Press.
29. **Rebiere, J. L., Maatallah, M. N., and Gamby, D.**, Initiation and growth of transverse and longitudinal cracks in composite cross-ply laminates. *Composite Structures*, 2001, **53** (2), 173-187.
30. **Worden, K.**, Structural fault detection using a novelty measure. *Journal of Sound and Vibration*, 1997, **201** (1), 85-101.
31. **Talreja, R.**, *Fatigue of composite materials*. 1987: Technomic
32. **Staszewski, W. J.**, Monitoring on-line integrated technologies for operational reliability - MONITOR. *Air & Space Europe*, 2000, **2** (4), 67–72.
33. **Pagano, N. J. and Schoeppner, G. A.**, *Delamination of Polymer Matrix Composites: Problems and Assessment*. Comprehensive Composite Materials, ed. Kelly, A. and Zweben, C. Vol. 2. 2000: Elsevier.
34. **O'Brien, T. K.** Composite Materials: Testing and Design, ed. Garbo, S.P. Vol. 9. 1990, Philadelphia: American Society for Testing and Materials.
35. **Pagano, N. J. and Pipes, R. B.**, The influence of stacking sequence on laminate strength. *Journal of Composite Materials*, 1971, **5** (1), 50-57.
36. **Cunningham, P. R., Dulieu-Barton, J. M., Dutton, A. G., and Shenoi, R. A.**, Thermoelastic characterisation of damage around a circular hole in a GRP component. *Key Engineering Materials*, 2001, **204-205**, 453-463.
37. **Padhi, G. S., Shenoi, R. A., Moy, S. S. J., and Hawkins, G. L.**, Progressive failure and ultimate collapse of laminated composite plates in bending. *Composite Structures*, 1998, **40** (3-4), 277-291.
38. **Guild, F. J. and Adams, R. D.**, Detection of cracks in damaged composite materials. *Journal of Physics D: Applied Physics*, 1981, **14** (8), 1561-1573.

39. **Marks, P.**, Warning Signs. *New Scientist*, 2006, 38-41.
40. **Larsen, W. E., Cooksy, K. D., and Zuk, J.**, Managing aviation safety through inspection information technology *IEEE Industry Applications Magazine*, 2001 **7**(3), 40-45.
41. **Anon**, *Nondestructive active testing techniques for structural composites*, in *MIL-HDBK-793(AR)*. 1989.
42. **Khan-Biman, A. U.**, Non-destructive testing applications in commercial aircraft maintenance. *The e-Journal of Nondestructive Testing & Ultrasonics*, 1999, **4** (6)
43. **Cheeke, J. D. N.**, *Fundamentals and applications of ultrasonic waves*. 2002: CRC Press.
44. *Nondestructive active testing techniques for structural composites*. 1989.
45. **Dance, W. E. and Middlebrook, J. B.**, *Neutron Radiographic Nondestructive Inspection for Bonded Composite Structures, Nondestructive Evaluation and Flaw Criticality for Composite Materials*. ASTM STP 696, ed. Pipes, R.B. 1979, Philadelphia American Society for Testing and Materials.
46. **Maldague, X. P. V.**, *Theory and Practice of Infrared Technology for Nondestructive Testing*, ed. Chang, K. 2001: John Wiley and Sons.
47. **Maldague, X., Galmiche, F., and Ziadi, A.**, Advances in pulsed phase thermography. *Infrared Physics & Technology*, 2002, **43** (3), 175–181.
48. **Krishnapillai, M., Jones, R., Marshall, I. H., Bannister, M., and Rajic, N.**, Thermography as a tool for damage assessment *Composite Structures*, 2005, **67** (2), 149-155.
49. **Hung, Y. Y.**, Applications of digital shearography for testing of composite structures. *Composites Part B: Engineering*, 1999, **30** (7), 765–773.
50. **Badcock, R. A. and Fernando, G. F.**, An intensity-based optical fibre sensor for fatigue damage detection in advanced fibre-reinforced composites. *Smart Material Structures*, 1995 **4**,223-230.
51. **Hearn, E. J.**, *Mechanics of materials: an introduction to the mechanics of elastic and plastic deformation of solids and structural materials* 1985: Butterworth-Heinemann Ltd.
52. **Richardson, M. O. W., Zhang, Z. Y., Wisheart, M., Tyrer, J. R., and Petzing, J.**, ESPI non-destructive testing of GRP composite materials containing impact damage. *Composites Part A: Applied science and manufacturing*, 1998, **29** (7), 721-729.
53. **Chau, F. S., Toh, S. L., Tay, C. J., and Shang, H. M.**, Some examples of non destructive flaw detection by shearography. *Journal of Nondestructive Evaluation*, 1989, **8** (4), 225-234.
54. **Brillaud, J. and Lagattu, F.**, Limits and possibilities of laser speckle and white-light image-correlation methods: theory and experiments. *Applied Optics*, 2002, **41** (31), 6603-6613.
55. **Clocksin, W. F., da Fonseca, J. Q., Withers, P. J., and Torr, P. H. S.** *Image processing issues in digital strain mapping*. In *Applications of Digital Image Processing XXV*. 2002: Proceedings of SPIE.
56. **Anon**, *Optical deformation and strain field imaging*, LA Vision.
57. **Godara, A. and Raabe, D.**, Influence of fiber orientation on global mechanical behaviour and mesoscale strain localisation in a short glass-fiber-reinforced epoxy polymer composite during tensile deformation investigated using digital image correlation. *Composites Science and Technology*, 2007, **In press**
58. **Tomlinson, R. A. and Calvert, G. C.**, Industrial applications of thermoelastic stress analysis. *Applied Mechanics and Materials*, 2004, **1-2**, 165-170.
59. **Paynter, R. J. H. and Dutton, A. G.**, The use of a second harmonic correlation to detect damage in composite structures using thermoelastic stress measurements. *Strain*, 2003, **39** (2), 73-78.
60. **Dulieu-Barton, J. M. and Stanley, P.**, Applications of thermoelastic stress analysis to composite materials. *Strain*, 1999, **35** (2), 41-48.

61. **Pitarresi, G., Found, M. S., and Patterson, E. A.**, An investigation of the influence of macroscopic heterogeneity on the thermoelastic response of fibre reinforced plastics. *Composites Science and Technology*, 2005, **65** (2), 269-280.
62. **Mackin, T. J. and Roberts, M. C.**, Evaluation of damage evolution in ceramic-matrix composites using thermoelastic stress analysis. *Journal of American Ceramic Society*, 2000, **83** (2), 337-343.
63. **Cunningham, P. R., Dulieu-Barton, J. M., Dutton, A. G., and Shenoi, R. A.**, The effect of ply lay-up on the thermoelastic repsonse of laminated composites. *Key Engineering Materials*, 2002, **221-222**, 325-336.
64. **Santulli, C., Dulieu-Barton, J. M., and Cantwell, W.** *Thermoelastic investigation of impact damaged woven GRP composites*. In *International Conference on Modern Practice in Stress and Vibration Analysis*. 2000. Nottingham.
65. **Ratcliffe, C. P. and Bagaria, W. J.**, Technique for locating delamination in a composite beam. *American Institute of Aeronautics and Astronautics Journal*, 1998, **36** (6), 1074-1077.
66. **Gherlone, M., Mattone, M., Surace, C., Tassotti, A., and Tessler, A.**, Novel vibration-based methods for detecting delamination damage in composite plate and shell laminates. *Key Engineering Materials*, 2005, **293-294**, 289-296.
67. **Trendafilova, I.**, An investigation on vibration-based damage detection in an aircraft wing scaled model. *Key Engineering Materials*, 2005, **293-294**, 321-328.
68. **Wevers, M.**, Listening to the sound of materials: acoustic emission for the analysis of material behaviour. *NDT&E International*, 1997, **30** (2), 99-102.
69. **Huguet, S., Godin, N., Gaertner, R., Salmon, L., and Villard, D.**, Use of acoustic emission to identify damage modes in glass fibre reinforced polyester. *Composites Science and Technology*, 2002, **62** (10-11), 1433-1444.
70. **Wevers, M. and Surgeon, M.**, *Acoustic Emission and Composites*. Comprehensive Composite Materials. Vol. 5. 2000: Elsevier.
71. **Horn, G., Mackin, T. J., and Kurath, P.**, Estimating residual life of polyurethane composites using thermoelasticity. *Symposium on Nondestructive Evaluation (NDE) and Materials Properties IV as presented at the 1999 TMS Annual Meeting; San Diego*, 1999, 11-14.
72. **Horn, G. P., Mackin, T. J., and Kurath, P.**, Estimating the residual fatigue lifetimes of impact-damaged composites using thermoelastic stress analysis. *Polymer Composites*, 2001, **22** (3), 420-431.
73. **Thompson, W.**, Dynamical theory of heat with numerical results deduced from Mr Joule's equivalent of a thermal unit and M Regnault's observation on steam. *Transactions of the Royal Society of Edinburgh*, 1853, **20**, 261-283.
74. **Biot, M. A.**, Thermoelasticity and irreversible thermodynamics *Journal of Applied Physics*, 1956, **27**, 241-242.
75. **Aiello, M. A. and Ombres, L.**, Environmental effects on the mechanical properties of Glass-FRP and Aramid-FRP rebars. *Mechanics of Composite Materials*, 2000, **36** (5), 395-398.
76. **Rogers, G. F. C. and Mayhew, Y. R.**, *Engineering Thermodynamics: Work and Heat Transfer*. Fourth ed. 1992: Longman.
77. **Potter, R. T.**, *Stress analysis in laminated fibre composites by thermoelastic emission*, in *Proceedings of the 2nd international conference on stress analysis by thermoelastic techniques*. 1987: London, UK. p. 110-120.
78. **Bakis, C. E. and Reifsnider, K. L.**, The adiabatic thermoelastic effect in laminated fiber composites. *Journal of Composite Materials*, 1991, **25** (7), 809-830.
79. **Wong, A. K.**, A non-adiabatic thermoelastic theory for composite laminates. *Journal of Physics and Chemistry Solids*, 1991, **52** (3), 483-494.
80. **Belgen, M. H.**, Structural stress measurements with an infrared radiometer. *Instrument Society of America Transcripts*, 1967, **6**, 49-53.

81. **Lesniak, J. R. and Boyce, B. R. A.** *High-speed differential thermographic camera*. In *Proceedings of Society for Experimental Mechanics Spring Conference*. 1994. Baltimore.
82. **Anon**. *Stress Photonics - Technical Specifications*. [cited 2007 18th March]; Available from: http://www.stressphotonics.com/TSA/TSA_Intro.html.
83. **Childs, P. R. N.**, *Practical temperature measurement*. First Edition ed. 2001: Butterworth-Heinemann.
84. **Nicholas, J. V. and White, D. R.**, *Traceable Temperatures*. Second ed. 2001: Wiley.
85. **Harwood, N. and Cummings, W. N.**, *Thermoelastic stress analysis*. 1991, New York: Adam Hilger.
86. **Jamieson, J. A., McFee, R. H., Plass, G. N., Grube, R. H., and Richards, R. G.**, *Infrared Physics and Engineering*. 1963: McGraw-Hill.
87. **Haselgrove, C. B. and Miller, J. C. P.**, *Mathematical tables* Tables of the Riemann zeta function. Vol. 6 1960: Royal Society Mathematical Tables Committee.
88. **Kobayashi, A. S.**, *Handbook on experimental mechanics*. 1987: Prentice-Hall International.
89. **Enke, N. F. and Sandor, B. I.** *Cyclic plasticity analysis by differential infrared thermography*. In *Proceedings Sixth International Congress Experimental Mechanics*. 1988. Portland.
90. **Quinn, S.**, *Thermoelastic stress analysis of oblique holes in flat plates and cylinders*. 2000 University of Liverpool
91. **Fulton, M. C.**, *Advanced topics in thermoelastic stress analysis* 1998 University of Liverpool.
92. **Ometron**, *The Ometron 4010 Series for SPATE and VPI*, in *Operator's manual*. 1997: London.
93. **Dulieu-Barton, J. M., Earl, J. S., and Shenoi, R. A.**, Determination of the stress distribution in foam-cored sandwich construction composite tee joints. *The Journal of Strain Analysis for Engineering Design.*, 2001, **36** (6), 545-560.
94. **Dulieu-Barton, J. M., Quinn, S., Eyre, C., and Cunningham, P. R.** *Development of a temperature calibration device for thermoelastic stress analysis*. In *Advances in Experimental Mechanics* 2004: Trans Tech.
95. **Hahn, F., Kensche, C. W., Paynter, R. J. H., and Dutton, A. G.**, Design, fatigue test and NDE of a sectional wind turbine rotor blade. *Journal of Thermoplastic Composite Materials*, 2002, **15** (3), 267-277.
96. **Mackin, T. J. and Purcell, T. E.**, The use of thermoelasticity to evaluate stress redistribution and notch sensitivity in ceramic matrix composites. *Experimental Techniques*, 1996, **20** (2), 15-20.
97. **Brown, K.** *Calibration studies - Collaborative report by the United Kingdom Stress Pattern Analysis by Thermal Emission (SPATE) users' group*. In *Proceedings of 2nd International Conference on Stress Analysis by Thermoelastic Techniques*. 1987 London, UK: Society of Photo-Optical Instrumentation Engineers.
98. **Dunn, S. A.**, Analysis of thermal conduction effects on thermoelastic temperature measurements for composite materials. *Journal of Applied Mechanics*, 1992, **59** (3), 552-558.
99. **El-Hajjar, R. F. and Haj-Ali, R. M.**, A quantitative thermoelastic stress analysis method for pultruded composites. *Composites Science and Technology*, 2003, **3** (7), 967-978.
100. **Barone, S. and Patterson, E. A.**, Polymer coating as a strain witness in thermoelasticity. *Journal of Strain Analysis*, 1998, **33** (3), 223-232.
101. **Mahoney, B. J.**, *Quantifying distributed damage in composites via the thermoelastic effect*. 1991, Wisconsin University.
102. **El-Hajjar, R. F. and Haj-Ali, R. M.**, IR-Thermography for strain analysis in pultruded fibre reinforced plastics. *Experimental Techniques*, 2004, **28** (2), 19-22.

103. **Cunningham, P. R., Dulieu-Barton, J. M., Dutton, A. G., and Shenoi, R. A.**, Thermoelastic characteristic of damage around a circular hole in a GRP component. *Key Engineering Materials*, 2001, **204-205**, 453-463.
104. **Uenoya, T. and Fujii, T.** *Characterization of real damage in carbon fabric composite with toughened matrix through thermoelastic technique*. In *4th International Conference on Deformation and Fracture of Composites*. 1997. Manchester.
105. **Dulieu-Barton, J. M. and Chapman, L. E.**, On the thermoelastic analysis of impact damage on foam-cored sandwich-construction composites. *Key Engineering Materials*, 1999, **167-168** 35-42.
106. **Jones, R., Heller, M., Lomardo, D., Dunn, S., Paul, J., and Saunders, D.**, Thermoelastic assessment of damage growth in composites. *Composite Structures*, 1989, **12** (4), 291-314.
107. **Datoo, M.**, *Mechanics of Fibrous Composites*. 1991: Elsevier Applied Science.
108. **Kalogiannakis, G., Hemelrijck, D. V., and Assche, G. V.**, Measurements of Thermal Properties of Carbon/Epoxy and Glass/Epoxy using Modulated Temperature Differential Scanning Calorimetry. *Journal of Composite Materials*, 2004, **38** (2), 163-175.
109. **Dulieu-Smith, J. M. and Stanley, P.**, On the interpretation and significance of the Grüneisen parameter in thermoelastic stress analysis. *Journal of Materials Processing Technology*, 1998, **78** (1), 75-83.
110. **Dulieu-Smith, J. M.**, *Development and application of thermoelastic stress analysis* 1993, University of Manchester.
111. **Lesniak, J. R., Boyce, B. R., and Sandor, B. I.**, *Thermographic stress analysis / NDE via focal-plane array detectors* in *NASA Contract Report 19262*. 1991
112. **Gamestedt, K. E., Redon, O., and Brøndsted, P.** *Fatigue dissipation and Failure in Unidirectional and Angle-Ply Glass fibre/Carbon Fibre Hybrid Laminates*. In *5th seminar on Experimental Techniques and Design in Composite Materials*. 2002: Key Engineering Materials.
113. **Pye, C. J. and Adams, R. D.**, Heat emission from damaged composite materials and its use in non-destructive testing. *Journal of Physics D: Applied Physics*, 1981, **14** (5), 927-941.
114. **Reifsnider, K. L. and Williams, R. S.**, Determination of fatigue-related heat emission in composite materials *Experimental Mechanics*, 1974, **14** (12), 479-485.
115. **Farrar, C. R. and Worden, K.**, An introduction to structural health monitoring. *Philosphical Transactions of the Royal Society*, 2007, **365** (1851), 303-315.
116. **Bai, W. and Wong, B. S.**, Evaluation of defects in composite plates under convective environments using lock-in thermography. *Measurement Science and Technology*, 2001, **12** (2), 142-150.
117. **Dreyfus, M. G.**, Spectral variation of blackbody radiation. *Applied Optics*, 1963, **2** (11), 1113-1116.
118. **Mitchell, D., Wyndham, C. H., and Hodgson, T.**, The selection of a biothermal radiometer. *Journal of Science Instruments*, 1967, **44** (10), 847-851.
119. **Dulieu-Barton, J. M., Quinn, S., Eyre, C., and Cunningham, P. R.**, Development of a temperature calibration device for thermoelastic stress analysis. *Applied Mechanics and Materials*, 2004, **1-2**, 197-204
120. **Masters, J. E. and Reifsnider, K. L.**, eds. *An investigation of cumulative damage development in quasi-isotropic graphite/epoxy laminates*. Damage in composite materials, ASTM STP 775, ed. Reifsnider, K.L. 1982, American Society for Testing and Materials. 40 - 62.
121. **Tao, J. and Sun, C. T.**, Influence of Ply Orientation on Delamination in Composite Laminates *Journal of Composite Materials*, 1998, **32** (21), 1933-1947.
122. **Talreja, R.**, Damage analysis for structural integrity and durability of composite materials. *Fatigue and Fracture of Engineering Materials and Structures*, 2005, **29** (7), 481–506.

123. **Rowlands, R. E., Daniel, I. M., and Whiteside, J. B.**, Stress and failure analysis of a glass-epoxy composite plate with a circular hole. *Experimental Mechanics*, 1973, **13** (1), 31-37
124. **Sendeckyj, G. P., Maddux, G. E., and Porter, E.**, eds. *Damage documentation in composites by stereo radiography*. Damage in composite materials, ASTM STP 775, ed. Reifsnider, K.L. 1982, American Society for Testing and Materials. 16 - 26.
125. **Rotem, A. and Hashin, Z.**, Fatigue failure of angle ply laminates. *AIAA Journal*, 1976, **14**, 868-872.
126. **Amara, K., Tounsi, A., Megueni, A., and Adda-Bedia, E. A.**, Effect of transverse cracks on the mechanical properties of angle-ply composite laminates. *Theoretical and Applied Fracture Mechanics*, 2006, **45** (1), 72-78.
127. **Rotem, A.**, Fatigue failure of multidirectional laminate. *AIAA Journal*, 1979, **17** (3), 271-277.
128. **Carlsson, L.**, Interlaminar stresses at a hole in a composite member subjected to in-plane loading. *Journal of Composite Materials*, 1983, **17** (3), 238-249.
129. **Van Paepegem, W. and Degrieck, J.**, Coupled residual stiffness and strength model for fatigue of fibre-reinforced composite materials. *Composite Science and Technology*, 2002, **62** (5), 687–696.
130. **Parepegem, W. V. and Degrieck, J.**, Experimental setup for and numerical modelling of bending fatigue experiments on plain woven glass/epoxy composites. *Composite Structures*, 2001, **51** (1), 1-8.
131. **Instron**. *Performance Envelope Plot*. 2006 [cited 20th August 2006]; Available from: http://www.instron.co.uk.
132. **Pradham, B. and Panda, S. K.**, The influence of ply sequence and thermoelastic stress field on asymmetric delamination crack growth behaviour of embedded elliptical delaminations in laminated FRP composites. *Composites Science and Technology*, 2006, **66** (3-4), 417-426.
133. **Drew, R. C. and White, R. G.** *An investigation into damage propagation and its effect upon dynamic properties of CFRP composite materials*. In *Proceedings of the Fourth International Conference on Composite Structures*. 1987. Paisley College of Technology.
134. **Herakovich, C. T.**, On the relationship between engineering properties and delamination of composite materials. *Journal of Composite Materials*, 1981, **15** (3), 336-348.
135. **Maldague, X. and Marinetti, S.**, Pulse phase infrared thermography. *Journal Applied Physics*, 1996, **79** (5), 2694-2698.
136. **Krishnapillaia, M., Jonesa, R., Marshalla, I. H., Bannisterb, M., and Rajic, N.** *NDTE using pulse thermography: Numerical modeling of composite subsurface defects*. In *Thirteenth International Conference on Composite Structures - ICCS/13* 2006.
137. **Marinetti, S., Plotnikov, Y. A., Winfree, W. P., and Braggiotti, A.**, *Pulse phase thermography for defect detection and visualization*. Nondestructive Evaluation of Aging Aircraft, Airports, and Aerospace Hardware III, ed. Mal, A.K. Vol. 3586. 1999: Proceedings of SPIE.
138. **Ibarra-Castanedo, C., González, D. A., and Maldague, X.** *Automatic algorithm for quantitative pulsed phase thermography calculations*. In *WCNDT - World Conference on Nondestructive Testing*. 2004. Montreal (QC).
139. **Ibarra-Castanedo, C. and Maldague, X.** *Defect depth retrieval from pulsed phase thermographic data on plexiglas and aluminum samples*. In *Thermosense XXVI*. 2004: Proceedings of SPIE - The International Society for Optical Engineering.
140. **Dulieu-Barton, J. M., Earl, J. S., and Shenoi, R. A.**, Determination of the stress distribution in foam-cored sandwich construction composite tee joints. *The Journal of Strain Analysis for Engineering Design*, 2001, **36** (6), 545-560.

141. **Highsmith, A. L. and Reifsnider, K. L.**, eds. *Internal load distribution effects during fatigue loading of composite laminates*. Composite Materials: Fatigue and Fracture, ed. Hahn, H.T. 1986, ASTM: Philadelphia.

Appendices

Appendix A Test specimen manufacture

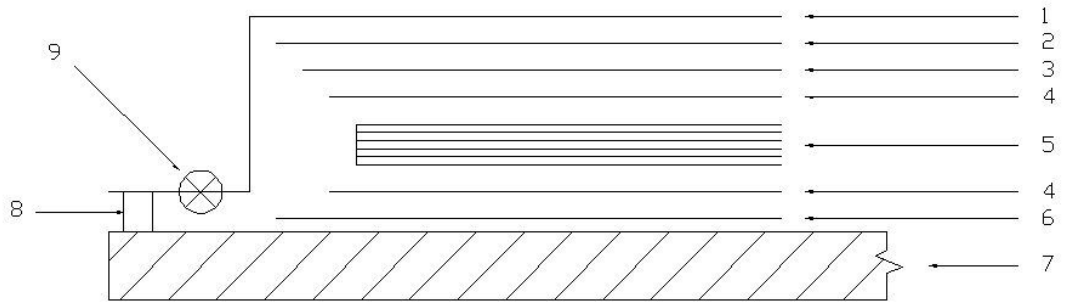

Cross sectional view of pre-preg lay-up routine

Description and purpose of items used in the manufacture of a pre-preg laminate

No.	Item	Purpose / Application
1	Vacuum bagging film	Seal laminate and consumables to the tooling surface (Mould)
2	Breather / bleed fabric	Create a uniform vacuum environment over the entire surface
3	Perforated release film	Allow removal of laminate from stack, allow resin and volatiles to bleed out of the laminate in a controlled manner
4	Peel ply	Leave a clean, textured surface on the laminate
5	Laminate	Composition as determined by desired structure
6	Release agent	Allows removal of laminate after cure cycle
7	Mould	Plate upon which laminate will take the shape
8	Sealant tape	Provide vacuum tight seal around mould
9	Breach valve	Permits evacuation of bagged volume

Appendix B Calibration Tables

B. 1. Strain calibration constant

Calibration constant for DeltaTherm settings

DeltaTherm system	Settings	Calibration constant
DT 1400	35 Hz, 0.986 msec	0.000000177
DT 1400	35 Hz, 1.534 msec	0.000000088
DT 1000	22	0.000000753

B. 2. Temperature calibration files

Temperature calibration files

#	DeltaTherm system	Settings		Temp range (Kelvin)	Material
		Iris	Shutter		
1	DT1000	35		295 – 320	Duralumin
File	DC3=(DC1.^5*(-0.00000000000000923103))+(DC1.^4*0.00000000010123392876)-(DC1.^3*0.00000043735769614886)+(DC1.^2*0.00092158251068846200)-(DC1.*0.91053821882723900000)+614.51154630769700000000				
2	DT1000	22		295 – 320	GFRP
File	DC3=(0.00000000000001484224*(DC1.^5))+(-0.00000000016638189323*(DC1.^4))+(0.00000074132163719440*(DC1.^3))-(0.00164975498875992000*(DC1.^2))+(1.86898911195752000000*(DC1.^1))-(576.56647783883900000000);				
3	DT1410	0.963ms	35 Hz	295 – 320	Duralumin
File	DC3=(0.00000000000000000080*(DC1^5))-(0.00000000000003937891*(DC1^4))+(0.00000000076857328064*(DC1^3))-(0.00000760957243990629*(DC1^2))+(0.04215251216772070000*(DC1^1))+(197.01222574956500000000)				
4	DT1410	1.069 ms	21.8 Hz	295 – 320	GFRP
File	DC3=(-0.00000000000000000090*(DC1.^5))+(0.00000000000004412833*(DC1.^4))-(0.00000000083975495882*(DC1.^3))+(0.00000761603049915303*(DC1.^2))-(0.02841521807041730000*(DC1.^1))+(322.33341627879400000000);				
5	DT1410	0.963ms	35 Hz	295 – 320	GFRP
File	DC3=(0.00000000000000000080*(DC1^5))-(0.00000000000003937891*(DC1^4))+(0.00000000076857328064*(DC1^3))-(0.00000760957243990629*(DC1^2))+(0.04215251216772070000*(DC1^1))+(197.01222574956500000000)				
6	DT1410	1.534 ms	35 Hz	295 – 320	GFRP
File	DC3=(-0.00000000000000000063*(DC1.^5))+(0.00000000000003592786*(DC1.^4))-(0.00000000079782578813*(DC1.^3))+(0.00000849848880579994*(DC1.^2))-(0.03962719513268590000*(DC1.^1))+(347.98170125633800000000);				

Appendix C MATLAB code

C. 1. DeltaVision software header and footer

```
f=fopen('Deltavision_File_IP.asc','wt');          % Data file created in Deltavision

fprintf(f,DT_256_Matrix_Header_IP1,'wt');         % Inputs first line of text
fprintf(f,'\n','wt');                             % Text break

fprintf(f,DT_256_Matrix_Header_IP2,'wt');         % Inputs second line of text
fprintf(f,'\n','wt');                             % Text break

% Repeats for remaining lines of software header

fprintf(f,DT_256_Matrix_Header_IP3,'wt');
fprintf(f,'\n','wt');
fprintf(f,DT_256_Matrix_Header_IP4,'wt');
fprintf(f,'\n','wt');
fprintf(f,DT_256_Matrix_Header_IP5,'wt');
fprintf(f,'\n','wt');
fprintf(f,DT_256_Matrix_Header_IP6,'wt');
fprintf(f,'\n','wt');
fprintf(f,DT_256_Matrix_Header_IP7,'wt');
fprintf(f,'\n','wt');
fprintf(f,DT_256_Matrix_Header_IP8,'wt');
fprintf(f,'\n','wt');
fprintf(f,DT_256_Matrix_Header_IP9,'wt');
fprintf(f,'\n','wt');
fprintf(f,DT_256_Matrix_Header_IP10,'wt');
fprintf(f,'\n','wt');
fprintf(f,DT_256_Matrix_Header_IP11,'wt');
fprintf(f,'\n','wt');
fprintf(f,DT_256_Matrix_Header_IP12,'wt');
fprintf(f,'\n','wt');
fprintf(f,DT_256_Matrix_Header_IP13,'wt');
fprintf(f,'\n','wt');
fprintf(f,DT_256_Matrix_Header_IP14,'wt');
fprintf(f,'\n','wt');
fprintf(f,DT_256_Matrix_Header_IP15,'wt');
fprintf(f,'\n','wt');
fprintf(f,DT_256_Matrix_Header_IP16,'wt');
fprintf(f,'\n','wt');
fprintf(f,DT_256_Matrix_Header_IP17,'wt');
fprintf(f,'\n','wt');
fprintf(f,DT_256_Matrix_Header_IP18,'wt');
fprintf(f,'\n','wt');
fprintf(f,DT_256_Matrix_Header_IP19,'wt');
fprintf(f,'\n','wt');
fprintf(f,DT_256_Matrix_Header_IP20,'wt');
fprintf(f,'\n','wt');
```

```
fprintf(f,DT_256_Matrix_Header_IP21,'wt');
fprintf(f,'\n','wt');
fprintf(f,DT_256_Matrix_Header_IP22,'wt');
fprintf(f,'\n','wt');
fprintf(f,DT_256_Matrix_Header_IP23,'wt');
fprintf(f,'\n','wt');
fprintf(f,DT_256_Matrix_Header_IP24,'wt');
fprintf(f,'\n','wt');
fprintf(f,DT_256_Matrix_Header_IP25,'wt');
fprintf(f,'\n','wt');
fprintf(f,DT_256_Matrix_Header_IP26,'wt');
fprintf(f,'\n','wt');
fprintf(f,DT_256_Matrix_Header_IP27,'wt');
fprintf(f,'\n','wt');
fprintf(f,DT_256_Matrix_Header_IP28,'wt');
fprintf(f,'\n','wt');
fprintf(f,DT_256_Matrix_Header_IP29,'wt');
fprintf(f,'\n','wt');
fprintf(f,DT_256_Matrix_Header_IP30,'wt');
fprintf(f,'\n','wt');
fprintf(f,DT_256_Matrix_Header_IP31,'wt');
fprintf(f,'\n','wt');
fprintf(f,DT_256_Matrix_Header_IP32,'wt');
fprintf(f,'\n','wt');
fprintf(f,DT_256_Matrix_Header_IP33,'wt');
fprintf(f,'\n','wt');
fprintf(f,DT_256_Matrix_Header_IP34,'wt');
fprintf(f,'\n','wt');
fprintf(f,DT_256_Matrix_Header_IP35,'wt');
fprintf(f,'\n','wt');
fprintf(f,DT_256_Matrix_Header_IP36,'wt');
fprintf(f,'\n','wt');
fprintf(f,DT_256_Matrix_Header_IP37,'wt');
fprintf(f,'\n','wt');
fprintf(f,DT_256_Matrix_Header_IP38,'wt');
fprintf(f,'\n','wt');
fprintf(f,DT_256_Matrix_Header_IP39,'wt');
fprintf(f,'\n','wt');
fprintf(f,DT_256_Matrix_Header_IP40,'wt');
fprintf(f,'\n','wt');
fprintf(f,DT_256_Matrix_Header_IP41,'wt');
fprintf(f,'\n','wt');
fprintf(f,DT_256_Matrix_Header_IP42,'wt');
fprintf(f,'\n','wt');
fprintf(f,DT_256_Matrix_Header_IP43,'wt');
fprintf(f,'\n','wt');
fprintf(f,DT_256_Matrix_Header_IP44,'wt');
fprintf(f,'\n','wt');
fprintf(f,DT_256_Matrix_Header_IP45,'wt');
fprintf(f,'\n','wt');
fprintf(f,DT_256_Matrix_Header_IP46,'wt');
fprintf(f,'\n','wt');
fprintf(f,DT_256_Matrix_Header_IP47,'wt');
fprintf(f,'\n','wt');
fprintf(f,DT_256_Matrix_Header_IP48,'wt');
fprintf(f,'\n','wt');
fprintf(f,DT_256_Matrix_Header_IP49,'wt');
fprintf(f,'\n','wt');
fprintf(f,DT_256_Matrix_Header_IP50,'wt');
```

```
fprintf(f,'\n','wt');
fprintf(f,DT_256_Matrix_Header_IP51,'wt');
fprintf(f,'\n','wt');
fprintf(f,DT_256_Matrix_Header_IP52,'wt');
fprintf(f,'\n','wt');
fprintf(f,DT_256_Matrix_Header_IP53,'wt');
fprintf(f,'\n','wt');
fprintf(f,DT_256_Matrix_Header_IP54,'wt');
fprintf(f,'\n','wt');
fprintf(f,DT_256_Matrix_Header_IP55,'wt');
fprintf(f,'\n','wt');
fprintf(f,DT_256_Matrix_Header_IP56,'wt');
fprintf(f,'\n','wt');
fprintf(f,DT_256_Matrix_Header_IP57,'wt');
fprintf(f,'\n','wt');
fprintf(f,DT_256_Matrix_Header_IP58,'wt');
fprintf(f,'\n','wt');
fprintf(f,DT_256_Matrix_Header_IP59,'wt');
fprintf(f,'\n','wt');
fprintf(f,DT_256_Matrix_Header_IP60,'wt');
fprintf(f,'\n','wt');
fprintf(f,DT_256_Matrix_Header_IP61,'wt');
fprintf(f,'\n','wt');
fprintf(f,DT_256_Matrix_Header_IP62,'wt');
fprintf(f,'\n','wt');
fprintf(f,DT_256_Matrix_Header_IP63,'wt');
fprintf(f,'\n','wt');
fprintf(f,DT_256_Matrix_Header_IP64,'wt');
fprintf(f,'\n','wt');
fprintf(f,DT_256_Matrix_Header_IP65,'wt');
fprintf(f,'\n','wt');
fprintf(f,DT_256_Matrix_Header_IP66,'wt');
fprintf(f,'\n','wt');
fprintf(f,DT_256_Matrix_Header_IP67,'wt');
fprintf(f,'\n','wt');
fprintf(f,DT_256_Matrix_Header_IP68,'wt');
fprintf(f,'\n','wt');
fprintf(f,DT_256_Matrix_Header_IP69,'wt');
fprintf(f,'\n','wt');
fprintf(f,DT_256_Matrix_Header_IP70,'wt');
fprintf(f,'\n','wt');
fprintf(f,DT_256_Matrix_Header_IP71,'wt');
fprintf(f,'\n','wt');
fprintf(f,DT_256_Matrix_Header_IP72,'wt');
fprintf(f,'\n','wt');
%
% Inserts data set of manipulated data
fprintf(f,'d\n',numbers);
fprintf(f,DT_256_Matrix_Header_IP73,'wt');          % Software footer
fprintf(f,'\n','wt');                               % Text break
fprintf(f,DT_256_Matrix_Header_IP74,'wt');          % Software footer
fprintf(f,'\n','wt');                               % Text break
fclose(f);                                          % Creates & closes file
```

C. 2. Strain calibration

```
inputfilename1='AC1.txt';              % T/elastic data-set saved from Deltavision as DC1 in ASCII

tempdata1=load(inputfilename1);        % Loads AC1

rows=256;                              % 256 cells to suit DT1410 data array
columns=256;                           % 256 cells to suit DT1410 data array

AC1=zeros(columns,rows);               % Creates 256*256 matrix

tempdata1=tempdata1(:,3);              % Selects DC1 data for manipulation from third column of data set

for index=1:256^2
   AC1(index)=tempdata1(index);        % Applies data to 256*256 matrix
end

display('Material properites')         % GUI display

Alpha=35e-6;
Er=8400;
vR=0.25;
A=1.1452118e-7;

R=((A*(1-vR))/(Alpha*Er));             % Correction factor division
AC5=(AC1.*R)';                         % Manipulation of elevated temperature thermoelastic data

AC5tr=AC5';                            % Produces the transposed of manipulated data for display purposes
   ACOP5=zeros(256*256,1);
for index=1:(256*256) %256x256 matrix
  ACOPstrain(index)=AC5tr(index);

end

strain_file;                           %Application of software header and footer for t/elastic data

save('AC5.txt','AC5','-ascii')
```

C. 3. Integration of Planck's Law

```
function Q=planck(w)
global To                          % Defines working variable To

h=6.6260775e-34;                   % Planck's constant
c=2.99792458e8;                    % Speed of light in a vacuo
k=1.380658e-23;                    % Boltzmann's constant
a=(2*pi*c);                        % Working equation
b=(w.^4);                          % Working equation
g=c*h;                             % Working equation
j=To*w*k;                          % Working equation
z=(g./j);                          % Working equation
d=exp(z);                          % Working equation
[m,n]=size(d);                     % Creates matrix [m, n]
abyb=(a./b);                       % Working equation
abyb=repmat(abyb,m,1);             % Creates matrix copying values of abyb
Q=abyb.*(1./(d-1));                % Calculation
```

Integration for each temperature increment

```
global To                          % Defines working variable To
format short e                     % Scientific numbering to 4dp
for i=1:30                         % Temperature range of 30 Kelvin
   To=293.15+i;                    % Start of temperature range
   area=quad8('Planck',2e-6,5e-6); % Performs 'Planck' between limits
   disp([To,area])                 % Emittance at temperature values
   disp([log(To),log(area)])       % Log/log values
end
```

C. 4. Temperature calibration

```
inputfilename1='DC1.txt';                % Thermal data-set saved from Deltavision as DC1 in ASCII
tempdata1=load(inputfilename1);          % Loads DC1
rows=256;                                % 256 cells to suit DT1410 data array
columns=256;                             % 256 cells to suit DT1410 data array
DC1=zeros(columns,rows);                 % Creates 256*256 matrix

tempdata1=tempdata1(:,3);                % Selects DC1 data for manipulation from third column of data set

for index=1:256^2                        % Applies data to 256*256 matrix
   DC1(index)=tempdata1(index);
end

% Calibration polynomial

DC3=(0.000000000000000080*(DC1.^5))-
(0.000000000000003937891*(DC1.^4))+(0.000000000076857328064*(DC1.^3))-
(0.000076095724399062 9*(DC1.^2))+(0.042152512167720700 00*(DC1.^1))+(197.01222574956500000
000);

DC3tr=DC3;                               % Produces the transposed "row after row" for visualisation

DCOP3=zeros(256*256,1);

display('Data corrected - Run Saving_Text_Numbers');       % GUI
```

C. 5. Temperature correction

```
inputfilename1='DC1.txt';                % Baseline thermal data. Saved as DC1 in ASCII
inputfilename2='DC2.txt';                % Elevated thermal data. Saved as DC2 in ASCII
inputfilename3='AC3.txt';                % Baseline t/elastic data. Saved as AC3 in ASCII
inputfilename4='AC4.txt';                % Elevated t/elastic data. Saved as AC3 in ASCII

display('Correcting data for temperature influence')                % GUI display

tempdata1=load(inputfilename1);          % Loads DC1
tempdata2=load(inputfilename2);          % Loads DC2
tempdata3=load(inputfilename3);          % Loads AC3
tempdata4=load(inputfilename4);          % Loads AC4

rows=256;                        % 256 cells to suit DT1410 data array
columns=256;          % 256 cells to suit DT1410 data array

DC1=zeros(columns,rows);                 % Creates 256*256 matrix
DC2=zeros(columns,rows);                 % Creates 256*256 matrix
AC3=zeros(columns,rows);                 % Creates 256*256 matrix
AC4=zeros(columns,rows);                 % Creates 256*256 matrix

tempdata1=tempdata1(:,3);                % Selects DC1 data from third column of data set
tempdata2=tempdata2(:,3);                % Selects DC2 data from third column of data set
tempdata3=tempdata3(:,3);                % Selects AC3 data from third column of data set
tempdata4=tempdata4(:,3);                % Selects AC4 data from third column of data set

for index=1:256^2
   DC1(index)=tempdata1(index);          % Applies data to 256*256 matrix
   DC2(index)=tempdata2(index);          % Applies data to 256*256 matrix
   AC3(index)=tempdata3(index);          % Applies data to 256*256 matrix
   AC4(index)=tempdata4(index);          % Applies data to 256*256 matrix
end

% GUI display
display('Calibration of thermal data')
display('Operating parameters, please select camera settings to allow temperature calibration')

% Calibration polynomial for manipulation of thermal data to absolute temperature
C=(-0.00000000000000000090*(DC1.^5))+(0.0000000000000004412833*(DC1.^4))-
(0.0000000083975495882*(DC1.^3))+(0.000076160304991530 3*(DC1.^2))-
(0.02841521807041730000*(DC1.^1))+(322.33341627879400000000);
D=(-0.00000000000000000090*(DC1.^5))+(0.0000000000000004412833*(DC1.^4))-
(0.0000000083975495882*(DC1.^3))+(0.000076160304991530 3*(DC1.^2))-
(0.02841521807041730000*(DC1.^1))+(322.33341627879400000000);
E=(-0.00000000000000000090*(DC1.^5))+(0.0000000000000004412833*(DC1.^4))-
(0.0000000083975495882*(DC1.^3))+(0.000076160304991530 3*(DC1.^2))-
(0.02841521807041730000*(DC1.^1))+(322.33341627879400000000); F=(-
0.00000000000000000090*(DC1.^5))+(0.0000000000000004412833*(DC1.^4))-
(0.0000000083975495882*(DC1.^3))+(0.000076160304991530 3*(DC1.^2))-
(0.02841521807041730000*(DC1.^1))+(322.33341627879400000000);

DC_baseline=input('If 35Hz/0.986ms enter C, if 22Hz/1.534ms enter D>, If....');
DC_modified=input('If 35Hz/0.986ms enter C, if 22Hz/1.534ms enter D>, If....');

DC3=DC_baseline;
DC4=DC_modified;
```

```
A=9.5;
B=9.8;

display('Selection of operating hardware')                    % GUI display

n=input('If DT1000 enter A or DT1410 enter B>');              % Power index

display('Correction of thermoelastic data for temperature variation') % GUI display

R=(DC3./DC4);                                                 % Correction factor division
R2=(R.^n);                                                    % Correction factor ^n
AC5=(AC4.*R2)';                                % Manipulation of elevated temperature t/elastic data

AC5tr=AC5';                                    % Produces the transposed of manipulated data for display
ACOP5=zeros(256*256,1);

for index=1:(256*256)
   ACOP5(index)=AC5tr(index);
end

% GUI display
display('Data corrected')
display('Run - Saving Text Numbers - to allow data to be visualised in Deltavision')
```

C. 6. TSA damage analysis

```
inputfilename1='AC1.txt';          %Baseline t/elastic data. Saved as AC1 in ASCII
inputfilename2='AC2.txt';          % Damaged t/elastic data. Saved as AC1 in ASCII

tempdata1=load(inputfilename1);    % Loads AC1
tempdata2=load(inputfilename2);    % Loads AC2

rows=256;                          % 256 cells to suit DT1410 data array
columns=256;                       % 256 cells to suit DT1410 data array

AC1=zeros(columns,rows);           % Creates 256*256 matrix
AC2=zeros(columns,rows);           % Creates 256*256 matrix

tempdata1=tempdata1(:,3);          % Selects AC1 data for manipulation from third column of data set
tempdata2=tempdata2(:,3);          % Selects AC2 data for manipulation from third column of data set

for index=1:256^2
   AC1(index)=tempdata1(index);    % Applies data to 256*256 matrix
   AC2(index)=tempdata2(index);    % Applies data to 256*256 matrix
end

AC5=(AC2-AC1);
AC6=(AC5./AC1)*100;

iim1=find(AC6<=-15);
iim0=find((AC6>-15)&(AC6<15));
iip1=find(AC6>20);
iihigh=find(AC6>500);

output=zeros(size(AC6));           %matrix of size
output(iim1)=0;
output(iip1)=1;
output(iim0)=0;

dave=output;
ben=dave.*AC6;

AC5tr=ben;                         % Produces the transposed of manipulated data for display purposes
   ACOP5=zeros(256*256,1);
for index=1:(256*256)
  ACOP5(index)=AC5tr(index);
end
```

Appendix D Temperature calibrated plots

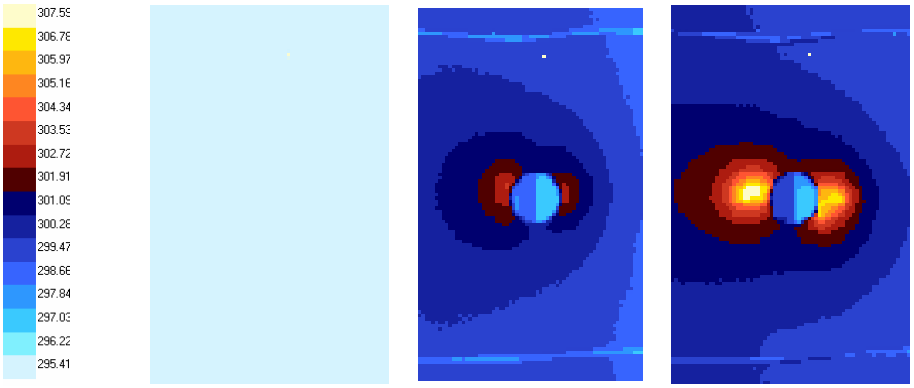

Scale (Kelvin) a) Step 1 b) Step 14 c) Step 16

Temperature distribution for Crossply

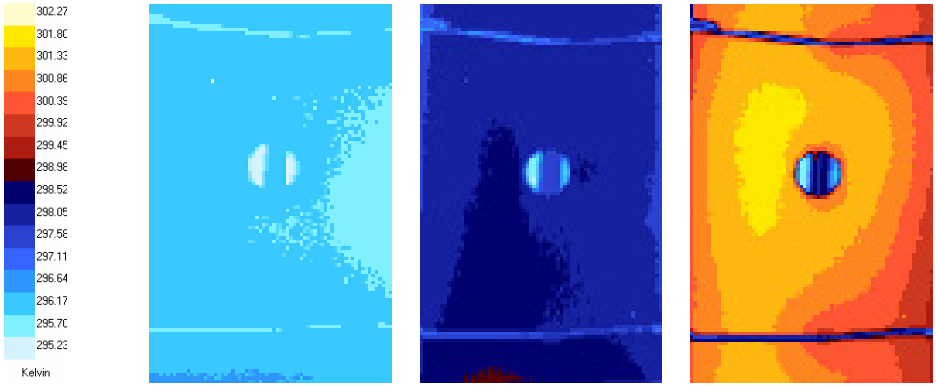

Scale (Kelvin) a) Step 1 b) Step 8 c) Step 16

Temperature distribution for Quasi-isotropic

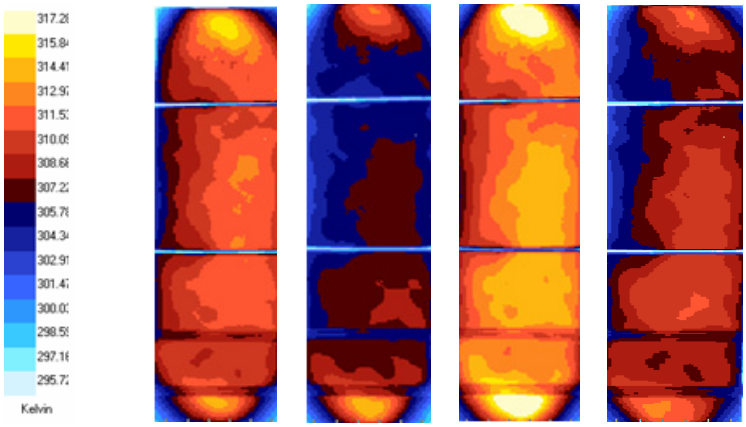

Scale (Kelvin) a) Step 1 b) Step 3 c) Step 4 c) Step 9

Temperature distribution for Angle ply

Appendix E List of publications

1. **Emery, T., Dulieu-Barton, J. M., and Cunningham, P. R.,** *Identification of damage in composite structures using thermoelastic stress analysis.* Key Engineering Materials, 2005, **279-288**, 583-590.
2. **Dulieu-Barton, J. M., Emery, T. R., Quinn, S., and Cunningham, P. R.,** *A temperature correction methodology for quantitative thermoelastic stress analysis and damage assessment.* Measurement Science and Technology, 2006 **17** (6), 1627-1637.
3. **Emery, T. R. and Dulieu-Barton, J. M.,** *Damage monitoring of composite materials using pulsed phase thermography and thermoelastic stress analysis.* Key Engineering Materials, 2007, **347**, 621-626.
4. **Emery, T. R., Dulieu-Barton, J. M., Earl, J., and Cunningham, P. R.,** *A generalised approach to the calibration of orthotropic materials for thermoelastic stress analysis*. Submitted to Composites Science and Technology, 2007.
5. **Emery, T. R. and Dulieu-Barton, J. M.,** *Thermoelastic stress analysis of damage mechanisms in composite materials*. Submitted to Composites Part A, 2007.